Mid-infrared InGaAs/InAlAs Quantum Cascade Lasers(Dissertation_全文)

AUTHOR(S):

Fujita, Kazuue

Mid-infrared InGaAs/InAlAs Quantum Cascade Lasers

Kazuue FUJITA

2014

Abstract

Quantum cascade (QC) lasers are one of the best arenas for wave function engineering, using ultrathin semiconductor layers grown by molecular beam epitaxy (MBE) or metal organic vapor phase epitaxy (MOVPE) techniques. By using wavefunction engineering, different from band structure engineering, the basic properties of QC lasers, such as the transition strength, the lifetime of each state, and the strength of the coupling between states, are uniquely determined by the design of the wavefunctions in quantum cascade structures.

Since the earliest demonstration of QC lasers, tremendous efforts have been made to obtain a stronger population inversion, by the design of the quantum cascade structures: a large dipole matrix element, short lower laser-state lifetime, long upper laser state lifetime, and high injection efficiency for the upper laser state. As a consequence, a lot of active region designs, such as single, multiple phonon resonance, chirped superlattices, bound-to-continuum, and injectorless designs, have been proposed. The continuous-wave (CW) operation of quantum cascade lasers above room temperature have been demonstrated in a wide wavelength range between 3–12 μm. On the short wavelength side (4.9 μm), a high output power of more than 5 W as well as a wall plug efficiency (WPE) of 27% have been achieved. Meanwhile, on the longer wavelength side (>8 μm), despite the larger absorption coefficient, high performance CW and pulsed operation of QCLs has been reported by several research groups. However, in the end, for the pump scheme, only the direct pump scheme in which the upper laser states are pumped directly by electron tunneling from the ground state in the injector has continued to be used. In other words,

not much attention has been paid to the electron dynamics in the QCL structure.

In this thesis, two novel upper quantum-state designs: an indirect pump (IDP) scheme and an anticrossed dual upper-state (DAU) design are presented. They lead to high laser performances as well as high characteristic temperatures (T_0-value) by taking advantage of a strong suppression of the electron populations in the injectors. The IDP scheme for QC lasers is an alternative pump scheme resulting in high device performance for the long wavelength range. The absorption quenching induced by the decrease of the electron population in the injector significantly affects the temperature dependent threshold current density: as a result, the characteristic temperatures of these IDP-QC lasers have been observed to be very high, compared to those of conventional direct pumping QC lasers. In fact, IDP lasers, operating at λ ~15 μm, exhibit a low threshold current-density of ~3.5 kA/cm^2 and a high maximum output power of ~216 mW with a high slope efficiency of 346 mW/A, all at room temperature. An extremely high T_0-value for the threshold current is observed: T_0 ~450 K over a wide temperature range, 320–380 K.

On the other hand, the broad-gain QC laser based on the anti-crossed DAU design shows homogeneous wide electroluminescence spectra of which the shapes are insensitive to voltage changes. These lasers, emitting at λ ~8.7 μm, demonstrate an astonishingly high T_0-value over 1000 K as well as super-linear current-light output characteristics which have never been reported in the literature for QC lasers. The distinctive characteristics of these DAU lasers are revealed to be attributable to optical absorption quenching. In these lasers, the optical absorptions in the injector decreases steeply with increasing current for lasing with increasing device temperature. The steep decrease in the electron population can take place in the DAU-QC lasers since in this design the electrons are distributed in three states: two upper states and the ground state in the injector. As a result, the

electron population n_1 at high pump current is smaller than that in the conventional direct pump design. By taking advantage of such a strong suppression of the electron populations in the injectors, QC lasers based on both the indirect pump scheme and the anticrossed DAU designs have demonstrated remarkably high characteristic temperatures.

Furthermore, as a result of optimizing the anticrossed DAU design, an extremely wide electroluminescence ($>$600 cm^{-1} FWHM, $\Delta\lambda/\lambda_0 \sim$0.4) has been demonstrated at room temperature. Despite showing such broad electroluminescence spectra, the buried hetero-structured lasers operating at 6.8 μm demonstrate a low threshold current density of $\sim$1.5 kA/cm^2 and a high power of $>$500 mW with a high slope efficiency of $\sim$1.6 W/A in CW mode at 300 K. By using this device, a wide tuning range of 248 cm^{-1} in CW operation has been achieved with external cavity setup.

Contents

Chapter 1

Introduction

Since the proposal of semiconductor superlattice structures by Esaki and Tsu in 1970 [1], extensive research on electron transport in superlattice and multiple quantum well structures has been carried out using ultrathin semiconductor layers grown by molecular beam epitaxy (MBE) or metal organic vapor phase epitaxy (MOVPE). In particular, the quantum well laser and the high electron mobility transistor (HEMT) have already been put to practical use as important devices for advanced information and communication technology. Superlattice and quantum well structures have the potential to create additional subbands and minibands, therefore allowing of modulating the current–voltage characteristics and generating negative differential resistance. In addition, wavefunction engineering, unlike band structure engineering, proposed by Sakaki in 1986, allows of uniquely determining basic device properties by designing wavefunctions in quantum structures [2, 3, 4]. These discoveries broke new ground in many research areas, some of them leading to revolutionary inventions that provide great benefits. Among them, the quantum cascade (QC) laser is one of the best arenas for wavefunction engineering [5]. QC lasers, unlike conventional semiconductor diode lasers, are based on intersubband transitions between the conduction band states due to the size quantization in semiconductor quantum wells. In conventional semiconductor lasers, the wavelength is determined by the band gap of the active layer material, since the light emission results from radiative recombination of electron–hole pairs at the band edge or at near band-edge quantum states. On the other hand, the emission wavelength of QC lasers is determined

by energy level differences controlled by the well and barrier thicknesses and the applied electric field. QC lasers with the same material systems, such as InGaAs/InAlAs, GaAs/AlGaAs, and InAs/AlSb, cover a broad wavelength area: mid-infrared, 3–24 μm or the terahertz region.

Currently, in the mid-infrared range, it has become the most promising light source for many applications, such as trace gas sensing, environmental monitoring, homeland security, health diagnostics, and other biomedical applications. In addition, by making full use of wavefunction engineering, QC lasers provide high design flexibility: the basic properties of QC lasers, such as their transition strength, the lifetime of each state, and the strength of the coupling between states, are uniquely determined by the design of the wavefunctions in the quantum cascade structures. However, for the pump scheme, only the direct pump (DP) scheme in which the upper laser states are pumped directly by electron tunneling from the ground state in the injector has continued to be utilized. In other words, not much attention has been paid to the electron dynamics in the QC laser structure relevant to the upper quantum states. In this thesis, we exploit the advantages of a QC structure with designed upper quantum states and develop several novel design concepts which lead to high device performance by taking advantage of the electron dynamics in QC structure.

1.1 Birth of the quantum cascade laser

The idea of light amplification in the intersubband transitions within semiconductor quantum wells was first proposed by Kazarinov and Suris in 1971 [6, 7], when electrons are transported through a semiconductor superlattice. In this scheme, electrons are transferred from the ground state 1 to the excited state 2 in an adjacent quantum well (QW) by tunneling, with simultaneous emission. Population inversion is made possible by the relatively long non-radiative relaxation time associated with the diagonal transition between adjacent wells. During the same period, Cho and Arthur of Bell Labs invented the molecular beam epitaxy (MBE) technique, which can deposit single atomic layers on a surface [8, 9]. This allows the fabrication of superlattices and semiconductor quantum well structures. Ten

years later, a breakthrough in intersubband and superlattice researchers was accomplished: the first observation of intersubband absorption in a GaAs/AlGaAs quantum well in 1985 [10] and the first observation of sequential resonant tunneling in a superlattice by Capasso et al. in 1986 [11]. In sequential resonant tunneling, electrons are injected into the second excited state of a quantum well, followed by a laser transition to the lower excited state and non-radiative relaxation via longitudinal (LO) phonon scattering from the latter to the ground state. Electrons are then reinjected into the next stage and so on, sequentially through many quantum wells. Helm et al. demonstrated the first intersubband emission in the terahertz range, pumped by thermal excitation [12] and by resonant tunneling [13]. The main technological challenge to achieving laser action in a unipolar intersubband laser was the prevention of undesirable field-domain formation and establishing a population inversion. The quantum leap happened when Faist and co-workers developed the first quantum cascade laser in 1994 at Bell Labs in the group of Capasso [5].

The first quantum cascade laser was grown using MBE in a lattice matched InGaAs/InAlAs/InP material system. The wavelength of the laser was 4.2 μm and the laser operation with high threshold current density ($\sim$14 kA/cm^2) was limited in pulsed mode at low temperature. A schematic illustration of the band structure is shown in Fig 1.1. In this design of the three coupled quantum wells, electrical pumping was achieved by 25-period active regions with compositionally graded layers. The straight arrow indicates the optical transition in the active region between states 3 and 2 where the wave functions are spatially diagonal in real space to increase the non-radiative relaxation time. To achieve population inversion, the energy separation between the lower laser states 2 and 1 is designed to be separated by one phonon energy, which results in very fast electron depopulation from the lower laser state 2 via LO phonon scattering. This scattering is much faster than the relaxation between states 3 and 2 due to the large in-plane momentum transfer. The graded superlattice region (injector region) gathers electrons from the lower states 2 and 1, and the region in which electrons are injected into the upper laser state 3 in the next stage by resonant tunneling through the injection barrier. The injector region functions as an electron reservoir. In each injector region, the center part is doped with n-type impurity

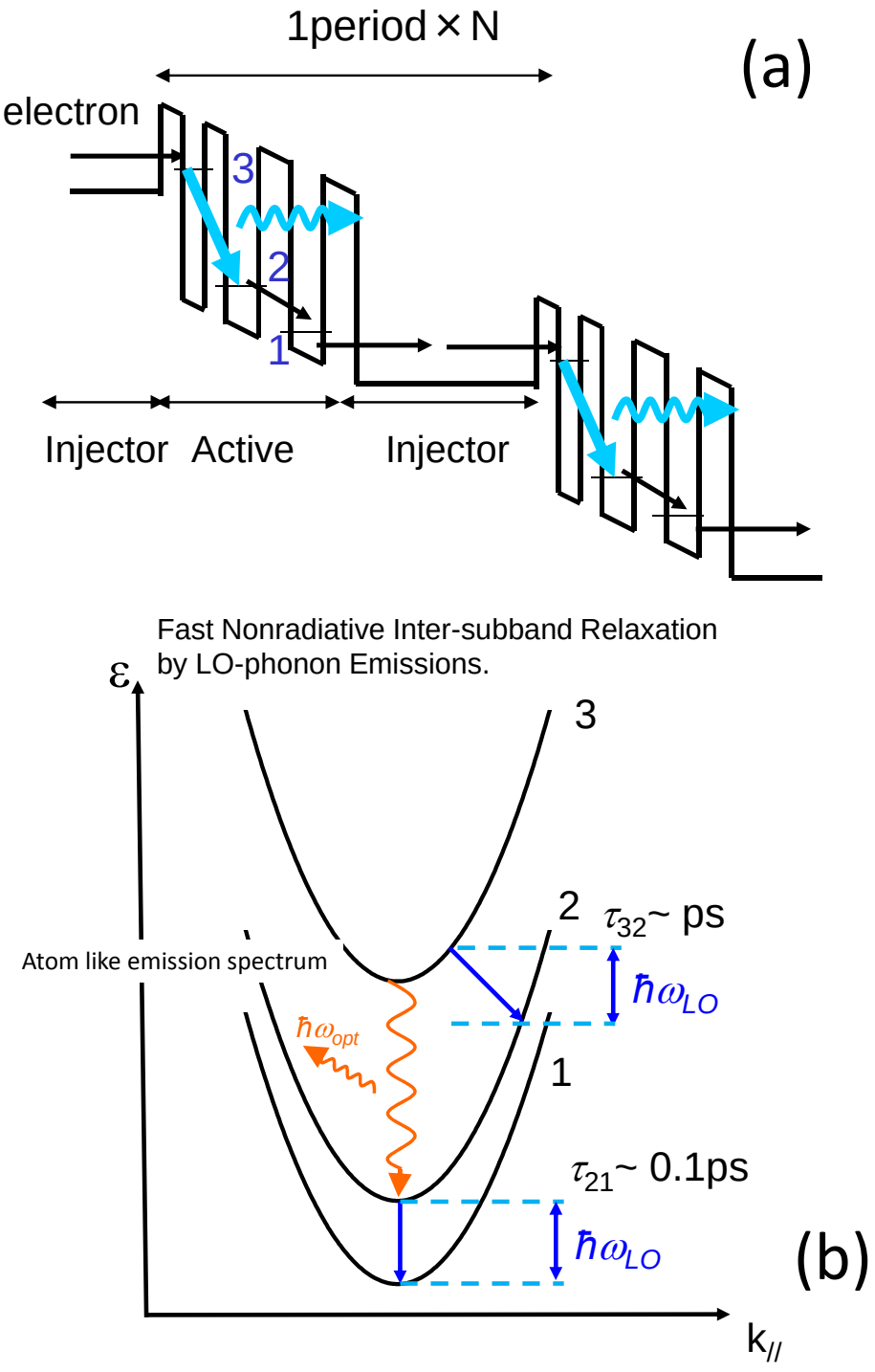

Figure 1.1: (a) Schematic of quantum cascade laser, including conduction band profile. (b) In-plane momentum space (kk) diagram of subbands and allowed relaxation paths via LO phonon and photon emission.

(typically silicon) to prevent space charge effects, and to supply electrons in the active region. Electrons are recycled in multiple cascade stages, and fundamentally, the maximum photon number is determined by the total number of active region stages.

1.2 Material system for quantum cascade laser

Because of the flexible nature of intersubband transitions, quantum cascade lasers are not restricted to some specific material systems, though the conduction band offset limits the shortest operating wavelength. So far, in addition to the original InGaAs/InAlAs/InP material system, several heterostructure material systems have been demonstrated, such as GaAs/AlGaAs [14], InAs/AlSb [15, 16], and InGaAs/AlAsSb [17, 18]. However, the performance of GaAs/AlGaAs QC lasers has been inferior to that of InP-based QC lasers because of the heavier effective electron masses as well as the lower conduction band offsets in the GaAs/AlGaAs material system, though the first terahertz QC lasers were demonstrated in GaAs/AlGaAs due to the flexibility in barrier heights in the long wavelength range [19]. InAs/AlSb and InGaAs/AlAsSb material systems are difficult to handle compared to the InGaAs/InAlAs/InP material system, and less developed so far. Currently, QC lasers based on these material systems still exhibit high threshold current densities. In the end, room temperature continuous wave operation of QC lasers has only been achieved in the lattice matched or strain-compensated InGaAs/InAlAs/InP material system. This material combination, used throughout the present study, has the following advantages over the other material systems. First, the electron masses (InGaAs: $m^* = 0.043m_0$) are relatively lighter, leading to both larger oscillator strengths and smaller optical phonon scattering rates. The large band offset $\Delta E_c = 0.52 - 0.8$ eV enables the design of lasers in a large wavelength range from $\lambda > 3.0$ μm [20]. In addition, the InP substrate has a lower refractive index than either InAlAs or GaInAs: it is suitable for cladding material. Furthermore, because it is a binary material, it provides good thermal transport, reducing the thermal resistance of the device. In this thesis, the InGaAs/InAlAs heterostructure of the QC lasers has been grown by MBE or MOVPE growth technique, which is now a well established

platform for high volume production of reliable semiconductor lasers. The laser performances of both the MBE and MOVPE grown devices are comparable.

Table 1.1: Values of band offsets (eV) and effective masses for various semiconductor heterostructures.

	GaAs/AlGaAs	InGaAs/InAlAs	InGaAs/AlAsSb	InAs/AlSb
ΔE_c	0-0.035	0.5-0.8	1.6	2.1
m^*/m_0	0.067	0.043	0.043	0.023

1.3 Development of active region designs

Since their invention, QC lasers have made dramatic progress in terms of device performance. In the QC structures, there exists the dominant non-radiative scattering due to LO phonon emission. For this reason, quantum cascade lasers tend to exhibit very high threshold current densities compared to conventional diode lasers, thus, the optimization of the active region design is an essential part of the development of QC lasers. The upper state lifetime is basically controlled by the LO phonon emission rate. The fundamental limit on the threshold current density is estimated to be around 1 kA/cm^2 at room temperature for lasers in the 4–10 μm wavelength range. The threshold current is pushed up by parasitic processes such as the injection efficiency for the upper state, escape of electrons from the upper state, and the long relaxation time of the lower state.

Vertical transition design and injector minigap [21]

In the first QC laser, the upper state was located close to the top of the barriers, in this case, an electron could escape into the continuum. In order to minimize the escape into the continuum, Faist et al. demonstrated an active region with an injector minigap of the superlattice in which the electrons in the upper state are confined by Bragg reflection. Using this concept, a vertical transition which improved the radiative overlap and led to a relatively narrow linewidth has also

been achieved. A device employing this design exhibits a lower threshold current density of 3 kA/cm^2 at 100 K [21], compared to the original laser.

Three quantum well active region [22]

Although the threshold current density of a laser based on the vertical transition design is successfully reduced at low temperature, the maximum operating temperature is still limited to slightly above 200 K. This is mainly because the injection efficiency for the upper laser state might decrease as the temperature increases. In 1996, Faist et al. proposed a modified vertical transition design by adding a third thin quantum well to the structure. This design, called the three quantum well active region design, enhances the coupling of the upper state with the ground state of the injector while maintaining a weak coupling between injector states and the lower laser state. Lasers with this design have successfully operated above room temperature in pulsed operation [22, 23].

Chirped superlattice active regions [24, 25]

In another line of work, active regions based on superlattice structures were demonstrated by Scamarcio et al., in which the laser transition occurs between the states of a superlattice minigap. A key feature of the designs is the large oscillator strength of the optical transition at the Brillouin zone boundary of the superlattice. Population inversion is easily obtained with the very short lifetime at the top of the first lower miniband 1 ($\sim$ 0.1 ps) compared to the longer lifetime from the upper miniband 2. Although a high doping for the active superlattice region, which causes high optical losses and line broadening of the optical transition, was required for maintaining a flat band profile at the first attempt, later Tredicucci et al. presented a chirped superlattice active region design in which the doping is restricted to the injector region: as a result, this room temperature operation is possible with a high output power in pulsed mode [25]. This design was successful for operating QC lasers in the long wavelength region (>15 μm) [27, 28, 29, 30] and the first terahertz QC laser was achieved with this design [19].

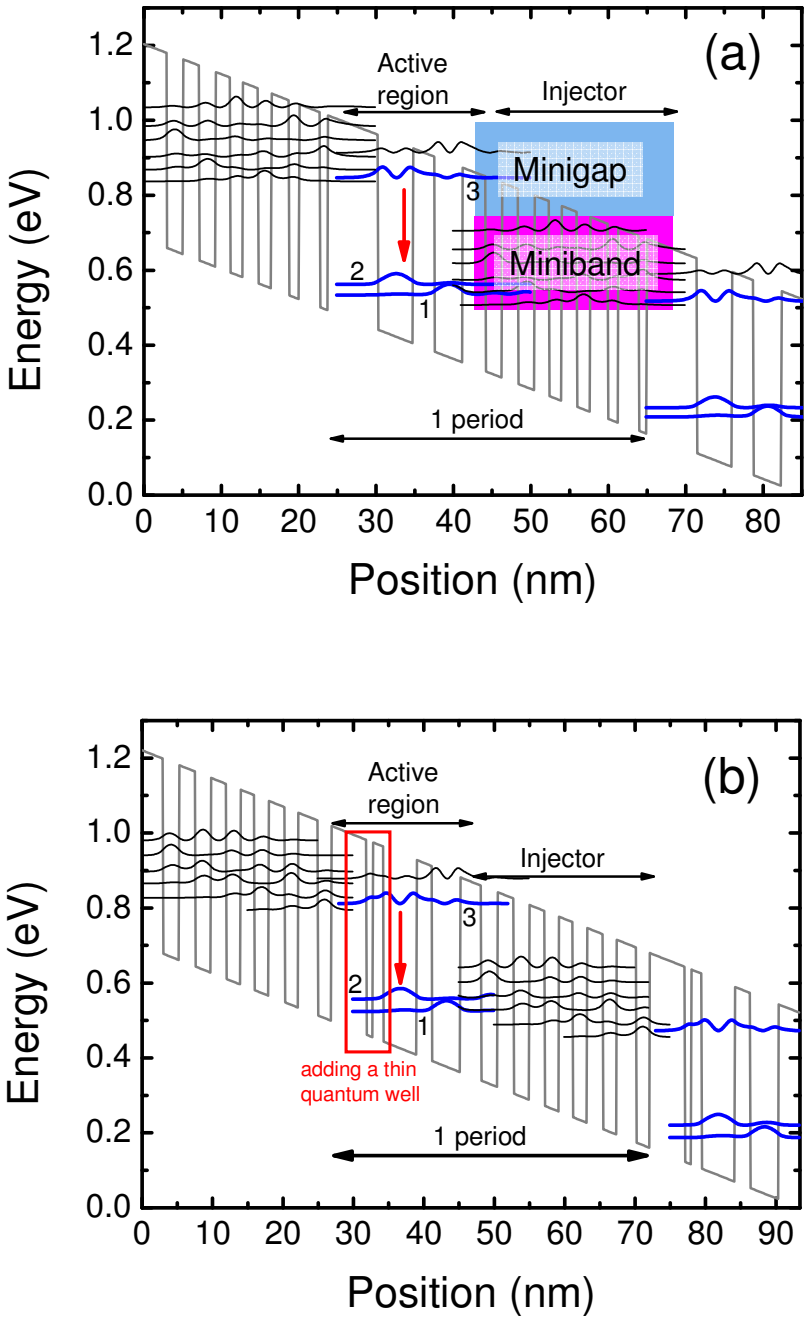

Figure 1.2: Schematic conduction band diagram of a portion of the active region of the structure. The red arrows indicate the transition (3–2) responsible for laser action. The moduli squared of the relevant wave functions are shown. (a) Band diagram of a portion of the two quantum well quantum cascade laser structure based on vertical transition scheme [21]. (b) Band diagram of a portion of the three quantum-well active region [22].

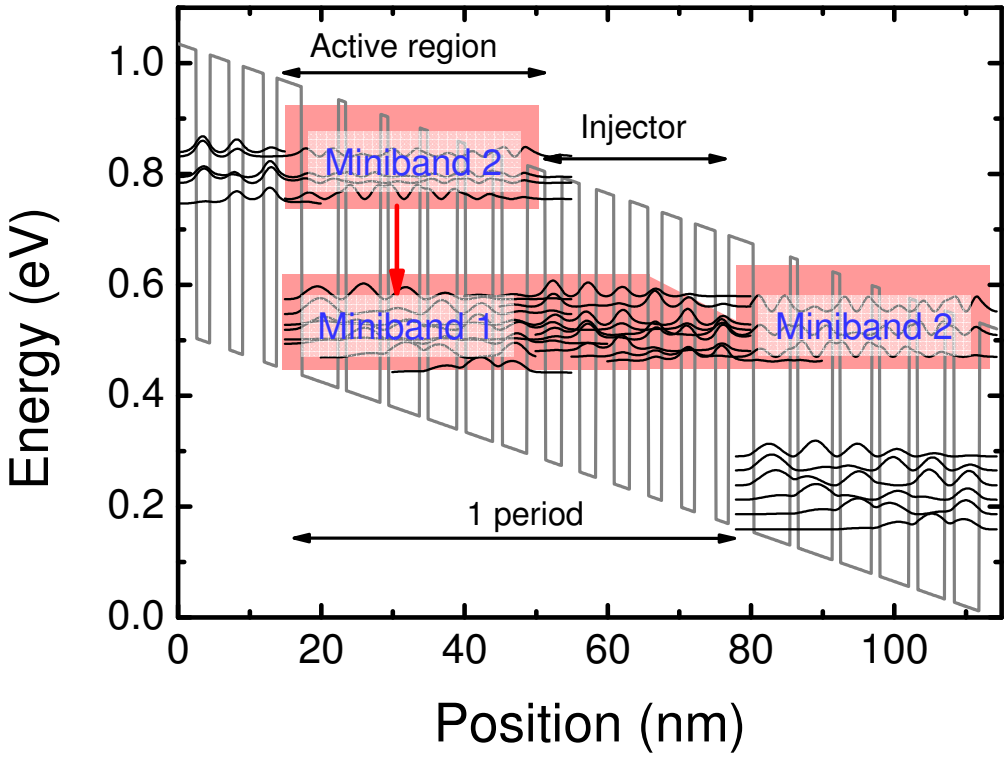

Figure 1.3: Conduction band profile of the chirped superlattice active region. The shaded regions indicate the energy and spatial extension of the manifold of miniband-like states. The red arrow shows the lasing transition between the levels 2 and 1 at the edge of the minigap; the moduli squared of their wavefunctions are also plotted [25].

Two phonon resonance active region and bound-to-continuum transition [31]

Although the three quantum well and chirped superlattice designs demonstrated room temperature operation, they were obtained only in pulsed mode. The three quantum well active region suffered from a limited extraction from the lower state of the active region. Conversely, in the chirped superlattice active region, current injection was not very efficient. Thus, further optimization was performed on two active regions. First, the two phonon resonance active region design is based on a four level system with the laser transition occurring between the level 4 and 3, while the three lower levels are separated by optical phonon energy [32, 33]. In this way, a high injection efficiency can be obtained while thermal backfilling of the lower laser state is reduced. Another approach, the bound-to-continuum design, combines the upper state of the three quantum well design with the lower miniband of the superlattice design [34]. In this design, a thin first well is added in the chirped superlattice design without a separation between active region and injector region. As a result, the upper state is localized around the thin first well while the lower state is spread out over the whole active and injector regions. This design inherently results in diagonal transition and therefore suitable for long wavelength operation [35]. The first CW operation at room temperature by a QC laser was achieved based on the two phonon resonance active region [36], so that these two designs are widely used in the QC laser community.

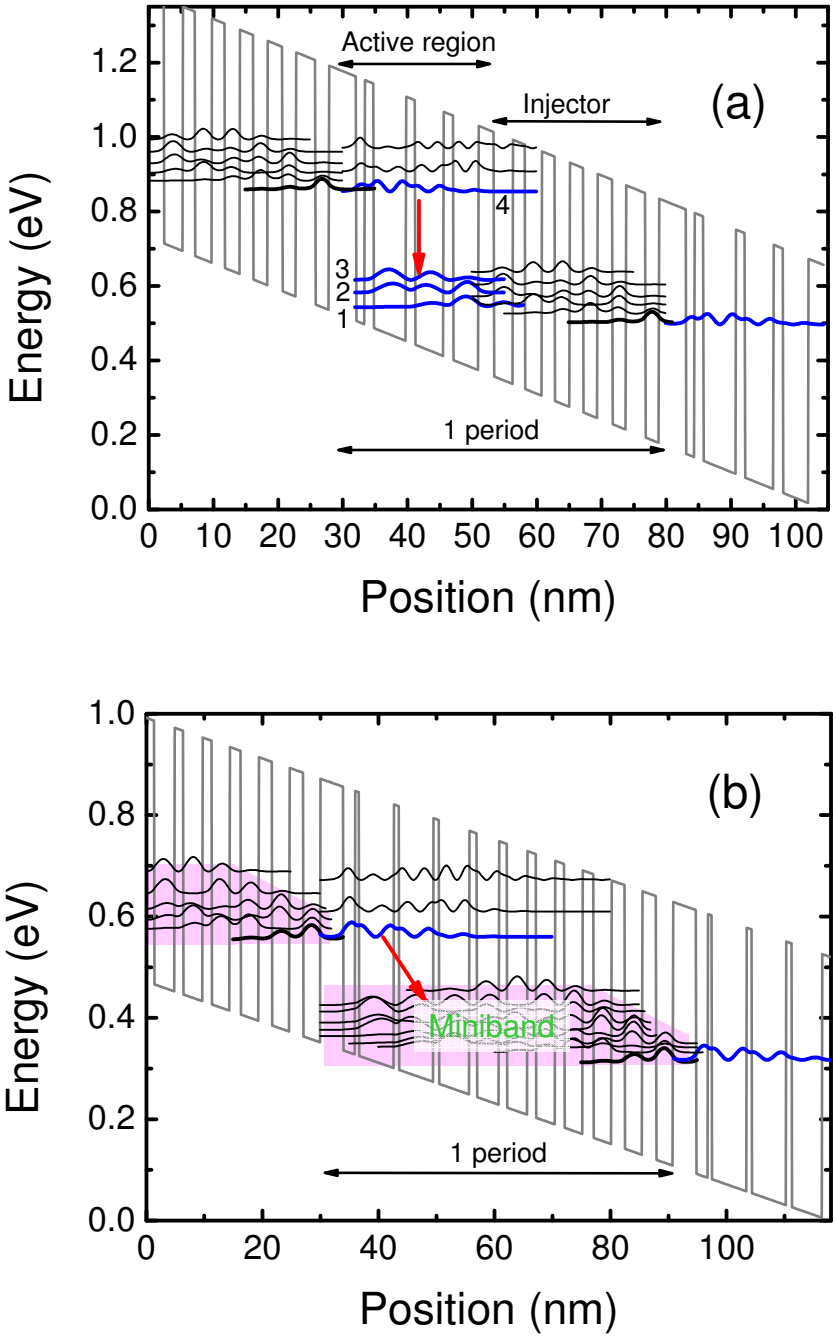

Figure 1.4: (a) Schematic conduction band diagram of a portion of the two phonon resonance active region design and moduli squared of the relevant wave functions of a 5.3 μm QC laser with a 4 QW active layers [32]. (b) Band diagram of the bound to continuum active region design [34].

1.4 The state of the art QC lasers

Continuous-wave operation of QC laser above room temperature

As a result of an optimization of the active region designs and an improvement in thermal management, using a buried hetero-structure, Beck et al. demonstrated the first continuous-wave operation of a QC laser at room temperature, emitting at 9 μm, with an output power of 17 mW [36]. The first CW-QC laser was based on a two-phonon resonance active region and adopting for the waveguide undoped InP and epi-down mounting on diamond, resulting in a reduction of the thermal resistance. One year later, Yu et al. at Northwestern University demonstrated room temperature continuous wave operation at 6 μm [37]. They also exhibit CW operation at room temperature for several wavelengths with high output power [38, 39, 40, 41]. In 2006, Diehl et al. at Harvard University demonstrated CW operation up to 400 K and high output powers of 312 and 204 mW at $\lambda\sim$5.3 and 8.4 μm, respectively [42, 43]. The lasers were based on the double phonon resonance design and were grown by MOVPE, using Iron doped InP to bury the active region. More recently, Bai et al. at Northwestern University and Lyakh et al. at Pranalytica independently demonstrated high output power, greater than the Watt level, at $\lambda\sim$4.6 μm [44, 45], by optimizing the doping of the waveguide and device geometry. Currently, a record wallplug efficiency at room temperature of 27% in CW operation was achieved for a $\lambda\sim$4.9 μm QC laser [46]. The maximum output power of the device reaches 5 W at room temperature.

Broad-gain quantum cascade laser sources

The gain curve (or electroluminescence) in QC lasers is inherently narrow due to the inter-subband transition, but a broader gain bandwidth is required for many applications. A broad gain bandwidth leads to a higher threshold current density since the peak gain is proportional to the inverse of the gain bandwidth. A typical EL linewidth due to bound-to-bound vertical transition shows $\sim$20 meV of FWHM at room temperature [47, 48]. On the other hand, the bound-to-continuum design exhibits a broader EL linewidth $\sim$35 meV. However, the

linewidth decreases steeply with increasing applied bias [48]. In order to obtain a broader gain spectrum, heterogeneous active regions with different emission wavelengths in one laser core have been proposed [49]. Using this approach, Gmachl et al. demonstrated an ultra-broadband spectral width of over 400 cm^{-1}. On the other hand, Maulini et al. and Wittmann et al. demonstrated combined two bound-to-continuum designs, in which the center wavelength of the individual stacks was designed for emission at 8.4 and 9.6 μm, ensuring a spectral overlap [51, 52]. These heterogeneous cascade techniques have been used for many applications, by being integrated with external cavity systems and an array of distributed feedback laser configurations [53].

External cavity systems [50] including QC lasers are the most promising configuration for broadband wavelength tuning. Recently, QC lasers with multiple stacks of active regions [49, 52, 54] have been developed to expand the tuning wavelength range of external cavity QC lasers. For instance, a 5 stack laser [54] demonstrates a wide wavelength tuning of 432 cm^{-1} and another 2 stack laser [52] also had a tuning range of 292 cm^{-1}, both at room temperature. The latter laser achieved CW operation above room temperature by using a combination of epi-side down mounting with a diamond heat-sink and buried hetero-structure. However, in QC lasers with a number of stacks with different resonant wavelengths, a serious mode competition [55] inhibiting the stable single mode operation may take place unless the gain curves of the different cascade stages overlap sufficiently.

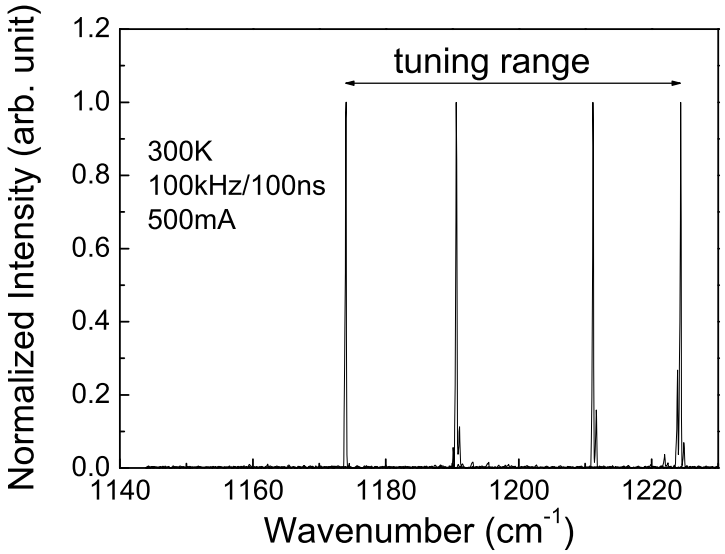

Figure 1.5: Typical tuning behavior of an external cavity QC laser with translational symmetry active region at various wavelengths.

1.5 Scope and organization of this thesis

The objective of the research described in this thesis is to improve device performance by using wavefunction engineering. This study focuses on exploiting the design flexibility in QC structures. We propose novel upper quantum-state designs: indirect pump (IDP) scheme and anti-crossed dual-upper-state (DAU) design. In these designs, another upper quantum state is incorporated to improve laser performances. Although room temperature CW operation of QC lasers has already been achieved by the adoption of the two phonon resonance and bound-to-continuum active region designs, in the end, for a pump scheme, only a direct pump scheme in which the upper laser levels are pumped directly by electron tunneling from the ground level of the injector have continued to be used. In other words, not much attention has been paid to the electron dynamics in a QC laser structure. On the basis of a rate equation model of three types of upper quantum states, we clarify the advantages of the IDP scheme and the anti-crossed DAU design over the conventional direct pump scheme. The IDP scheme for QC lasers proposed in this study is an alternative pump scheme resulting in high device

performance for the long wavelength range by taking advantage of the electron dynamics in the injector. The absorption quenching induced by the decrease of the electron population in the injector significantly affects the temperature dependent threshold current density: as a result, the characteristic temperatures of these IDP-QC lasers have been observed to be very high, compared to those of conventional direct pumping QC lasers. On the other hand, QC lasers with anti-crossed DAU designs have demonstrated a wide electroluminescence and high characteristic temperatures, in which a weak temperature dependence of the peak gain, in addition to the electron dynamics, has an important role in the threshold current density. Despite showing such broad electroluminescence spectra, the buried hetero-structured lasers demonstrate a low threshold current density and high power with a high slope efficiency in CW mode at room temperature. The author believes that the results of this study will strongly influence approaches to the design and modeling of QC lasers. The outline of this thesis is summarized in Fig. 1.6.

Chapter 2 $\cdots$ The theoretical models used to design the quantum cascade laser structure are discussed, including the calculation of the radiative and non-radiative intersubband transition rates, and the modeling of the resonant tunneling transport. In addition, we clarify the advantages of the indirect pump scheme and the dual-upper-state design by using a rate equation approach.

Chapter 3 $\cdots$ This chapter presents specific design methods for QC lasers from the aspect of wave function engineering and waveguides. Based on this method, we demonstrate CW operation of the QC lasers with a newly proposed single phonon resonance-continuum depopulation (SPC-depopulation) structure at room temperature by taking advantage of the high device performance as well as the expected allowance for device-to-device fluctuations of the energy separation between the lower states. Furthermore, we develop the SPC depopulation structure and achieve the highest wall-plug efficiency in the wavelength range of 7–9 μm.

Chapter 4 $\cdots$ A novel pump scheme, called the indirect pump scheme, for QC lasers is presented and discussed. Lasers with the IDP scheme exhibit a

high device performance at the long wavelength of ∼15 μm. As a result of a felicitous design of the active region and waveguide structure, a low threshold current-density of ∼3.5 kA/cm^2, a high maximum output power of ∼216 mW, and a high slope efficiency of 346 mW/A, all at room temperature, are obtained for the λ∼15 μm laser based on the IDP scheme. The observed extremely high characteristic temperature of the threshold current, T_0 ∼450 K over a wide temperature range, 320–380 K, is ascribed to a strong suppression of the electron populations in the injectors.

Chapter 5 ⋯ In Chapter 5, we present a broad-gain QC laser design with anti-crossed dual-upper-states and experimental results showing homogeneous wide electroluminescence spectra of which the shapes are insensitive to voltage changes. The laser, emitting at λ∼8.7 μm, demonstrates a high CW output power of 170 mW together with a high constant slope efficiency of ∼0.8 W/A at room temperature. In addition, the device performance is observed to be very insensitive to temperature changes, exhibiting superlinear current light output characteristics. These distinctive features are attributed to the absorption quenching in the injector.

Chapter 6 ⋯ In Chapter 6, we further improve the dual-upper-state design. The devices based on the anti-crossed dual-upper-state to continuum transition design exhibit extremely wide electroluminescence (>600 cm^{-1} FWHM) and subthreshold amplified spontaneous emission (∼570 cm^{-1}) spectra at room temperature. Despite showing such broad electroluminescence spectra, the lasers operating at 6.8 μm demonstrate a low threshold current density of ∼1.5 kA/cm^2 and a high power of >500 mW with a high slope efficiency of ∼1.6 W/A in CW mode at 300 K. The performance is good enough for practical applications. In fact, with external cavity set-up, this device enables a wide tuning range even in CW operation.

Chapter 7 ⋯ This chapter concludes the thesis, summarizing the achievements and significance throughout this study. This conclusion includes the research progress in QC lasers.

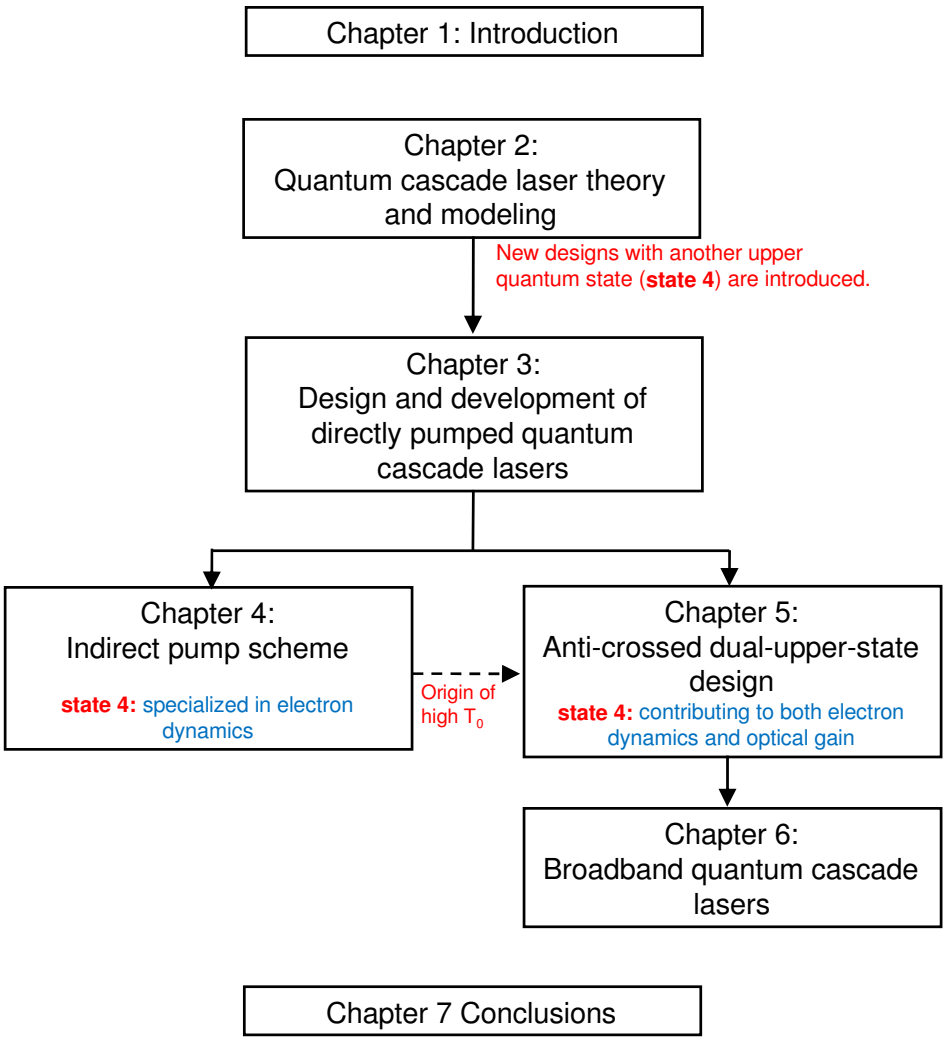

Figure 1.6: Outline of this thesis.

References

[1] L. Esaki and R. Tsu, "Superlattice and negative differential conductivity in semiconductors," IBM J. Res. Dev. **14**, 61 (1970).

[2] H. Sakaki, "Advances in microfabrication and microstructure physics," (Invited paper), Proc. Int. Symposium on Foundation of Quantum Mechanics (held in Tokyo, 1982), 94 (1983).

[3] H. Sakaki, "Evolution of new device concepts in quantum wells and superlattices," (Invited plenary paper), Proc. 15th International Conf. on Solid State Devices and Materials (held in Tokyo, 1983), 3 (1983).

[4] H. Sakaki, "Physical limits of heterostructure field-effect transistors and possibilities of novel quantum field-effect devices," IEEE J. Quantum Electron. **22**, 1845 (1986).

[5] J. Faist, F. Capasso, D. Sivco, C. Sirtori, A. Hutchinson, and A. Cho, "Quantum cascade laser," Science **264**, 553 (1994).

[6] R. Kazarinov and R. A. Suris, "Possibility of amplification of electromagnetic waves in a semiconductor with a superlattice," Sov. Phys. Semicond. **5**, 707 (1971).

[7] R. Kazarinov and R. A. Suris, "Electric and electromagnetic properties of semiconductors with a superlattice," Sov. Phys. Semicond. **6**, 120 (1972).

[8] A. Y. Cho, "Growth of periodic structures by the molecular-beam method," Appl. Phys. Lett. **19**, 467 (1971).

[9] A. Y. Cho and J. R. Arthur, "Molecular beam epitaxy," Prog. in Solid State Chem. **10**, 157 (1975).

[10] L. C. West and S. J. Eglash, "First observation of an extremely large-dipole infrared transition within the conduction band of a GaAs quantum well," Appl. Phys. Lett. **46**, 1156 (1985).

REFERENCES

[11] F. Capasso, K. Mohammed, and A. Cho, "Resonant tunneling through double barriers, perpendicular quantum transport phenomena in superlattices, and their device applications," IEEE J. Quantum Electron. **22**, 1853 (1986).

[12] M. Helm, E. Colas, P. England, F. DeRosa, and S. J. Allen, "Observation of gratinginduced intersubband emission from GaAs/AlGaAs superlattices," Appl. Phys. Lett. **53**, 1714 (1988).

[13] M. Helm, P. England, E. Colas, F. DeRosa, and S. J. Allen, "Intersubband emission from semiconductor superlattices excited by sequential resonant tunneling," Phys. Rev. Lett. **63**, 74 (1989).

[14] C. Sirtori, P. Kruck, S. Barbieri, P. Collot, J. Nagle, M. Beck, J. Faist, and U. Oesterle, "GaAs/AlGaAs quantum cascade lasers," Appl. Phys. Lett. **73**, 3486 (1998).

[15] K. Ohtani and H. Ohno, "An InAs-based intersubband quantum cascade laser," Jpn. J. Appl. Phys **41**, 1279 (2002).

[16] K. Ohtani and H. Ohno, "InAs/AlSb quantum cascade lasers operating at 10 μm," Appl. Phys. Lett. **82**, 1003 (2003).

[17] Q. Yang, C. Manz, W. Bronner, K. Kohler, and J. Wagner, "Room-temperature short-wavelength ($\lambda \sim$3.7-3.9 μm) GaInAs/AlAsSb quantum-cascade lasers," Appl. Phys. Lett. **88**, 121127 (2006).

[18] D. G. Revin, J. W. Cockburn, M. J. Steer, R. J. Airey, M. Hopkinson, A. B. Krysa, L. R. Wilson, and S. Menzel, "InGaAs/AlAsSb/InP quantum cascade lasers operating at wavelengths close to 3 μm," Appl. Phys. Lett. **90**, 021108 (2007).

[19] R. Kohler, A. Tredicucci, F. Beltram, H. E. Beere, E. H. Linfield, A. G. Davies, D. A. Ritchie, R. C. Iotti, and F. Rossi, "Terahertz semiconductor-heterostructure laser," Nature **417**, 156 (2002).

[20] N. Bandyopadhyay, Y. Bai, S.Tsao, S. Nida, S. Slivken, and M. Razeghi, "Room temperature continuous wave operation of $\lambda \sim$3–3.2 μm quantum cascade lasers," Appl. Phys. Lett. **101**, 241110 (2012).

[21] J. Faist, F. Capasso, C. Sirtori, D. L. Sivco, A. L. Hutchinson, and A. Y. Cho, "Vertical transition quantum cascade laser with Bragg confined excited-state," Appl. Phys. Lett. **66**, 538 (1995).

[22] J. Faist, F. Capasso, C. Sirtori, D. L. Sivco, J. N. Baillargeon, A. L. Hutchinson, S. N. G. Chu, and A. Y. Cho, "High power mid-infrared ($\lambda \sim 5$ μm) quantum cascade lasers operating above room temperature," Appl. Phys. Lett. **68**, 3680 (1996).

[23] C. Gmachl, A. Tredicucci, F. Capasso, A. L. Hutchinson, D. L. Sivco, J. N. Baillargeon, and A. Y. Cho, "High-power $\lambda \approx 8$ μm quantum cascade lasers with near optimum performance," Appl. Phys. Lett. **72**, 3130 (1998).

[24] G. Scamarcio, F. Capasso, C. Sirtori, J. Faist, A. L. Hutchinson, D. Sivco, and A. Cho, "High-Power infrared (8-micrometer wavelength) superlattice laser," Science **276**, 773 (1997).

[25] A. Tredicucci, F. Capasso, C. Gmachl, D. L. Sivco, A. L. Hutchinson, and A. Y. Cho, "High performance interminiband quantum cascade lasers with graded superlattices," Appl. Phys. Lett. **73**, 2101 (1998).

[26] F. Capasso, A. Tredicucci, C. Gmachl, D. L. Sivco, A. L. Hutchinson, A. Y. Cho, and G. Scamarcio, "High-Performance superlattice quantum cascade lasers," IEEE J. Sel. Top. Quantum Electron. **5**, 792 (1999).

[27] A. Tredicucci, C. Gmachl, F. Capasso, D. L. Sivco, A. L. Hutchinson, and A. Y. Cho, "Long wavelength superlattice quantum cascade lasers at $\lambda \approx 17$ μm,"Appl. Phys. Lett. **74**, 638 (1999).

[28] A. Tredicucci, C. Gmachl, M. C. Wanke, F. Capasso, A. L. Hutchinson, D. L. Sivco, S. G. Chu, and A. Y. Cho, "Surface plasmon quantum cascade lasers at $\lambda \sim 19$ μm," Appl. Phys. Lett. **77**, 2286 (2000).

[29] R. Colombelli, F. Capasso, C. Gmachl, A. L. Hutchinson, D. L. Sivco, A. Tredicucci, M. C. Wanke, A. M. Sergent, and A. Y. Cho, "Far-infrared surface-plasmon quantum-cascade lasers at 21.5 μm and 24 μm wavelengths" Appl. Phys. Lett. **78**, 2620 (2001).

[30] F. Capasso, A. Tredicucci, C. Gmachl, D. L. Sivco, A. L. Hutchinson, A. Y. Cho, and G. Scamarcio, "High-Performance superlattice quantum cascade lasers" IEEE J. Sel. Top. Quantum Electron. **5**, 792 (1999).

[31] J. Faist, D. Hofstetter, M. Beck, T. Aellen, M. Rochat, and S. Blaser, "Bound-to-continuum and two-phonon resonance quantum cascade lasers for high duty cycle, high temperature operation," IEEE J. Quantum Electron. **38**, 533 (2002).

REFERENCES

[32] D. Hofstetter, M. Beck, T. Aellen, and J. Faist, "High-temperature operation of distributed feedback quantum-cascade lasers at 5.3 μm," Appl. Phys. Lett. **78**, 396 (2001).

[33] D. Hofstetter, M. Beck, T. Aellen, J. Faist, U. Oesterle, M. Ilegems, E. Gini, and H. Melchior, "Continuous wave operation of a 9.3 μm quantum cascade laser on a Peltier cooler," Appl. Phys. Lett. **78**, 1964 (2001).

[34] J. Faist, M. Beck, T. Aellen, and E. Gini, "Quantum Cascade Lasers based on a bound-to-continuum transition," Appl. Phys. Lett. **78**, 147 (2001).

[35] M. Rochat, D. Hofstetter, M. Beck, and J. Faist, "Long-wavelength ($\lambda \approx$16 μm), room-temperature, single-frequency quantum-cascade lasers based on a bound-to-continuum transition," Appl. Phys. Lett. **79**, 4271 (2001).

[36] M. Beck, D. Hofstetter, T. Aellen, J. Faist, U. Oesterle, M. Ilegems, E. Gini, and H. Melchior, "Continuous-wave operation of a mid-infrared semiconductor laser at room-temperature," Science **295**, 301 (2002)

[37] J. S. Yu, S. Slivken, A. Evans, L. Doris, and M. Razeghi, "High-power continuous-wave operation of a 6 μm quantum-cascade laser at room temperature," Appl. Phys. Lett. **83**, 2503 (2003).

[38] A. Evans, J. S. Yu, S. Slivken, and M. Razeghi, "Continuous-wave operation of $\lambda\sim$4.8 μm quantum-cascade lasers at room temperature," Appl. Phys. Lett. **85**, 2166 (2004).

[39] J. S. Yu, S. R. Darvish, A. Evans, J. Nguyen, S. Slivken, and M. Razeghi, "Room-temperature continuous-wave operation of quantum-cascade lasers at $\lambda \sim$4 μm," Appl. Phys. Lett. **88**, 041111 (2006).

[40] A. Evans, J. Nguyen, S. Slivken, J. S. Yu, S. R. Darvish, and M. Razeghi, "Quantum-cascade lasers operating in continuous-wave mode above 90 ^{o}C at $\lambda \sim$5.25 μm," Appl. Phys. Lett. **88**, 051105 (2006).

[41] J. S. Yu, S. Slivken, A. Evans, S. R. Darvish, J. Nguyen, and M. Razeghi, "High-power $\lambda \sim$9.5 μm quantum-cascade lasers operating above room temperature in continuous-wave mode," Appl. Phys. Lett. **88**, 091113 (2006).

[42] L. Diehl, D. Bour, S. Corzine, J. Zhu, G. Hofler, M. Loncar, M. Troccoli, and F. Capasso, "High-temperature continuous wave operation of strain-balanced quantum cascade lasers grown by metal organic vapor-phase epitaxy," Appl. Phys. Lett. **89**, 081101 (2006).

[43] L. Diehl, D. Bour, S. Corzine, J. Zhu, G. Hofler, M. Loncar, M. Troccoli, and F. Capasso, "High-power quantum cascade lasers grown by low-pressure metal organic vapor-phase epitaxy operating in continuous wave above 400 K," Appl. Phys. Lett. **88**, 201115 (2006).

[44] A. Lyakh, C. Pflugl, L. Diehl, Q. J. Wang, F. Capasso, X. J. Wang, J. Y. Fan, T. Tanbun-Ek, R. Maulini, A. Tsekoun, R. Go, and C. K. N. Patel, "1.6 W high wall plug efficiency, continuous-wave room temperature quantum cascade laser emitting at 4.6 μm," Appl. Phys. Lett. **92**, 111110 (2008).

[45] Y. Bai, S. R. Darvish, S. Slivken, W. Zhang, A. Evans, J. Nguyen, and M. Razeghi, "Room temperature continuous wave operation of quantum cascade lasers with Watt-level optical power," Appl. Phys. Lett. **92**, 101105 (2008).

[46] Y. Bai, N. Bandyopadhyay, S. Tsao, S. Slivken, and M. Razeghi, "Room temperature quantum cascade lasers with 27% wall plug efficiency," Appl. Phys. Lett. **98**, 181102 (2011).

[47] T. Aellen, M. Beck, N. Hoyler, M. Giovannini, J. Faist, and E. Gini, "Doping in quantum cascade lasers. I. InAlAs-InGaAs/InP midinfrared devices," J. Appl. Phys. **100**, 43101 (2006).

[48] A. Wittmann, Y. Bonetti, J. Faist, E. Gini, and M. Giovannini, "Intersubband linewidths in quantum cascade laser designs," Appl. Phys. Lett. **93**, 141103 (2008).

[49] C. Gmachl, D. L. Sivco, R. Colombelli, F. Capasso, and A. Y. Cho, "Ultra-broadband semiconductor laser," Nature **415**, 883 (2002).

[50] G. P. Luo, C. Peng, H. Q. Le, S. S. Pei, W.-Y. Hwang, B. Ishaug, J. Um, J. N. Baillargeon, and C.-H. Lin, "Grating-tuned external-cavity quantum-cascade semiconductor lasers," Appl. Phys. Lett. **78**, 2834 (2001).

[51] R. Maulini, A. Mohan, M. Giovannini, J. Faist, and E. Gini, "External cavity quantum-cascade laser tunable from 8.2 to 10.4 μm using a gain element with a heterogeneous cascade," Appl. Phys. Lett. **88**, 201113 (2006).

[52] A. Wittmann, A. Hugi, E. Gini, N. Hoyler, and J. Faist, "Heterogeneous high-performance quantum-cascade laser sources for broad-band tuning," IEEE J. Quantum Electron. **44**, 1083 (2008).

[53] B. G. Lee, M. A. Belkin, R. Audet, J. MacArthur, L. Diehl, C. Pflugl, F. Capasso, D. C. Oakley, D. Chapman, A. Napoleone, D. Bour, S. Corzine, G. Hofler, and J. Faist, "Widely tunable single-mode quantum cascade laser source for midinfrared spectroscopy," Appl. Phys. Lett. **91**, 231101 (2007).

[54] A. Hugi, R. Terazzi, Y. Bonetti, A. Wittmann, M. Fischer, M. Beck, J. Faist, and E. Gini, "External cavity quantum cascade laser tunable from 7.6 to 11.4 μm," Appl. Phys. Lett. **95**, 061103 (2009).

[55] M. Geiser, C. Pflugl, A. Belyanin, Q. J. Wang, N. Yu, T. Edamura, M. Yamanishi, H. Kan, M. Fischer, A. Wittmann, J. Faist, and F. Capasso, "Gain competition in dual wavelength quantum cascade lasers," Opt. Express **18**, 9900 (2010).

Chapter 2

Quantum cascade laser theory and modeling

2.1 Introduction

In this chapter, we will describe the relevant theory and modeling for the design of quantum cascade lasers, which will be applied to the design of the QC laser active regions presented in the following chapters. While these are based on the theory of semiconductor heterostructure, we consider only the intersubband transitions in the conduction band in $In_xGa_{1-x}As/In_yAl_{1-y}As$ material system. In the first section, the basic quantum structure models and fundamental mechanisms determining the basic properties of semiconductor heterostructures are reviewed. Then, the rate equation approaches to three level systems are described, which give important features of the quantum cascade structure as well as the formulation of the threshold current density. In the last section, we will present the features of various upper quantum state designs as well as an analysis of the electron dynamics for the schemes with rate equations.

2.2 Fundamentals of quantum cascade lasers

The basic mechanism of quantum cascade lasers relies on the knowledge of semiconductor band structure. The quantum cascade laser consists of periodic layers

of two semiconductor materials, which form a series of coupled quantum wells and barriers with a repeated structure. When the thickness of the alternating layers is comparable to the de Broglie wavelength of the electron, quantization of the electron motion in the direction perpendicular to the layers produces a set of discrete energy levels. In this section, we describe the relevant quantum mechanical models.

2.2.1 Semiconductor quantum wells

For the calculation of the wavefunctions and the quantum states in semiconductor heterostructures, we solve a one-dimensional Schrödinger equation to obtain the eigenenergies E_i and wavefunctions ϕ_i in the conduction band formed by the quantum confinement in the epitaxial growth direction. The one-dimensional Schrödinger equation in the epitaxial growth direction is given by

$$\left(-\frac{\hbar^2}{2}\frac{\mathrm{d}}{\mathrm{d}z}\left[\frac{1}{m^*(z)}\frac{\mathrm{d}}{\mathrm{d}z}\right]+V(z)\right)\phi_n(z)=E_n\phi_n(z) \tag{2.1}$$

where $m^*(z)$ is the mass of the electron and $V(z)$ is the electron potential. Since the motion in the in-plane direction is not restricted, the energy of an electron in subband n is

$$E_n(k)=E_n+\frac{\hbar^2k^2}{2m^*} \tag{2.2}$$

where k is the in-plane momentum. For the calculation of eigenenergies, we take into account the effect of the non-parabolic energy dispersion of the conduction band, which arise from the influence of the valence band. The band non-parabolicity is considered by introducing an energy dependent electron effective mass $m^*(E)$. Using the four-band Kane model [1], the energy dependent effective mass is given by

$$\frac{1}{m^*(E,z)}=\frac{1}{m_0}\left[\frac{2}{3}\frac{E_\mathrm{p}}{E-E_\mathrm{lh}}+\frac{1}{3}\frac{E_\mathrm{p}}{E-E_\mathrm{so}}\right], \tag{2.3}$$

where E_p, E_lh, E_so is the Kane energy, the light-hole energy, and the split-off energy, respectively. Figure 2.1 depicts the significance of the band nonparabolicity effects from the interaction of the conduction and valence band. The energy

levels of a single quantum well are compared between the case with (dashed line) and without the nonparabolicity effect (solid line).

The squared moduli of the wavefunctions represent the probability distribution of the electron's location in the growth direction. In the conduction band diagrams, the energy states are represented as the moduli squared of the wavefunctions at the calculated energetic positions. Using the calculated wavefunctions and eigenenergies, the dipole matrix elements can also be obtained, which provide the strength of the optical transitions between the upper and lower states. The dipole matrix element between the states i and j is

$$Z_{ij} = \langle \phi_i | z | \phi_j \rangle. \tag{2.4}$$

2.2.2 Building blocks for quantum cascade structures

QC structures consist of many quantum wells and barriers which generate many quantum levels. In this section, we consider basic building blocks, coupled quantum wells and a superlattice. This is very important for designing QC structures.

2.2.2.1 Coupled quantum wells

First, we consider two quantum wells coupled through a tunnel barrier [2]. We can describe this system in a tight binding model in which we have a base formed by the solution of the individual quantum wells. This system can be solved directly by using the Hamiltonian of the whole structure. The wave functions of the lowest two states in the coupled quantum wells consist of mixing of the lowest states in each of the two different quantum wells, Φ_{L} and Φ_{R}. The Hamiltonian is written as

$$H = \frac{p_z^2}{2m^*} + V_{\mathrm{L}} + V_{\mathrm{R}}, \tag{2.5}$$

where V_{L} and V_{R} are the left and right potential wells. Here, Φ_{L} and Φ_{R} are solutions to different Schrödinger equations,

$$\left(\frac{p_z^2}{2m^*} + V_{\mathrm{L}}\right)\Phi_{\mathrm{L}} = \epsilon\Phi_{\mathrm{L}}, \quad \left(\frac{p_z^2}{2m^*} + V_{\mathrm{R}}\right)\Phi_{\mathrm{R}} = \epsilon\Phi_{\mathrm{R}}. \tag{2.6}$$

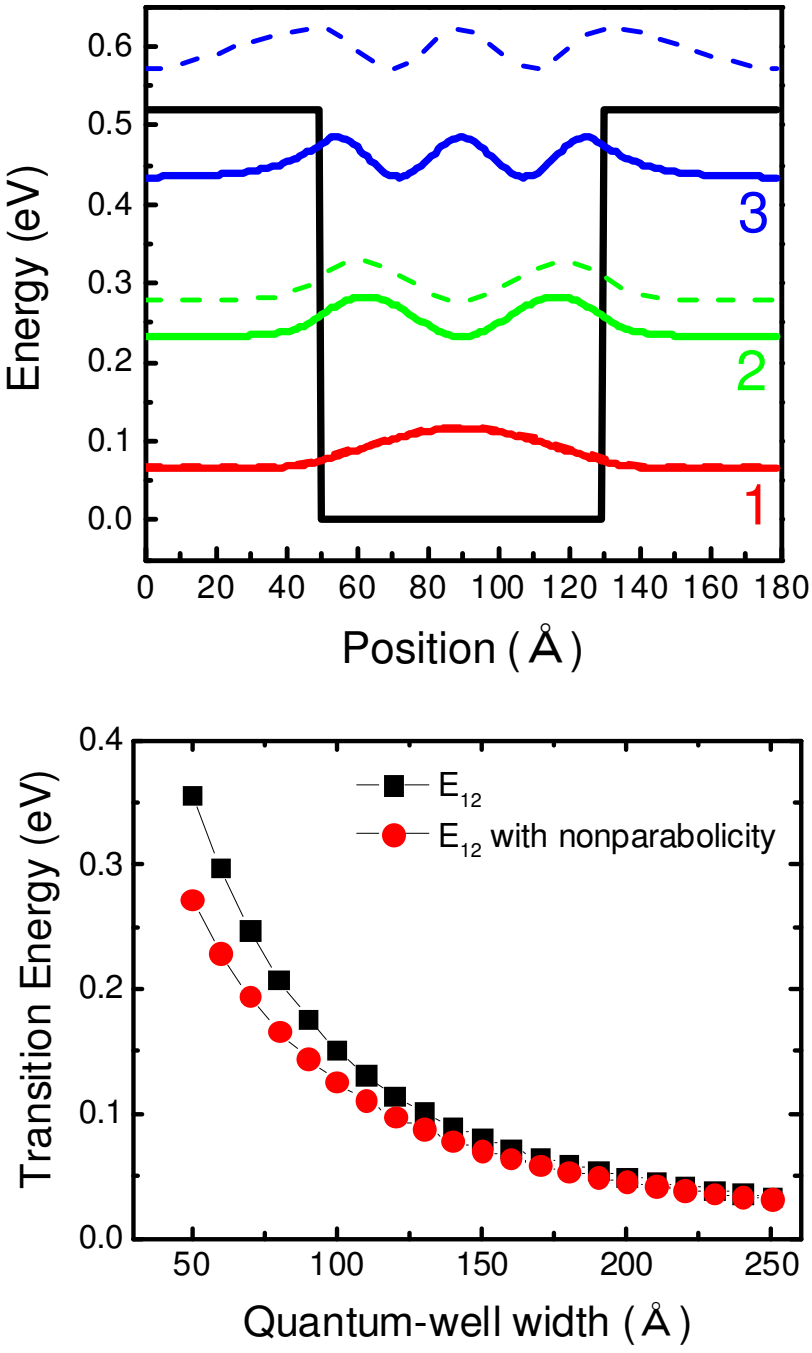

Figure 2.1: (a) Computation of the energy levels E_i and conduction band wavefunctions in a 80 Å-wide QW with (solid lines) and without (dashed lines) nonparabolicity. (b) Transition energy E_{12} as a function of the quantum-well width

The desired wave function is given as sum over all Φ_i with coefficients, $\Psi = \sum a_n \Phi_n$, where n runs over L and R. The restricted Schrödinger equation is

$$H \sum_n a_n \Phi_n = E \sum_n a_n \Phi_n. \tag{2.7}$$

By multiplying Φ_m from both sides, we obtain matrices,

$$\sum_n H_{mn} a_n = E \sum_n S_{mn} a_n \tag{2.8}$$

whose elements are

$$H_{mn} = \int \Phi_m^* H \Phi_n, S_{mn} = \int \Phi_m^* \Phi_n. \tag{2.9}$$

Thus, we solve the matrix equation $\mathbf{H}a{=}E\mathbf{S}a$. The matrix element H_{LL} is

$$H_{\mathrm{LL}} = \int \Phi_{\mathrm{L}}^* \left(\frac{p_z^2}{2m^*} + V_{\mathrm{L}} + V_{\mathrm{R}} \right) \Phi_{\mathrm{L}} \mathrm{d}z = \epsilon + \int \Phi_{\mathrm{L}}^* V_{\mathrm{R}} \Phi_{\mathrm{L}} \mathrm{d}z \equiv \epsilon - c. \tag{2.10}$$

The term with $p_z^2/2m^* + V_{\mathrm{L}}$ provides ϵ using the Schrödinger equation for Φ_{L}. The other term provides the anticipated values of the added potential V_{R} for the wavefunction Φ_{L}, and which is called the crystal field. The other diagonal element H_{RR} is the same. The two off-diagonal terms are

$$\begin{aligned} H_{\mathrm{RL}} &= \int \Phi_{\mathrm{R}}^* \left(\frac{p_z^2}{2m^*} + V_{\mathrm{L}} + V_{\mathrm{R}} \right) \Phi_{\mathrm{L}} \mathrm{d}z \\ &= \epsilon \int \Phi_{\mathrm{R}}^* \Phi_{\mathrm{L}} \mathrm{d}z + \int \Phi_{\mathrm{R}}^* V_{\mathrm{R}} \Phi_{\mathrm{L}} \mathrm{d}z = \epsilon s - t. \end{aligned} \tag{2.11}$$

The term $-t$ is called the transfer overlap integral, which represents transfers an electron from one well to the other, and this contains the product of the two wave functions. After normalization of the wave functions, the diagonal elements of $\mathbf{S}$ are unity. The off-diagonal elements are both s. Hence,

$$\mathbf{H} = \begin{pmatrix} \epsilon - c & \epsilon s - t \\ \epsilon s - t & \epsilon - c \end{pmatrix}, \ \mathbf{S} = \begin{pmatrix} 1 & s \\ s & 1 \end{pmatrix}, \tag{2.12}$$

the energies are obtained by the secular equation. The matrix equation is

$$E_- = \epsilon - \frac{c}{1+s} - \frac{t}{1+s}, \ E_+ = \epsilon - \frac{c}{1-s} - \frac{t}{1-s}. \tag{2.13}$$

In this equation, the transfer integral is most important, since this corresponds to the splitting between the two states, as illustrated in Figure 2.2(b). Hence, a larger transfer integral results in a wider spacing between the two states.

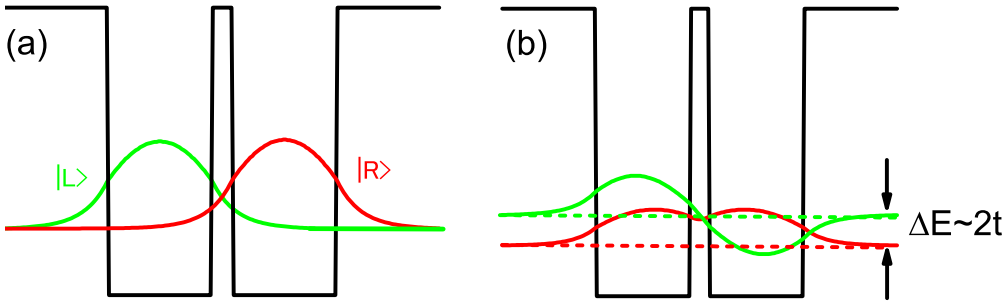

Figure 2.2: Two potential quantum wells. (a) Wave functions and energy levels of individual quantum wells, (b) wave functions and energies of even and odd states of coupled quantum wells, showing splitting of approximately $\pm t$

2.2.2.2 Superlattice

The results obtained for coupled quantum wells can be straightforwardly modified to more dimensions [2, 3]. The energy state for coupled quantum wells is split into two levels separated by $2t$. The energy splitting increases when decreasing the barrier width. Increasing the number N of quantum wells causes their energy level to split into N values and these form a continuous band. Superlattices is defined as the sum of the potentials $V_{\mathrm{SL}}(z)$ for the single quantum wells:

$$V_{\mathrm{SL}}(z) = \sum_{n}^{\infty} V_{\mathrm{SL}}(z - nd) \tag{2.14}$$

with

$$V_{\mathrm{SL}}(z - nd) = \begin{cases} 0, (z - nd) \leq L/2 \\ V_{\mathrm{SL}}, (z - nd) > L/2 \end{cases} \tag{2.15}$$

The wave functions for the quantum wells are given by:

$$\psi(z) = \alpha \exp\left\{\mathrm{i}k_{\mathrm{w}}(z - nd)\right\} + \beta \exp\left\{-\mathrm{i}k_{\mathrm{w}}(z - nd)\right\} \tag{2.16}$$

For the barriers, the wavefunction is also given by:

$$\psi(z) = \gamma \exp\left\{\mathrm{i}k_{\mathrm{b}}(z - nd - d/2)\right\} + \delta \exp\left\{-\mathrm{i}k_{\mathrm{b}}(z - nd - d/2)\right\}. \tag{2.17}$$

Due to the periodicity of the superlattice structure, we can use the boundary conditions at interfaces of the quantum wells. The corresponding real space depiction of a superlattice is shown in Fig. 2.3(b).

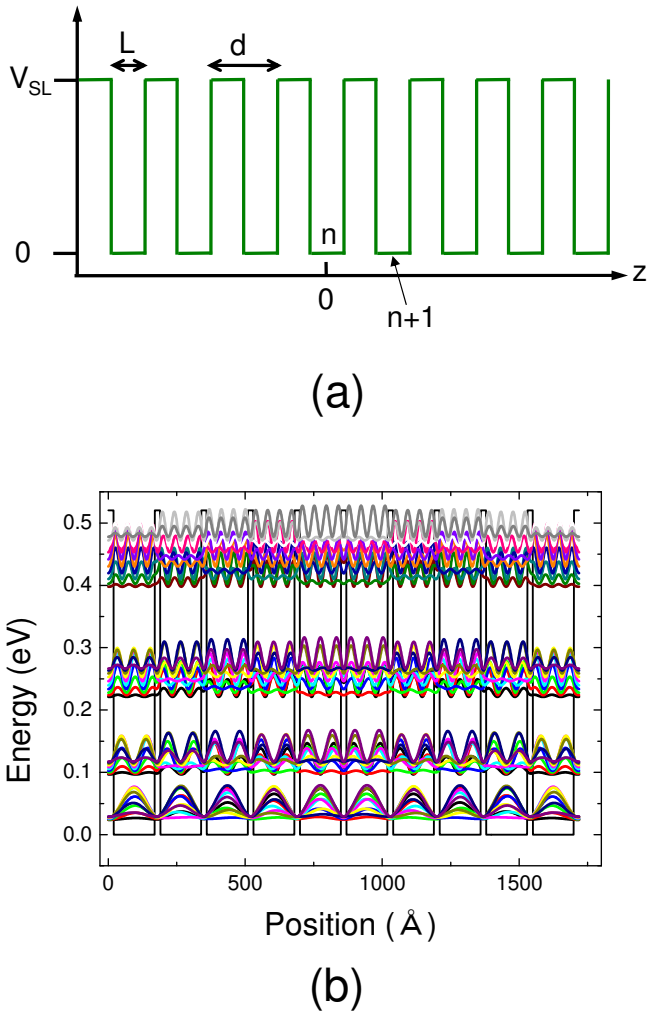

Figure 2.3: (a)Schematic band structure of a superlattice. (b)Wavefunctions and energy levels of InGaAs/InAlAs superlattice.

2.2.3 Resonant tunneling

Resonant tunneling is the dominant transport mechanism in QC structures. A fundamental understanding of this process has been the basis for the engineering of quantum devices. In this section, we will present some basic methods for the analysis of tunneling that are useful for QC laser design [4, 5]. Now, we consider electron tunneling from state $1'$ to state 2. The schematic illustration for a two-level system is shown in Fig. 2.4. With the density matrix formalism based on the localized wavefunction (tight binding) model, the wave function for an electron is given by

$$|\Psi(t)\rangle = \sum c_i(t)|i\rangle \tag{2.18}$$

and we can define the density matrix ρ for a mixed state by the ensemble average

$$\rho_{ij} = \langle c_i c_j^* \rangle. \tag{2.19}$$

The diagonal elements ρ_{ii} correspond to the state populations, and the off-diagonal elements represent the average degree of coherence between basis states. The time evolution of ρ is described by the equation of motion,

$$\frac{\mathrm{d}}{\mathrm{d}t}\rho = \frac{\mathrm{i}}{\hbar}[H, \rho] \tag{2.20}$$

where H is the Hamiltonian of the total system, as shown in Fig. 2.4. We obtain the following set of coupled equations that describes both the population difference $\rho_{11} - \rho_{22}$ and the off-diagonal element ρ_{21}.

The equation of motion for the nondiagonal element ρ_{21} of the density operator is, in general, given by

$$\frac{\mathrm{d}\rho_{21}}{\mathrm{d}t} = \frac{\mathrm{i}\Omega_{1'2}(\rho_{11} - \rho_{22})}{2} - \frac{\mathrm{i}E_{21'}\rho_{21}}{\hbar} - \frac{\rho_{21}}{\tau_{\mathrm{deph}}}, \tag{2.21}$$

where the anti-crossing gap is $\hbar\Omega_{1'2}$, the energy difference between levels $1'$ and 2 is $E_{21'}$, and the dephasing time is τ_{deph}. The driving term $\mathrm{i}(\Omega_{1'2}/2)(\rho_{11} - \rho_{22})$ is not time-dependent at steady state condition, unlike the usual two-level system which is illuminated with input light $E_{\mathrm{in}}\cos(\omega t)$, and hence, $\mathrm{d}\rho_{21}/\mathrm{d}t = 0$ so that the steady state nondiagonal element is given by

$$\rho_{21} = \frac{\mathrm{i}\hbar\Omega_{1'2}(\rho_{11} - \rho_{22})}{2\left(\hbar/\tau_{\mathrm{deph}} + \mathrm{i}E_{21}\right)}, \tag{2.22}$$

On the other hand, the current density is, in general, represented by

$$j = N_{\mathrm{s}} e \mathrm{Tr}\left\{\hat{v}_z \rho\right\} = N_{\mathrm{s}} e \left\{v_{11}\rho_{11} + v_{12}\rho_{21} + v_{21}\rho_{12} + v_{22}\rho_{22}\right\} \tag{2.23}$$

where N_{s} is the density of states of the quantum system. The z-component $\hat{v}_{\mathrm{z}} = (\mathrm{i}/\hbar)[\hat{H}, z]$, because $[\hat{H}, z] = (1/2m)[p_z^2, z] = -(1/2m)\left\{[z, p_z]p_z - p_z[p_z, z]\right\} = -(\mathrm{i}\hbar/m)p_z = -\mathrm{i}\hbar\hat{v}_z$ notifying $[z, p_z] = \mathrm{i}\hbar$. Hence,

$$\begin{aligned} v_{11} &= (\mathrm{i}/\hbar)(H_{11}z_{11} + H_{12}z_{21} - z_{11}H_{11} - z_{21}H_{21}) \\ &= (\mathrm{i}/\hbar)(H_{12}z_{21} - z_{12}H_{21}) = 0, \end{aligned} \tag{2.24}$$

$$(H_{12} = H_{21}, z_{21} = z_{12} : \text{real number})$$

$$v_{22} = 0, \tag{2.25}$$

$$\begin{aligned} v_{12} &= (\mathrm{i}/\hbar)(H_{11}z_{12} + H_{12}z_{22} - z_{11}H_{12} - z_{12}H_{22}) \\ &= (\mathrm{i}/\hbar)\left\{H_{12}(z_{22} - z_{11}) + z_{12}(H_{11} - H_{22})\right\} = v_{21}^*, \end{aligned} \tag{2.26}$$

Here, $H_{12} = -(1/2)\hbar\Omega_{1'2}$ and $H_{11} - H_{22} = -E_{21'}$ so that

$$v_{12} = (\mathrm{i}/\hbar)\left\{-(1/2)\hbar\Omega_{1'2}(z_{22} - z_{11}) - z_{12}E_{21'}\right\} \sim -\mathrm{i}(1/2)\Omega_{1'2}(z_{22} - z_{11}),$$

because $z_{21} \sim 0$ due to tight binding model. Similarly,
$v_{21} = v_{12}^* \sim \mathrm{i}(1/2)\Omega_{1'2}(z_{22} - z_{11})$.
By substituting the obtained results for the velocity components into eq. (2.23), one obtains the current density, in general,

$$j = N_{\mathrm{s}} e \times \mathrm{i}\frac{\Omega_{1'2}}{2}(z_{22} - z_{11})(\rho_{12} - \rho_{21}). \tag{2.27}$$

From eq. (2.21), the difference in the nondiagonal elements of density matrix is given by

$$\rho_{21} - \rho_{12} = \frac{\mathrm{i}\hbar\Omega_{1'2}(\rho_{11} - \rho_{22})(\hbar/\tau_{\mathrm{deph}})}{(\hbar/\tau_{\mathrm{deph}})^2 + (E_{21'})^2}. \tag{2.28}$$

By plugging eq. (2.28) into eq. (2.27), the current density at steady state is

$$j = N_{\mathrm{s}} e(\rho_{11} - \rho_{22})(z_{22} - z_{11})(1/2)\Omega_{1'2}^2\tau_{\mathrm{deph}}/[1 + (E_{21'}/\hbar)^2\tau_{\mathrm{deph}}^2]. \tag{2.29}$$

Because $N_s(\rho_{11}-\rho_{22})(z_{22}-z_{11}) \rightarrow N_s \int(\rho_{11}-\rho_{22})\mathrm{d}z = (n_1-n_2)$, one obtains for the steady state current density

$$j = \frac{e(n_1-n_2)}{\left[1+\left(E_{21'}/\hbar\right)^2 \tau_{\mathrm{deph}}^2\right]\tau_{\mathrm{tunn}}}, \tag{2.30}$$

where the tunneling time is defined as $\tau_{\mathrm{tunn}} = 2/\Omega_{1'2}^2\tau_{\mathrm{deph}}$ with the Rabi oscillation frequency $\Omega_{1'2}$, as the time it takes for such a localized state to move through the barrier. The population difference, (n_1-n_2) can be identified by using usual rate equations as well as particle conservation: $n_{\mathrm{inj}} = \sum n_j$.

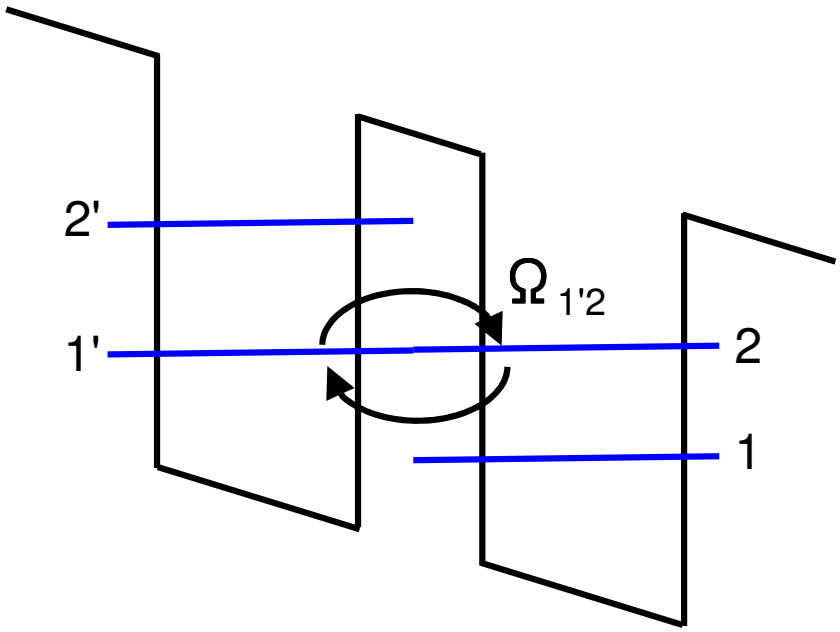

Figure 2.4: Schematic of tight-binding resonant tunneling model with interaction.

2.2.4 Spontaneous emission and scattering processes in quantum wells

The nonradiative scattering time and spontaneous emission lifetime are key parameters which characterize the laser action in a QC laser. In this section we consider intersubband transitions and scattering rates of the various processes in quantum-confined structures, which will be used for the calculation of the laser performance of QC lasers in following chapters.

2.2.4.1 Spontaneous emission [6][1]

To compute the radiative inter-subband transition rate R of a hetero-structure eigenstate $|\Psi_2\rangle$ limited by transitions to all the final states $|\Psi_1\rangle$, induced by an electron–photon interaction Hamiltonian $H_{\mathrm{e-p}}$, we start with Fermi's golden rule,

$$R = (2\pi/\hbar) \sum_{2} |\langle \Psi_2 | H_{\mathrm{e-p}} | \Psi_1 \rangle|^2 \, \delta(E_2 - \hbar\omega - E_1), \tag{2.31}$$

where $\hbar\omega$ is the emitted photon energy, and states 2 and 1 correspond to levels 2 and 1 in the inset of Fig. 2.5. In the framework of the envelope function formalism, we restrict our considerations to a parabolic band scheme. This means that the envelope conduction states are represented as

$$\Psi_2(\mathbf{r}) = (1/S_{\mathrm{qc}})^{1/2} \exp(\mathrm{i}\mathbf{k} \cdot \rho) \phi_2(z), \tag{2.32}$$

corresponding to the energy

$$E_2(\mathbf{k}) = E_2 + \frac{\hbar^2 k^2}{2m^*}, \tag{2.33}$$

where S_{qc} is the in-plane area of the quantum-confinement structure, and $\rho = (x, y)$ and $\mathbf{k} = (k_x, k_y)$ are the in-plane components of the electron position and

[1]

wave vectors, respectively, E_2 is the energy at the subband edge, $\phi_2(z)$ is the associated envelope function, and m^* is the electron effective mass. Expressions similar to (2.32) and (2.33) hold for the final states. Obviously, the energy separation $E_2(\mathbf{k}) - E_1(\mathbf{k})$ in the δ-function of (2.31) is independent of the in-plane electron wave vector $\mathbf{k}$ in the framework of the parabolic band, $E_2(\mathbf{k}) - E_1(\mathbf{k}) = E_2 - E_1$ which means a single lobe lineshape function for stimulated and spontaneous emissions. Under the one-band effective mass approximation, the interaction Hamiltonian is given by

$$H_{\mathrm{e-p}} = -(e/m^*)\mathbf{A} \cdot \mathbf{p}, \tag{2.34}$$

where $\mathbf{A}$ and $\mathbf{p}$ are the photon-field vector potential and electron momentum operators. The vector potential in free space is given by

$$\mathbf{A} = \sum_{\nu} (\hbar/2\epsilon_0 n_{\mathrm{index}}^2 \omega_\nu V)^{1/2} \left[a_\nu^+ \mathbf{e}_\nu \exp(\mathrm{i}\mathbf{k} \cdot \mathbf{r}) + \mathrm{h.c.} \right], \tag{2.35}$$

where ϵ_0 is the dielectric constant in vacuum, n_{index} and V are the refractive index and the large size cavity volume, and ω_ν, a_ν^+, $\mathbf{e}_\nu$ and $\mathbf{k}_\nu$ are the angular frequency, the creation operator, the polarization unit vector, and the wave vector of the photons (all at mode ν), respectively. By using (2.31)–(2.35), one obtains the radiative transition rate in free space,

$$\begin{aligned} R = & \sum_{\nu} (\pi e^2 \omega_\nu \sin^2\theta_\nu / \epsilon_0 n_{\mathrm{index}}^2 V) Z_{21}^2 \\ & \times (N_{\mathrm{photon},\nu} + 1) \delta(E_2 - \hbar\omega_\nu - E_1), \end{aligned} \tag{2.36}$$

where $N_{\mathrm{photon},\nu}$ is the photon population at mode ν, and θ_ν is the angle of wave vector $\mathbf{k}$, measured from the z-axis perpendicular to the quantum well plane. Here, the well known relation, $\langle \phi_2 | p_z | \phi_1 \rangle = \mathrm{i}m^*[E_2 - E_1/\hbar] \langle \phi_2 | z | \phi_1 \rangle$ was used in the derivation of (2.36). The angular dependent term, $\sin^2\theta_\nu$ in (2.36), is brought about by the z-oriented dipole moment, $\langle \phi_2 | z | \phi_1 \rangle$. Obviously, equation (2.36) indicates the Einstein relationship that the stimulated emission rate per one photon equals the spontaneous emission rate.

By taking the summation over the mode-numbers, namely, carrying out the integration in the wave vector $\mathbf{k}$-space and putting N for the number of photons

in (2.36), the spontaneous emission rate in free space is found:

$$1/\tau_{\mathrm{rf}} = (4\pi^2 e^2 n_{\mathrm{index}}/\epsilon_0 \hbar \lambda_0^3) Z_{21}^2, \tag{2.37}$$

where λ_0 is the photon wavelength in vacuum. The lifetime τ_{rf} increases with a cubic wavelength dependence as the emission wavelength increases.

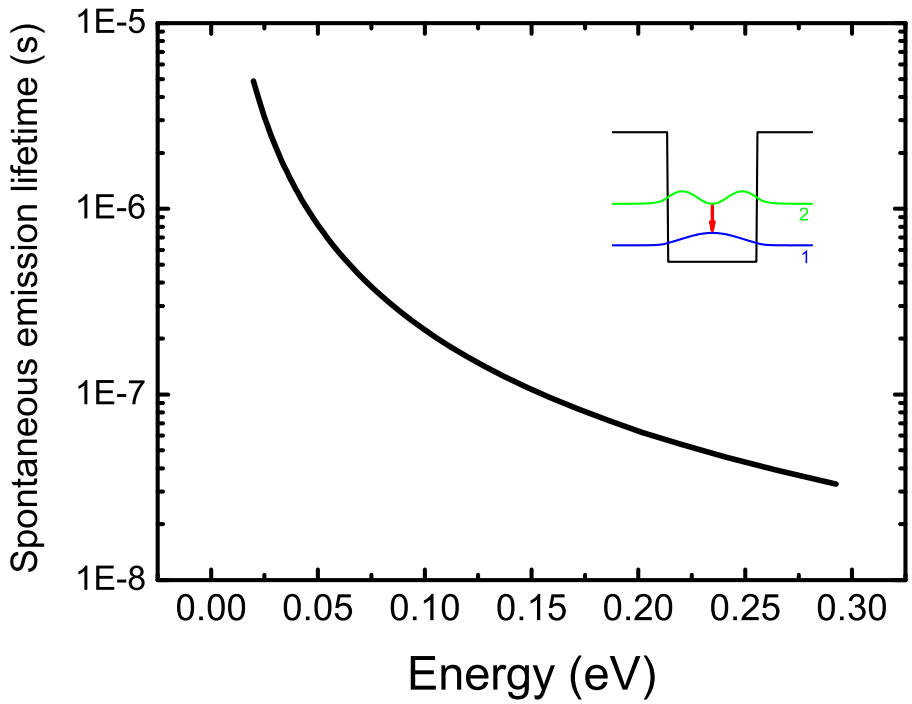

Figure 2.5: Spontaneous emission lifetime as a function of transition energy in a $In_{0.53}Ga_{0.47}As$ single quantum well.

2.2.4.2 Scattering rate by longitudinal optical phonons

The phonon scattering is mainly determined by the interaction between the electron and the piezoelectric potential produced by the local lattice deformation [3, 7, 8]. The longitudinal optical (LO) phonons can be assumed to be energetically uniform due to its little dispersion. In this case, electrons with an wavevector k_i in the upper subband and energy E_i are scattered to the lower subband at k_f.

The electron loses an energy of $\hbar\omega_{\mathrm{LO}}$ in the process as drawn schematically in Fig. 2.6. The exchanged momentum Q in the process is

$$Q = \sqrt{k_i^2 + k_f^2 - 2k_i k_f \cos\theta}. \tag{2.38}$$

Using Fermi's golden rule the scattering rate is calculated. The scattering rate is

$$1/\tau_{\mathrm{LO}} = \frac{m^* e^2 \omega_{\mathrm{LO}}}{2\hbar^2 \epsilon} \sum_f \int_0^{2\pi} \mathrm{d}\theta \frac{I^{ij}(Q)}{Q} \tag{2.39}$$

where the effective dielectric constant entering the Frölich's Hamiltonian is

$$\frac{1}{\epsilon} = \frac{1}{\epsilon_\infty} + \frac{1}{\epsilon_{\mathrm{s}}} \tag{2.40}$$

where ϵ_∞ and ϵ_{s} are the high frequency and the static dielectric function. Using the envelope wavefunctions, the form factor in (2.39) is calculated:

$$I^{ij}(Q) = \int \mathrm{d}z \int \mathrm{d}z' \phi_i(z)\phi_j(z) e^{-Q|z-z'|} \phi_i(z')\phi_j(z'). \tag{2.41}$$

Fig. 2.7 shows the LO phonon scattering time calculated for a single quantum well, as a function of the transition energy. The scattering time is rapidly reduced when the energy separation of two states is close to the LO phonon energy. This increase in LO phonon scattering time is very important for designing quantum cascade structures.

However, the scattering time discussed above was calculated for the spontaneous emission of an optical phonon. In reality, stimulated emission and absorption of optical phonons should be considered by introducing the spontaneous emission factor. Using the Bose–Einstein distribution, the phonon population N_{phonon} is given by:

$$N_{\mathrm{phonon}} = \frac{1}{\exp(\hbar\omega_{\mathrm{LO}}/k_{\mathrm{B}}T) - 1} \tag{2.42}$$

The total LO phonon scattering time is obtained by taking into account the emission and absorption processes:

$$1/\tau_{\mathrm{LO,tot}} = (1 + N_{\mathrm{phonon}}) \times (1/\tau_0^{(\mathrm{e})}) + N_{\mathrm{phonon}} \times (1/\tau_0^{(\mathrm{ab})}) \tag{2.43}$$

where $1/\tau_0^{(\mathrm{e})}$ and $1/\tau_0^{(\mathrm{ab})}$ are the optical phonon emission and absorption rates calculated by (2.39).

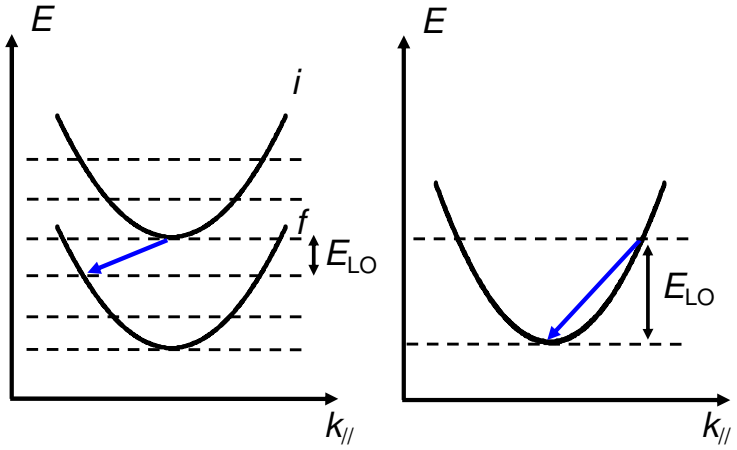

Figure 2.6: (a) Schematic illustration of intersubband scattering between levels i and f separated by more than the LO phonon energy. (b) Intrasubband scattering by the LO phonon.

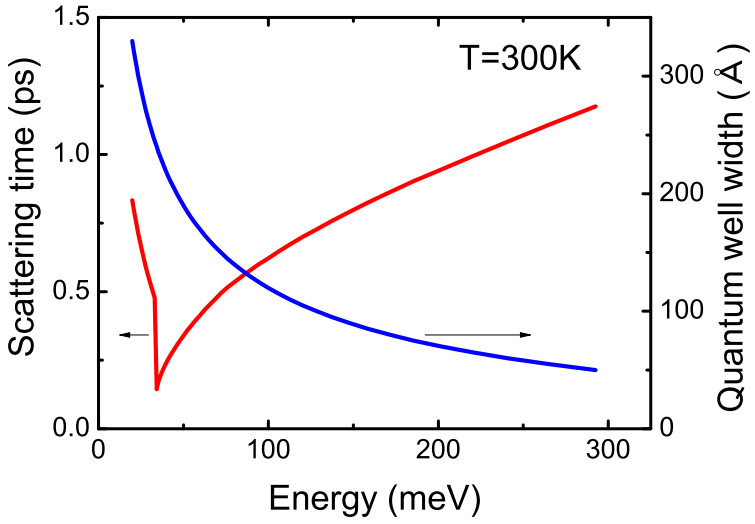

Figure 2.7: LO phonon scattering time as a function of transition energy in a single quantum well, whose width is indicated in the right vertical axis.

2.2.4.3 Elastic intersubband process: alloy disorder and interface roughness scatterings

As shown in the previous section, LO phonon scattering is the dominant process between subbands separated by more than the LO phonon energy. When the energy separation between subbands is smaller than the LO phonon energy, the LO phonon scattering process may be frozen out, depending on the temperature. In this condition, the lifetime is determined by various scattering schemes, such as thermally activated LO phonon, interface roughness, alloy, electron–electron, and other scatterings. Although the electron–electron scattering plays an important role in highly doped structures, this scattering is less important in the devices with a low doping level, as in this thesis. Thus, we discuss the interface roughness and alloy disorder scatterings which have an influence on some particular cases. These may occur either through collision with an ionized impurity or through scattering at an interface step [7, 9]. For the alloy disorder scattering potential, we use δV_{w}=0.6 eV in GaInAs and δV_{B}=1.4 eV in InAlAs. The scattering rate due to the alloy disorder contribution is given by

$$1/\tau_{\mathrm{alloy}} = \frac{m^*}{\hbar^3}\Omega\left[\delta V_{\mathrm{w}}^2 x_{\mathrm{w}}(1-x_{\mathrm{w}})\sum_{\mathrm{well}}\int_{\mathrm{w}}\Phi_i^2\Phi_j^2 dz \right. \\ \left. +\delta V_{\mathrm{B}}^2 x_{\mathrm{B}}(1-x_{\mathrm{B}})\sum_{\mathrm{Barrier}}\int_{\mathrm{B}}\Phi_i^2\Phi_j^2 dz\right], \qquad (2.44)$$

where Ω is the volume of unit cell with $a = 5.8$ Å (the lattice constant), $\Phi(z_i)$ is the wavefuntion of the subbandand, and x_{w} and x_{b} are the mole fraction compositions of the alloy for quantum well and barrier.

On the other hand, in InGaAs/InAlAs QWs, the interface fluctuations are formed at the InGaAs to InAlAs interface. Inter- and intra-subband scatterings due to the interface roughness between subbands spaced less than the LO phonon energy are revealed to be very fast. For the calculation of interface roughness, assuming a Gaussian autocorrelation of the roughness, with an average roughness height Δ=1.2 Å and a correlation length λ=90 Å, the intersubband scattering due to interface roughness can be calculated as:

$$1/\tau_{\mathrm{IF}} = \frac{\pi m^*}{\hbar^3}\left(\frac{\delta V_{\mathrm{c}}}{2}\right)^2 \lambda^2 \exp\left[-\frac{\lambda^2}{2}\left\{\frac{m^*}{\hbar^2}\left(E_i - E_f\right) + k_{i\|}^2\right\}\right] \times I_0\left(\frac{\lambda^2}{2} k_{i\|}\sqrt{\frac{2m^*}{\hbar^2}\left(E_i - E_f\right) + k_{i\|}^2}\right) \sum_{\mathrm{Interface}} \int_{-\Delta}^{\Delta} \Phi_i^2(z)\Phi_j^2(z)\mathrm{d}z \quad (2.45)$$

where $I_0(z)$ is a modified Bessel function, $I_0(0) = 0$ at $k_{i\|} = 0$, and δV_{c} is the conduction band offset. The scattering time for the upper quantum state of conventional quantum cascade lasers is substantially longer than that from LO phonon scattering. However, in the anti-crossed states of coupled quantum wells, the interface roughness scattering is extremely fast. This makes for a very important feature of the dual-upper-state QC lasers, as will be seen in Chapter 5.

The interface roughness scattering has also a large effect on the linewidth of the intersubband transition in the quantum wells [10, 11]. The linewidth broadening due to interface roughness is calculated as:

$$\Gamma = \frac{\pi m^*}{\hbar^2}\Delta^2\Lambda^2 \sum_{ij}\left[c_{ij} U(z_i)\left|\Phi(z_i)\right|^2 U(z_j)\left|\Phi(z_j)\right|^2\right] \quad (2.46)$$

where $U(z_i)$ is the potential step at the interface z_i, and c_{ij} is the vertical correlation of the interface roughness between interfaces z_i and z_j. The vertical correlation between the different interfaces is ignorable in lattice matched InGaAs/InAlAs QWs [11]. The equation for the linewidth broadening is simplified:

$$\Gamma = \frac{\pi m^*}{\hbar^2}\Delta^2\Lambda^2 \sum_{i}\left[U(z_i)^2\left|\Phi(z_i)\right|^4\right] \quad (2.47)$$

The interface roughness scattering is determined by the interface parameters Δ and Γ depending on the epitaxial growth conditions.

2.3 Rate equation and the threshold current

A rate equation approach is useful to estimate important quantities, such as the threshold current density and slope efficiency [6][1]. For the active region of

[1] ©2008 IEEE.

a mid-infrared single mode QC laser, we restrict the rate equation analysis to a standard three-level system [12] that consists of the state, level 1 merged to states in an injector with sheet doping $N_{\mathrm{inj}i}$, and the two states, levels 3 and 2, of the lasing transition with electron populations N_{3i} and N_{2i}, as depicted in Fig. 2.8. The isolated level (not band) model is justified since, within the framework of a parabolic band model, the lineshape function relevant to inter-subband transitions is represented by a δ-like function, both for stimulated and spontaneous emission, independent of the quantum number and the in-plane wavenumber in each subband. The three-level model may be valid for almost any type of active region in a mid-infrared QC laser by simply inserting the appropriate numerical values for the parameters [12]. Electrons are scattered nonradiatively from level 3 to levels 2 and 1 by LO phonon emissions. The scattering rate is given by the summation $1/\tau_{\mathrm{nr}i}=1/\tau_{32i}+1/\tau_{31i}$ of the order of the inverse of picoseconds [13, 14, 15], much higher than the spontaneous emission rate $1/\tau_{\mathrm{r}i}$, the inverse of ten nanoseconds as shown in a mid-infrared QC laser. The reverse processes from levels 2 and 1 to level 3, indicated by the dashed arrows in Fig. 2.8, are ignored in the mid-infrared case. In order to maintain a sufficient population inversion ratio, the scattering rate $1/\tau_{21i}$ out of level 2 is usually settled down to be substantially higher than the total rate, $1/\tau_{\mathrm{t}i} = 1/\tau_{\mathrm{r}i} + 1/\tau_{\mathrm{nr}i} \sim 1/\tau_{\mathrm{nr}i}$ out of level 3. The electron population N_{2i} is relaxed toward the thermal level $N_{2i\mathrm{therm}}$, of which the relaxation rate is represented by $(N_{2i} - N_{2i\mathrm{therm}})/\tau_{21i}$. This can be easily justified by the principle of detailed balance for transitions between levels 2 and 1 at (quasi) thermal equilibrium. The rate equations for the electron populations N_{3i} and N_{2i}, at the ith stage, and the photon population N_{photon} in a single lasing mode and their time derivatives are

$$\mathrm{d}N_{3i}/\mathrm{d}t = \eta_i P_i - N_{3i}/\tau_{\mathrm{nr}i} - N_{3i}/\tau_{\mathrm{r}i} - B_{32i}(1 - N_{2i}/N_{3i})N_{\mathrm{photon}} \tag{2.48}$$

$$\begin{aligned}\mathrm{d}N_{2i}/\mathrm{d}t = {} & (1-\eta_i)P_i + N_{3i}/\tau_{32i} + N_{3i}/\tau_{\mathrm{r}i} \\ & + B_{32i}(1 - N_{2i}/N_{3i})N_{\mathrm{photon}} - (N_{2i} - N_{2i\mathrm{therm}})/\tau_{21i},\end{aligned} \tag{2.49}$$

$$\mathrm{d}N_{\mathrm{photon}}/\mathrm{d}t = -\left[\gamma - \sum B_{32i}(1 - N_{2i}/N_{3i})\right] N_{\mathrm{photon}} + \sum \beta_i N_{3i}/\tau_{\mathrm{r}i}, \tag{2.50}$$

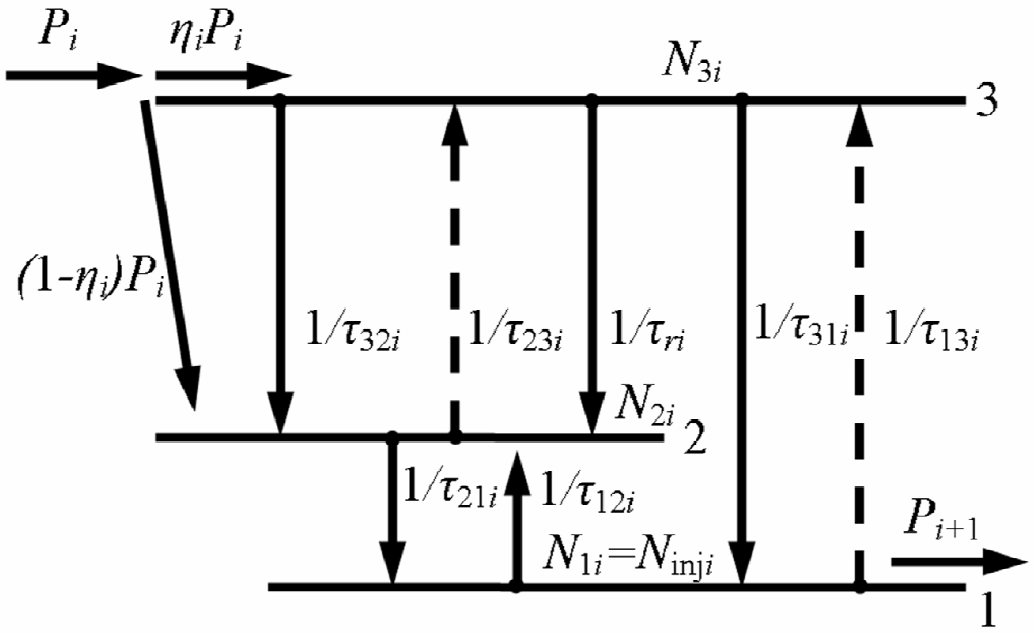

Figure 2.8: Three-level model system of the ith stage of the active region in a QC laser used in the rate equation analyses [6]. ©2008 IEEE.

where P_i is the pump rate given by the current I_i over the electron charge e, i.e., $P_i = I_i/e$, η_i is the pump efficiency for level 3, B_{32i} is the stimulated emission rate per one photon, and β_i the coupling efficiency of spontaneous emission into the single lasing mode, all in the ith cascade stage. Here, γ is the photon decay rate in a cavity, given by $\gamma = c(\alpha_{\rm int}+\alpha_{\rm m})$ where c, $\alpha_{\rm int}$, and $\alpha_{\rm m}$ are the group light velocity in the waveguide, the internal loss, and the mirror loss, respectively. The decay rate γ is typically $10^{11} \sim 10^{12}$ 1/s in a QC laser without external cavity, which has the same order of magnitude as that in a bipolar semiconductor laser. On proceeding to the rate equation analysis, the Einstein relationship is used, that the stimulated emission rate per one photon in an optical mode should be, in general, equal to the rate of spontaneous emission coupled into the same mode, i.e., in the present case, $B_{32i} = \beta_i N_{3i}/\tau_{{\rm r}i}$. The lasing characteristics of a QC laser would be described by the coupled spontaneous emission rate $\beta_i/\tau_{{\rm r}i}$ which is connected to a gain coefficient in Section 2.2.4.1. Explicit forms and numerical examples for the coupling efficiency of spontaneous emission β_i and the spontaneous emission lifetime $\tau_{{\rm r}i}$ are given in Section 2.2.4.1. The rate equations written by the coupled spontaneous emission rate $\beta_i/\tau_{{\rm r}i}$ (not by the optical gain coefficient) simplifies the theoretical treatments, consequently one can easily catch the heart of the physics behind the laser action. Using (2.48) and (2.49), one obtains the relation at steady state condition, ${\rm d}/{\rm d}t \to 0$ below threshold for the onset of lasing, i.e., $N_{\rm photon} = 0$,

$$N_{3i} - (N_{2i} - N_{2i{\rm therm}}) = N_{3i}/n_{\rm sp}, \tag{2.51}$$

where the population inversion parameter (or spontaneous emission factor) $n_{\rm sp}$ is defined by

$$n_{\rm sp} = \left[1 - (\tau_{21i}/\tau_{{\rm t}i})(1/\eta_i - \tau_{{\rm t}i}/\tau_{31i})\right]^{-1}. \tag{2.52}$$

Physically, the population inversion parameter $n_{\rm sp}$ means, below threshold ($N_{\rm photon}$ =0), the ratio of coupled spontaneous emission rate $(\beta_i/\tau_{{\rm r}i})N_{3i}$ to the increment, $(\beta_i/\tau_{{\rm r}i})[N_{3i} - (N_{2i} - N_{2i{\rm therm}})]$, of net stimulated emission rate per one photon from the absorption rate, $-(\beta_i/\tau_{{\rm r}i})N_{2i{\rm therm}}$. Similarly, by using (2.48) and (2.49)

together with the Einstein relationship and (2.52), the electron population difference at steady state condition is, also, expressed as

$$N_{3i} - N_{2i} = \frac{\eta_i P_i \tau_{ti}/n_{sp} - N_{2i\text{therm}}}{1 + \beta_{\text{eff}}(1 + \tau_{21i}/\tau_{31i})N_{\text{photon}}}, \tag{2.53}$$

where the effective coupling efficiency $\beta_{\text{eff}i}$, involved in the gain saturation term is given by

$$\beta_{\text{eff}i} = \tau_{ti}\beta_i/\tau_{ri}. \tag{2.54}$$

The effective coupling efficiency $\beta_{\text{eff}i}$ is defined as the fractional rate, $(\beta_i/\tau_{ri})/(1/\tau_{ti})$, of spontaneous emission coupled into a lasing mode to the non-lasing transition. Equation (2.53) indicates that the saturation of gain $(\beta_i/\tau_{ri})(N_{3i} - N_{2i})$, linked to the onset of lasing takes place with the photon populations $N_{\text{photon}} > 1/\beta_{\text{eff}i}(1 + \tau_{21i}/\tau_{31i})$. Thus, the effective coupling efficiency $\beta_{\text{eff}i}$ is anticipated to play an important role in understanding the physics behind narrow LWs [6]. By putting $N_{\text{photon}} \sim 0$ in (2.53) and by using the loss–gain balance relation $\sum_i \beta_i(N_{3i} - N_{2i})/\tau_{ri} \sim \gamma$, the threshold pump current is approximated as

$$I_{\text{th}} = \frac{e\,(\gamma + \sum \beta_i N_{2i\text{therm}}/\tau_{ri})}{\sum \beta_{\text{eff}i}\eta_i/n_{sp}}. \tag{2.55}$$

Now we consider an ideal case where all the physical parameters take common values, independently of the stage number i, namely translational symmetry of the active region, dropping the suffix i from the physical parameters in what follows in this section. The rate equations with the help of the Einstein relationship lead to the steady state photon population N_{photon} as a function of the normalized pump current $r = eP/I_{\text{th}} = I_0/I_{\text{th}}$,

$$N_{\text{photon}} = \left[\frac{1 + F_{\text{bf}}}{2\beta_{\text{eff}}(1 + \tau_{21}/\tau_{31})}\right]\left\{\left[(r-1) + \frac{r n_{sp}(\tau_{21}\beta_{\text{eff}}/\tau_t)}{\eta} + \frac{\beta_{\text{eff}}F_{\text{bf}}}{1 + F_{\text{bf}}}\right]\right.$$
$$\left. + \sqrt{\left[(r-1) + \frac{r n_{sp}(\tau_{21}\beta_{\text{eff}}/\tau_t)}{\eta} + \frac{\beta_{\text{eff}}F_{\text{bf}}}{1 + F_{\text{bf}}}\right]^2 + \frac{4r\beta_{\text{eff}}n_{sp}(1 + \tau_{21}/\tau_{31})}{1 + F_{\text{bf}}}}\right\}, \tag{2.56}$$

where the back-filling parameter F_{bf} is defined, for the total number M of cascade stages, as

$$F_{\text{bf}} = \frac{M\beta_{\text{eff}}N_{2\text{therm}}}{\gamma\tau_t}, \tag{2.57}$$

and the approximate threshold current density is given

$$I_{\rm th} = \frac{en_{\rm sp}\gamma(1+F_{\rm bf})}{\eta M \beta_{\rm eff}}. \tag{2.58}$$

Obviously, a small value for the effective coupling efficiency $\beta_{\rm eff} \sim 10^{-7}$ pushes up the threshold current, which can be partially recovered by adopting a large value for the cascade stage number M. To be accurate, from (2.58), the threshold condition is $(r-1) + rn_{\rm sp}(\tau_{21}\beta_{\rm eff}/\tau_{\rm t})/\eta + \beta_{\rm eff}F_{\rm bf}/(1+F_{\rm bf}) = 0$, i.e., $r = [1-\beta_{\rm eff}F_{\rm bf}/(1+F_{\rm bf})]\,/\,[1+n_{\rm sp}(\tau_{21}\beta_{\rm eff}/\tau_{\rm t})/\eta] < 1$ so that the accurate threshold current is always lower than the approximate one given by (2.58). In particular, if the term $\beta_{\rm eff}F_{\rm bf}/(1+F_{\rm bf})$ is close to unity, i.e., $\tau_{\rm r} \sim \tau_{\rm t}$, $\beta \sim 1$ and $F_{\rm bf}/(1+F_{\rm bf}) \sim 1$, the threshold current would be very low, close to zero. This is similar to the predicted lasing without population inversion, caused by a strong photon recycling in a semiconductor micro-cavity laser [16]. However, equation (2.58) can be safely used for the estimation of the threshold current in a real QC laser since the correction terms $\beta_{\rm eff}F_{\rm bf}/(1+F_{\rm bf})$ and $n_{\rm sp}(\tau_{21}\beta_{\rm eff}/\tau_{\rm t})/\eta$ are negligibly small in a QC laser. Here, one can easily obtain an expression for the threshold current density since $\beta_{\rm eff}$, i.e., $\beta_{\rm r}/\tau_{\rm r}$ is given by a form being inversely proportional to the area $L_{\rm qc}w_{\rm qc}$ of the quantum confinement structure in the active region. A generalized expression (2.56) for the photon population $N_{\rm photon}$ holds rigorously for a wide range of pump currents, continuously from below to above threshold, and delineates an extremely steep change of the photon population around the threshold in a QC laser.

Because of $n_{\rm sp}(\tau_{21}\beta_{\rm eff}/\tau_t)/\eta$, $\beta_{\rm eff}F_{\rm bf}/(1+F_{\rm bf})$, and $\beta_{\rm eff}n_{\rm sp}(1+\tau_{21}/\tau_{31})/(1+F_{\rm bf}) << 1$ in a real QC laser, the photon population $N_{\rm photon}$ is approximated to be, above the threshold $r > 1$,

$$\begin{aligned} N_{\rm photon} &\sim \left[\frac{(1+F_{\rm bf})}{\beta_{\rm eff}(1+\tau_{21}/\tau_{31})}\right](r-1) \\ &\sim \left[\frac{\eta M}{en_{\rm sp}\gamma(1+\tau_{21}/\tau_{31})}\right][I_0 - I_{\rm th}], \end{aligned} \tag{2.59}$$

and, below the threshold $r < 1$,

$$N_{\rm photon} \sim \frac{n_{\rm sp}r}{1-r} \sim \left[\frac{\eta M \beta_{\rm eff}}{e\gamma(1+F_{\rm bf})}\right] I_0. \tag{2.60}$$

The calculated photon number N_{photon} as functions of the pump current I_0 is plotted in Fig. 2.9(a), indicating that the photon population jumps up to a high level immediately-above threshold, by a factor of $\sim 1/\beta_{\text{eff}}$ being, as confirmed by (2.56), independent of the pump efficiency, the stage number M and the photon decay rate. In a realistic mid-infrared QC laser, the situation is very radical, namely the effective coupling efficiency is very small, $\beta_{\text{eff}} \sim 10^{-7}$, because of $\tau_{\text{t}} \sim \tau_{\text{nr}} \sim$ 1 ps and $\tau_{\text{r}} \sim$10 ns, i.e., $\tau_{\text{t}}/\tau_{\text{r}} \sim 10^{-4}$, despite of a relatively large coupling efficiency, $\beta \sim 10^{-3}$, much larger than that, $\beta = 10^{-4}$–10^{-5} of a near-infrared bipolar laser in which nonradiative relaxation is usually disregarded ($\beta_{\text{eff}} \sim \beta$). Figure 2.9(b) shows our own experimental results of output intensity vs injection current of a 7.7 μm 3-quantum well single-mode DFB QC laser at 80 K as well as of, as a reference device, a conventional 800 nm AlGaAs single-transverse-mode bipolar laser at room temperature in comparison with the theoretical photon population N_{photon} at a single mode. The predicted explosive jump of the photon population of a QC laser around threshold is supported by our experimental result of the output intensity which is to be in proportion to the internal photon population N_{photon} in the cavity.

The use of (2.59) and population N_3 along with the loss-gain balance relation $M(\beta/\tau_{\text{r}})(N_3 - N_2) \sim \gamma$ leads to the ratio of net stimulated emission rate $M(\beta/\tau_{\text{r}})(N_3 - N_2)N_{\text{photon}}$ to rate $M(\beta/\tau_{\text{r}})N_3$ of spontaneous emission coupled into a lasing mode above threshold. The stimulated emission rate brought about by "a moderate normalized pump current ($I_0/I_{\text{th}} \sim 2$)" in the limit $\tau_{21} \ll \tau_{\text{t}}$ is $\sim 1/\beta_{\text{eff}} \sim 10^7$ times as high as the rate of spontaneous emission coupled into the lasing mode. Obviously, such a high stimulated-to-coupled-spontaneous emission rate ration is linked to a very small effective coupling coefficient $\beta_{\text{eff}} \sim 10^{-7}$, namely, to short nonradiative scattering time τ_{nr} for upper-level electrons. This fact leads to an extremely narrow linewidth of QC laser [6].

2.4 Pump schemes for quantum cascade lasers

In the previous section, we clarified the usefulness of the rate equation method for modeling a QC laser. Here, we propose two new upper quantum state designs,

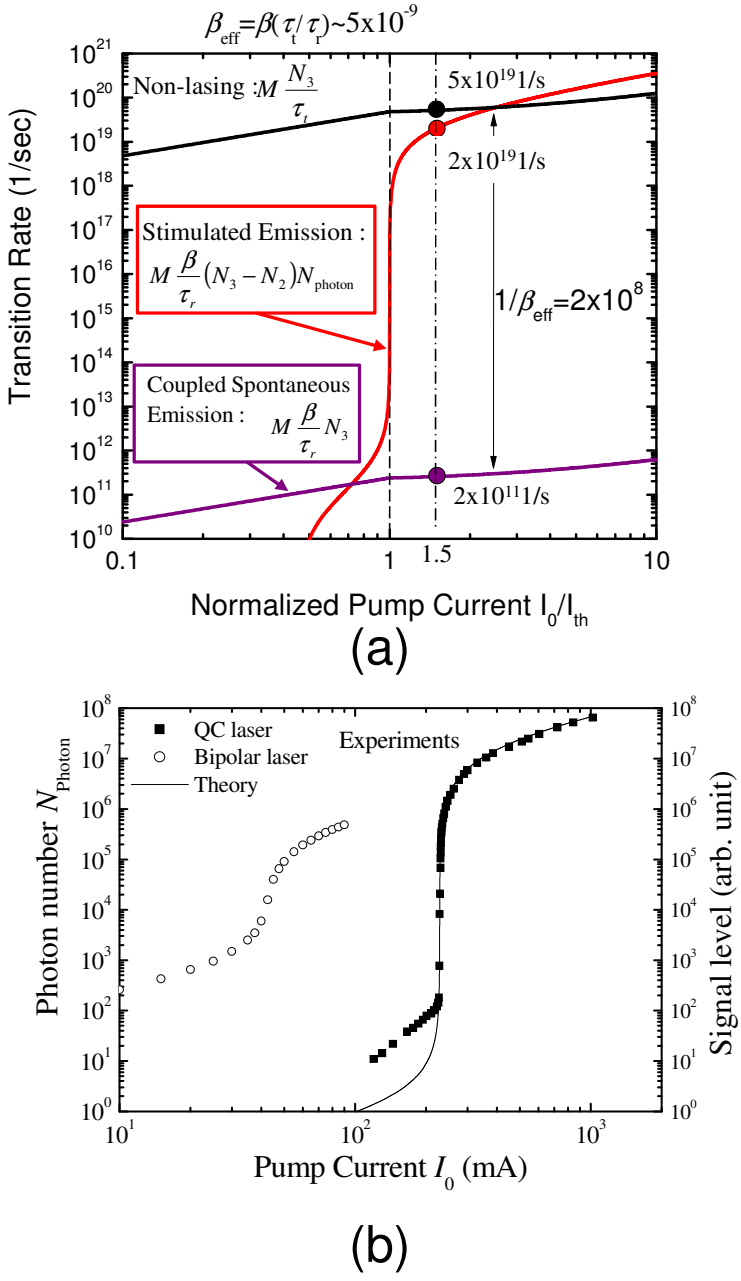

Figure 2.9: (a) Stimulated emission rate, nonlasing rate and the rate of spontaneous emission coupled into the lasing mode, as functions of the normalized pump current. (b) Experimental results of output intensity versus injection current of a 7.7 μm three-quantum-well single mode DFB QC laser at 80 K as well as of a conventional 800-nm AlGaAs single-transverse-mode bipolar laser at room temperature [6]. ©2008 IEEE.

the indirect pump scheme and the dual-upper-state design, and exhibit their advantages over the conventional direct pump scheme by the using rate equation approach. Schematic illustrations for the pump schemes are shown in Fig. 2.10. For the IDP scheme, electrons are injected into the intermediate state, level 4 (not level 3), and then are relaxed quickly to the upper laser state, level 3, by LO phonon emissions. On the other hand, for the DAU design (Fig. 2.10(c)), electrons are injected into the higher upper state, state 4, via resonant tunneling from the ground state, level 1′, and then are quickly distributed in the two upper laser states by LO phonon scattering or by elastic scattering (electron–electorn, interface roughness, alloy scattering, or impurity scattering). Above room temperature, the electron populations in the both upper laser states are kept equal, because of the small energy gap between the two upper states ($E_{43} \sim 20$ meV) and the fast elastic scatterings.

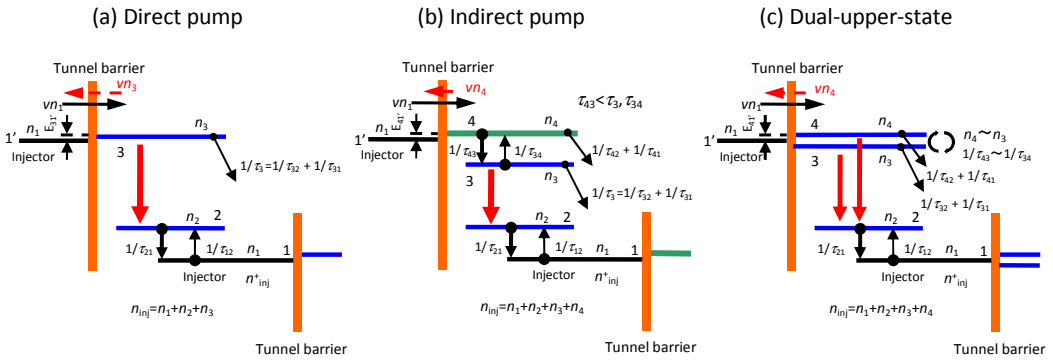

Figure 2.10: Schematic illustration of various types of upper quantum states. (a) direct pump scheme (b) indirect pump scheme (c) dual-upper-state design

In order to investigate the pump schemes, the rate equation models are developed for three types of upper quantum states, the DP, IDP, and DAU, in which the injection efficiency is assumed to be unity for the sake of comparing the pump schemes. As described in Section 2.3 [4], the (net) tunneling current density for the DP cases is represented by

$$j = \frac{e(n_1 - n_3)}{[1 + (E_{31'}/\hbar)^2 \tau_{\mathrm{deph}}^2]\tau_{\mathrm{tunn}}}, \tag{2.61}$$

where $E_{31'}$ and $\tau_{\rm deph}$ are the energy separation between levels 3 and 1′, and the dephasing time. The tunneling time is defined as $\tau_{\rm tunn} = 2/(\Omega_{31'}^2\tau_{\rm deph})$ with the Rabi oscillation frequency $\Omega_{31'}$. The current consists of forward (n_1) and backward (n_3) components. In the conventional DP case, the backward tunneling current, represented by the (red colored) dashed arrow in Fig. 2.10(a), is almost equal to the forward current at the maximum limit, and in turn the electron population n_1 must remain in one-half of the injector doping density $n_{\rm inj}$. In an approach based on rate equations with fixed relaxation times for the relaxation processes with the help of Eq. (2.61) and of particle conservation (charge neutrality in each cascade stage), $n_{\rm inj} = n_1 + n_2 + n_3$, the tunneling current density without stimulated emission reads

$$j = \frac{en_{\rm inj}}{(1+\tau_{21}/\tau_{12})[1+(E_{31'}/\hbar)^2\tau_{\rm deph}^2]\tau_{\rm tunn}+\tau_{\rm relax}}, \tag{2.62}$$

where the global relaxation time is given by $\tau_{\rm relax}$=$\tau_3(3-1/n_{\rm sp}+\tau_{21}/\tau_{12})$, where $1/\tau_3 = 1/\tau_{32} + 1/\tau_{31}$ for the DP case. The population inversion parameter (or spontaneous emission factor) is defined as $n_{\rm sp} = 1/[1-\tau_{21}/\tau_{32}]$ for the DP case. From the principle of detailed balance, the lifetime ratios are, regardless of the details of the system, represented simply by $\tau_{21}/\tau_{12} = \exp(E_{21}/k_{\rm B}T)$. The electron populations for the DP case at levels 1∼3 are

$$\begin{aligned} n_1/n_{\rm inj} &= [1/(1+\tau_{21}/\tau_{12})][1-(2-1/n_{\rm sp})(j\tau_3/en_{\rm inj})], \\ n_2/n_{\rm inj} &= (\tau_{21}/\tau_{12})(n_1/n_{\rm inj}) + (1-1/n_{\rm sp})(j\tau_3/en_{\rm inj}), \\ n_3/n_{\rm inj} &= j\tau_3/en_{\rm inj}. \end{aligned} \tag{2.63}$$

The electron population $n_2/n_{\rm inj}$ at the lower laser state, level 2, consists of the thermal back filling $(\tau_{21}/\tau_{12})(n_1/n_{\rm inj}) = n_{2\rm therm}/n_{\rm inj}$ and the excess term $(1-1/n_{\rm sp})(j\tau_3/en_{\rm inj})$. On the other hand, for the IDP scheme (Fig. 2.10(b)), the electron population n_4 at level 4 is expected to be low, $n_4 = (\tau_{43}/\tau_3+\tau_{43}/\tau_{34})n_3 < n_3$ where $1/\tau_3 = 1/\tau_{32}+1/\tau_{31}$. Thus, the backward tunneling current, represented by the (red colored) dashed arrow in Fig. 2.10(b), is kept to be low even when the electron population n_3 at level 3 approaches a high value, comparable to the injector doping density $n_{\rm inj}$. With the rate equations and particle conservation $n_{\rm inj} =$

$n_1+n_2+n_3+n_4$, the tunneling current density without stimulated emission is as in the DP case (2.62) but after replacing $E_{31'}$ with $E_{41'}$. The global relaxation time is given by $\tau_{\rm relax} = \eta_{\rm pump}\tau_3[2-1/n_{\rm sp}+(2+\tau_{21}/\tau_{12})(\tau_{43}/\tau_{34}+\tau_{43}/\tau_3)]$ for the IDP case. The pump efficiency in the IDP case for level 3 is defined as $\eta_{\rm pump} = (n_4/\tau_{43} - n_3/\tau_{34})/(j/e) = \eta_0/[1+(\tau_3/\tau_{34})(1-\eta_0)]$ with $\eta_0 = (1/\tau_{43})/[1/\tau_{43}+1/\tau_{42}+1/\tau_{41}]$. The population inversion parameter (or spontaneous emission factor) is also defined as $n_{\rm sp} = 1/\left\{1-\tau_{21}[1/\tau_{32}+(1/\tau_{42})(1/\eta_{\rm pump}-1)/(\tau_3/\tau_{42}+\tau_3/\tau_{41})]\right\}$ for the IDP case. The life time ratios are also represented by $\tau_{43}/\tau_{34} = \exp(-E_{43}/k_{\rm B}T)$. The electron populations for the IDP case at levels 1∼4 read

$$\begin{aligned} n_1/n_{\rm inj} &= [1/(1+\tau_{21}/\tau_{12})][1-(2-1/n_{\rm sp}+\tau_{43}/\tau_{34}+\tau_{43}/\tau_3)(\eta_{\rm pump}j\tau_3/en_{\rm inj})], \\ n_2/n_{\rm inj} &= (\tau_{21}/\tau_{12})(n_1/n_{\rm inj})+(1-1/n_{\rm sp})(\eta_{\rm pump}j\tau_3/en_{\rm inj}), \\ n_3/n_{\rm inj} &= (\eta_{\rm pump}j\tau_3/en_{\rm inj}) = [1/(\tau_{43}/\tau_{34}+\tau_{43}/\tau_3)](n_4/n_{\rm inj}). \end{aligned} \tag{2.64}$$

In an ideal IDP situation, $n_{\rm sp}\sim 1$, $\tau_{43}/\tau_{34}+\tau_{43}/\tau_3 \ll 1$ and $\tau_{\rm tunn} \ll \tau_{\rm relax}$ under near resonance, $(E_{41'}/\hbar)^2\tau_{\rm deph}^2 < 1$, the maximum current density, $\eta_{\rm pump}j_{\rm max}$, actually available for pumping of level 3 is given by $\eta_{\rm pump}j_{\rm max} = en_{\rm inj}/\tau_3$, that is, regardless of the value of $\eta_{\rm pump}$, *twice* as high as that, $en_{\rm inj}/2\tau_3$of the DP case for the same doping level of the injector, $n_{\rm inj}$. Namely, in the IDP case, under the extreme assumption that the electrons originally existing in the injector are perfectly transferred to the upper laser state, level 3, $n_3 \sim n_{\rm inj}$ and, in turn, the population n_1 in the injector is completely depleted, i.e., ultimately, $n_1 \sim n_4 \ll n_3 \sim n_{\rm inj}$. The IDP scheme presents the obvious advantages over the conventional DP, of a higher available population at the upper laser level and a lower population in the injector, i.e., $n_3 \sim n_1 \sim n_{\rm inj}/2$ in the strong pump limit.

Finally, for the DAU case, the tunneling current density in a below-threshold case also reads as (2.62), and the global relaxation time and the population inversion parameter are given by, respectively, $\tau_{\rm relax}=\tau_{\rm up}(4-1/n_{\rm sp}+\tau_{21}/\tau_{12})$ and $n_{\rm sp} = 1/[1-\tau_{21}(1/\tau_{32}+1/\tau_{42})]$. The electron populations for the DAU case at level 1∼4 read:

$$\begin{aligned} n_1/n_{\rm inj} &= [1/(1+\tau_{21}/\tau_{12})][1-(3-1/n_{\rm sp})(j\tau_{\rm up}/en_{\rm inj})], \\ n_2/n_{\rm inj} &= (\tau_{21}/\tau_{12})(n_1/n_{\rm inj})+(1-1/n_{\rm sp})(j\tau_{\rm up}/en_{\rm inj}), \\ n_4/n_{\rm inj} &= n_3/n_{\rm inj} = j\tau_{\rm up}/en_{\rm inj}, \end{aligned} \tag{2.65}$$

where $1/\tau_{\rm up} = 1/\tau_{42} + 1/\tau_{41} + 1/\tau_{32} + 1/\tau_{31}$. For the case $\tau_4 \sim \tau_3$, the maximum current density is given by $j_{\rm max} = en_{\rm inj}/3\tau_{\rm up} = 2en_{\rm inj}/3\tau_3$. The population n_1 in the injector decreases to one-third of the electron population originally in the injector. Thus, the population in the DAU case is substantially smaller than that in the DP case, and in this view, the DAU design still has an advantage over the DP scheme.

In a realistic device, however, even in the IDP scheme, the population inversion parameter $n_{\rm sp}$ may be larger than unity and the sum of the relaxation time ratios $\tau_{43}/\tau_{34} + \tau_{43}/\tau_3$ may take a value nominally smaller than unity at high temperatures $T \sim 300$ K. By using realistic values for the important parameters, i.e., $n_{\rm sp} \sim 1.17$ for each case and $\tau_{43}/\tau_{34} + \tau_{43}/\tau_3 = 0.477$ for the IDP case (see the caption of Fig. 2.11), the normalized electron populations for all the cases are computed with Eqs. (2.62), (2.63), (2.64), and (2.65), which are shown in Fig. 2.11. In the IDP case, the upper level population n_3 is able to be, still, higher than the ground state one n_1 near the maximum current, namely global population inversion. The ground state population n_1 of the IDP and DAU ones decreases strongly with increasing current, compared with that of the DP one, implying a stronger absorption quenching optical loss due to off-resonant intersubband transitions in the injector [17] . The quality factor for lasing, defined here as $Q \sim (n_3 - n_2)/n_1$, of the IDP case is twice that of the DP around the maximum current. In addition, the Q-values of the IDP and DAU lasers increase super-linearly with increasing current. The loss–gain balance relation at threshold conditions, $G_{\rm c}(n_3 - n_2) = \alpha_{\rm cinj}n_1 + \alpha_{\rm g} + \alpha_{\rm m} \sim \alpha_{\rm cinj}n_1$ where $G_{\rm c}$ is the modal gain cross section, $\alpha_{\rm cinj}$ is the absorption cross section in the injector, $\alpha_{\rm g}(< 1\,{\rm cm}^{-1})$ is the passive waveguide loss, and $\alpha_{\rm m}$ is the mirror loss, leads to the simple relation approximately, $Q \sim \alpha_{\rm cinj}/G_{\rm c}$ where $\alpha_{\rm g}$ is negligible. Thus, a steeper increase in the Q-value is linked to a higher T_0-value, as will be seen in Chapter 4. The differential Q-factors for each scheme, as a function of the normalized current, are shown in Fig. 2.12. The Q-factors in the IDP and DAU cases are dramatically elevated and at the maximum current are more than twice that of the DP. The large values of the differential Q-factors could serve to elevate the T_0-values in realistic device.

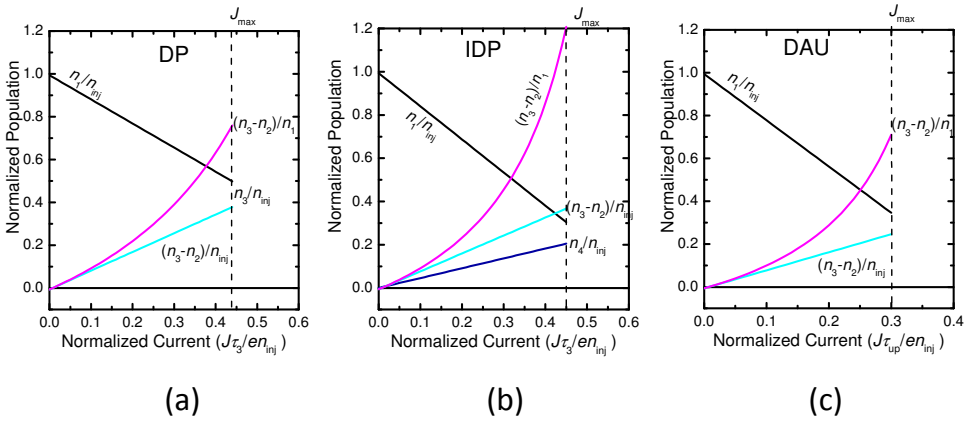

Figure 2.11: Electron populations of pump schemes. (a) Normalized electron populations in a DP laser, computed with Eq. (2.63) using the parameters: n_{sp}=1.15, $\tau_{21}/\tau_{12} \sim 0.0065$, and τ_{tunn}/τ_3=0.18. (b) Normalized electron populations in an IDP laser, computed with Eq. (2.64) using the parameters: n_{sp}=1.17, $\tau_{21}/\tau_{12} \sim 0.0065$, and $\tau_{43}/\tau_{34} + \tau_{43}/\tau_3 = 0.477$; and the normalized maximum current density computed with Eq. (2.62) using τ_{tunn}/τ_3=0.18 and η_{pump}=0.8. (c) Normalized electron populations in a DAU laser, computed with Eq. (2.65) using the parameters: n_{sp}=1.2, $\tau_{21}/\tau_{12} \sim 0.0065$, and τ_{tunn}/τ_3=0.18. These parameter values are very close to room temperature values actually used in the computation of the threshold current density of the test devices operating at around 8 μm.

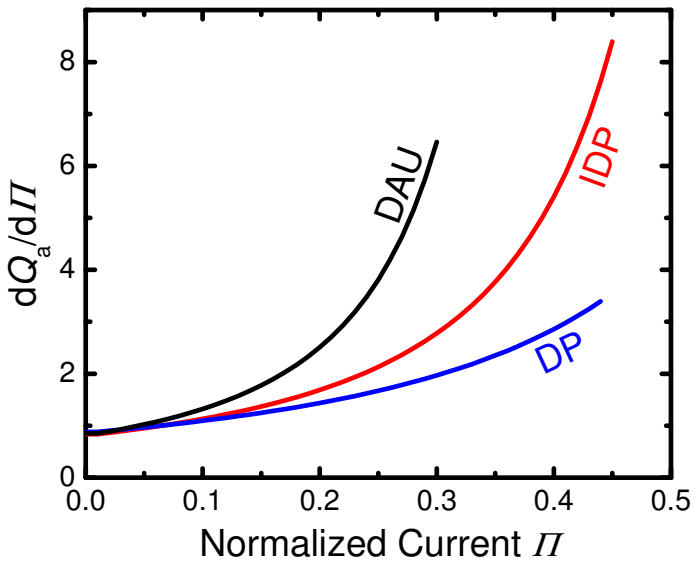

Figure 2.12: Differential Q-factors shown in Fig.2.11 as a function of the normalized current, $\Pi = j\tau_3/en_{\rm inj}$, or $= j\tau_{\rm up}/en_{\rm inj}$.

2.5 Conclusion

In this chapter, we presented the basic theoretical tools for modeling a quantum cascade laser. Electron transport in QC structure was modeled by finding the energetic states and wave functions of the Schrödinger equation. Besides, spontaneous emission and nonradiative transition dominated by LO phonon were calculated. By using these methods, the rate equation approach can demonstrate the electron dynamics of a QC laser and develop an expression for its threshold current density. The electron dynamics determine the population as well as the internal optical absorption in the injector. This newly proposed indirect pump scheme and dual-upper-state design show a strong decrease in the electron population in the ground state, n_1. This implies that the IDP scheme and DAU design can be anticipated to have better temperature performances than the direct pump, since the intersubband absorption is proportional to the electron population n_1.

References

[1] C. Sirtori, F. Capasso, and J. Faist, "Nonparabolicity and a sum rule associated with bound-to-bound and bound-to-continuum intersubband transitions in quantum wells," Phys. Rev. B **50**, 8663 (1994).

[2] J. H. Davies "The physics of low-dimensional semiconductors," Cambridge University Press, 276 (1998).

[3] J. Faist, "Quantum cascade lasers," Oxford University Press, (2013).

[4] H. Callebaut and Q. Hu, "Importance of coherence for electron transport in terahertz quantum cascade lasers," J. Appl. Phys. **98**, 104505 (2005).

[5] M. Yamanishi, unpublished note (2008).

[6] M. Yamanishi, T. Edamura, K. Fujita, N. Akikusa, and H. Kan, "Theory of the intrinsic linewidth of quantum-cascade lasers: Hidden reason for the narrow linewidth and line-broadening by thermal photons," IEEE J. Quantum Electron. **46**, 12 (2008). ©2008 IEEE.

[7] R. Ferreira and G. Bastard, "Evaluation of some scattering times for electrons in unbiased and biased single- and multiple-quantum-well structures," Phys. Rev. B **40**, 1074 (1989).

[8] D. Ahn and S. L. Chuang, "Electric field dependence of intrasubband polar-optical-phonon scattering in a quantum well," Phys. Rev. B, **37**, 2529 (1988).

[9] G. Bastard, "Energy levels and alloy scattering in InP - In (Ga)As heterojunctions," Appl. Phys. Lett. **43**, 591 (1983).

[10] T. Unuma, M. Yoshita, T. Noda, H. Sakaki, and H. Akiyama, "Intersubband absorption linewidth in GaAs quantum wells due to scattering by interface roughness, phonons, alloy disorder, and impurities," J. Appl. Phys. **93**, 1586 (2003).

[11] S. Tsujino, A. Borak, E. Muller, M. Scheinert, C. V. Falub, H. Sigg, D. Grutzmacher, M. Giovannini, and J. Faist, "Interface-roughness-induced broadening of intersubband electroluminescence in p-SiGe and n-GaInAs/AlInAs quantum-cascade structures," Appl. Phys. Lett. **86**, 062113 (2005).

[12] J. Faist, F. Capasso, C. Sirtori, D. L. Sivco, and A. L. Cho, "Quantum cascade lasers," in Intersubband Transitions in Quantum Wells: Physics and Device Applications II, edited by H. C. Liu and F. Capasso, Eds. San Diego, 1 (2000).

[13] D. Ahn and S. L. Chuang, "Electric field dependence of intrasubband polar-optical-phonon scattering in a quantum well," Phys. Rev. B **37**, 2529 (1988).

[14] R. Ferreira and G. Bastard, "Evaluation of some scattering times for electrons in unbiased and biased single- and multiple-quantum-well structures," Phys. Rev. B **40**, 1074 (1989).

[15] J. Kim, M. Lerttamrab, S. L. Chuang, C. Gmachl, D. L. Sivco, F. Capasso, and A. L. Cho, "Theoretical and experimental study of optical gain and linewidth enhancement factor of type-I quantum cascade lasers," IEEE J. Quantum Electron. **40**, 1663 (2004).

[16] G. Bjork and Y. Yamamoto, "Analysis of semiconductor microcavity lasers using rate equations," IEEE J. Quantum Electron. **27**, 2386 (1991).

[17] A. Wittmann, T. Gresch, E. Gini, L. Hovzdara, N. Hoyler, M. Giovannini, and J. Faist, "High-performance bound-to-continuum quantum-cascade lasers for broad-gain applications," IEEE J. Quantum Electron. **44**, 36 (2008).

Chapter 3

Design and development of directly pumped quantum cascade lasers

3.1 Introduction

Room temperature CW operation has already been achieved by the adoption of the two phonon resonance and bound-to-continuum active region designs [1, 2]. The threshold current and slope efficiency of the state of the art QC lasers are close to the theoretical values [3] obtained from the expressions in Chapter 2. To achieve such high performance, high quality epitaxial growth processing techniques, as well as a proper design of the laser structures, is required. In this chapter, we consider the conditions for obtaining the maximum performance from different point of view. First, the design procedures of the active region and waveguide are described. The optimization of the active region design, using wavefunction engineering, is an essential part of QC laser design since the fundamental limit on threshold current density is determined by the active region design. In fact, high performance is attained only for some particular designs mentioned above, which have to fulfill key requirements. Second, we will describe the characteristics of a QC laser design called the single phonon resonance-continuum

depopulation (SPC-depopulation) structure, which demonstrates CW operation at room temperature by taking advantage of high laser performance as well as the expected allowance for device-to-device fluctuations of the energy separation between the lower states, i.e., a high yield in mass production. In the final section, we develop QC lasers based on the SPC depopulation design to improve the laser performance. For the QC lasers, the highest performance in the wavelength range of 7–9 μm has been successfully achieved by choosing the most suitable configuration for the CW and pulsed modes.

3.2 Design of quantum cascade lasers

3.2.1 Design of QC structures

We will describe procedures for designing the QC structure. As discussed before, the QC structure consists of active parts and injectors, which comprise multiple quantum wells. In the design of the active region, the energy levels of the quantum wells in the injector are engineered to be flat at the designed bias and as a result, the electrons are injected into the upper state as shown in Fig. 3.1. The design procedures are as follows:

(1) Determination of active region design

First, the active region structure is chosen for the purpose at hand (long or short wavelength, high power, broadband, etc.). An the optical phonon resonance depopulation designs with coupled quantum wells [4], inter-miniband transition and depopulation [5], or bound-to-continuum transition [2] designs are widely used for high performance QC lasers. In the optical phonon resonance depopulation scheme, a short lifetime, τ_2, results from designing the spacing between the lower laser level 2 and level 1-mb to be resonant to the optical phonon energy. In the miniband relaxation schemes, the lifetime, τ_2, in the miniband is very short due to a phase space where electrons are scattered in any point in the miniband. Here we describe the single phonon resonance-continuum depopulation structure (see Section 3.3 for details).

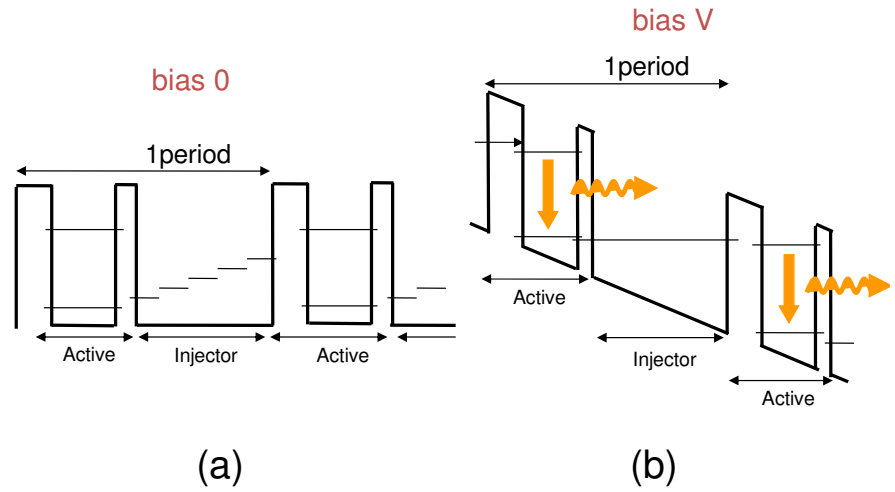

Figure 3.1: Schematic for operation of quantum cascade structure (a) bias 0 [V] (b) bias V [V]

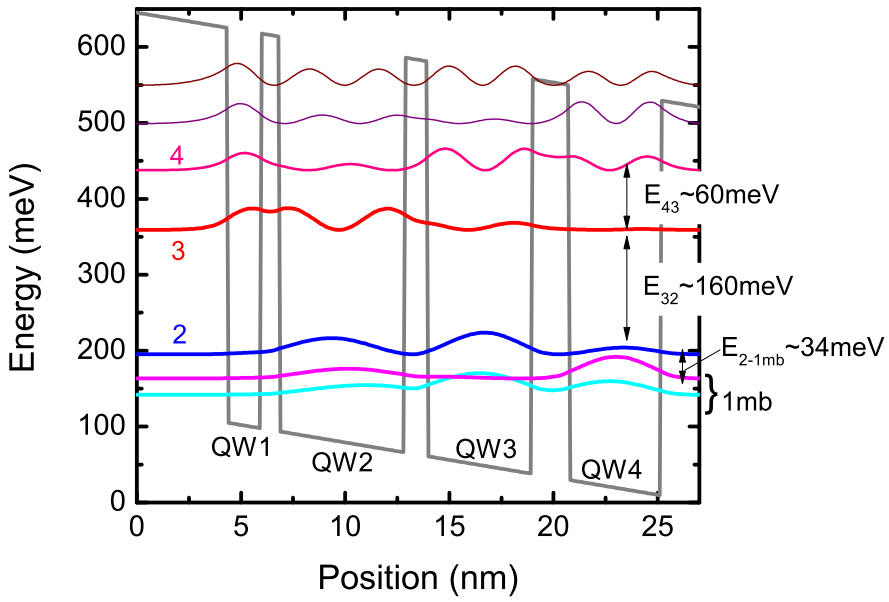

Figure 3.2: Energy band diagram and plot of the magnitude squired envelop wavefunctions for an active part of QC laser design.

(2) Determination of emission wavelength

An energy separation between the upper level 3 and lower level 2 providing a lasing wavelength is determined according to the thicknesses of the quantum well and barrier layers in the active part, and the applied electric field. The number of quantum wells used in the active part depends on the active region structure. For example, the SPC depopulation structure uses four quantum wells, while the chirped superlattice active regions structure consists of 4–6 quantum wells. The energy separation between the laser upper level 3 and the higher state 4 is designed to be large so as to enhance the injection efficiency since the activated electrons can be thermally excited to move from the upper level 3 to the higher levels. For the designed energy separation of E_{32} ∼160 meV, $E_{2-1\mathrm{mb}} \sim E_{\mathrm{LO}}$ ∼35 meV, E_{43} ∼60 meV, the layer thicknesses of the active part are designed to be 16/**9**/60/**11**/50/**18**/44/**20** where $In_{0.48}Al_{0.52}As$ barrier layers are in bold, $In_{0.53}Ga_{0.47}As$ QW layers in roman, under an assumed electric field. Ground states of coupled quantum wells 2-4 (Fig 3.2) provide lower laser state 2 as well as miniband 1-mb. On the other hand, the upper laser state 3 as well as higher parasitic states located at higher energy positions originates from coupled states of all quantum wells in active part, in which second states of the quantum wells 2-4 are strongly coupled in addition to a ground state of the first quantum well 1. The layer thicknesses are determined as a result of considering not only energy separation of each state but also spatial overlap and amplitude of wavefunctions. Note that the quantum well width and the thicknesses of the barrier which determine the emission wavelength cannot be determined independently since the wave function of each level is influenced strongly by each quantum well and barrier layer.

(3) Design parameters and applied electric field

The operating electric field is designed based on a roughly estimated total layer thickness of the active region structure of one period and a voltage drop. After the design procedure of the active region described above, we have to evaluate the design parameters, the upper state lifetime τ_3, lower state lifetime τ_{21}, and the dipole matrix element Z_{32}. The upper state lifetime and the dipole matrix element strongly depend on an the overlap of the wave functions between the upper and

lower laser levels, which are engineered in the design of the active region. A vertical transition which enhances the wavefunction overlap between the initial laser state 3 and the final state 2 results in a large dipole matrix element compared to a diagonal transition [6], while the lifetime will be substantially shorter than the value of the diagonal transition [4]. Thus, the diagonal transition has been preferably utilized for long wavelength (>10 μm) lasers.

(4) Design of injector layers

In the injector region, a miniband formed by a graded superlattice is used for electron transport and relaxation [7]. By narrowing the energy width of the relaxation miniband toward the active region of the subsequent stage, high injection efficiency from the ground level 1 into the upper laser level 3 is obtained. In this configuration, the quantum well thicknesses monotonically decrease from the active region side of the same stage toward that of the next stage, while the barrier thicknesses excluding the exit barrier monotonically increase. The exit barrier which divides the active region and injector region has an important role in the electron transport. If the exit barrier is excessively thick, the electron transport time from the active layer to the injector is slow. However, if the barrier is excessively thin, the wave functions between the active region and injector are strongly coupled. The thicknesses of the quantum wells and the barriers on the exit barrier side in the injector are designed to provide enough of an energy width of the miniband, so that electrons at lower levels below the lower laser level 2 in the active region are transported to a miniband in the injector. On the other hand, leakage from the upper laser level 3 can be suppressed by designing the injector to satisfy the Bragg reflection condition [6]. In addition, the energy width of the miniband should be narrowed so that electrons are injected into the upper laser level 3 of the subsequent stage. Another important point of the injector design is the suppression of thermal backfilling of carriers from the ground state of the injector. This can be sufficiently suppressed by designing a large energy difference Δ_{inj} between the lower laser level and the ground level in the injector. In general, the value is chosen to be 100–150 meV for high performance QC lasers since the

operation bias increases with Δ_{inj}.

(5) Determination of injection barrier thickness

Finally, the injection barrier thickness is determined by designing the "anticrossing gap" which represents the strength of the coupling between ground level 1′ in the previous stage and upper laser level 3. The anticrossing gap is directly connected with the tunneling time, limiting the maximum current density of a QC laser via Eq (2.62) described in Chapter 2. Typically the anticrossing gap is chosen to be 4-10 meV.

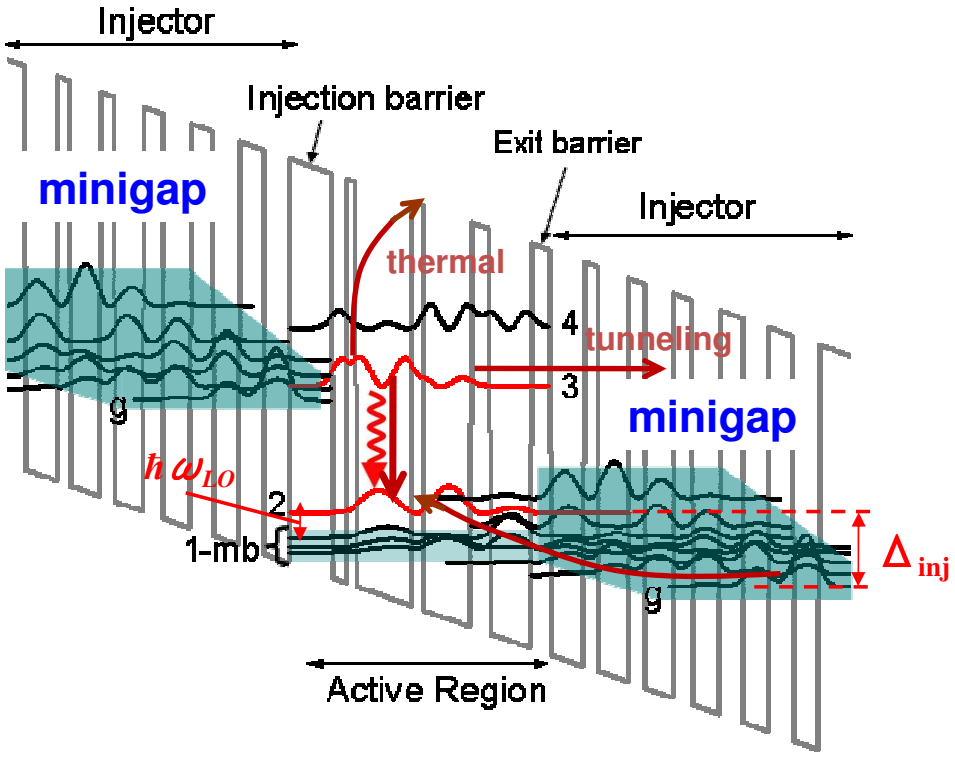

Figure 3.3: Band diagram and moduli squared of the relevant wavefunctions of the single phonon resonance-continuum depopulation design. The radiative transition takes place between level 3 and 2. The levels 2 and miniband 1-mb are separated by the optical phonon energy $\hbar\omega_{\mathrm{LO}}$. Δ_{inj} is the energy separation between the ground level in the injector and the lower laser level 2.

3.2.2 Waveguide

For better waveguide, both low optical losses and a large mode confinement are required. The waveguide for a multi-layer slab waveguide is composed of slabs of infinite length in the in-plane directions. For the TM modes of waveguide, the mode profile is given by

$$\boldsymbol{H}(y,z) = H_x(z)\exp(\mathrm{i}k_0 n_{\mathrm{eff}} y)\hat{\boldsymbol{x}}, \tag{3.1}$$

where z is along the growth direction, β is the propagation constant of the mode, k_0 is the free space propagation constant ($k_0 = \omega/c$), $H_x(z)$ is the magnetic field amplitude, and n_{eff} is the effective refractive index. The solution must fulfill the Helmholtz equation with refractive index profile $n(z)$:

$$\nabla^2 \boldsymbol{H} + k_0^2 n(z)^2 \boldsymbol{H} = 0. \tag{3.2}$$

Substituting equation (3.1) into equation (3.2), we obtain

$$\frac{\mathrm{d}^2 H_x(z)}{\mathrm{d}z^2} - \left(n_{\mathrm{eff}}^2 - n(z)^2\right) k_0^2 H_x(z) = 0. \tag{3.3}$$

Here, the boundary conditions require the continuity of H_x and $(1/\epsilon)\partial H_x/\partial x$. On the other hand, $\boldsymbol{E}$ with a y component is given by

$$E_y(z) = \frac{\mathrm{i}}{\omega\epsilon_0}\left(\frac{1}{n^2(z)}\frac{\mathrm{d}H_x(z)}{\mathrm{d}z}\right). \tag{3.4}$$

Figure 3.4 shows the TM mode profile in waveguide of a $\sim$8 μm QC laser with 50 period-active region. Using the mode profile, the overlap factor Γ, which represents the optical overlap with the active region, can be calculated:

$$\Gamma = \frac{\int_{\mathrm{active}} |E_y|^2 \,\mathrm{d}z}{\int_{-\infty}^{\infty} |E_y|^2 \,\mathrm{d}z}. \tag{3.5}$$

In general, the gain coefficient is proportional to Γ as shown in equation (3.5), a higher confinement is preferable for high device performance. In addition, there exists a free carrier absorption in the cladding layers, though this can be reduced by the adoption of very lightly doped layers. The waveguide layers must be doped enough to flow current and to avoid Joule heating in the layers. However,

in highly doped layers, the refractive index is changed and free carrier absorption is induced. The complex refractive index can be calculated using the Drude model [8].

$$\tilde{n}^2 = \epsilon_\infty \left[1 - \frac{\omega_\mathrm{p}^2}{\omega^2(1 + 1/(\omega\tau_\mathrm{r})^2)} \left(1 + \frac{\mathrm{i}}{\omega\tau_\mathrm{r}}\right)\right], \tag{3.6}$$

where the plasma frequency is

$$\omega_\mathrm{p} = \sqrt{\frac{Ne^2}{\epsilon_\infty \epsilon_0 m^*}}, \tag{3.7}$$

where ϵ_∞ is the high frequency dielectric constant, τ_r is the carrier lifetime, and N the carrier concentration. The scattering time is defined as $\tau_\mathrm{r} = \mu N m^*/e$. From (3.6), the optical loss due to free carrier absorption can be written as

$$\alpha = \frac{Ne^2\lambda_0^2}{4\pi^2 c^3 n_\mathrm{eff} \epsilon_0 m^* \tau_\mathrm{r}}. \tag{3.8}$$

Obviously, the free carrier losses increase linearly with the doping level and increase as the square of the wavelength.

3.3 Fabrication and measurement

3.3.1 Fabrication

All fabrication was performed at the Hamamatsu Photonics K.K. in the Central Research Laboratories. All our designed QC structures were grown by metal organic vapor phase epitaxy (MOVPE) and by molecular beam epitaxy (MBE) on n type InP wafers. The waveguide and contact layers of all samples were grown by MOVPE. For the epitaxial growth of QC structures, precise control of not only doping level but also the layer thickness is required, since the design requires very thin layers (few ML). Figure 3.6 shows the x-ray diffraction spectrum of a QC laser wafer grown by MOVPE, in comparison with the simulation result. Satellite peaks are clearly observed, indicating the presence of a periodic structure and excellent hetero-interface quality. The average thickness of the QC stages can be inferred from the observed spectrum. The period of the active region is assigned

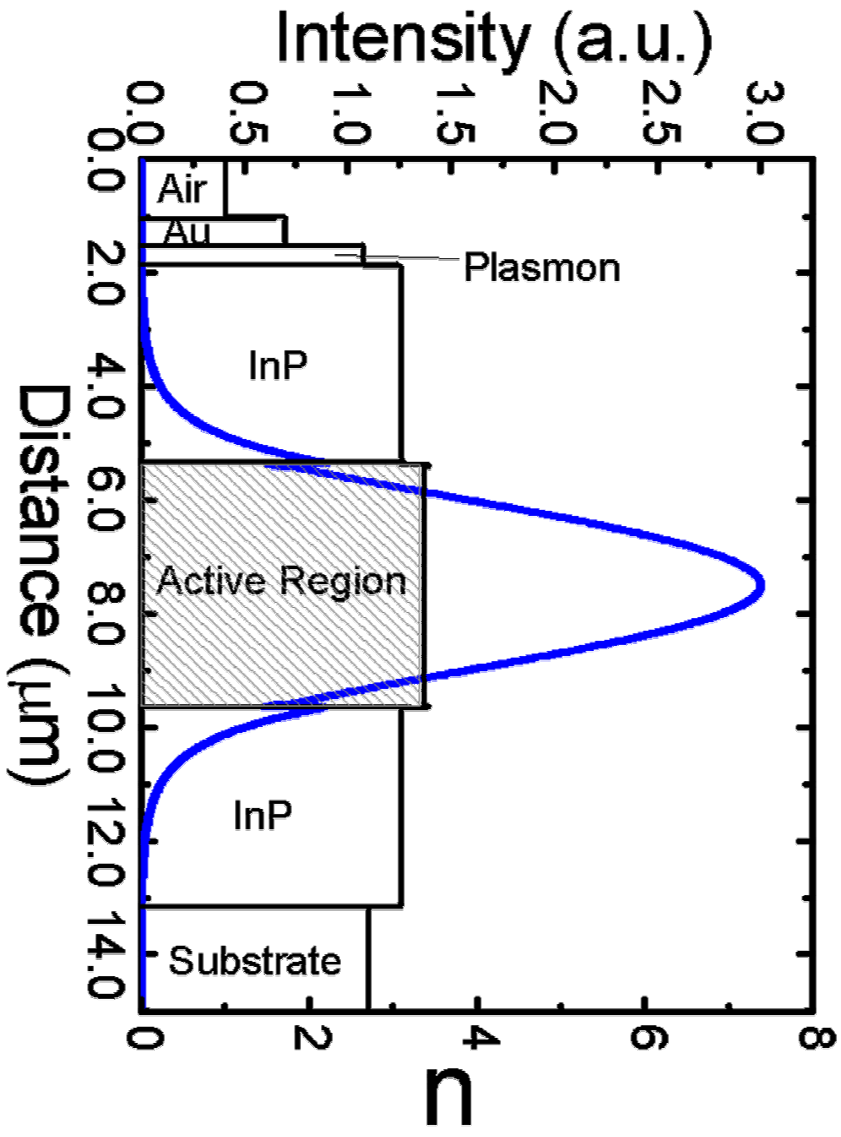

Figure 3.4: Fundamental TM mode intensity and refractive index of waveguide for a 8.2 μm QC laser

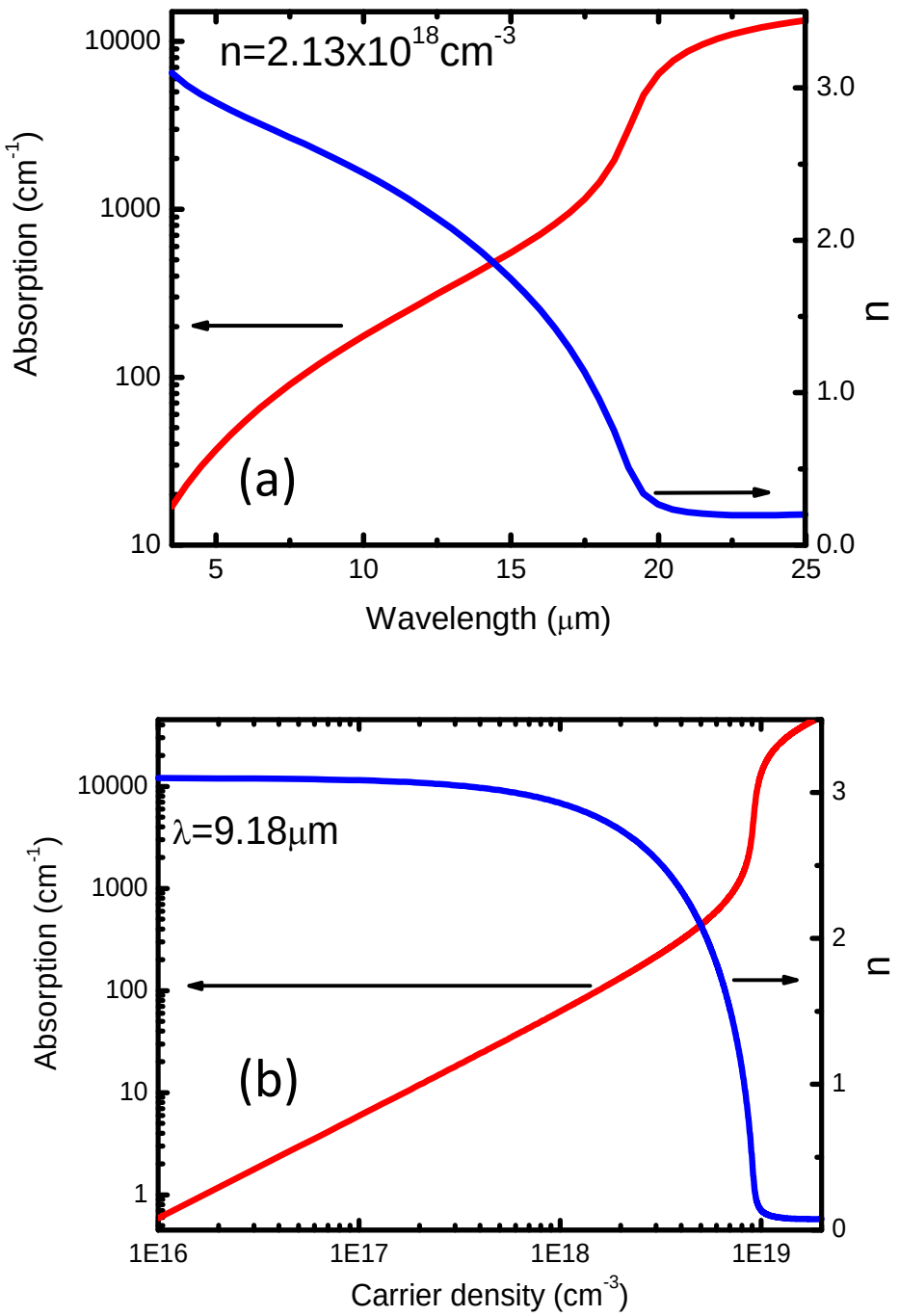

Figure 3.5: (a) Calculated refractive index and absorption vs. wavelength for InGaAs with a doping level of 2.13×10^{18} cm^{-3} at 300 K. (b) Calculated refractive index and absorption vs. doping for InGaAs at 300 K for 9.18 μm wavelength.

to be 55.0 nm by the observed result. This is slightly thinner than the designed thickness 55.5 nm. The measured spectrum corresponds to the simulation one, implying well-controlled layer thicknesses, interfaces, material compositions, and uniformity throughout the 33-period layer sequences.

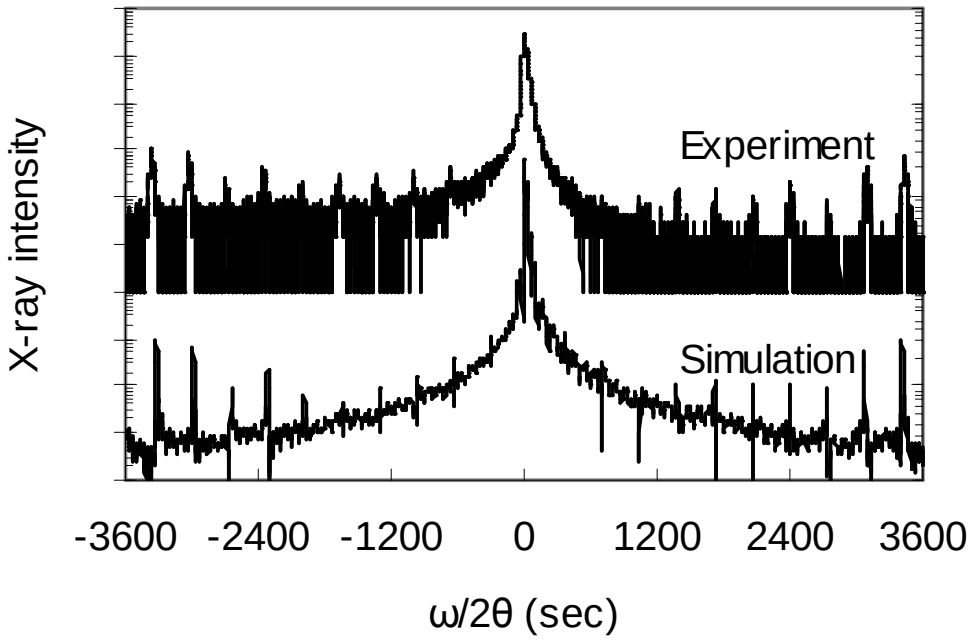

Figure 3.6: Experimental and simulated X-ray diffraction patterns of the wafer.

After the growth, the wafers were processed into mesa devices for spectral electroluminescence (EL) characterization and laser structures: either a simple ridge structure or buried heterostructures (BHs), as shown in Fig. 3.7. From a laser performance point of view, the BH waveguides have the advantages of lower lateral waveguide losses and better heat dissipation, compared to the simple ridge waveguide (see Fig. 3.8). However, the BH waveguides require the regrowth of InP around the stripes containing the active region. Thus, we have adopted the BH waveguides only for the case that room temperature CW operation could be expected. All processing was performed according to the standard procedure using photolithography and both wet and dry etching. Finally, the evaporation of the top Ti/Au contacts was followed by electroplating of a thick 5 μm Au

layer on top of the ridge. Cleaved lasers were bonded on a copper submount with Indium solder. The processing procedures were carried out by a processing team at the Hamamatsu Photonics K. K.

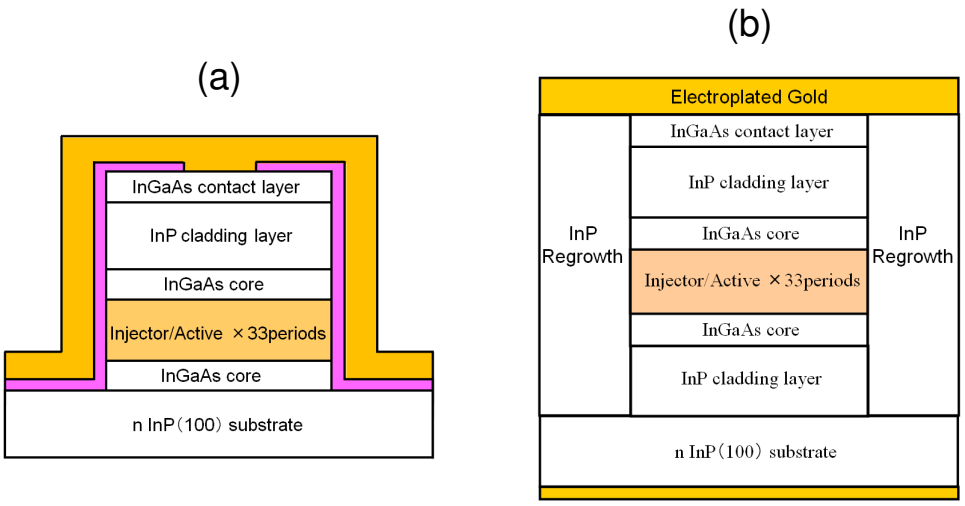

Figure 3.7: Schematic diagram of typical laser structures (a) ridge waveguide with Si_3N_4 passivation, (b) buried heterostructure waveguide

3.3.2 Measurement

Several types of measurements were used to characterize the QC devices. Initially, the basic device performance characteristics of QC lasers are current versus voltage (I–V) and current versus light output characteristics (I–L) as well as the laser spectrum. These measurements are done for various temperatures and operating conditions. In pulsed operation, the devices are repetitively turned on and off by an external applied bias. Due to the internal heating, QC lasers are strongly influenced by the duty cycle, which is defined as the ratio of the on-time to the total modulated period. Thus, in order to investigate the inherent performance of the lasers, the duty cycle is chosen to be below 1% to minimize the heating effect. For I–L characterization, the laser output power was measured by either a thermopile detector or a mercury-cadmium-telluride (MCT) detector. Furthermore, the measurement of electroluminescence is very important

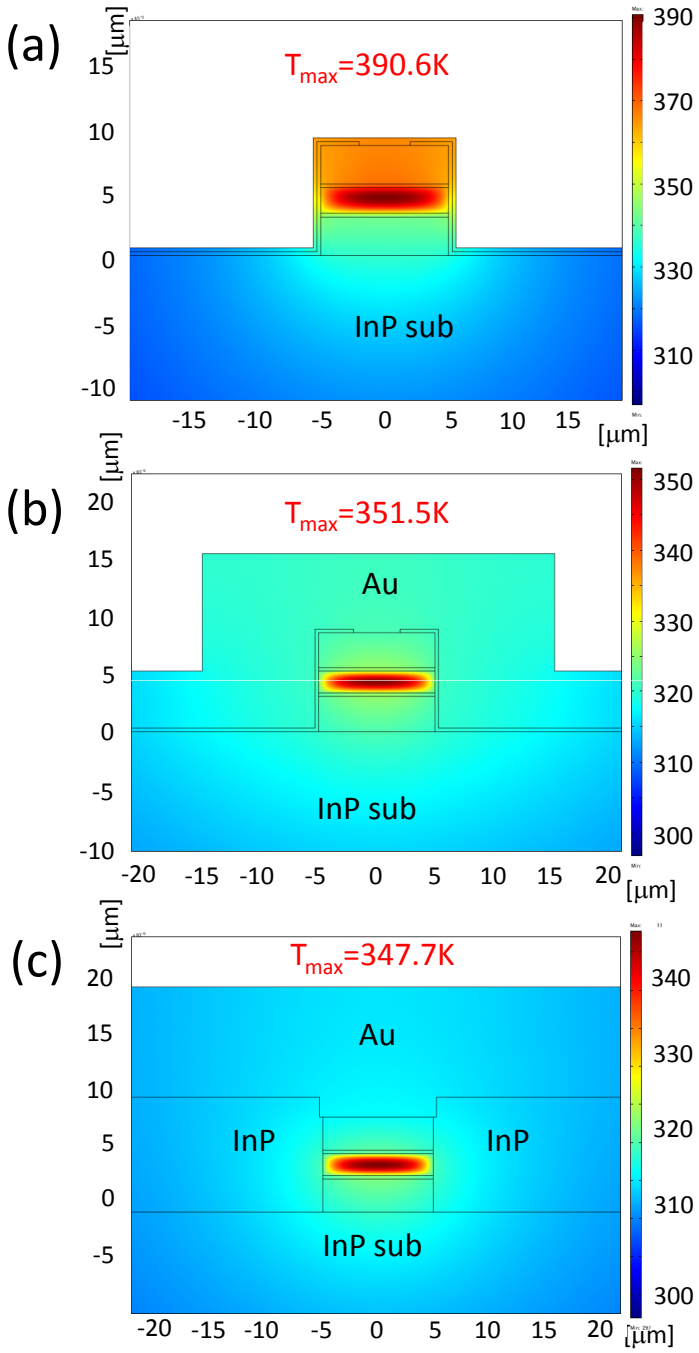

Figure 3.8: Temperature mappings of the front facet of QC laser structures for an input electrical power of 5 W. A ridge waveguide with Si_3N_4 passivation and 0.2 μm (a) and 10 μm (b) top gold, (c) buried heterostructure waveguide design with thick gold.

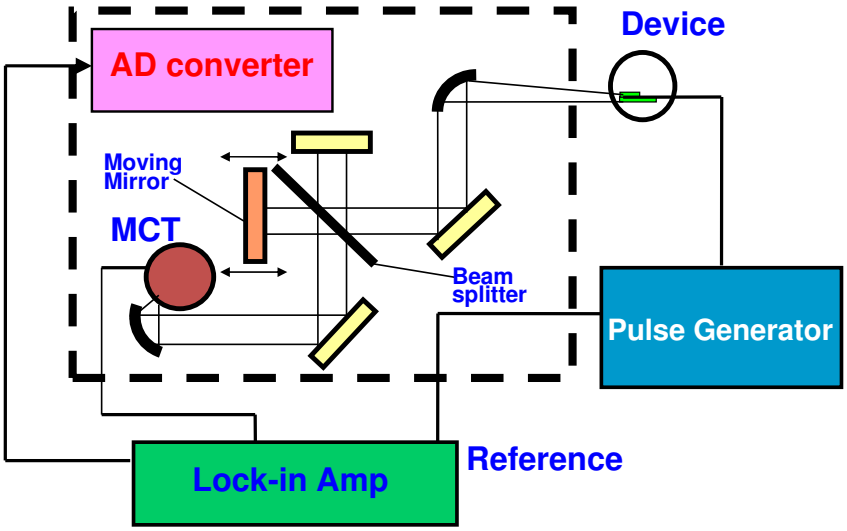

Figure 3.9: Experimental setup for emission measurements.

to comprehend quantum states in the QC structures since the EL signal provide a lot of information on the energy separations between the subbands in the QC structure. The laser emission and EL spectra are measured with a Fourier transform infrared spectrometer (FTIR). The experimental setup for measuring the spectra is shown in Fig. 3.9. The FTIR spectrometer is based on a Michelson interferometer, where all spectral components of the measured infrared radiation are modulated simultaneously in the time domain by interference. The input signal is split into two paths by a beam splitter. One of the two paths is reflected by a moving mirror and the other one is reflected by a fixed mirror. Then, these are combined and detected by MCT. An interferogram containing all the information in the frequency domain can be obtained by the superposition of two signals. In this thesis, we implemented two types of FTIR spectral acquisition modes: rapid-scan and step-scan. The main difference between rapid-scan and step-scan spectroscopy is that in the latter case, the mirror is moved stepwise and not continuously.

Laser emission experiments are performed in rapid-scan mode, where the moving mirror translates continuously while tracing the interferogram. When sufficient light intensity is obtained, this method allows for the much faster collection

of data. On the other hand, EL (spontaneous emission) measurements are done in step scan mode, where the moving mirror pauses at each step to allow measurement of the small detector signal with the lock-in amplifier. This technique is suitable for measuring the small EL signal above the blackbody background.

3.4 Single phonon resonance-continuum depopulation structure

In the section 3.2, we describe all design procedures of QC lasers how to realize high laser performance, using wavefunction-engineering. In order to achieve higher characteristics, a new design concept is important in addition to simple optimization of design parameters and fabrication techniques. In this section a new depopulation structure, single phonon resonance-continuum depopulation structure is proposed to improve the laser performance. Using the proposed design, we demonstrate CW operation at room temperature. Observed threshold current densities and its temperature dependencies are compared to the lasers with the double-phonon resonance design.

3.4.1 Design and experiment

In order to achieve high performance characteristics of QC lasers at room temperature, the active region and device structures have to be optimized for lower threshold current density and the higher heat dissipation rate. Currently, the most advanced designs are BTC and double phonon resonance (DPR) active region structures [9]. The BTC lasers have demonstrated high temperature CW operation. However, the EL spectra of BTC lasers are relatively broadened by the presence of many states involved in the continuum band [10], which mean that the peak gains of the BTC lasers are relatively low. In this view, the BTC structure may not be the most suitable configuration for high temperature CW operation, though it suggests the wide wavelength tunability by using an external cavity. Meanwhile, the DPR structure is the most successful one for keeping high performance above room temperature, until now. Room temperature, CW operation of QC lasers employing the DPR design has been demonstrated over the

wide wavelength range. However, the energy separation between discrete lower three states in the DPR design has to match strictly LO phonon energy. In other words, in the DPR design, mismatching of the energy separation between the lower states with LO phonon energy, particularly toward lower side, may give rise to serious deterioration of laser performances.

Here, we propose a new depopulation structure with single phonon resonance-continuum depopulation (SPC-depopulation) and demonstrate CW operation of the proposed QC lasers at room temperature by taking advantages of high device performance as well as expected allowance for device-to-device fluctuations of the energy separation between the lower states, i.e., a high yield in mass-production. In the proposed structure, the lowest states form a miniband and their wavefunctions extend to the injector region. The lower lasing state of the active region is designed to be separated by one phonon energy from the top state of the miniband. The proposed SPC-structure allows us fast electron depopulation from the lower lasing state and subsequent fast electron extraction without bottleneck that is usually observed with single phonon depopulation design.

Figure 3.10(a) shows the conduction-band diagram of injection-active-injection parts of the active region. The $In_{0.53}Ga_{0.47}As$ / $In_{0.52}Al_{0.48}As$ layer sequence of one period of the active layers, in nanometers, starting from the injection barrier is as follows: **4.4**/1.6/**0.9**/6.0/**1.1**/5.0/**1.8**/4.4/**2.0**/3.5/**1.5**/3.3/**1.6**/3.1/**1.9**/3.0/ **2.3**/ 2.8/ **2.5** /2.8 where $In_{0.52}Al_{0.48}As$ barrier layers are in bold, $In_{0.53}Ga_{0.47}As$ QW layers in roman, and doped layers (Si, 1×10^{17} cm^{-3}) are underlined. The upper and lower lasing states are associated with the wavefunctions labeled by numbers 3 and 2, respectively, which lead to bound-to-bound vertical transitions. The energy of the laser transition between states 3 and 2 is designed as 160 meV. The energy separation between states 2 and the top state of miniband 1-mb was designed to be one-phonon energy. It should be noted that the strict energy matching between them is not always required in the present scheme. Figure 3.10(b) is enlarged illustration of lower energy levels displaying the electron extraction from state 2. Electrons at state 2 are very quickly depopulated via intersubband LO phonon scatterings, τ_2=0.18 ps into the miniband. The electron extraction by using miniband 1-mb, in the injector region is also expected to be very efficient. The energy separation between state 2 and the ground state g of

the injector region is designed to be 130 meV, large enough to avoid the thermal back-filling. The upper lasing state lifetime caused by LO phonon scatterings from the upper lasing state to lower states is calculated to be a much longer intersubband scattering time, τ_{up}=1.45 ps. The exit barrier is designed carefully to suppress extension of wavefunctions from the injector miniband to the active region, and, in turn, the lasing transition is expected favorably to be bound-to-bound one. The energy separation between the upper lasing state and parasitic state 4 is important for avoiding electron injection into the higher state. The separation is designed to be 75 meV, sufficiently larger than thermal energy ∼25 meV. Thus, the high injection efficiency for state 3 is obtainable even at high temperatures >30 °C.

All the layer structures were grown on an n type InP (Si, 3×10^{18} cm^{-3}) substrate by MOVPE technique. The active/injector stages with 33 repetitions were used as the emitting region and sandwiched between two 0.4 m thick n-$In_{0.53}Ga_{0.47}As$ layers (Si, 5×10^{16} cm^{-3}). The upper cladding layer consists of a 3 μm thick n-InP (Si, 1×10^{17} cm^{-3}), followed by a 0.3 μm thick n^+-$Ga_{0.47}In_{0.53}As$ (Si, 8×10^{18} cm^{-3}) cap layer. After the growth, the wafer was processed into buried hetero-structure. Finally, the evaporation of the top Ti/Au contacts was followed by electroplating of a thick 5 μm Au layer on top of the ridge.

3.4.2 Device characterization

In general, EL spectrum of a device by bound-to-bound design is narrower than that by BTC design. In order to confirm that the present SPC-depopulation design leads to bound-to-bound transitions, we measured EL spectra of a (partially pumped) SPC-QC laser without stripe structure, of which results at 30 °C are shown in Fig. 3.11. The spectral measurement was performed with a Fourier transform infrared spectrometer using a step scan and lock-in detection technique. The spectra taken with pulsed injection currents of 2 μs width at a repetition rate of 100 kHz show no stark shifts at all, demonstrating a full width at half maximum (FWHM) of 18.2 meV, substantially narrower than BTC one, typically ∼35 meV [10] and comparable to DPR one, ∼20 meV [11]. This is a clear evidence for bound-to-bound, vertical transitions.

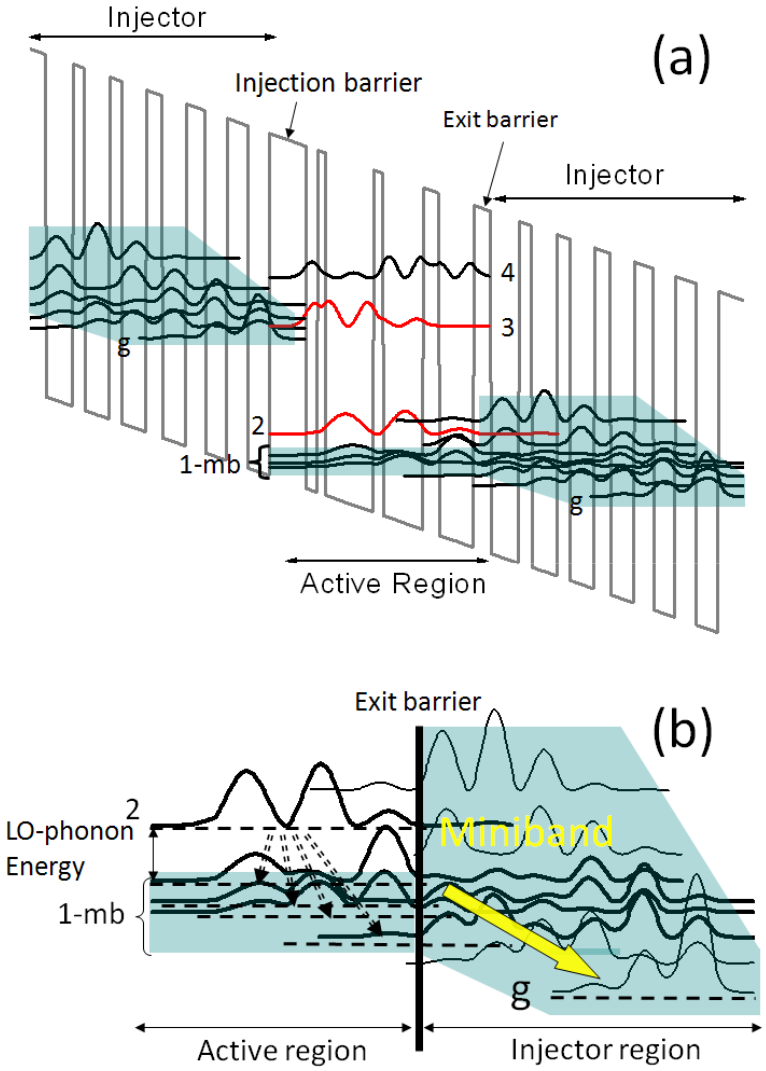

Figure 3.10: (a)Schematic conduction band diagram and moduli squared of the relevant wavefunctions of injector/active/injector parts in the SPC active region. An electric field of 45 kV/cm was applied to align the structure. (b) Schematic illustration of the lower energy states and SPC-depopulation process.

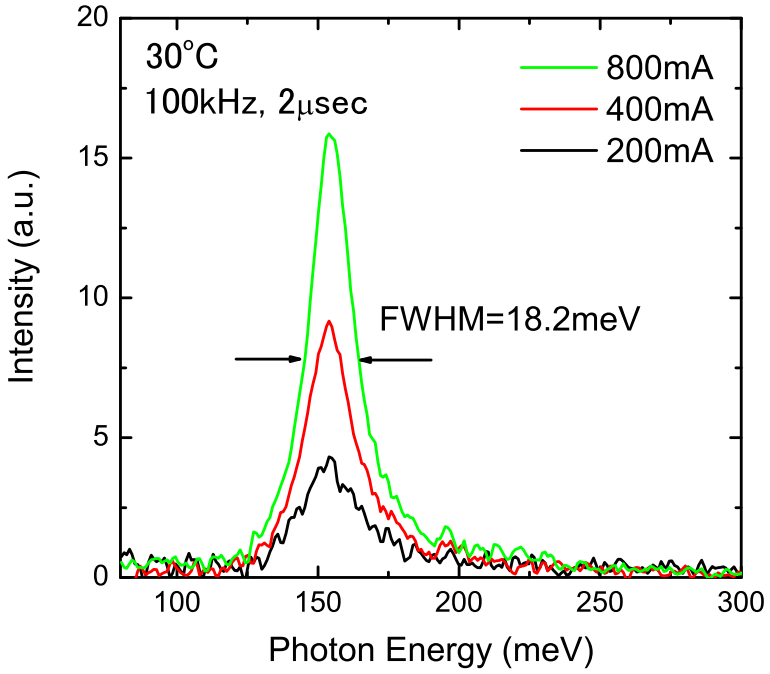

Figure 3.11: Intersubband EL spectra of the SPC device without stripe structure at 30 °C.

Figure 3.12 shows the CW I-L characteristics of a HR coated, 5 μm wide, and 3.0 mm long laser at different heat sink temperatures. The optical output power was measured by a calibrated thermopile detector. The V-I characteristics at 0 °C and 60 °C are also given, and the lasing spectrum is shown as the inset. The threshold current density at 30 °C was observed to be 2.23 kA/cm^2 and a CW optical output power of 36 mW at 7.91 μm wavelength was obtained at 30 °C. The device demonstrated the CW operation at higher temperatures up to slightly above 60 °C.

The relationship between threshold current density and heat sink temperature is shown in Fig. 3.13 for HR-coated lasers in pulsed and CW operation. For the pulsed measurements, a 50 ns pulse width was used at a repetition rate of 1 kHz. Pulsed measurements were performed up to a maximum temperature of 360 K. The dashed curves are given for fitting by the empirical exponential function, $J_{\rm th} = J_0 \exp(T/T_0)$. The characteristic temperature T_0 was identified to be 181 K and 135 K for pulsed and CW operation, respectively. These values are comparable to DPR ones. We believe that these high characteristic temperatures are brought about by the efficient electron transport from the miniband 1-mb to the ground state g. The thermal resistance $R_{\rm th}$ at the threshold was estimated to be 6.9 K/W by finding the temperature of the heat sink in pulsed mode that gives the same threshold current as in CW mode at 30 °C.

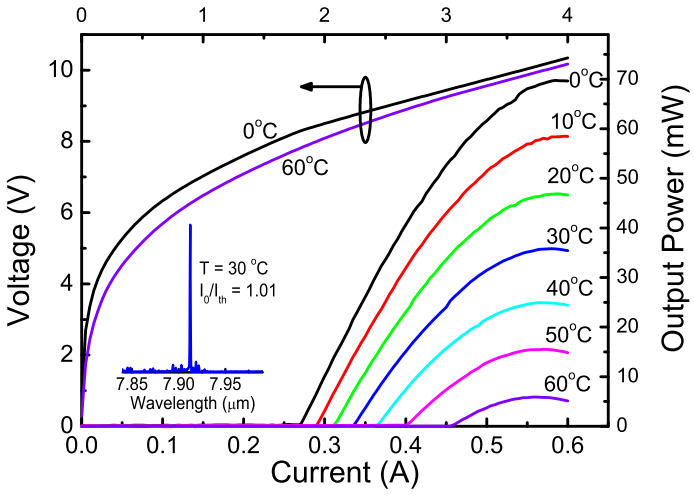

Figure 3.12: The CW current-light output characteristics of a HR coated, 5 μm wide, and 3.0 mm long, SPC laser at different heat sink temperatures. The voltage-current characteristics at 0 and 60 °C are also shown. The inset shows the laser spectrum at 30 °C.

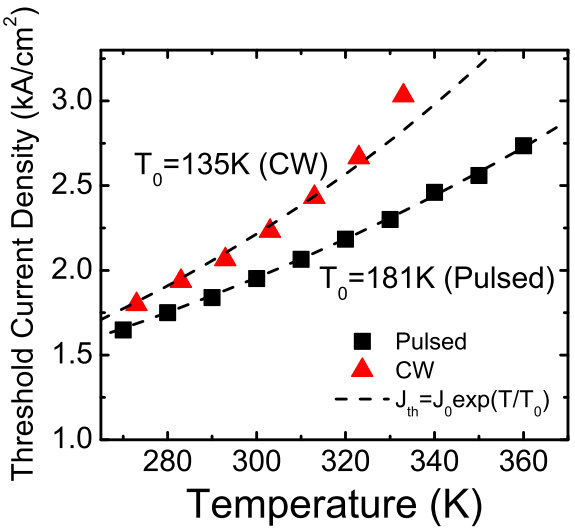

Figure 3.13: Threshold current densities of the SPC laser as functions of heat sink temperature in CW and pulsed operations.

3.5 Optimization of quantum cascade laser performances

In the last section, by the adoption of the SPC depopulation structure, CW operation has been successfully demonstrated at room temperature, emitting at $\lambda \sim$7.9 μm. In this section [12][1], we further develop the SPC depopulation structure to improve the laser performance. Although the threshold current density and characteristic temperature are comparable to other CW-QC lasers, state-of-the-art QC lasers operating at same wavelength range exhibit lower threshold current density and higher output power. Meanwhile, in the second atmospheric window (8-13 μm), high performance CW operation of QC lasers has been reported by several research groups. A high performance $\lambda \sim$8.38 μm QC laser with buried heterostructure has demonstrated a high CW output power of 204 mW and a maximum operation temperature of above 400 K [13]. A QC laser without buried hetero-structures, emitting at $\lambda \sim$8.8 μm, has exhibited a high performance: CW output power of 294 mW at 298 K, operating up to 85 °C [14]. More recently, very high power operation of $\lambda \sim$10.6 μm QC lasers has been reported at room temperature [15]. However, high performance QC lasers with a high wall-plug efficiency (WPE) of more than 10% have not been realized yet even in pulsed operation so far. In this wavelength, unlike the short wavelength case, it is not easy to actualize the high WPE because of higher waveguide loss and shorter upper state lifetime. In fact, a theoretical model based on a rate equation analysis predicts that the WPE of 9 μm QC lasers is limited to be less than 13% [3].

3.5.1 Design and experiment

Figure 3.14 shows the conduction-band diagram of injector-active-injector parts of the active region based on 5QW SPC structure. The energy width of the lower miniband 1-mb in the 4QW SPC design was designed to be 22 meV. In such case, electrons in miniband 1-mb relax by electron-electron scatterings or by LO phonon scatterings after resonant tunneling into the injector states as the miniband width

[1] ©2010 IEEE.

in the active region is less than LO phonon energy. The miniband energy width in the present 5QW active region design is designed to be larger (>50 meV) than LO phonon energy and to speed up the electron depopulation. Electrons in miniband 1-mb are very efficiently relaxed both by intra-miniband LO phonon scatterings and electron-electron scatterings. The upper and lower lasing state lifetime, caused by LO phonon scatterings, is calculated to be τ_{up}=1.25 ps and τ_{low}=0.22 ps. On the other hand, the transition dipole matrix element can be designed to be larger value of $Z_{32}\sim$3.0 nm than previous 4QW design one ($\sim$2.4 nm), thanks to the vertical transition design based on the 5QW structure in the active region. As the modal gain is proportional to square of the dipole matrix element, these modifications of the design may significantly contribute to improving laser performance, although the upper and lower lasing state lifetimes are comparable to previous design.

Using the 5QW SPC structure, we fabricated two different types of wafers, consisting of 33 and 70 cascade stages. The devices with 33 stages, which is the same number of stages as used in the device of the previous section, were chosen to confirm the feasibility of the proposed active region design. On the other hand, the QC lasers with a higher number of cascade stages are expected to lead to very high optical confinement factor and high peak power [16]. The confinement factor increases from 0.51 to 0.73 with increasing stage number from 33 to 70. All the layer structures of the two types of lasers were grown on n-type InP substrates (Si, 1×10^{17} cm^{-3}) by MOVPE technique. The waveguide configurations are identical to 4QW SPC device in the previous section except for the active region doping. The doping level in the injector (Si, 8×10^{10} cm^{-2}) is optimized to reduce the internal loss. The active/injector stages were sandwiched between two 0.3 μm thick n-$Ga_{0.47}In_{0.53}As$ layers (Si, 5×10^{16} cm^{-3}). The upper cladding layer consists of a 3.5 μm thick n-InP (Si, 1×10^{17} cm^{-3}), followed by a 0.3 μm thick n^{+}-$Ga_{0.47}In_{0.53}As$ cap layer (Si, 3×10^{18} cm^{-3}).

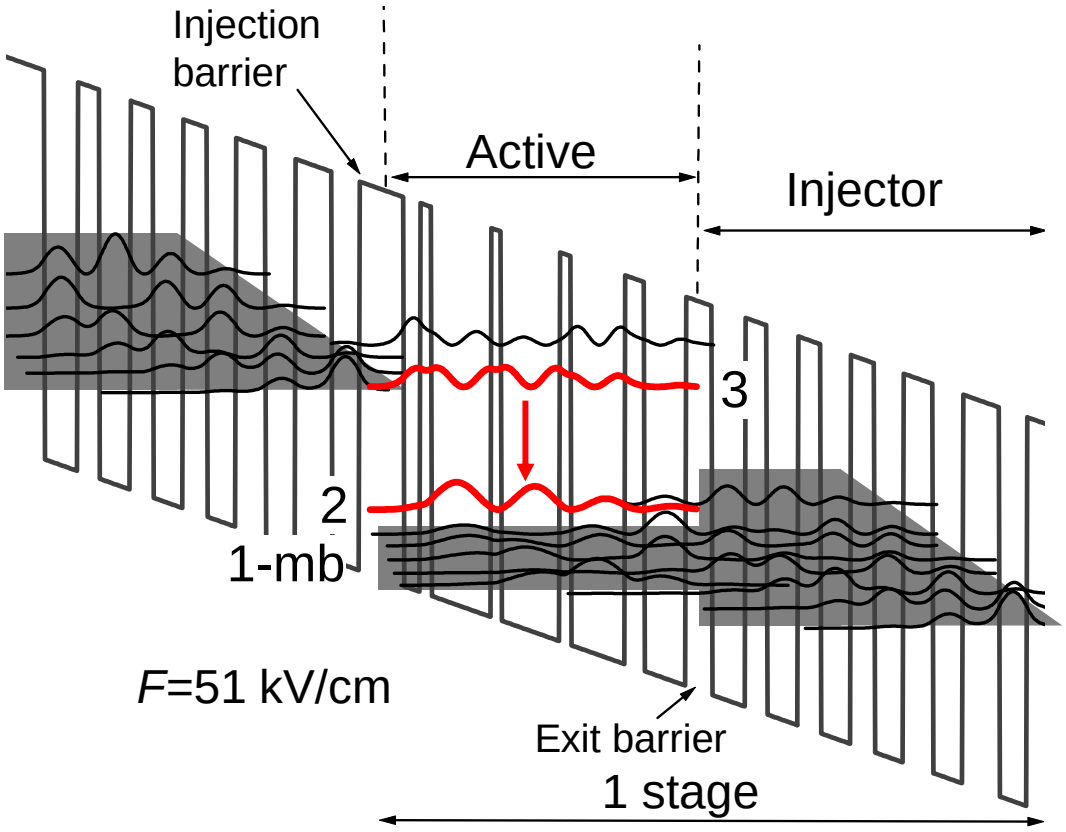

Figure 3.14: (a) Schematic conduction band diagram and moduli squared of the relevant wavefunctions of injector/active/injector parts in the 5QW-SPC active region [12]. An electric field of 51 kV/cm was applied to align the structure. The designed wavelength is around 8.5 μm at room temperature. The InGaAs/InAlAs layer sequence of one period of the active layers, in angstroms, starting from the injection barrier (toward the right side) is as follows: **38**/15/**9**/53/**8**/52/**9**/48/**16**/37/**22**/30/**18**/28/**19**/27/**20**/26/**25**/27/**31**/25 where InAlAs barrier layers are in bold, InGaAs QW layers in roman, and doped layers are underlined (Si, 8×10^{10} cm^{-2}). ©2010 IEEE.

3.5.2 Device characterization

3.5.2.1 Electroluminescence measurement

We measured EL spectra of mesa devices without stripe structures, of which results at various temperatures are shown in Fig. 3.15. The spectra were taken with pulsed injection currents of 500 ns width at a repetition rate of 100 kHz. The full widths at half maximum (FWHM) γ of the spectra ranges from 13.9 meV to 22.3 meV between 78 K and 300 K for the device with 33 stages, and from 12.9 meV to 23.3 meV between 78 K and 300 K for the device with 70 stages. These narrow linewidth γ indicate that the 5 QW based SPC design leads to bound-to-bound vertical transition. The linewidth γ of the device with 33 stages exhibits weaker temperature dependence than that of the device with 70 stages as shown in the inset of Fig. 3.15. In general, the EL linewidth γ is determined by dipole dephasing due to interface roughness scatterings and thermal broadening of the electron distribution in subbands, the latter one which is clearly temperature dependent. Moreover, due to thickness fluctuations, under operation conditions, a higher number of stages may lead to inhomogeneous electric field distribution over the whole stages. As a result, the inhomogeneous distribution broadens the luminescence linewidth of 70 stages device, which deteriorates the peak gain coefficient.

3.5.2.2 Characterization of simple ridge lasers

In order to compare the performances of the two types of lasers, the two wafers were processed into the 13.5 μm-wide simple-ridge-structure without any additional equipment, such as thick electroplated gold and high reflective (HR) coatings. Finally, the Ti/Au films were evaporated on top of the ridge. The laser facets were formed by simply cleaving (3 mm-long) and the lasers were bonded epi-side up on copper sub-mounts with Indium solder. For current-light output characterization, the peak output power emitted from single facets of the lasers was measured with a calibrated thermopile detector. Figure 3.16(a) shows the pulsed I-L characteristics of the device with 33 stages at different temperatures as well as the V-I characteristics. At low temperature (78 K), an output power of 1.08 W per facet is obtained with a threshold current density of 0.34 kA/cm^2

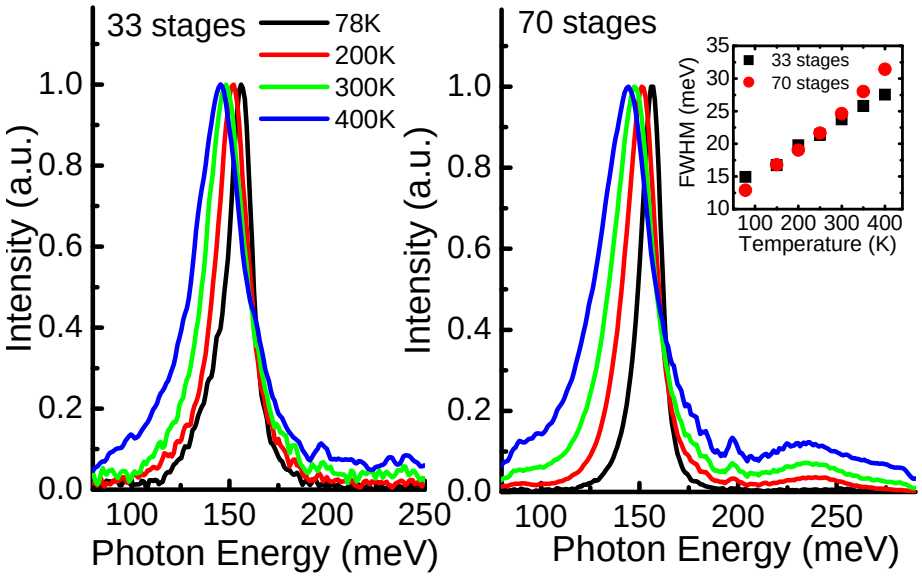

Figure 3.15: Intersubband EL spectra of the 33 and 70 stage 5QW-SPC devices without stripe structure for the various temperature [12]. The inset shows the temperature dependencies of linewidth FWHM. ©2010 IEEE.

and a slope efficiency of 0.93 W per facet, while 0.33 W per facet is done at high temperature (400 K) with a threshold current density of 1.80 kA/cm^2 and a slope efficiency of 0.59 W per facet. Figure 3.16(b) shows the pulsed I-L characteristics of the device with 70 stages at different temperatures as well as the V-I characteristics. At low temperature (78 K), an output power of ∼2.5 W per facet is obtained with a threshold current density of 0.17 kA/cm^2 and a slope efficiency of 2.23 W per facet, while the output power per facet attains to 0.85 W at high temperature (400 K) with a threshold current density of 1.77 kA/cm^2 and a slope efficiency of 1.3 W per facet. At room temperature (300 K), the observed threshold current densities are 1.12 kA/cm^2 for the device with 33 stages and 0.97 kA/cm^2 for the device with 70 stages. These values are about half the threshold current at 300 K reported with our previous device. The dissipation powers at threshold are 3.2 W for the device with 33 stages and 4.9 W for the device with 70 stages. Figure 3.17 shows the pulsed threshold current density as a function of heat sink temperature for the two devices with 33 and 70 stages. The characteristic temperature T_0 in the pulsed operation is identified to be 201

K for the device with 33 stages around RT. On the other hand, the T_0 value for the device with 70 stages is 142 K that is significantly smaller than the value of the device with 33 stages. This is mainly caused by the steeper temperature dependence of FWHM of the device with 70 stages as shown in the inset of Fig 3.15.

The temperature dependences of slope efficiency per stage of the two devices are also shown in Fig. 3.17. The slope efficiencies per stage of the devices vary from 28.0 to 22.5 mW/A and from 31.8 to 23.7 mW/A between 78 and 300 K, for 33 and 70 stages respectively. The decrease in the slope efficiency is attributed to thermal excitation of electrons from state 3 to state 4. Table 3.1 shows measured J_{th}, V_{th}, P_{th}, $\mathrm{d}P/\mathrm{d}I$ and T_0 of the two lasers at room temperature. For high temperature CW operation, the lower threshold power density and weaker temperature dependence are required. In this view, the device with 33 stages exhibiting the lower threshold electrical power density and higher T_0-value are suitable for high temperature CW operation. Actually, the epi-side up mounted simple-ridge laser, despite lacks of HR coatings and any additional heat dissipation equipments has operated successfully in CW mode at RT. In contrast, the device with higher 70 stages promises of high peak power operation due to the very high slope efficiency that is proportional to the number of stages. In the following section, we show high performance operation of QC lasers processed in buried hetero structure for 33 stages and wide ridge structure for 70 stages.

Table 3.1: Values J_{th} (kA/cm^2), V_{th} (V), P_{th} (W), $\mathrm{d}P/\mathrm{d}I$ (W/A) and T_0 (K) of the devices with 33 and 70 stages at room temperature

	J_{th}	V_{th}	P_{th}	$\mathrm{d}P/\mathrm{d}I$	T_0
33 stage	1.12	7.1	3.2	0.74	201
70 stage	0.97	12.6	4.9	1.66	142

3.5.2.3 High temperature continuous wave operation of QC lasers

For high temperature CW operation, the wafer with 33 stages was processed into buried heterostructure lasers. 8 μm wide ridges were defined by conventional

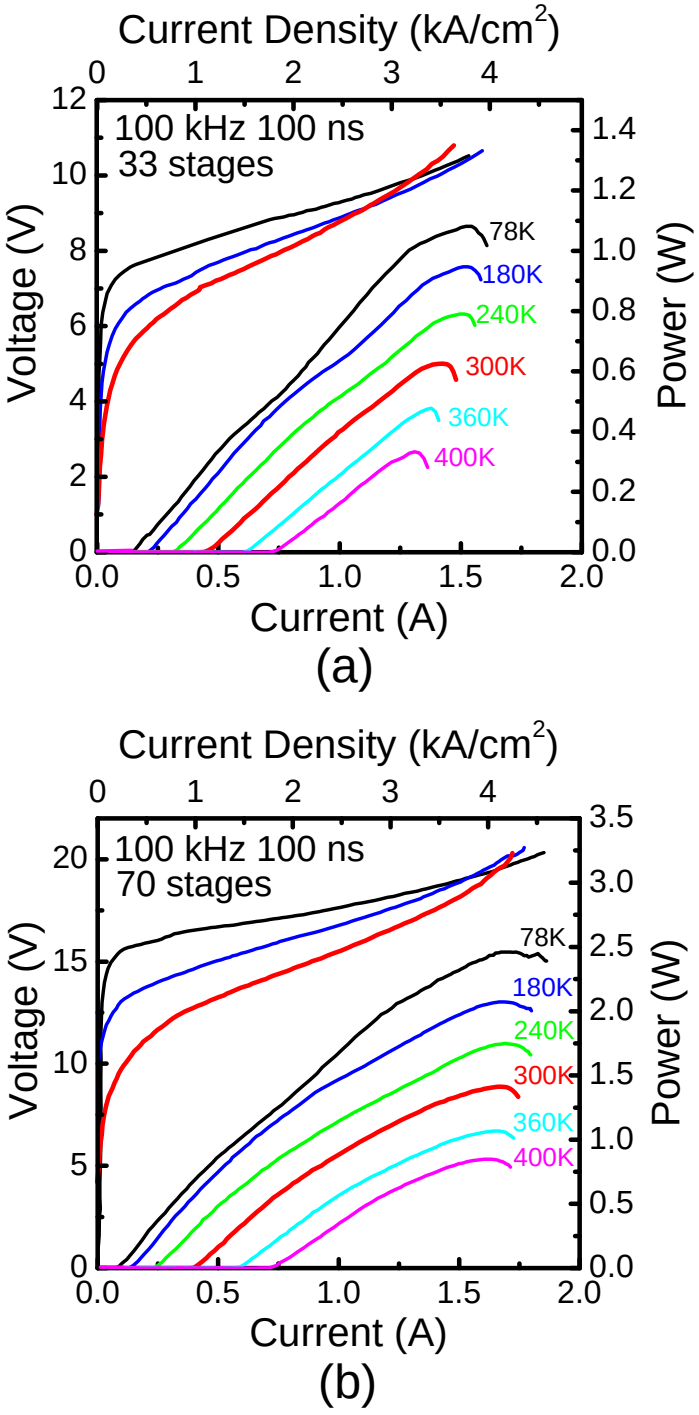

Figure 3.16: Pulsed current-light output characteristics of 13.5 μm-wide, 3.0 mm-long, ridge structured, 5QW-SPC lasers with 33 and 70 stages at different heat sink temperatures [12]. The voltage-current characteristics are also shown. ©2010 IEEE.

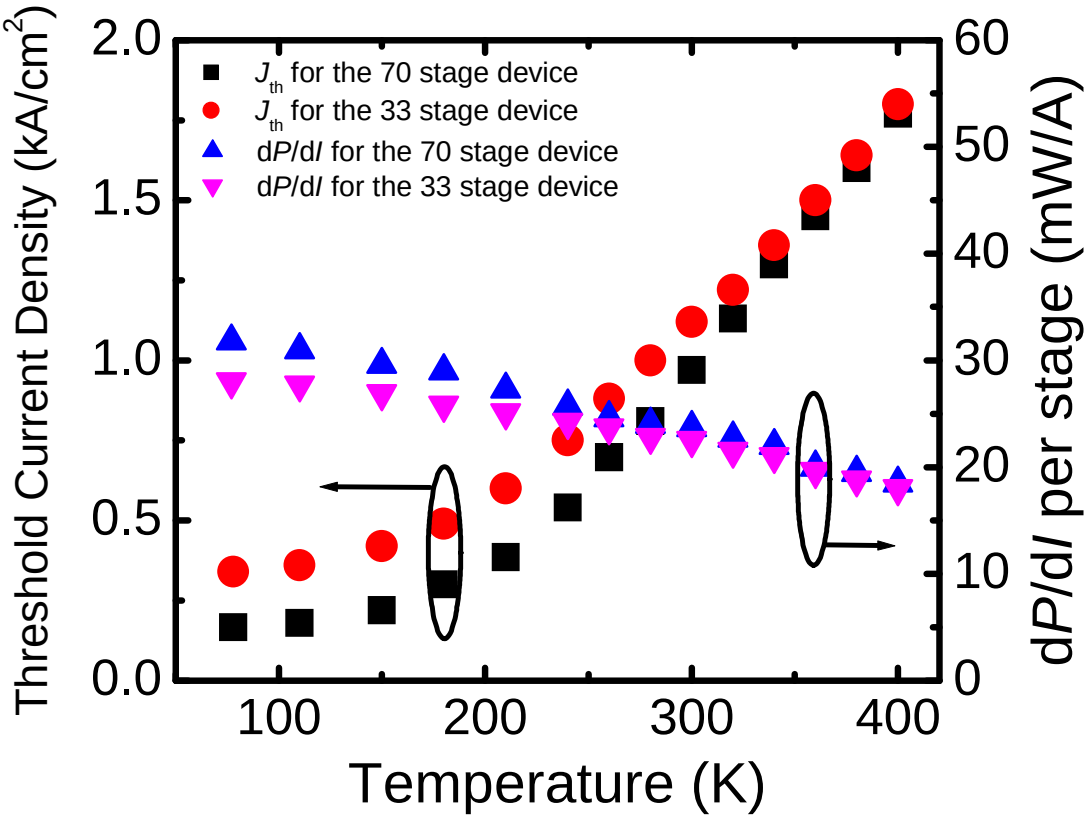

Figure 3.17: Threshold current densities and the slope efficiencies per stage for the 5QW-SPC lasers with 33 and 70 stages as functions of heat sink temperature in pulsed operation [12]. ©2010 IEEE.

photolithography techniques and etched down to the lower cladding layer by dry etching. Then, InP doped with Fe was selectively regrown, by MOVPE, around the ridges to enhance the lateral heat dissipation from the active region. After the regrowth, the evaporation of the top Ti/Au contacts was followed by electroplating of a thick 5 μm layer on top of the ridge.

Figure 3.18 shows a series of I-V-L curves of the 4 mm-long, 8 μm-wide, HR-coated laser at different temperatures. The laser has demonstrated high CW performance: a low CW threshold current density of 1.35 kA/cm^2, a high maximum output power of 313 mW, a high slope efficiency of 547 mW/A at 30 °C. The maximum WPE of 2.74% is obtained at I=0.94 A and V=9.55 V. The maximum CW operation temperature of the device is above 120 °C. These CW performances of the QC laser are the comparable with the high-performance QC lasers in the same wavelength [13, 14]. The maximum output power and the slope efficiency at room temperature are slightly higher than the best reported ~8 μm QC laser [14].

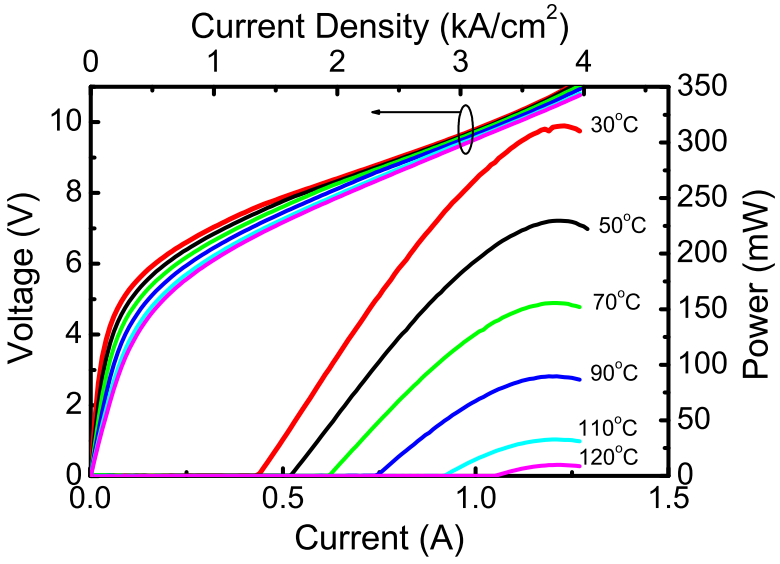

Figure 3.18: The CW current-light output characteristics of a HR coated, 8 μm-wide, 4.0 mm-long, 5QW-SPC laser at different heat sink temperatures [12]. The voltage-current characteristics at 30 °C and 120 °C are also shown. ©2010 IEEE.

In order to investigate thermal behavior, we measured the device performances at different heat sink temperatures in CW and pulsed mode. The relationship between threshold current density and heat sink temperature is shown in Fig. 3.19 for HR-coated lasers in pulsed and CW operation. The characteristic temperature T_0 is identified to be 197 K and 110 K for pulsed and CW operation, respectively. The thermal resistance R_{th} at the threshold is estimated to be 11.0 K/W (corresponding to thermal conductance G_{th}=284 W/Kcm^2) by finding the temperature of the heat sink in pulsed mode that gives the same threshold current as in CW mode at 30 °C.

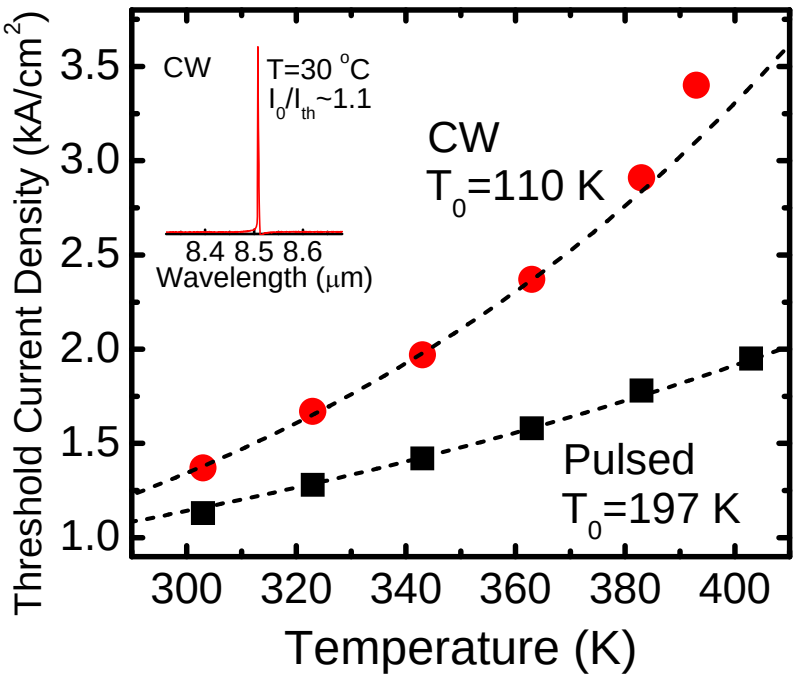

Figure 3.19: Threshold current densities as functions of heat sink temperature in CW and pulsed operations for the device shown in Fig. 3.18 [12]. The dashed curves represent fits by the empirical exponential function, $J_{\mathrm{th}} = J_0 \exp(T/T_0)$. The inset shows the laser spectrum at 30 °C. ©2010 IEEE.

3.5.2.4 High peak power, high wall-plug efficiency QC lasers

Finally, for 70 stages, a 22 μm-wide, 4 mm-long, HR-coated ridge laser with electroplated thick gold layer on the top of device has been tested. The laser was mounted epi-side up to a copper sub-mount with Indium solder. Figure 3.20 shows current-light curves of the device at 300 K in pulsed operation. A high optical output power of 6.3 W is obtained with a low threshold current density of 0.76 kA/cm^2, a slope efficiency of 2.7 W/A (corresponding to an differential quantum yield $\eta_{\text{ext}}=(e/\hbar\omega_{\text{out}})\mathrm{d}p_{\text{out}}/\mathrm{d}I_0=1806\%$). High output power and high slope efficiency can be achieved by increasing the number of cascade stages [16] while a large number of active region stages lead to an increase in a voltage at threshold. Figure 3.21 shows the maximum average power as a function of duty cycle around room temperature. The maximum average power of 495 mW at 280 K, 426 mW at 300 K, and 363 mW at 320 K are obtained at duty cycles of 12-15%. In contrast to the 33 stage ridge device that have achieved high temperature CW operation, the inferior thermal behavior is observed for the 70 stage ridge laser because of high operation voltage. Nevertheless, a WPE of the device is 10.8% at 300 K. A previously reported QC laser at λ=9 μm in pulsed operation had a slope efficiency of 1.05 W/A and WPE of 6% [17]. A slope efficiency and WPE are the highest values ever reported with long wavelength range ($>$ 8 μm) devices. The high WPE is close to the fundamental limit predicted by the rate equation analysis [18].

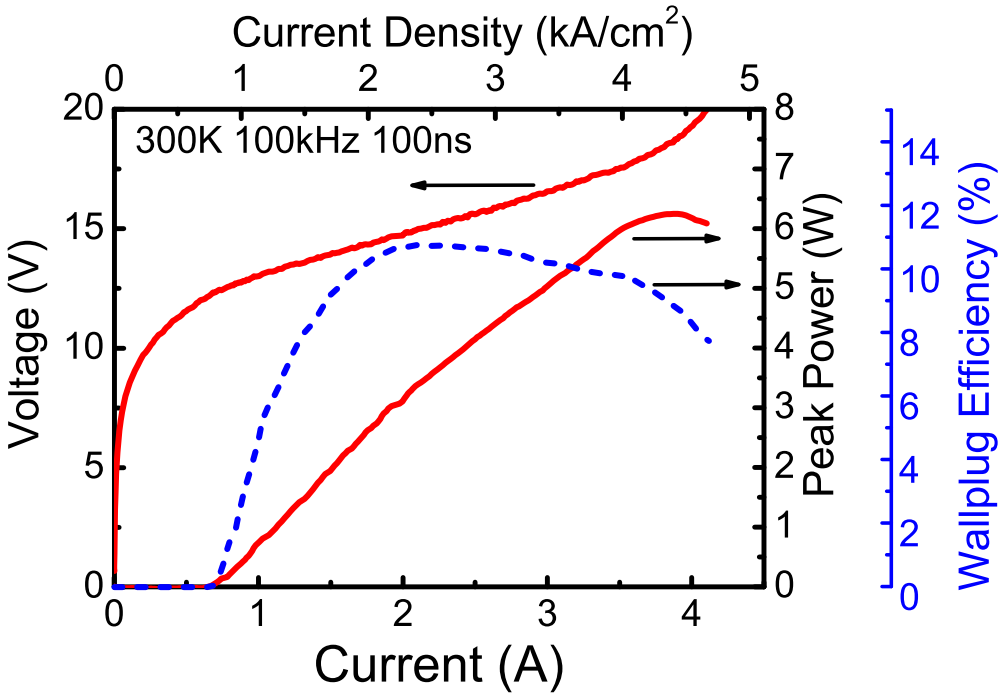

Figure 3.20: Current-light output characteristic of a HR coated, 22 μm-wide, 4.0 mm-long, 70 stage, 5QW-SPC laser with a thick gold film at 300 K in the pulsed operation [12]. The voltage-current characteristic at 300 K is also shown. ©2010 IEEE.

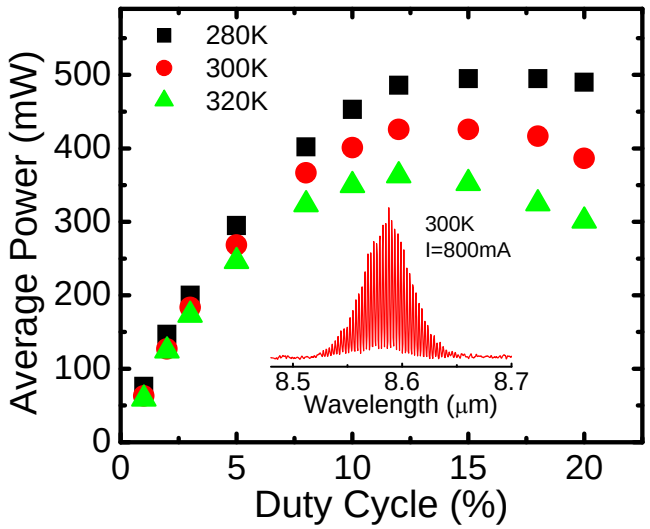

Figure 3.21: Average power in function of duty cycle for the device shown in Fig. 3.20 [12]. The figure inset shows the emitting spectrum at 300 K. ©2010 IEEE.

3.6 Conclusion

In this chapter, we presented the design procedure of QC lasers as well as an improvement of the laser performance, using the SPC depopulation design. The details of QC laser design for achieving high laser performance were described. We have presented a SPC depopulation design. As a consequence of careful design of the active region, including the doping level, and the adoption of the SPC-depopulation scheme, the devices with the 5 QW SPC-depopulation structures, grown by MOVPE, exhibit high device performances. HR-coated buried hetero-structure lasers with 33 stages have demonstrated high performance CW operation. By using a larger number of cascade stages ($N = 70$), HR-coated lasers have exhibited a high maximum output power of 6.3 W and a high slope efficiency of 2.7 W/A. The measured WPE (10.8%) at 300 K is close to the theoretical limit. The high WPE QC lasers in the long wavelength may open up the possibility of a new high power light source as an alternative to the CO_2 laser.

References

[1] M. Beck, D. Hofstetter, T. Aellen, J. Faist, U. Oesterle, M. Ilegems, E. Gini, and H. Melchior, "Continuous-wave operation of a mid-infrared semiconductor laser at room-temperature," Science **295**, 301 (2002).

[2] J. Faist, M. Beck, T. Aellen, and E. Gini, "Quantum cascade lasers based on a bound-to-continuum transition," Appl. Phys. Lett. **78**, 147 (2001).

[3] J. Faist, "Wallplug efficiency of quantum cascade lasers: Critical parameters and fundamental limits," Appl. Phys. Lett. **90**, 253512 (2007).

[4] J. Faist, F. Capasso, D. Sivco, C. Sirtori, A. Hutchinson, and A. Cho, "Quantum cascade laser," Science **264**, 553 (1994).

[5] F. Capasso, A. Tredicucci, C. Gmachl, D. L. Sivco, A. L. Hutchinson, A. Y. Cho, and G. Scamarcio, "High-Performance superlattice quantum cascade lasers," IEEE J. Sel. Top. Quantum Electron. **5**, 792 (1999).

[6] J. Faist, F. Capasso, C. Sirtori, D. L. Sivco, A. L. Hutchinson, and A. Y. Cho, "Vertical transition quantum cascade laser with Bragg confined excited-state," Appl. Phys. Lett. **66**, 538 (1995).

[7] J. Faist, F. Capasso, C. Sirtori, D. L. Sivco, J. N. Baillargeon, A. L. Hutchinson, S. N. G. Chu, and A. Y. Cho, "High power mid-infrared ($\lambda \sim 5$ μm) quantum cascade lasers operating above room temperature," Appl. Phys. Lett. **68**, 3680 (1996).

[8] B. Jensen, "Handbook of optical constants and solids," edited by E. D. Palik, 169 (1985).

[9] J. Faist, D. Hofstetter, M. Beck, T. Aellen, M. Rochat, and S. Blaser, "Bound-to-continuum and two-phonon resonance quantum cascade lasers for high duty cycle, high temperature operation," IEEE J. Quantum Electron. **38**, 533 (2002).

[10] R. Maulini, M. Beck, J. Faist, and E. Gini, "Broadband tuning of external cavity bound-to-continuum quantum-cascade lasers," Appl. Phys. Lett. **84**, 1659 (2004).

[11] M. Beck, D. Hofstetter, T. Aellen, J. Faist, U. Oesterle, M. Ilegems, E. Gini, and H. Melchior, "Continuous-wave operation of a mid-infrared semiconductor laser at room-temperature," Science **295**, 301 (2002).

[12] Kazuue Fujita, Shinich Furuta, Atsushi Sugiyama, Takahide Ochiai, Tadataka Edamura, Naota Akikusa, Masamichi Yamanishi and Hirofumi Kan, "High-performance λ ∼8.6 μm quantum cascade lasers with single phonon-continuum depopulation structures," IEEE Journal of Quantum Electronics **46**, 683 — 688 (2010). ©2010 IEEE.

[13] L. Diehl, D. Bour, S. Corzine, J. Zhu, G. Hofler, M. Loncar, M. Troccoli, and F. Capasso, "High-power quantum cascade lasers grown by low-pressure metal organic vapor-phase epitaxy operating in continuous wave above 400 K," Appl. Phys. Lett. **88**, 201115 (2006).

[14] J. S. Yu, S. Slivken, A. Evans, and M. Razeghi, "High-performance, continuous-wave quantum-cascade lasers operating up to 85 °C at λ ∼8.8 μm," Appl. Phys. A: Materials Science & Processing. **93**, 405 (2008).

[15] S. Slivken, A. Evans, W. Zhang, and M. Razeghi, "High-power, continuous-operation intersubband laser for wavelengths greater than 10 μm," Appl. Phys. Lett. **90**, 151115 (2007).

[16] C. Gmachl, F. Capasso, A. Tredicucci, D. Sivco, R. Kohler, A. Hutchinson, and A. Cho, "Dependence of the device performance on the number of stages in quantum-cascade lasers," IEEE J. Sel. Top. Quantum Electron. **5**, 808 (1999).

[17] Q. J. Wang, C. Pfugl, L. Diehl, F. Capasso, T. Edamura, S. Furuta, M. Yamanishi, and H. Kan, "High performance quantum cascade lasers based on three-phonon-resonance design," Appl. Phys. Lett. **94**, 011103 (2009).

[18] J. Faist, "Wallplug efficiency of quantum cascade lasers: Critical parameters and fundamental limits," Appl. Phys. Lett. **90**, 253512 (2007).

Chapter 4

Indirect pump scheme

4.1 Introduction

As described in Chapter 3, the continuous-wave operation of QC lasers at room temperature has been demonstrated for a wide wavelength range in mid-infrared region. The high laser performance has been achieved by the adoption of bound-to-continuum [1], double phonon resonance [2] or single phonon resonance continuum (SPC) depopulation scheme, each which results in fast electron extraction ($\sim$0.1 ps) from lower laser states and low thermal electron population at the lower laser states, due to high energy differences (>130 meV) between the lower laser states and ground ones in the injector. On the other hand, as mentioned in Chapter 2, since the first demonstration of QC laser operation, for pump process, only the direct pump scheme has been utilized except for an accidental case [3] at cryogenic temperature, $\sim$10 K and an intentional one [4]. In this chapter, we examine the alternative pump scheme, named indirect pump (IDP) scheme, to reveal its advantages over the conventional direct pump scheme for long wavelength range and show the importance of electron transport in QC lasers. First, we will present the quantum structure based on the indirect pump scheme, designed for the wavelength of 8 μm, and discuss its structural features as well as electron dynamics. Then we will describe laser performances of 8 μm IDP QC lasers. The results clarify that the IDP scheme is especially beneficial for longer

wavelength range. In Section 4.4, performances of long wavelength (∼15μm) IDP QC laser are demonstrated, in which low threshold current density and very high characteristic temperature are obtained. Finally the underlying physics in terms of temperature dependences of IDP QC lasers will be discussed.

4.2 Design and electron dynamics

In the alternative pump scheme named IDP one, shown in Fig. 4.1, as discussed in Chapter 2, electrons are injected into the intermediate state, level 4 (not level 3) via electron tunneling from the ground state, level 1′ in the previous injector and then, are relaxed quickly down to the upper laser state, level 3 by LO phonon emissions.

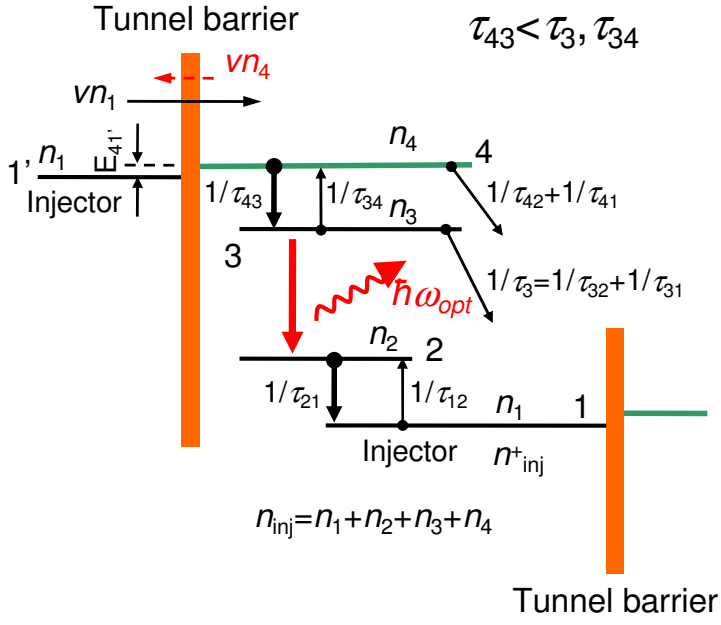

Figure 4.1: Schematic illustration of the IDP scheme.

The BTC active regions were designed, as shown in Fig. 4.2, to incorporate the intermediate state, level 4 for the IDP process and importantly so as to avoid couplings of injector states with adjacent upper laser states, level 3 under any bias

fields. The pump efficiency can be designed to be sufficiently high, $\eta_{\rm pump}$ ∼0.8 at room temperature. Note that the designed energy separation, E_{21} ∼60 meV, between the lower laser states and injector ground state is substantially lower than those (>130 meV) of the high performance QC lasers reported previously [1, 2]. The relaxation times at zero phonon temperature and the Rabi oscillation frequency are estimated: τ_{43}=0.27 ps, τ_{420}=3 ps ($<< \tau_{410}$), $\tau_3 \sim \tau_{320}$=1.5 ps, and $\hbar\Omega_{1'4}$=7 meV ($> \hbar\Omega_{1'3}$3 meV), which will be actually used in the computation of the temperature dependencies of the threshold current density $j_{\rm th}$ and slope $\mathrm{d}j_{\rm th}/\mathrm{d}(1/L)$ of the threshold current density-versus-the inverse of cavity length. The transition dipole moment is, also, estimated to be enough large, Z_{32}=1.92 nm. Using designed parameters, the normalized electron populations are computed with Eqs. (2.62), (2.63), and (2.64), and the electron populations in the corresponding DP case are, similarly, computed, which are shown in Figs. 4.3(a) and (b), respectively. In the IDP case, the upper level population n_3 is able to be, still, higher than the ground state one n_1 near the maximum current.

All of the lattice-matched $In_{0.53}Ga_{0.47}As/In_{0.52}Al_{0.48}As$ layer structures, shown in Fig. 4.2, with a relatively low injector Si-doping of $n_{\rm inj} \sim 5 \times 10^{10}$ cm^{-2} were grown on an n-InP substrate by MBE technique. The active/injector stages with 33 repetitions were used as the emitting region and sandwiched between two 0.4 μm thick n-$In_{0.53}Ga_{0.47}As$ layers (Si, $\sim 10^{17}$ cm^{-3}). The upper cladding layer consists of a thick n-InP (Si, $\sim 10^{17}$ cm^{-3}) followed by a thin n^+-$In_{0.53}Ga_{0.47}As$ (Si, $\sim 10^{18}$ cm^{-3}) cap layer, both the layers which were grown by MOVPE technique. After the growth, the wafer was processed into a 12 μm-width ridge-structure. Finally, the Ti/Au films were evaporated on top of the ridge. The mirror facets of Fabry-Perot cavities were formed simply by cleaving. No high reflection coatings were employed for the mirror facets. The laser output from one facet was measured by using a calibrated HgCdTe detector in pulsed mode: 50 ns pulse width at a repetition rate of 1 kHz. The presence of the intermediate states, level 4 was, in fact, verified by EL spectral measurements, indicating an energy separation of E_{43} ∼40 meV between levels 4 and 3. The results of I-V measurements over the wide current range, 0-8 kA/cm^2, shown in Fig. 4.4(a), convince us of stable electron injection from the injector to intermediate states, level 4, being continuous over the current range for lasing, 0-5 kA/cm^2. The higher current

density (>5 kA/cm^2) is understood to be brought about by the alignment of injector states with the higher spurious states, level 5. The EL peak height ratio of 4-2 and 3-2 transitions in the current range, 0-5 kA/cm^2 was observed to be relatively insensitive to temperature change, as shown in Fig. 4.4 (b) and (c). For instance, the peak height ratio increased only by a factor of ∼1.6 with increasing temperature from 77 to 300 K. This fact supports more directly the electron transport from the injector to intermediate states, level 4 in the same current range, since from the excitation-relaxation balance $n_4/\tau_{43} - n_3/\tau_{34} = n_3/\tau_3$ at the upper laser states, level 3 under the IDP condition, the temperature dependence of the peak height ratio is represented by $n_4/n_3 = (\tau_{43}/\tau_3 + \tau_{43}/\tau_{34})$ which has a weak temperature-dependence, by a theoretical factor of 2.3 in the present case. Note that if electrons should transport directly from the injector to the upper laser states, level 3, because of $1/\tau_{43} >> 1/\tau_{42}$, $1/\tau_{41}$, the peak height ratio is to be proportional to $\tau_{43}/\tau_{34}\exp(-E_{43}/k_{\mathrm{B}}T)$ being strongly dependent on temperature by a factor of 80.

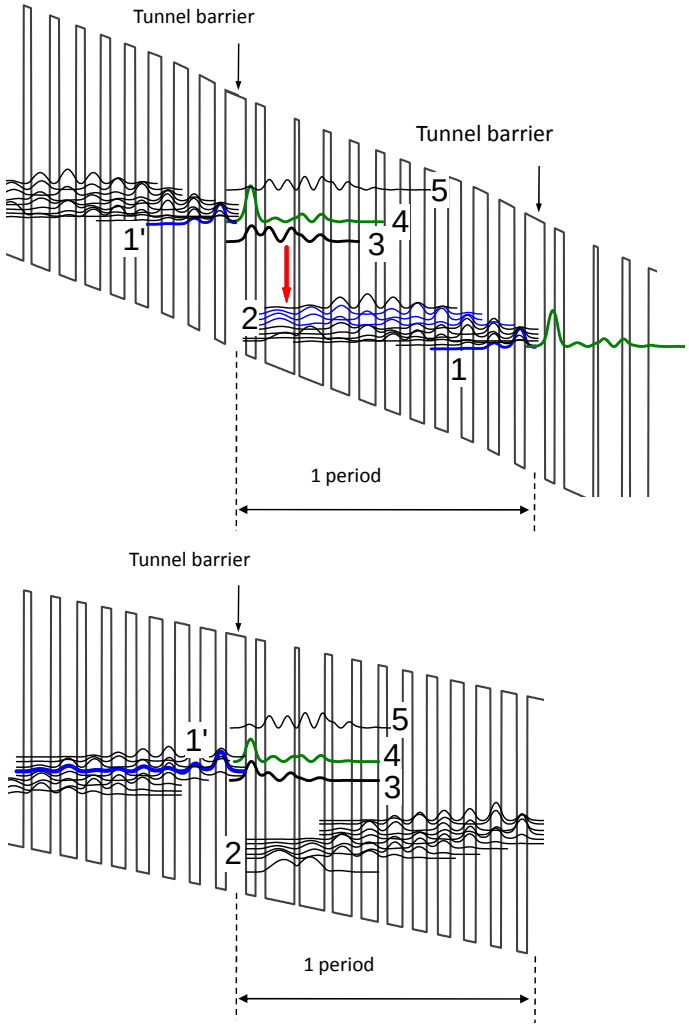

Figure 4.2: Conduction band diagram and moduli squared of the relevant wavefunctions in the designed active region of the IDP QC laser. The lattice-matched $In_{0.53}Ga_{0.47}As/In_{0.52}Al_{0.48}As$ layer sequence of one period of the active layers, in angstroms, starting from the injection barrier (toward the right side) is as follows: **45**/24/**21**/69/**10**/60/**17**/46/**21**/40/**20**/37/**22**/34/**24**/31/**30**/29/**33**/27/**35**/25 where $In_{0.52}Al_{0.48}As$ barrier layers are in bold, $In_{0.53}Ga_{0.47}As$ QW layers in roman, and doped layers (Si, $\sim 10^{17}$ cm^{-3}) are underlined. (a) The bias field is assumed to be strong, 34.5 kV/cm enough to align the ground state of the injector to the level 4. (b) The bias field is assumed to be weak, 18 kV/cm, corresponding to a current turn-on voltage. The injector state $1'$ is already located to be higher than the upper laser states, level 3. The structure is designed to avoid couplings of the injector states with the adjacent upper laser states, level 3 under any bias fields.

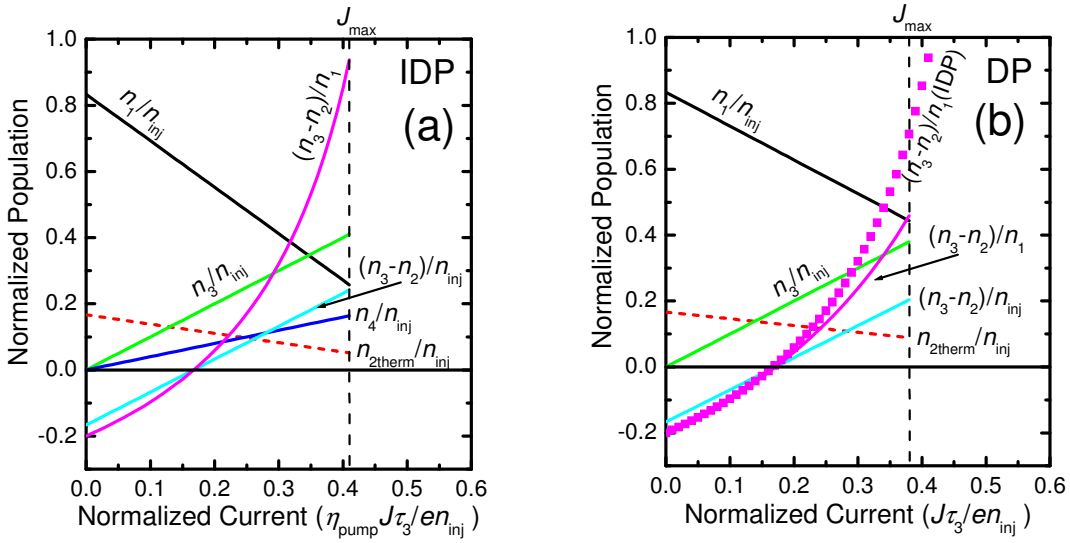

Figure 4.3: (a) Normalized electron populations in an IDP laser, computed with Eq. (2.64) using the parameters: $n_{\rm sp}$=1.4, τ_{21}/τ_{12}=0.2, $\tau_{43}/\tau_{34}+\tau_{43}/\tau_3$=0.4, and normalized maximum current density computed with Eq. (2.62) using $\tau_{\rm tunn}/\tau_3$=0.18 and $\eta_{\rm pump}$=0.8. These parameter values are very close to room temperature ones actually used in the computation of the threshold current density of the test devices. (b) Normalized electron populations in a DP laser, computed by using the corresponding parameters: $n_{\rm sp}$=1.3, τ_{21}/τ_{12}=0.2 and $\tau_{\rm tunn}/\tau_3$=0.18. The quality factor, $(n_3 - n_2)/n_1$ in the IDP case is also plotted. The vertical dashed lines indicate maximum normalized currents, commonly in Figs. (a) and (b).

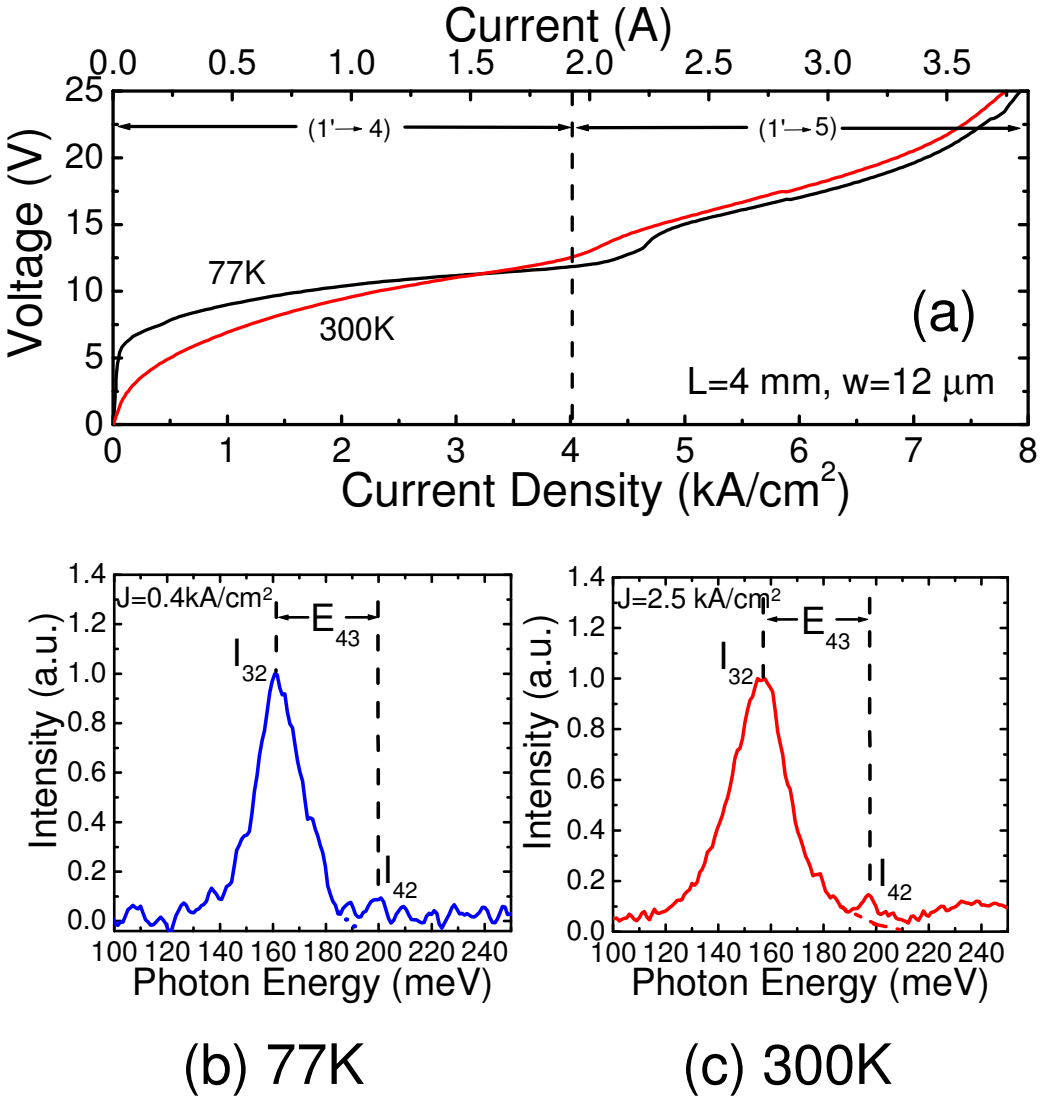

Figure 4.4: (a)Current-voltage characteristics of an IDP QC laser with a cavity length of 4 mm at 77 and 300 K. (b) Electroluminescence at 77 K. (c) Electroluminescence at 300 K.

4.3 Laser performance

4.3.1 Device characterization

An 8 μm IDP laser with a cavity length of 4 mm has demonstrated the high device performance (50 ns pulse width and 1 kHz repetition rate): a low threshold current density of 2.7 kA/cm^2 and a high maximum output power of 362 mW (from one facet) both at room temperature and a maximum lasing temperature of 390 K as shown in Fig. 4.5(a). Furthermore, despite the low energy separation, E_{21} ~60 meV, the temperature-dependence of the threshold current of the 4 mm-long laser has been observed to be weak, T_0 ~243 K around room temperature in marked contrast to T_0 ~74 K in the low temperature range, as shown in Fig. 4.6(a). Another 8 μm IDP laser with a shorter cavity length of 1.5 mm has, as shown in Fig. 4.6 (b), exhibited further weaker temperature-dependence: a surprisingly high T_0-value of 303 K around room temperature associated with a room-temperature threshold current density of 3.3 kA/cm^2, when compared with, for instance, a reported T_0-value of 231 K in an HR-coated 1.5-mm long 9.8 μm DP-QC laser with a threshold current density of 3.1 kA/cm^2 at room temperature in pulsed mode operation [5]. The differential quantum yield, $\eta_{\text{ext}} = (e/\hbar\omega_{\text{opt}})\mathrm{d}p_{\text{out}}/\mathrm{d}I_0$, of the 4-mm (1.5-mm) long laser has been maximized at 260 K (240 K): $\eta_{\text{ext,max}}$=539 % (516 %). In addition, the slope, $\mathrm{d}j_{\text{th}}/\mathrm{d}(1/L)$ of the threshold current density-versus-the inverse of cavity length tends to saturate and even to decrease slightly in the high temperature range, T$\geq$250K, as shown in Fig. 4.6 (b), which is very specific to the IDP lasers. It should be stressed that rather than further lowering of the threshold current density, the obtained high stability of the laser performances for temperature changes is quite beneficial to real device-applications. The remarkably weak temperature-dependencies of the threshold current density and slope in the high temperature range will be, below, interpreted in terms of substantial lowering of thermal backfilling populations at the lower laser states and of optical absorptions in the injectors, both associated with the anticipated suppressions of electron populations in the injectors with increasing current.

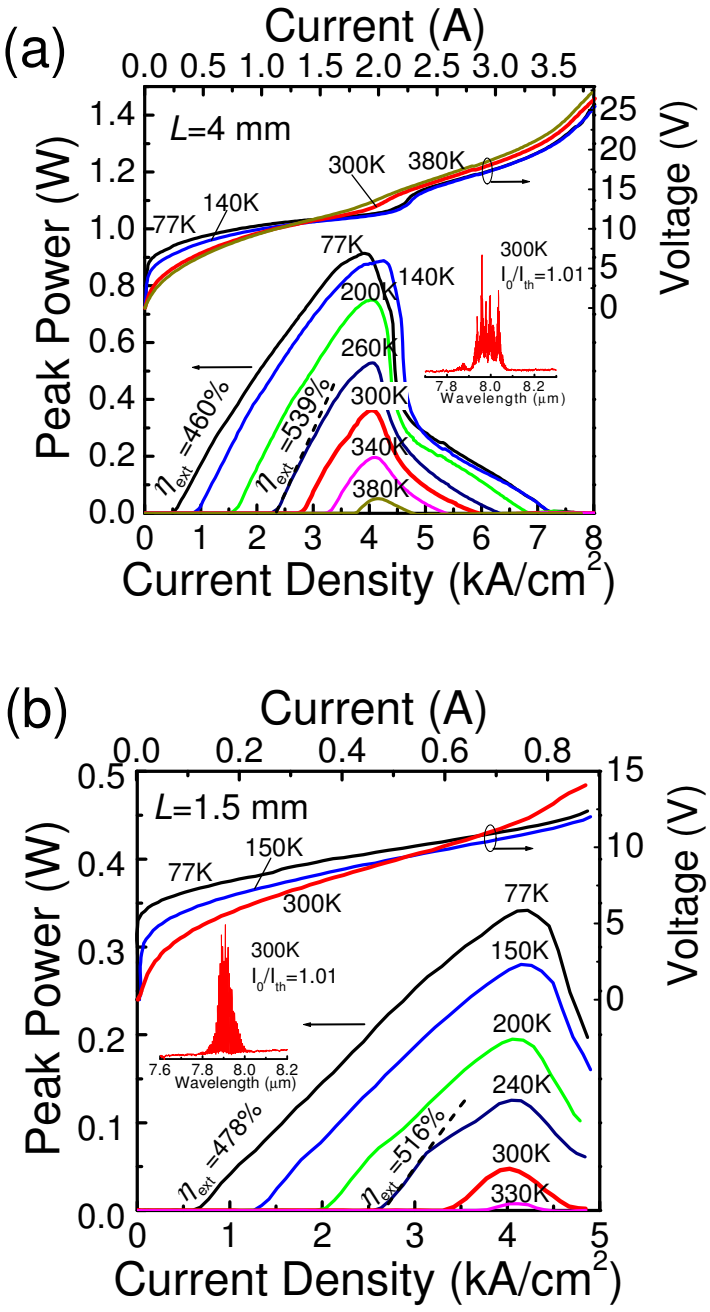

Figure 4.5: (a) Current-light output characteristics of an $\lambda\sim8$ μm IDP QC laser with a cavity length of 4 mm at different temperatures, 77-380 K. The current-voltage characteristics as well as the lasing spectrum at 300 K are also shown. (b) Current-light output and current-voltage characteristics of another IDP QC laser with a cavity length of 1.5 mm at different temperatures, 77-330 K, together with lasing spectrum at 300 K.

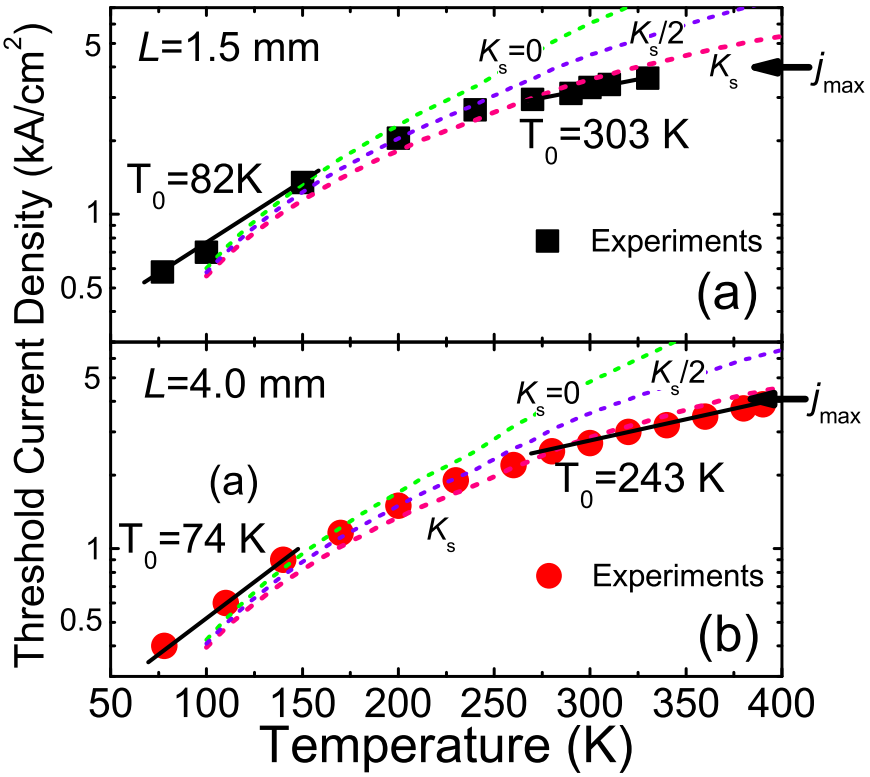

Figure 4.6: Plots of the threshold current densities of the 4-mm and 1.5-mm long lasers as functions of device temperature. Note that the vertical scales for two devices are shifted for a clear view. The straight lines represent fits, showing empirical T_0-values. The dashed curves labeled "K_s" are theoretical ones taking account of the suppression of the electron population in the injector. The dashed curves labeled "K_s=0" are obtained by assuming K_s=0 and ones labeled "K_s/2" are done with the half values for K_s. Note that the current range of both the curves is reasonably limited to be below the maximum current density. In Eq. (2.62), the uses of the injector doping $n_{\rm inj} = 5 \times 10^{10}$ 1/cm^2 together with the estimated value of $\tau_{\rm relax}$=1.73 ps (given by $\tau_3 \sim \tau_{32} = \tau_{320}/[(1+\delta)N_{\rm phonon}+1]$=0.82 ps, $n_{\rm sp}$=1.42, τ_{21}/τ_{12}=0.65, $\tau_{43}/\tau_{34} = 0.295$, and τ_{43}/τ_{34}=0.212) at T=380 K (weak-lasing temperature), and the tunneling time $\tau_{\rm tunn}$=0.175 ps (given by $\hbar\omega$=7 meV and $\tau_{\rm deph}$=100 fs) lead to a maximum current density of 3.96 kA/cm^2, shown by the horizontal arrows, which is fairly close to the observed current densities, 4.0 kA/cm^2, for maximum output powers at high temperatures (Figs. 4.5(a) and 4.5(b)), caused by the complete alignment of the injector states with the intermediate state, level 4.

4.3.2 Calculations and discussion

In a rate equation approach [6] taking account of current-dependencies of the thermal backfilling populations $n_{2\mathrm{therm}}(=(\tau_{21}/\tau_{12})n_1)$ and optical absorptions $\alpha_{\mathrm{inj}}(\propto n_1)$ in the injectors based on Eq. (2.62), the threshold current density for IDP scheme reads,

$$j_{\mathrm{th}} = \left(\frac{en_{\mathrm{sp}}}{\eta_{\mathrm{pump}}\tau_3}\right)\frac{[\alpha_{\mathrm{c}}+\alpha_{\mathrm{m}}]/Mg_{\mathrm{c}} + [\alpha_{\mathrm{inj}}^{(0)}/Mg_{\mathrm{c}} + (\tau_{21}/\tau_{12})n_{\mathrm{inj}}]/(1+\tau_{21}/\tau_{12})}{1+K_{\mathrm{s}}} \quad (4.1)$$

where α_{c}, $\alpha_{\mathrm{m}} = (1/L)\ln(1/R)$ and $\alpha_{\mathrm{inj}}^{(0)}$ are the passive waveguide loss, mirror loss and modal optical loss in the injector with $n_1 = n_{\mathrm{inj}}$, respectively, and $M(=33)$ and g_{c} are the stage repetition and the (modal) gain cross section per stage. In the denominator of Eq. (4.1), the key parameter K_{s} representing the influence of suppressions of the thermal backfilling and injector loss on the threshold current is defined as

$$K_{\mathrm{s}} = \frac{n_{\mathrm{sp}}(2-1/n_{\mathrm{sp}}+\tau_{43}/\tau_{34}+\tau_{43}/\tau_3)[\alpha_{\mathrm{inj}}^{(0)}+(\tau_{21}/\tau_{12})(n_{\mathrm{inj}}Mg_{\mathrm{c}})]}{(1+\tau_{21}/\tau_{12})(n_{\mathrm{inj}}Mg_{\mathrm{c}})}. \quad (4.2)$$

The temperature-dependencies of nonradiative relaxation rates may be represented by the following relations: for nearly resonant relaxations, for instance, $1/\tau_{43} = (N_{\mathrm{phonon}}+1)/\tau_{430}$ together with $\tau_{43}/\tau_{34} = \exp(-E_{43}/k_{\mathrm{B}}T)$, (similarly, for $1/\tau_{21}$ and τ_{21}/τ_{12}) and for off-resonant relaxations, for instance, $1/\tau_3 \sim 1/\tau_{32} = [(1+\delta)N_{\mathrm{phonon}}+1]/\tau_{320}$ (similarly, for $1/\tau_{42}$ and $1/\tau_{41}$) where phonon is the Bose-Einstein distribution function for the LO phonon system and the difference in transition matrix elements between the phonon-absorption and emission processes is accounted by the parameter, $\delta \sim 0.5$. From Eq. (4.1), one obtains the simple relation which includes only the loss term, $\alpha_{\mathrm{c}}+[\alpha_{\mathrm{inj}}^{(0)}+(\tau_{21}/\tau_{12})n_{\mathrm{inj}}Mg_{\mathrm{c}}]/(1+\tau_{21}/\tau_{12})$ and, as a result, is useful for the identification of $\alpha_{\mathrm{inj}}^{(0)}$ and g_{c} as will be demonstrated below,

$$\frac{j_{\mathrm{th0}}}{\mathrm{d}j_{\mathrm{th}}/\mathrm{d}(1/L)} = \frac{\alpha_{\mathrm{c}}+[\alpha_{\mathrm{inj}}^{(0)}+(\tau_{21}/\tau_{12})n_{\mathrm{inj}}Mg_{\mathrm{c}}]/(1+\tau_{21}/\tau_{12})}{\ln(1/R)}, \quad (4.3)$$

where j_{th0} is the threshold current density for $1/L = 0$. The threshold current density j_{th} and slope $\mathrm{d}j_{\mathrm{th}}/\mathrm{d}(1/L)$ is computed numerically, based on Eqs. (4.1)

and (4.2), with four steps including the empirical determination of g_c and τ_{21}/τ_{12}.

(I) The following values for the physical parameters were used to estimate n_{sp}, η_{pump}, τ_{43}/τ_{34} and τ_{43}/τ_3 as functions of temperature, in Eqs. (2.64), (4.1) and (4.2): τ_{43} = 0.27 ps, τ_{420} = 3 ps ($\ll \tau_{410}$), $\tau_3 \sim \tau_{320}$ = 1.5 ps, τ_{210}=0.3 ps and E_{43} = 40 meV.

(II) By neglecting the terms, $(\tau_{21}/\tau_{12})n_{inj}Mg_c$ and τ_{21}/τ_{12} in Eq. (4.3), the experimental value for $j_{th0}/\mathrm{d}j_{th}/\mathrm{d}(1/L)$ at the lowest temperature, $T\sim$77 K together with R=0.291 leads to $\alpha_c + \alpha_{inj}^{(0)} \sim \alpha_{inj}^{(0)}$ =8.92 cm^{-1} ($\alpha_c < 1$ cm^{-1} in the present devices), which is very close to the reported off-resonant intersubband absorption [7], $\Gamma\alpha_{ISB} \sim$10 cm^{-1}.

(III) Because of the difficulty involved in the identification of linewidth of each single transition in the inhomogeneous system, the BTC one, we take the following way for the estimation of the gain cross section g_c. In the low temperature range 100-200 K where the lasing thresholds take place at voltages relatively close to the turn-on voltages as shown in Fig. 4.5, the energy separation between the lower laser and ground states is safely determined to be $E_{21} \sim 60$ meV by using experimental values, V_{appl}, E_{43} = 40 meV and E_{32}=photon energy in the relation: $V_{appl}/M = E_{43} - E_{41} + E_{32} + E_{21}$ and by neglecting the voltage drop in the series resistance. The energy separation, $E_{41'}$ is estimated by using the experimental threshold current density as well as $\hbar\Omega_{1'4}$ = 7 meV and τ_{deph}=100 fs in Eq. (2.62). The uses of E_{21}=60 meV (for τ_{21}/τ_{12} =exp($-E_{21}/k_BT$)), $\alpha_{inj}^{(0)}$ =8.92 cm^{-1} and $n_{inj} = 5 \times 10^{10}$ 1/cm^2, and of experimental values of $j_{th0}/\mathrm{d}j_{th}/\mathrm{d}(1/L)$ in the low temperature range 100-200 K (shown in the inset of Fig. 4.7) again together with R=0.291 in Eq. (4.3) lead to the estimation of the gain cross section g_c. The obtained values of the gain cross section are also fitted by the curve to extrapolate the gain cross section in the higher temperature range, T >200 K as shown in Fig. 4.8(a). This manner for the evaluation of gain cross section is quite reliable since the gain cross section of the present BTC QC lasers at 300 K is extrapolated to be 3.55×10^{11} cm, reasonably smaller than the gain cross section, 4.3×10^{11} cm computed directly for a double phonon (bound-to-bound: homogeneous system) QC laser [8]. On the other hand, the term $[\alpha_{inj}^{(0)} + (\tau_{21}/\tau_{12})n_{inj}Mg_c]/(1 + \tau_{21}/\tau_{12})$

in the higher temperature range (400 K> T >200 K) is identified by substituting the experimental values of $j_{\rm th0}/{\rm d}j_{\rm th}/{\rm d}(1/L)$ over the same temperature range into Eq. (4.3), followed, without knowledge of E_{21}, by the determination of with uses of the extrapolated values of $g_{\rm c}$. Note that for $j_{\rm th0}/{\rm d}j_{\rm th}/{\rm d}(1/L)$ in the highest temperature range (T>350 K), its extrapolated values are used.

(IV) The key parameter $K_{\rm s}$ is now easily identified, which is linked to the (already identified) terms, $[\alpha_{\rm inj}^{(0)} + (\tau_{21}/\tau_{12})n_{\rm inj}Mg_{\rm c}]/(1 + \tau_{21}/\tau_{12})$ and $n_{\rm inj}Mg_{\rm c}$, in the frame work of the present model, as indicated by Eq. (4.2). Finally, the threshold current density $j_{\rm th}$ and the slope ${\rm d}j_{\rm th}/{\rm d}(1/L)$ are computed as functions of device temperature. The ratio of resonant loss to injector one $(\tau_{21}/\tau_{12})Mg_{\rm c}/(\alpha_{\rm inj}^{(0)}/n_{\rm inj})$, the electron population $n_{\rm 1th}$ in the injector and the population-inversion $(n_3 - n_2)_{\rm th}$ both at threshold condition are also obtained, which are shown in Fig. 4.8(b). The latter ones, $n_{\rm 1th}$ and $(n_3 - n_2)_{\rm th}$ are counted by substituting the experimental values of $j_{\rm th}$ of the lasers into j in Eq. (2.64).

The experimental data of the threshold current and slope are fitted consistently, without any intentional adjustments of the absolute values, by the theoretical curves labeled " $K_{\rm s}$ ", as shown in Figs. 4.7(a) and (b). The fair agreement between them indicates the validity of the present model where both the thermal backfilling populations $n_{\rm 2therm} = (\tau_{21}/\tau_{12})n_1$ at the lower laser states and optical absorptions $\alpha_{\rm inj} = (\alpha_{\rm inj}^{(0)}/n_{\rm inj})n_1$ in the injectors are viewed as being quenched with increasing current, as a consequence of suppressions of electron populations in the injectors. The agreement also implies that spurious leakage currents do not play any significant roles in the elevation of the T_0-values. Since the ratio $(\tau_{21}/\tau_{12})Mg_{\rm c}/(\alpha_{\rm inj}^{(0)}/n_{\rm inj})$ is larger than unity in the high temperature range, T ≥300 K, as shown in Fig. 4.8(b), the observed high T_0-values are ascribed primarily to the suppressions of the thermal backfilling at the lower laser states in the present devices. The electron population $n_{\rm 1th}$ in the injector at the lasing threshold decreases down to $n_{\rm 1th}/n_{\rm inj}$ ∼0.25 with increasing temperature, i.e. increasing threshold current density. Notifying the loss-gain balance at thresholds, the decrease in the required population-inversion $(n_3 - n_2)_{\rm th}$ with increasing temperature (T >250 K) (Fig. 4.8(b)) is really consistent to the quenching of the injector-loss $\alpha_{\rm inj}$ caused by the decreasing injector-population $n_{\rm 1th}$. From the

numerical results on n_1 (shown in Figs. 4.3(a) and (b)), the key parameter K_s of a corresponding DP laser is supposed to be about half that of the present IDP laser. The theoretical curves, labeled " $K_s/2$ " in Fig. 4.6, obtained with the half values for K_s, predict substantially lower T_0-values of 139 K and 127 K in L=4 mm and 1.5 mm DP-devices (with E_{21} ∼60 meV) in the temperature ranges: 270-330 K and 250-290 K. Moreover, in addition to the high stability of the laser performances for temperature changes, the IDP scheme may, also, make the threshold current density less sensitive to the detuning between peak gain and resonant wavelengths in a DFB or external cavity system since the key parameter K_s represented by Eq. (4.2) increases with decreasing gain-cross section g_c associated with the detuning.

By assuming the injector population to be clamped, $n_1 = n_{1th}$ above threshold, the quantum yield, defined as the ratio, $(p_{out}/\hbar\omega_{opt})/(I_0-I_{th})/e$, of output photon flux to the input electron flow, of a single-mode laser is represented by,

$$\eta_{ext} = \frac{1}{2}\left[\frac{M\eta_{pump}}{n_{sp}(1+\tau_{21}/\tau_{31})}\right]\frac{(1/L)\ln(1/R)}{\alpha_c + (1/L)\ln(1/R) + (\alpha_{inj}^{(0)}/n_{inj})n_{1th}}. \qquad (4.4)$$

The uses of the estimated values of n_{1th}/n_{inj} (for the 4-mm long laser, Fig. 4.8(b)) of the 4-mm (1.5-mm) long laser as well as the appropriate values for the remaining parameters in Eq. (4.4), lead to quantum yields of 328 % (614 %) at 77 K and 394 % (692 %) at 260 K (240 K), respectively. These theoretical values correspond to the experimental values: 460 % (478 %) at 77 K and 539 % (516 %) at 260 K (240 K) (see Figs. 4.5(a) and (b)), indicating qualitatively that the higher yield at the higher temperature is attributable to the stronger quenching of the injector loss. Further theoretical work including additional effects such as an unclamped n_1 above threshold is, however, required for quantitative understanding of the observed high yields of the 4-mm long laser.

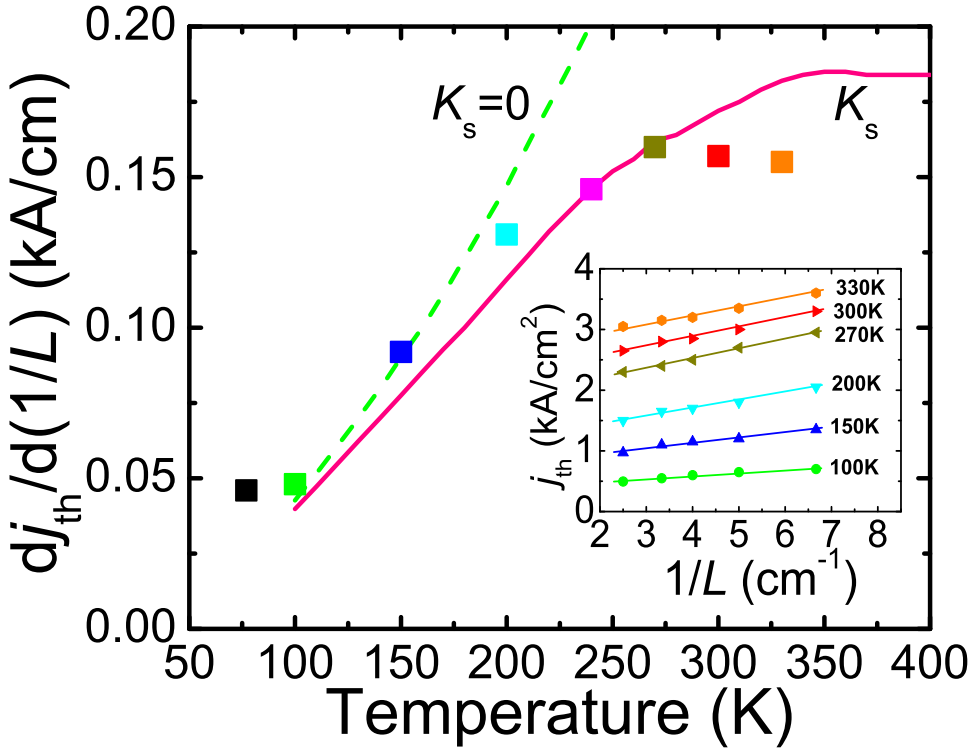

Figure 4.7: Plots of the slope $\mathrm{d}j_{\mathrm{th}}/\mathrm{d}(1/L)$ of the threshold current-density j_{th}-versus-the inverse of cavity length $1/L$ as a function of device temperature. The experimental data of the j_{th}-$(1/L)$ characteristics for different temperatures, 100-330 K are shown in the inset. The curve labeled "K_{s}" are theoretical one taking account of the suppression of the electron population in the injector. The curve labeled "K_{s}=0" are obtained by assuming K_{s}=0.

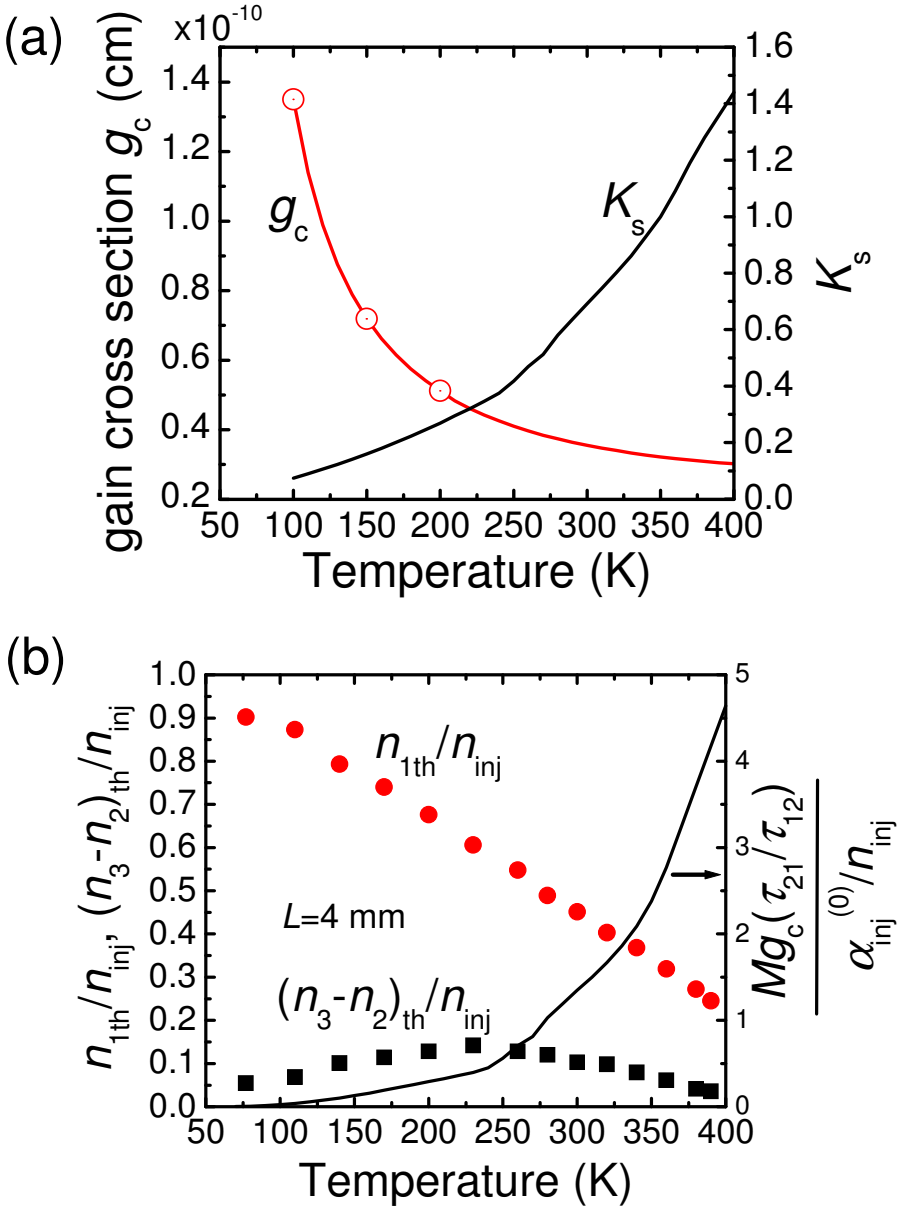

Figure 4.8: (a) Gain cross section g_c and key parameter K_s as functions of device temperature. The gain cross sections identified at three temperatures, 100 K, 150 K and 200 K are fitted by the curve represented by $g_c = G_c/(aT - bT^2 - 1)$ with $G_c = 1.19 \times 10^{-10}$ cm, a =0.021 1/K and b=2.16×10^{-5} 1/K^2 for the temperature range, 100-400 K. (b) Computed electron population n_{1th}/n_{inj} in the injector and population-inversion $(n_3-n_2)_{th}$ of the 4-mm long QC lasers at threshold conditions, and ratio $(\tau_{21}/\tau_{12})Mg_c/(\alpha_{inj}^{(0)}/n_{inj})$ as functions of device temperature.

4.4 Long wavelength laser

In addition to 8 μm QC laser, the IDP scheme is beneficial to longer wavelength QC lasers, since the scheme promises higher electron populations at upper laser states and, simultaneously, stronger suppressions of electron populations in injectors, the latter which may result in substantial absorption quenching. So far, there have been still only a few trials for room-temperature operation of longer wavelength (>13 μm) QC lasers [9]. For instance, a 16 μm direct pump (DP)-BTC laser exhibited a quite high threshold-current-density of $\sim$9 kA/cm^2 at room temperature though the characteristic temperature of the laser was T_0 $\sim$234 K. In these views, simultaneous realization of low threshold-current-density and high T_0 of such long wavelength QC lasers is a valuable target to be challenged.

4.4.1 Design of active region

The diagonal bound-to-bound active region with the SPC depopulation structure of the present lasers was designed, as shown in Fig. 4.9, to incorporate the intermediate state, level 4 for the IDP process and importantly so as to lead to strong coupling of the injector state with the intermediate state, $\hbar\Omega_{41'}\sim$7 meV. The active region consists of 5-quantum-well, instead of 4-quantum-well active region employed in previous section. Electron resonant-tunneling takes place from the injector state, level 1$'$ to level 4. The energy separation of the present devices was inferred to be $E_{43}\sim$30 meV from our results of EL spectral measurements. We simply assume resonant emissions of LO phonons, resulting in a short relaxation time, $\tau_{43}\sim$0.45 ps and a thermal excitation time, $\tau_{34} = \tau_{43}\exp(E_{43}/k_{\rm B}T)\sim$1.44 ps both for room-temperature, 300 K. The room-temperature relaxation time for the upper laser-state electrons is obtained to be relatively long, $\tau_3\sim\tau_{32}\sim$1.7 ps which was also evaluated by comparison of the observed maximum-current-density, $j_{\rm max}\sim$4.5 kA/cm^2 with theoretical one. The localized wavefunction of level 4 results in a long relaxation time for the transition. Thus, as a result of the diagonal structure, the pump efficiency for the upper laser-level is expected to be sufficiently high, $\eta_{\rm pump}\sim$0.9 because of $\tau_{43} \ll \tau_{42}$ $\sim$10 ps. The diagonal transition dipole moment is also estimated to be enough large, Z_{32} $\sim$3.4 nm. Under low excitation condition, i.e., $n_1\sim n_{\rm inj}\sim1\times10^{11}$ cm^{-2}, the non-resonant inter-subband

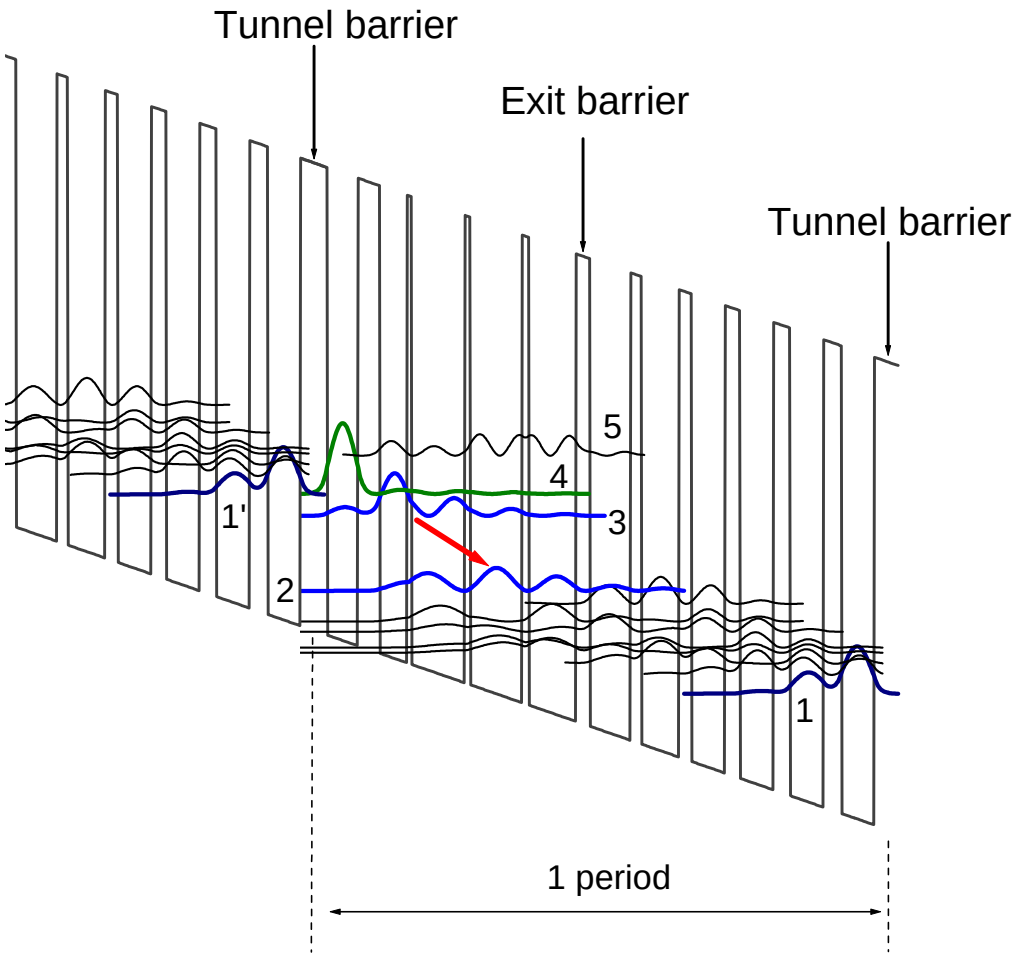

Figure 4.9: Conduction band diagram and moduli squared of the relevant wavefunctions in the designed active region of the long-wavelength (∼15 μm) IDP-QC laser. The lattice-matched $In_{0.53}Ga_{0.47}As/In_{0.52}Al_{0.48}As$ layer-sequence of one period of the active layers, in angstroms, starting from the injection barrier (toward the right side) is as follows: **33**/39/**27**/35/**5**/68/**6**/66/**8**/60/**17**/52/**13**/48/**15**/43/**18**/43/**20**/43/**22**/42 where $In_{0.52}Al_{0.48}As$ barrier layers are in bold, $In_{0.53}Ga_{0.47}As$ QW layers in roman, and doped layers are underlined. The bias field is assumed to be 30 kV/cm, high enough to align the ground state, level 1′ of the previous injector to level 4 of the active region.

absorption in the injector is unavoidably high, $\alpha_{\rm inj}^{(0)} = \alpha_{\rm cinj} n_{\rm inj} \sim 18$ cm^{-1} at room-temperature in the long-wavelength lasers, which was derived experimentally by comparison of threshold currents of devices with different mirror losses [7]. Fortunately, the difficulty would be resolved by the adoption of the IDP scheme by which the injector-electron population n_1 can be decreased substantially with increasing pump current. The back-filling population resulting in a resonant absorption is estimated to be very small, $n_{\rm 2therm}/n_{\rm inj} \sim 0.04$, compared with the population inversion $\sim$0.3, in the threshold condition at 300 K and even at 380 K in the present device with $E_{21} \sim 120$ meV.

All of the lattice-matched $In_{0.53}Ga_{0.47}As/In_{0.52}Al_{0.48}As$ layer structures, shown in Fig. 4.9, with an injector Si-doping of $n_{\rm inj} \sim 1 \times 10^{11}$ cm^{-2} were grown on an n-InP substrate by MBE technique. The active/injector stages with 55 repetitions were used as the emitting region and sandwiched by cladding materials, consisting of two very thin (0.05$\sim$0.1 μm) n-$In_{0.53}Ga_{0.47}As$ (Si, $\sim 5 \times 10^{16}$ cm^{-3}) and very thick ($\sim$5 μm), very low doping (Si, $\sim 5 \times 10^{16}$ cm^{-3}) InP layers grown by MOVPE. The waveguide design importantly, results in a very low passive (empty) waveguide loss of $\sim$3 cm^{-1} caused by weak free carrier absorption in the low doped InP layers.

4.4.2 Device characterization

Figure 4.10 shows current-light output characteristics of a 22 μm-width ridge-structured, 4 mm-long IDP-QC laser with HR-coated rear facet driven in pulse current mode: 100 ns width and 100 kHz repetition. The long-wavelength (14–15.5 μm) laser exhibits the high device performance: a low threshold-current-density of $\sim$3.5 kA/cm^2 and, as a result of the relatively wide dynamic range, a high maximum output power of $\sim$216 mW, both at room temperature, and a maximum lasing temperature of 390 K. The observed room-temperature threshold-current-density, $\sim$3.5 kA/cm^2 is obviously much lower than those of $\sim$9 kA/cm^2 of a similar long-wavelength ($\sim$16 μm) DP BTC-QC laser. A high slope efficiency of $\sim$346 mW/A of the present laser which is much higher than $\sim$37 mW/A of the 16 μm DP-BTC laser with a high waveguide loss, $\sim$30 cm^{-1} and non-resonant injector absorption $\sim$65 cm^{-1} both at room temperature, is brought about by the low

passive waveguide loss, ∼3 cm^{-1} and the quenched injector-loss, $\alpha_{\mathrm{cinj}} n_1$ ∼7 cm^{-1} originated from the substantial decrease in the injector population n_1/n_{inj}∼0.4 (see Fig. 4.12), specific to the IDP scheme. However, the characteristic temperature, T_1-value for the slope efficiency was identified to be ∼48 K above 340 K, primarily caused by carrier leakage through level 5 and partly by increasing absorption from level 3 to level 5 [10]. In addition, the voltage efficiency defined as $\eta = (M \times \hbar\omega_{\mathrm{opt}})/V$, where M is the number of cascade stages, is very important parameter for performance-evaluation particularly in such long wavelength laser. The voltage efficiency of the present laser is 55% at 300 K, which is relatively low and comparable to the values of ∼8 μm QC lasers.

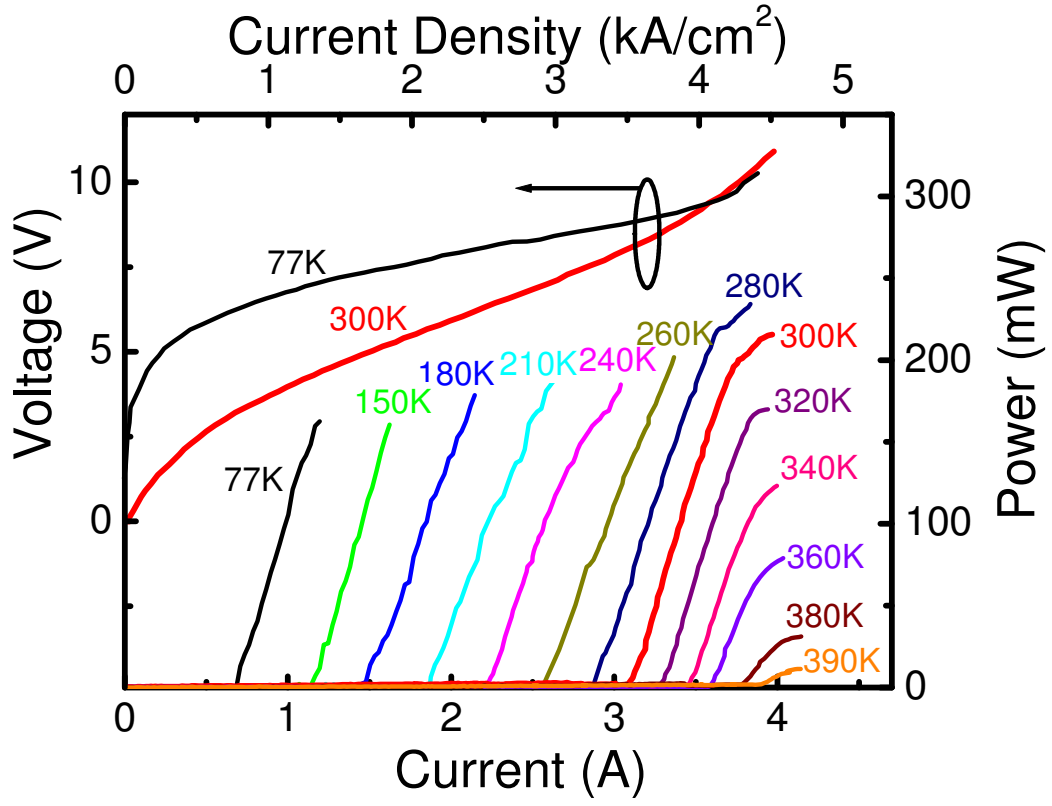

Figure 4.10: Current-light output characteristics of a long-wavelength (λ∼15 μm) 4 mm-long IDP-QC laser with HR coated rear facet at different temperatures, 77–390 K. The output intensities at room-temperature were calibrated by a thermopile detector. The current-voltage characteristics are also shown.

4.5 Temperature dependence of indirectly pumped QC lasers

Figure 4.11 shows the temperature dependences of various IDP QC lasers. The IDP lasers demonstrate very striking features in terms of temperature-dependence of the threshold current: remarkable elevation of the characteristic temperature from T_0∼150 K for the both lasers in the low temperature range, 77–200 K to T_0∼450 K for the 15 μm laser over the wide, high temperature range, 320–380 K, as shown in Fig. 4.11. An 8 μm IDP QC laser with bound-to-bound vertical transitions fabricated as a reference device also demonstrates similar temperature dependence of the threshold current. It turns out that clear changes of the slope of threshold current of the IDP lasers with respect to device temperature can be seen even in the linear plot shown in the inset. The extremely high T_0 of ∼450 K obtained with the long-wavelength low-threshold IDP laser is outstanding, compared with T_0 (234 K) of the DP long-wavelength laser[9] and with T_0 (180 K) of our 8 μm DP laser shown in the figure. However, the inherent robustness of threshold current for temperature change in the IDP laser, particularly around the highest temperature, ∼390 K would be masked by the presence of leakage current due to electron transport from injector states to parasitic states located at higher energy positions since the observed threshold currents of the present laser in the high temperature range are very close to the maximum current ($j_{\max}$ ∼4.5 kA/cm^2).

The underlying physics behind such high T_0-values will be clarified graphically below. Figure 4.12 shows computed results of the normalized electron-population $n_1/n_{\rm inj}$ in an injector and Q-factor defined as the ratio of population inversion to the injector population, $Q_{\rm a} = (n_3 - n_2)/n_1$ as functions of the normalized pump-current-density, $\Pi = j\tau_3/en_{\rm inj}$ without stimulated emissions. With recourse to increasing electron population n_4 at level 4 represented by $n_4/n_{\rm inj} = \tau_{43}(1/\tau_{34} + 1/\tau_3)\eta_{\rm pump}\Pi$ the injector population $n_1/n_{\rm inj}$ of an IDP laser with high pump efficiencies of $\eta_{\rm pump}$∼0.9, more steeply decreases with increasing current and temperature, compared with that of a DP laser. Consequently, the Q-value of the IDP laser increases super-linearly with current and temperature. For the 15 μm 5QW IDP-QC laser, the loss-gain balance relation

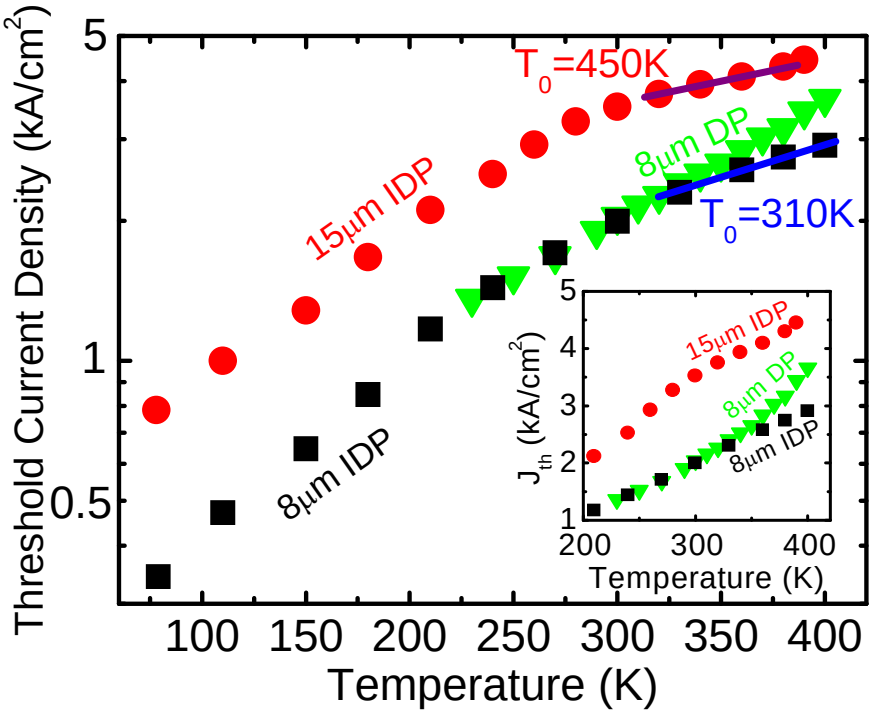

Figure 4.11: Semi-logarithmic plots of the threshold-current-densities of the long-wavelength (∼15 μm) 5QW-IDP-QC laser, and 8 μm-wavelength IDP-QC lasers as a function of heat-sink temperature. The linear plots of the threshold-current densities are also shown in the inset.

at threshold conditions, $G_c(n_3 - n_2) = \alpha_{cinj} n_1 + \alpha_g + \alpha_m \sim \alpha_{cinj} n_1$ where G_c is the modal gain cross section, $\alpha_g (\sim 3\ \mathrm{cm}^{-1})$, and $\alpha_m (\sim 1.5\ \mathrm{cm}^{-1})$, leads to the simple relation approximately, $Q_a \sim \alpha_{cinj}/G_c$. Thus, the steeper increase in the Q-value is linked to a higher T_0-value, given by $1/T_0 = (\Delta j_{th}/\Delta T)/j_{th} = \tau_3 \Delta(1/\tau_3)/\Delta T + [(\Delta\Pi/\Delta T)/\Pi]_{th}$. In fact, with a postulated value for the normalized change rate; $(G_c/\alpha_{cinj})\mathrm{d}(\alpha_{cinj}/G_c)/\mathrm{d}T \sim 2\times10^{-3}$ 1/K of which inverse is 500 K, the T_0-value of the 15 μm 5QW IDP laser averaged over the high temperature range, 350–400 K is estimated to be very high, $T_0 \sim 440$ K, compared with $T_0 \sim 300$ K of the corresponding DP laser and the same change rate, $(G_c/\alpha_{cinj})\mathrm{d}(\alpha_{cinj}/G_c)/\mathrm{d}T \sim 2\times10^{-3}$ 1/K. The IDP scheme functions to elevate the virtual characteristic temperature, i.e., the inverse of the second term, $[\Pi/(\Delta\Pi/\Delta T)]_{th}$ up to a surprisingly high value of $\sim$2260 K and, as a result, the resultant characteristic temperature, $T_0 \sim 440$ K is obtained to be closer to the inverse of the first term, $1/[\tau_3 \Delta(1/\tau_3)/\Delta T] \sim 546$ K, due to the temperature-dependent relaxation time τ_3 which exists regardless of pump schemes. However, with recourse to the presence of temperature-independent elastic (alloy disorder and interface roughness) scatterings in the InGaAs/InAlAs system [11], the upper-state relaxation time τ_3 may vary slower with temperature change. By assuming elastic scattering of about 20% of the total scattering rate at 380 K, the inverse of the first term is obtained to be $1/[\tau_3 \Delta(1/\tau_3)/\Delta T] \sim 655$ K. This obviously leads to a higher resultant T_0 of $\sim$508 K in the high temperature range, 350–400 K. The inherent robustness of threshold current for temperature change in the IDP laser, particularly around the highest temperatures, >350 K would be, however, masked by the presence of leakage current due to electron transport from injector states to parasitic states located at higher energy positions since the observed threshold currents of the present laser in the high temperature range are very close to the maximum current ($j_{max} \sim 4.5$ kA/cm^2).

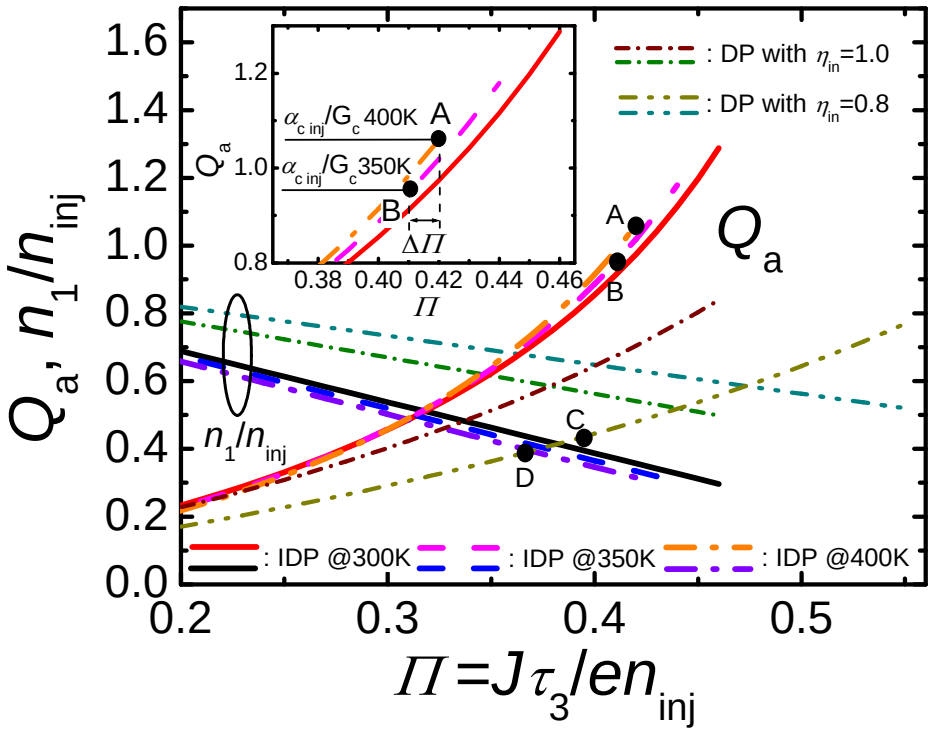

Figure 4.12: Computed normalized electron-population $n_1/n_{\rm inj}$ in an injector and Q-value, defined as $Q_{\rm a} = (n_3 - n_2)/n_1$, of active regions of an IDP and DP QC laser as functions of the normalized pump-current-density, $\Pi = j\tau_3/en_{\rm inj}$ without stimulated emissions. In the computation, eq. (2.64) for the IDP laser and the corresponding relation for the DP laser were used by assuming realistic numerical values, indicated in the interpretation of the band diagram, for relaxation times and by taking account of their temperature dependences. For the IDP laser, point A is chosen to represent the threshold-current-density at 400 K which is almost equal to the maximum current-density as in the real ∼15 μm IDP device shown in Fig. 4.10. For the DP laser, point C corresponds to the threshold-current-density, ∼3.5 kA/cm^2 at 400 K, which is substantially lower than the maximum current density, ∼5 kA/cm^2, as in the ∼8 μm-wavelength DP device. The vertical distances between points A and B and between points C and D are determined by $\Delta(\alpha_{\rm cinj}/G_{\rm c}) = [{\rm d}(\alpha_{\rm cinj}/G_{\rm c})/{\rm d}T](\Delta T) \sim 2 \times 10^{-3} \times\ 50(\alpha_{\rm cinj}/G_{\rm c})$ for the postulated change rate, $(G_{\rm c}/\alpha_{\rm cinj}){\rm d}(\alpha_{\rm cinj}/G_{\rm c})/{\rm d}T \sim 2\times10^{-3}$ 1/K and ΔT=50 K.

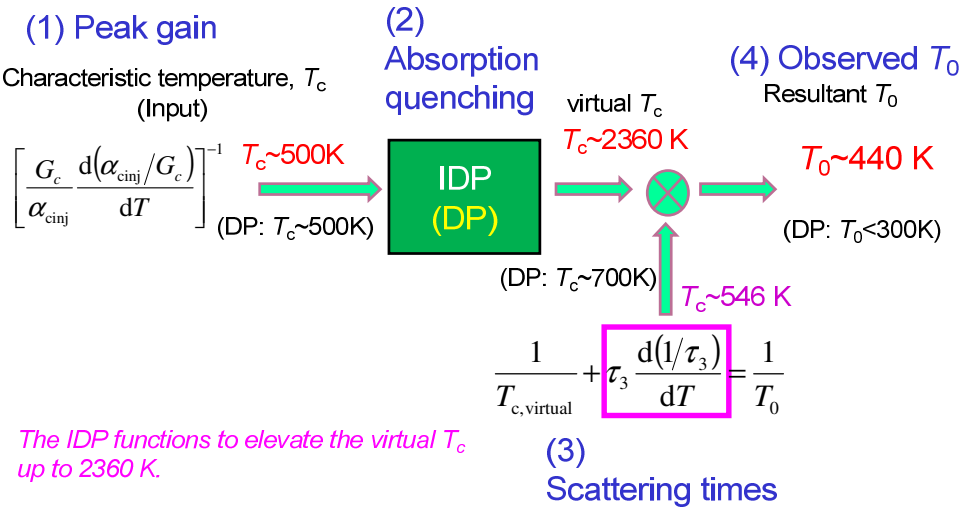

Figure 4.13: Summary of physics for high T_0.

4.6 Conclusion

In this chapter, quantum cascade lasers based on the indirect pump scheme have been demonstrated to clarify its own advantages over the conventional direct pump scheme. The performance of the buried hetero-structured 8 μm QC laser with a cavity length of 4 mm based on the indirect pump scheme has been demonstrated: a threshold current density of 2.7 kA/cm^2 and a maximum output power of 362 mW both at room temperature, and a maximum lasing temperature of 390 K. The long-wavelength (14-15.5 μm) indirect pump, QC laser with precisely designed active regions and low loss waveguide has exhibited very high performance: a low threshold-current-density of ~3.5 kA/cm^2, a high maximum output power of 216 mW, and a high slope efficiency of 346 mW/A with recourse to the nonresonant absorption quenching in the injector, all at room temperature, and an extremely high characteristic temperature of T_0 ~450 K over the high temperature range, 320-380 K. These are the best performance in long-wavelength (>13 μm) QC lasers at noncryogenic temperatures. The observed high characteristic temperature has been interpreted to be caused by strong suppression of electron

populations in injectors, associated with current-increase and temperature-rise, which are involved in the indirect pump scheme. The pump scheme would be a very powerful harness for high temperature (>250 K) operation of THz-QC lasers, which has not been achieved yet with the conventional direct pump scheme. In fact, several groups have been developed the THz-QC lasers based on IDP scheme [12, 13, 14, 15]. Kumar et al. demonstrated high temperature operation of IDP-THz-QC laser despite lower frequency range in THz region (∼1.8 THz) [12]. We also exhibit that there are a lot of potentials of IDP-QC laser in the THz range [15].

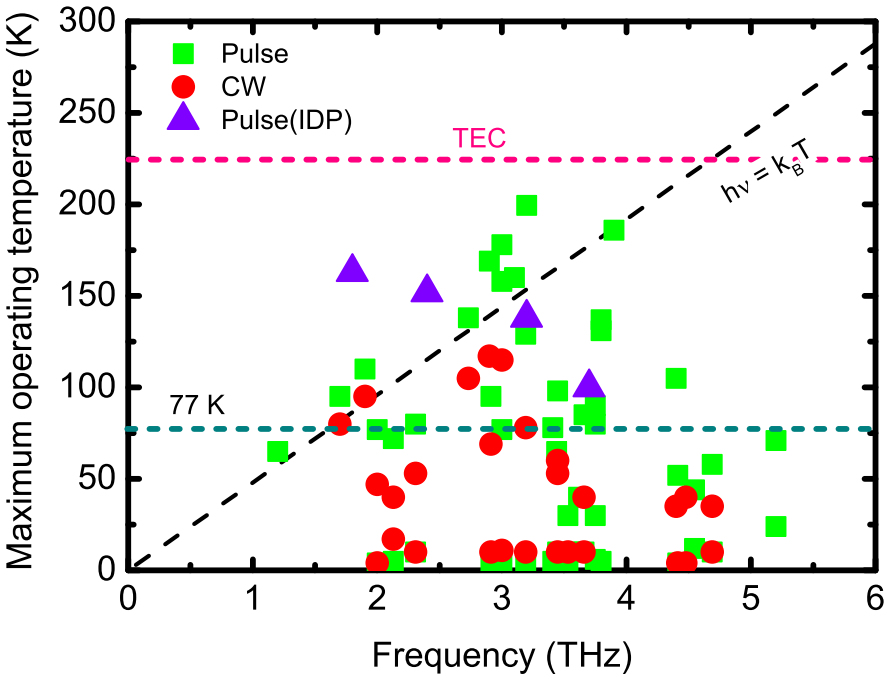

Figure 4.14: Maximum operating temperatures of THz-QC lasers as a function of lasing frequency.

References

[1] A. Wittmann, M. Giovannini, J. Faist, L. Hvozdara, S. Blaser, D. Hofstetter, and E. Gini, "Room temperature, continuous wave operation of distributed feedback quantum cascade lasers with widely spaced operation frequencies," Appl. Phys. Lett. **89**, 141116 (2006).

[2] M. Beck, D. Hofstetter, T. Aellen, J. Faist, U. Oesterle, M. Ilegems, E. Gini, and H. Melchior, "Continuous-wave operation of a mid-infrared semiconductor laser at room-temperature," Science **295**, 301, (2002).

[3] C. Sirtori, F. Capasso, J. Faist, A. L. Hutchinson, D. L. Sivco, and A. Y. Cho, "Resonant tunneling in quantum cascade lasers," IEEE J. Quantum Electron. **34**, 1722 (1998).

[4] G. Scamarcio, M. Troccoli, F. Capasso, A. L. Hutchinson, D. L. Sivco, and A. Y. Cho, "High peak power (2.2 W) superlattice quantum cascade laser," Electron. Lett. **37**, 295 (2001).

[5] Q. J. Wang, C. Pfluegl, L. Diehl, F. Capasso, S. Furuta, and H. Kan, "High-power long-wavelength room temperature MOVPE-grown quantum cascade lasers with air-semiconductor waveguide," Electron. Lett. **44**, 525 (2008).

[6] M. Yamanishi, T. Edamura, K. Fujita, N. Akikusa, and H. Kan, "Theory of the Intrinsic Linewidth of Quantum-Cascade Lasers: Hidden Reason for the Narrow Linewidth and Line-Broadening by Thermal Photons," IEEE J. Quantum Electron. **46**, 12 (2008).

[7] A. Wittmann, T. Gresch, E. Gini, L. Hovzdara, N. Hoyler, M. Giovannini, and J. Faist, "High-performance bound-to-continuum quantum-cascade lasers for broad-gain applications," IEEE J. Quantum Electron. **44**, 36 (2008).

[8] J. Faist, "Wallplug efficiency of quantum cascade lasers: Critical parameters and fundamental limits," Appl. Phys. Lett. **90**, 253512 (2007).

[9] M. Rochat, D. Hofstetter, M. Beck and J. Faist, "Long-wavelength $\lambda \approx 16$ μm., room-temperature, single-frequency quantum-cascade lasers based on a bound-to-continuum transition," Appl. Phys. Lett. **79**, 4271 (2001).

[10] D. Botez, S. Kumar, J. C. Shin, L. J. Mawst, I. Vurgaftman, and F. R. Mayer, "Temperature dependence of the key electro-optical characteristics for midinfrared emitting quantum cascade lasers," Appl. Phys. Lett. **97**, 071101 (2010).

[11] A. Vasanelli, A. Leuliet, C. Sirtori, A. Wade, G. Fedorov, D. Smirnov, G. Bastard, B. Vinter, M. Giovannini, and J. Faist, "Role of elastic scattering mechanism in GaInAs/AlInAs quantum cascade lasers," Appl. Phys. Lett. **89**, 172120 (2006).

[12] S. Kumar, C. W. I. Chan, Q. Hu, and J. L. Reno, "A 1.8-THz quntum cascade laser operating significantly abovethe temperature of $\hbar\omega/\mathrm{k_B}T$," Nat. Phys. **7**, 166 (2011).

[13] E. Dupont, S. Fathololoumi, Z. R. Wasilewski, G. Aers, S. R. Laframboise, M. Lindskog, S. G. Razavipour, A. Wacker, D. Ban, and H. C. Liu, "A phonon scattering assisted injection and extraction based terahertz quantumcascade laser," J. Appl. Phys. **111**, 073111 (2012).

[14] S. G. Razavipour, E. Dupont, S. Fathololoumi, C. W. I. Chan, M. Lindskog, Z. R. Wasilewski, G. Aers, S. R. Laframboise, A. Wacker, Q. Hu, D. Ban, and H. C. Liu, "An indirectly pumped terahertz quantum cascade laser with low injection coupling strength operating above 150K," J. Appl. Phys. **113**, 203107 (2013).

[15] K. Fujita, M. Yamanishi, S. Furuta, K. Tanaka, T. Edamura, T. Kubis, and G. Klimeck, "Indirectly pumped 3.7 THz InGaAs/InAlAs quantum-cascade lasers grown by metal-organic vapor-phase epitaxy," Opt. Express **20**, 20647 (2012).

Chapter 5

Anti-crossed dual-upper-state design

5.1 Introduction

In the previous chapter, we clarified the importance of the electron dynamics in QC lasers. Obviously the indirect pump scheme has advantages for long wavelength operation. As discussed in Chapter 2, the dual-upper-state (DAU) design also has an advantage over the direct pump scheme in terms of the electron dynamics in the injector. In addition, transitions from the two upper states would make it possible to generate broadband electroluminescence (EL). In the present chapter, we describe the characteristics of the QC lasers based on anti-crossed dual-upper-state designs, which exhibit high laser performance as well as a broad symmetric EL spectrum with its weak dependence on the voltage. First, we will present the anti-crossed DAU design and discuss its features in detail (Section 5.2). We will find DAU-QC lasers in which the slope efficiencies are enhanced with increasing current. In addition, a high temperature coefficient T_0 for threshold current can be obtained. Then we will discuss the electron dynamics in the anticrossed dual-upper-states and consider the spectral behavior of the DAU laser during lasing. In Section 5.5, we will exhibit its higher temperature performance with strain-compensated quantum wells. In the results, strong superlinear current–light output curves as well as extremely high characteristic temperatures are achieved. The underlying physics of these results will be discussed.

5.2 Design and electroluminescence

5.2.1 Design of active region

In a DAU design, the strongly anticrossed two upper laser states and the lower laser state are associated with the wavefunctions labeled by the numbers 4, 3, and 2, as shown in Fig. 5.1. In the anticrossed DAU active region, another upper laser state 4 is created by the thin quantum well adjacent to the injection barrier. The thin quantum well of which the ground state provides another upper laser state plays a crucial role in obtaining high laser performances since this reduces the coupling between the miniband states in the injector and higher lying states in the active region. In this sense, the DAU design is very different to the other broadband QC laser design with multiple upper states [1]. Although many QC laser designs have the thin quantum well to enhance injection efficiency [2], the ground state of the thin quantum well, assuming a single quantum well, is located in the higher energy side and enhances the coupling unlike in the present device.

As a result of precise designing, the wavefunctions of the both upper laser states extend over the whole active region from the injection barrier to the exit barrier and lead to large dipole matrix elements from both upper states to the lower state: $Z_{42} \sim Z_{32} \sim 1.8$ nm. The energy separation between the upper laser states and the parasitic state 5 can be designed to be large, ∼60 meV. Thus, a high injection efficiency for both upper states is obtainable even at high temperatures. Electrons are injected into the higher upper state, state 4, via resonant tunneling from the ground state, level $1'$, and then are distributed very quickly between the two upper laser states. The appropriate anticrossing gap and electron injection into the higher upper state at the design bias (∼40 kV/cm) are crucially important for achieving a wide and symmetric spectrum. At this point, it turns out that the alloy scattering and interface roughness scattering have an important role in the distribution process between the two upper states [3]. Namely, the electron scattering from the bottom of subband 4 to subband 3 are substantially faster (∼0.1 ps) than LO phonon and electron–electron scatterings (>1 ps) due to the very strong anticrossing of the two upper states [4]. On the other hand, in the case of electron pumping to the lower upper states, since

there is no ultrafast electron transfer processes from the bottom of subband 3 to subband 4, electrons at subband 3 are relaxed quickly into lower subbands via LO phonon emissions.

All the layer structures were grown on an n-type InP substrate using the MOVPE technique. The 40 period active regions with translational symmetry were used as the emitting region and sandwiched between two 0.25 μm thick n-$In_{0.53}Ga_{0.47}As$ layers (Si, 5×10^{16} cm^{-3}). The upper cladding layer consists of a 3.5 μm thick n-InP (Si, 1×10^{17} cm^{-3}) followed by a 0.3 μm thick n^+- InP (Si, $\sim10^{18}$ cm^{-3}) cap layer.

5.2.2 Electroluminescence

The EL spectra of the mesa device without stripe structure are shown in Fig. 5.2(a), which includes the results at various voltages at room temperature. The linewidth γ of the spectra taken with pulsed injection currents of 500 ns width at a repetition rate of 100 kHz was observed to be a very wide value of γ=40.8 meV (330 cm^{-1}) at 7.2 V, which was wider than the typical linewidth of the reported bound-to-continuum (BTC) QCL. The EL curves, which are attributed to the transitions from the two upper states to state 2, remain wide and almost spectrally homogeneous over the whole voltage range. For comparison, the linewidths of the DAU device, of a BTC, and a bound-to-bound device are shown in Fig. 5.2(b). The linewidth in the BTC device decreases steeply with increasing voltage. The BTC transitions are definitely sensitive to the electric field because the wavefunctions of the upper and lower states are spatially located in different regions [5]. On the other hand, the linewidth of the DAU device is insensitive to voltage changes since the anticrossed wavefunctions of the both upper laser states are basically located in the same space.

Figs. 5.3(b) and (c) show the calculated energy separations and dipole moment curves for the 4-to-2 and 3-to-2 transitions as a function of the electric field. In this design, as shown in Fig. 5.3(b), a large anticrossing gap of $\sim$20 meV is created around 40 kV/cm, and as a result, the dipole moments for both transitions are nearly equal over the operating range. In fact, the EL curves attributed to the transitions from the two upper states to state 2 remain wide and almost

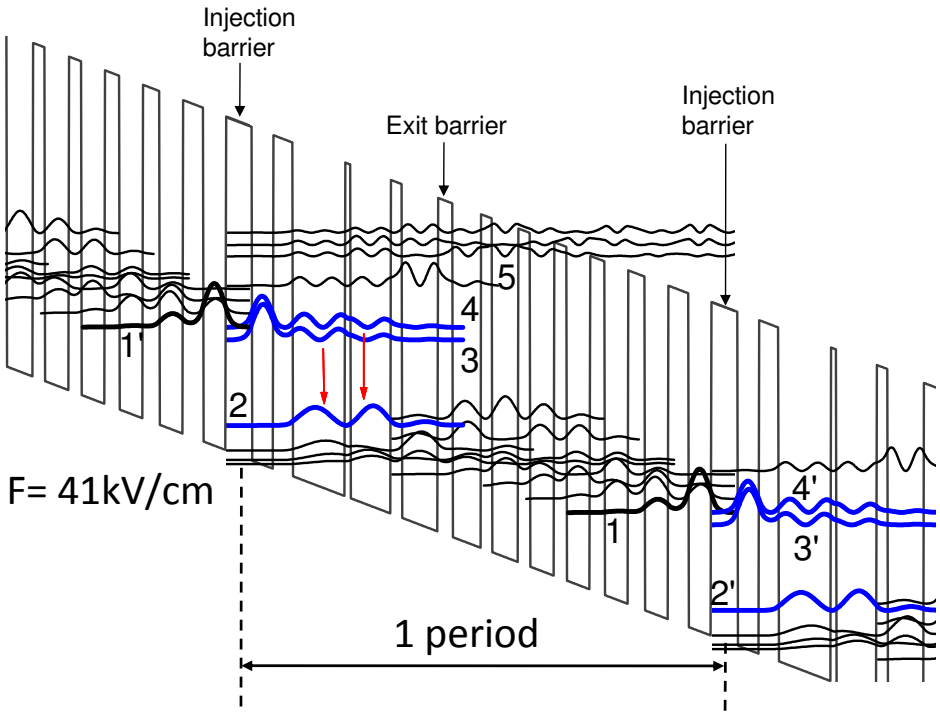

Figure 5.1: Schematic conduction band diagram and moduli squared of the relevant wavefunctions of injector/active/injector parts in the $\lambda\sim$8.4 μm anti-crossed DAU active region . An electric field of 41 kV/cm was applied to align the structure. The InGaAs/InAlAs layer sequence of one period of the active layers, in angstroms, starting from the injection barrier (toward the right side) is as follows: **37**/31/**27**/75/**7**/58/**15**/52/**18**/41/**15**/38/**16**/35/**17**/34/**20**/34/**23**/34/**28**/33 where InAlAs barrier layers are in bold, InGaAs QW layers in roman, and doped layers (Si, 5×10^{10} cm^{-2}) are underlined.

spectrally homogeneous over the whole voltage range. The EL spectral changes in the electric field correspond to the energy separation and dipole moment curves; namely in Fig. 5.3(a) the peak of the 3 to 2 transition rapidly increases, compared to that of the 4 to 2 transition, with increasing electric field. Fig. 5.4 shows the calculated EL spectra and measured EL spectra at various electric fields: 28 kV/cm, 38 kV/cm, and 49 kV/cm. Although the electron populations of the two upper states should be used as a weighting factor when calculating the gain spectrum, we assumed an equal electron distributions between the two upper laser states. Since there are ultrafast elastic scatterings in the strongly anticrossed two upper states, electrons distribute rapidly between the two upper states, as observed in the Section 5.4. The EL curves are in good agreement with the designed curves, in which the 4-2 and 3-2 transitions contribute to the optical gain.

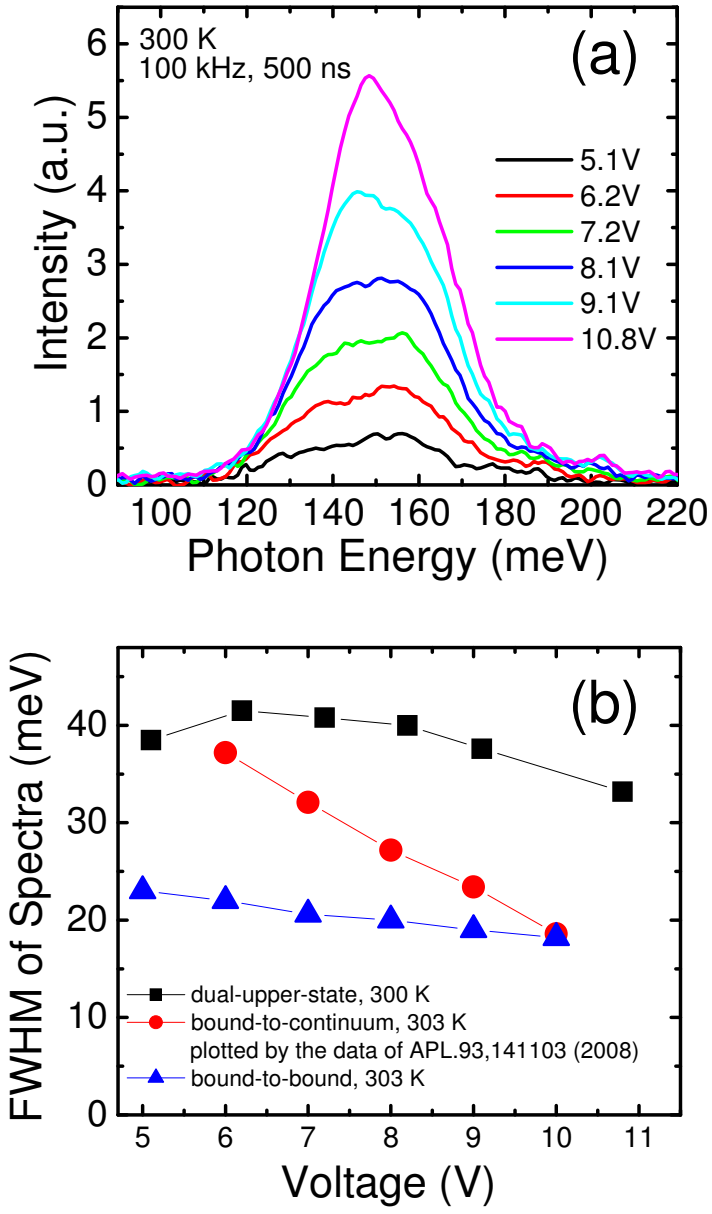

Figure 5.2: (a) Intersubband EL spectra of the mesa device for various voltage. (b) The FWHM of the spectra, for the DAU device as well as for the bound-to-continuum, described in Ref. [6], and the bound-to-bound devices, respectively, as functions of voltage.

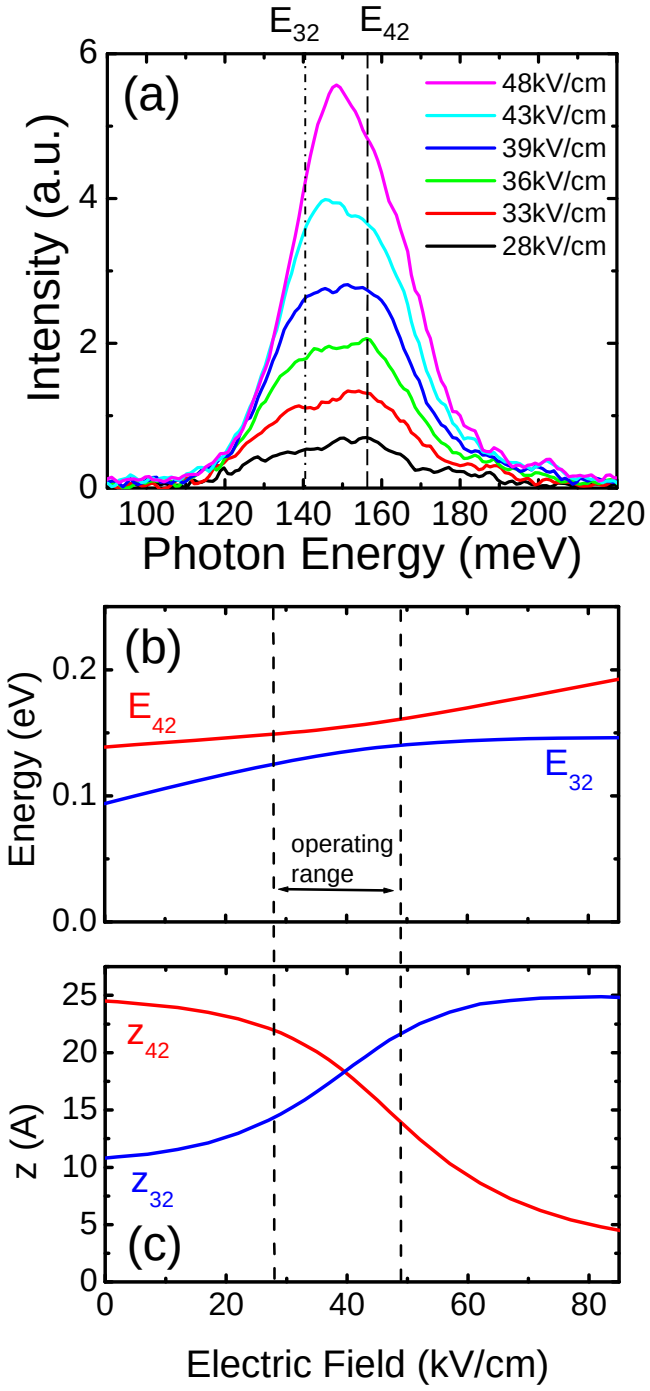

Figure 5.3: (a)Intersubband EL spectra of the 8 μm DAU device with a mesa structure for various voltages. (b) Energy separations between both upper laser states and lower laser state as a function of electric field. (c) Calculated dipole matrix element for 4-2 and 3-2 transitions as a function of electric field.

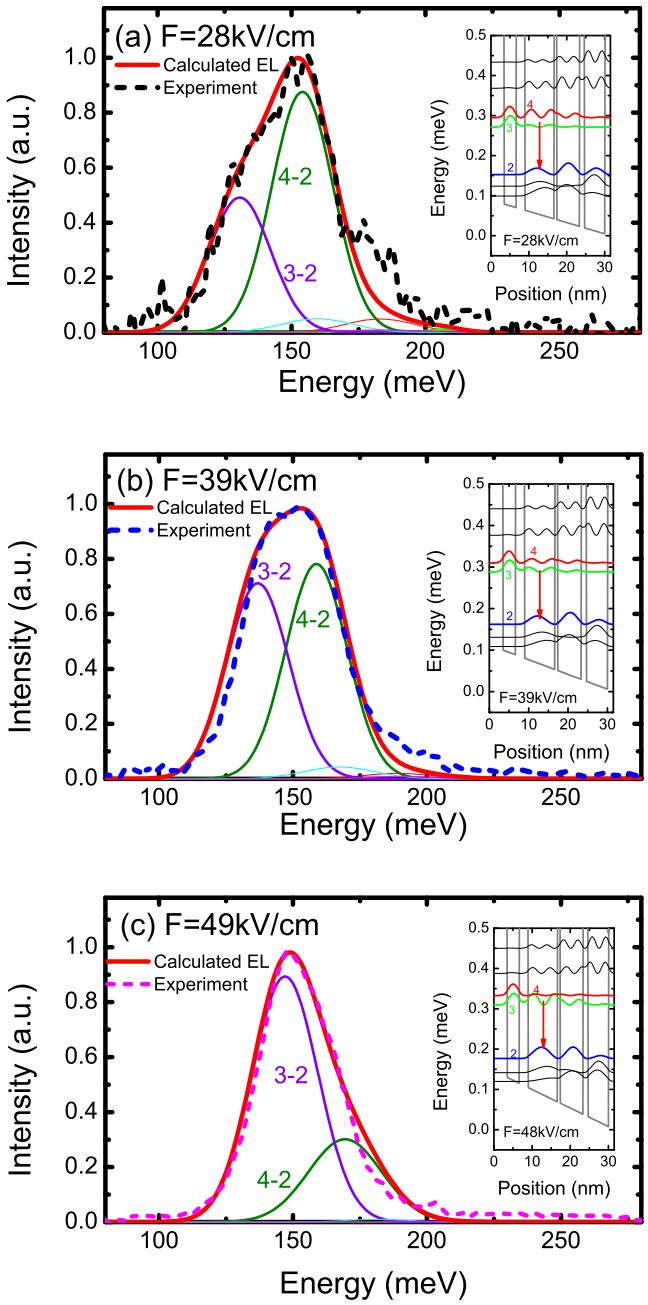

Figure 5.4: Calculated (solid line) and experimental (dashed line) EL (normalized) at an applied electric field of (a) 28 kV/cm, (b) 39 kV/cm, and (c) 49 kV/cm. The insets show the portions of the band diagrams, exhibiting the shape of wavefunctions of the dual upper states.

5.3 Laser performance

For laser characterization, after the growth, the wafer was processed into a buried hetero-structure. Finally, evaporation of the top Ti/Au contacts was followed by electroplating of a thick 5 μm Au layer on top of the ridge. The laser was bonded epi-side up on a copper sub-mount with Indium solder and mounted on a thermo-electrical cooling holder. For current–light output characterization, the peak output power was measured with a calibrated thermopile detector. The pulsed I-L characteristics at different temperatures as well as the V-I characteristics for an 8 μm-wide, 3 mm-long, HR-coated device, are shown in Fig. 5.5. The threshold current density at 300 K was observed to be $\sim$2.0 kA/cm^2 and an optical output power of 610 mW with a slope efficiency of $\sim$1.0 W/A was obtained at 300 K in pulsed operation, 100 kHz, 100 ns. The threshold current density as a function of temperature is shown in Fig. 5.6. The characteristic temperature T_0 is seen to be very high, $T_0\sim$306 K, which is comparable to those of the indirect-pump QC lasers.

Furthermore, the I-L curves are revealed to have super-linear behavior, and the slope efficiency at threshold is apparently constant up to a temperature change over a wide temperature range, 280–400 K (corresponding $T_1\sim$10000 K). These distinctive features are attributed to the dynamics of the electron transport described in Chapter 2. The optical absorption quenching in the injector with increasing temperature, namely increasing threshold current, has been clarified as taking place in the IDP case. In the proposed design, electrons are distributed in three states, 4, 3, and the ground state 1 in the injector. Thus, the electron population in the injector at high pump current is less than that in a conventional direct pump design. In addition, in the present device, despite the room temperature measurements, the negative differential resistance is clearly observed in the V-I curve at the maximum operating current. This implies a large energy gap between the upper laser state 4 and the higher parasitic state 5 as well as a lower leakage current to higher spurious states. The super-linear I-L curves may be caused by the resultant effect of both the electron dynamics in the injector and the high injection efficiency. However, further theoretical and experimental work is required for a quantitative understanding of this super-linearity.

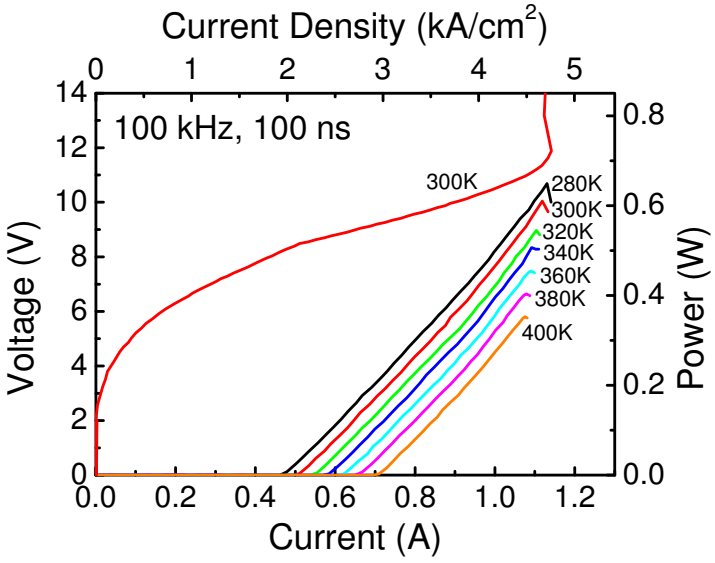

Figure 5.5: Pulsed current-light output characteristics of the 8.0 μm-wide, 3.0 mm-long, HR-coated, buried hetero structure, $\lambda\sim$8.4 μm DAU laser with a thick gold film at different heat sink temperatures. The voltage-current characteristic at 300 K is also shown.

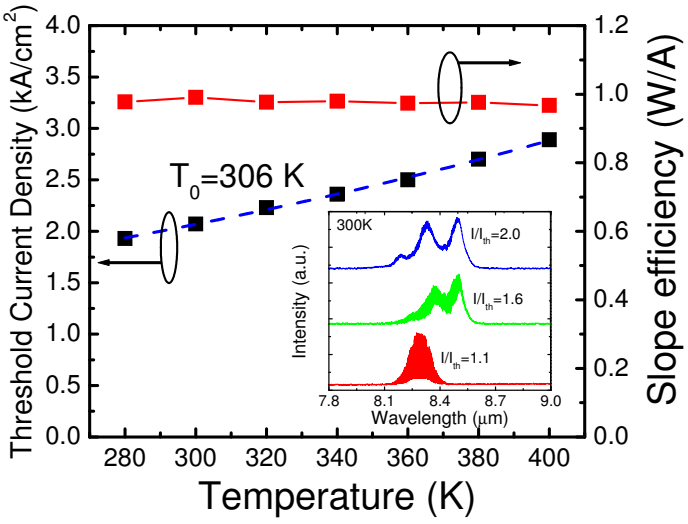

Figure 5.6: Threshold current density and slope efficiency at threshold as a function of heat sink temperature in pulsed operation. The dashed curves represent fits by the empirical exponential functions, $J_{\rm th} = J_0 \exp(T/T_0)$. The inset shows the laser spectra at various current.

The spectra, shown in inset of Fig. 5.6, broaden and split into several humps as the current increases. This behavior is observed for all samples measured and seems to be attributable to coherent instabilities [13]. On the other hand, at moderate pump levels, $1 < I/I_{\mathrm{th}} < 1.3$, there exist no modes outside the main longitudinal modes, implying that the gain is clamped. This gain clamping possibly originates from a very fast relaxation of the electron population between states 4 and 3, caused by elastic scattering. Fig. 5.7(a) shows the CW current–light curves of the device at different heat sink temperatures. The threshold current density at 300 K was observed to be 2.7 kA/cm^2 and a CW output power of 152 mW together with a high constant slope efficiency of 518 mW/A was obtained at 300 K in CW operation. The device was operated in the CW mode at higher temperatures up to 360 K. The active region temperature in CW operation at 360 K is extrapolated to be 475 K from the threshold current density and T_0-value in pulsed operation. Nevertheless, the temperature-dependence of the CW threshold current density has been observed to be weak, T_0 ∼215 K, as shown in Fig. 5.7(a) inset. The spectra of the DAU QC laser as well as the sub-threshold spectrum of a bound-to-bound QC laser, as a comparison, are shown in Fig 5.7(b). The sub-threshold (I/I_{th}=0.95) spectrum of the DAU QC laser has a very wide spectrum over 200 cm^{-1} when compared to that of the bound-to-bound QC laser. We believe the proposed QC laser is highly suitable for broadband tuning applications.

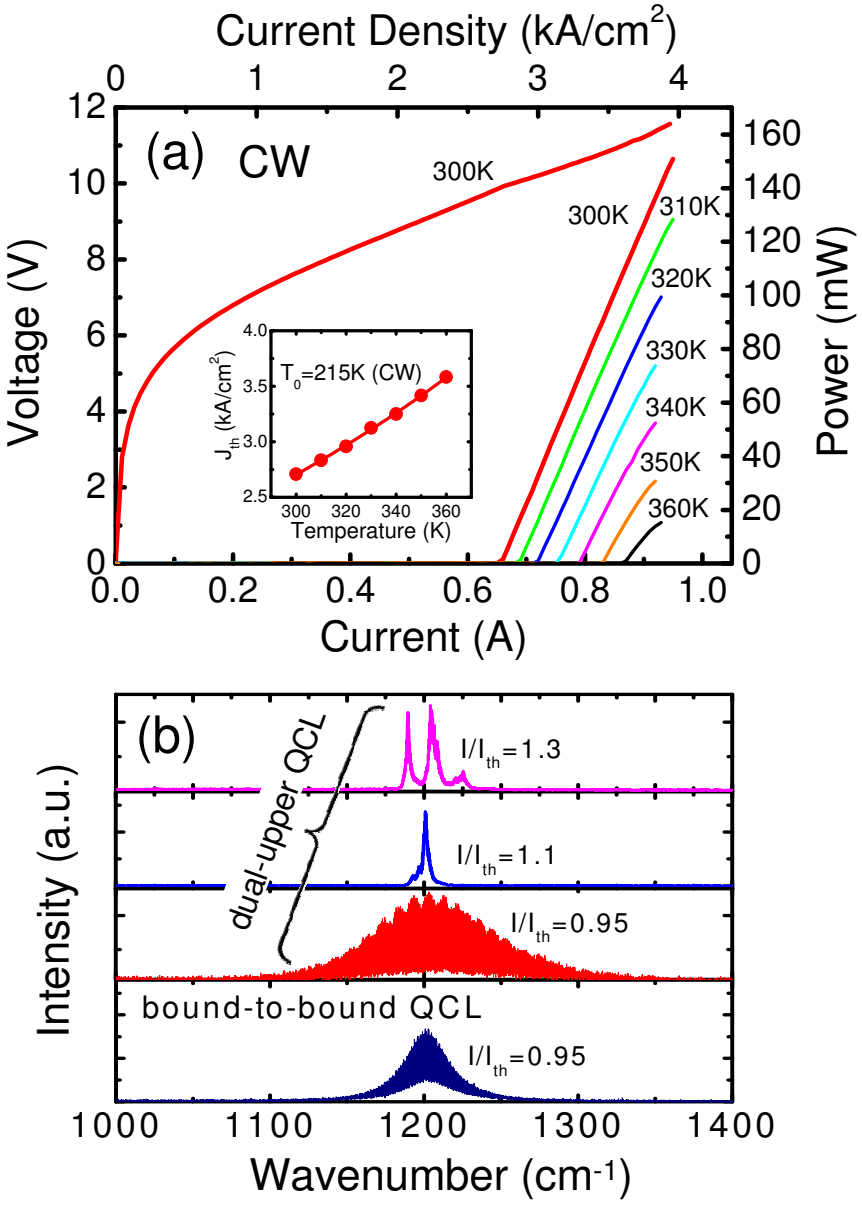

Figure 5.7: (a) CW current-light output characteristics of the $\lambda\sim8.4$ μm DAU laser at different heat sink temperatures. The voltage-current characteristic at 300 K is also shown. The inset shows threshold current density as functions of heat sink temperature in CW operation. (b) The spectra in both subthreshold and above-threshold operations of the DAU laser at 300 K. The subthreshold spectrum of the bound-to-bound device at 300 K is also shown as a comparison.

5.4 Electron dynamics and gain spectra

From EL measurements, we have confirmed that almost homogeneous spectra could be obtained for a QC device based on the DAU design. In this section, we consider the electron distribution in the DAU with the energy diffusion model [7]. Spectral behavior of the DAU laser under stimulated emission will be discussed.

As discussed in Chapter 2, elastic scattering due to interface roughness and alloy disorder play an important role in the transport of the QC structure [8, 9]. For the upper laser states of the DAU-QC laser, the elastic scattering rates are very high compared to what they would be in a single upper state design, since now there are two strongly coupled upper states, so that a significant overlap of the wave functions of the two upper states is created. In this situation, the scattering times between the two upper states due to interface roughness and alloy disorder have been calculated to be very fast, ∼100 fs and ∼500 fs. This ultra-fast elastic scattering is very important for spectrally homogeneous behavior, since broadband gain spectra of the DAU design rely on multiple transitions. Actually, the following fact was clarified for the longitudinal mode stability in bipolar laser. When the intraband relaxation time is longer than 3×10^{-13} s, the gain shows strong non-uniformity across spectral or energy distributions, and at the same time the gain of some resonating modes is increased [10]: this hinders single mode operation under wavelength tuning. Although a short relaxation lifetime 1×10^{-13} s in the case of bipolar lasers has been reported [11], even shorter relaxation times would be required for mode stability in QC lasers due to their very high stimulated emission rates [12]. On this issue, in an identical-stack (homogeneous cascade) QC laser, the depression of the electron population in an upper subband, induced by stimulated emissions, can, in an anticrossed DAU design, be compensated quickly by relaxation from other subbands in the same space because of the sufficient spatial overlap of the wave functions of the subbands. Thus, the gain spectrum of an identical-stack DAU QC laser would be viewed as a spectrally homogeneous one. Obviously, an inherently broad and spectrally homogeneous gain profile of the laser medium with translational symmetry is preferable for single mode operation in the external cavity applications of QC lasers.

As shown in Fig 5.8(a), in states 4 and 3 of the DAU design, the pumped electrons at a point A in subband 4 are quickly scattered to a point B or C in subband 3. At the same time, the electrons at the points B and C can also be scattered back to subband 4. On the other hand, the electrons at the bottom of subband 3 cannot be scattered to subband 4 via ultra-fast elastic scatterings. In addition, there is no very fast scattering process from B and C to the bottom of subband 3 since the energy spacing between B (or C) and the bottom of subband 3 in k-space is smaller than the LO phonon energy ($E_{\rm LO}$ ~34 meV). In this case, electrons are distributed via electron–electron scattering. Therefore, the electron populations of subband 3 and 4 are kept similar. In order to clarify this point, we counted the population distribution for the DAU design based on the so-called energy-diffusion model [7]. The essential points included in the energy-diffusion model are as follows. Suppose there occurs an intrasubband e–e scattering event in a quantum well. By the scattering event associated with a momentum transfer q, an electron with a momentum k may lose an amount of energy whereas the other electron may gain the same amount of energy because of energy conservation at the event. The energy transfer is represented by $\Delta E = (\hbar^2 k^2/2m^*)\{-2(q/k)\cos\theta + (q/k)^2\}$ where θ is the outer angle between k and q. Taking the average over the angles, $\pi/2 < \theta < 3\pi/2$ (energy gain) or $-\pi/2 < \theta < \pi/2$ (energy loss), the averaged energy transfer is given by $\langle \Delta E \rangle_{\rm av} = (\hbar^2 k^2/2m^*)\{\pm(4/\pi)(q/k) + (q/k)^2\}$. In general, e–e scattering potentials decrease sharply with increasing momentum transfer q larger than the inverse ($S \sim 2 \times 10^5$ 1/cm) of the screening length:

$$V(q)^2 \propto \left| \int\int {\rm d}z{\rm d}z' \Psi(z)^2 \Psi(z')^2 \exp\left[-Q\,|z - z'|\right] \right|^2 / Q^2, \tag{5.1}$$

where $Q^2 = q^2 + S^2$ and $\Psi(z)$ is the wavefunction in a subband. By taking the average-momentum transfer to be $q_{\rm av} \sim S$, one obtains $\langle \Delta E \rangle_{\rm av} \sim \pm 4/\pi(\hbar^2 k S/2m^*)$ since S is much smaller than $k \sim 10^6$ 1/cm under consideration. Thus, one may view the e–e scattering process as if it were a diffusion process in energy space. The energy-diffusion coefficient may be given by $D_{\rm e} = \{\langle \Delta E \rangle_{\rm av}/\tau_{\rm e-e}\}^2 \tau_{\rm e-e} = \{\langle \Delta E \rangle_{\rm av}\}^2/\tau_{\rm e-e}$, where $\tau_{\rm e-e}$ is the intrasubband e–e scattering time, typically ~100 fs [8]. The phenomenological relation including both the e–e (diffusion

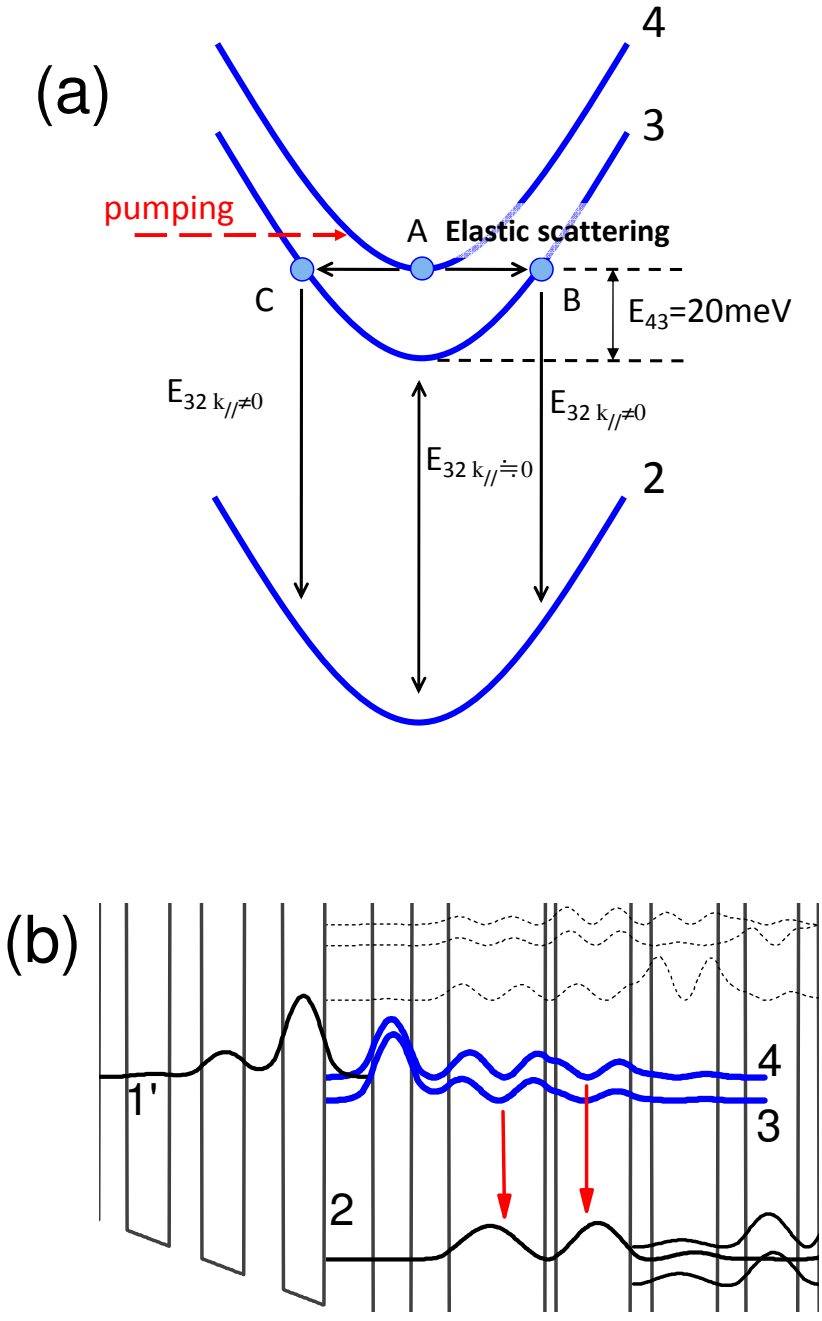

Figure 5.8: (a) Schematic illustrating scattering process for the dual-upper sates. Electrons are pumped at point A from the previous stage, and are scattered to point B and C. Optical transitions from points B and C give same energy with that from the bottom of subband 3. (b) Schematic illustration of the band diagram showing the dual-upper states and transitions from the states.

model) and LO phonon scatterings for a non-degenerate electron system in steady-state condition together with the boundary conditions $\mathrm{d}n(E)/\mathrm{d}E = 0$ at the subband edge and $n(E) \to 0$ for $E \to \infty$, was used to compute the energy-resolved electron population $n(E)$ for subband 4,

$$g_0 \exp\left(-\frac{E - E_4}{k_\mathrm{B}T}\right) + D_{\mathrm{e}4}\frac{\mathrm{d}^2 n_4(E)}{\mathrm{d}E^2} + \frac{n_3(E)}{\tau_\mathrm{ela}} - \left(\frac{1}{\tau_4} + \frac{1}{\tau_\mathrm{ela}}\right) n_4(E) = 0, \quad (5.2)$$

for subband 3, for $E_3 < E < E_4$

$$\frac{\mathrm{d}^2 n_3(E)}{\mathrm{d}E^2} - \frac{1}{D_{\mathrm{e}3}}\left(\frac{1}{\tau_3} + \frac{N_\mathrm{LO}}{\tau_\mathrm{LO}}\right) n_3(E) + \left(\frac{1 + N_\mathrm{LO}}{D_{\mathrm{e}3}\tau_\mathrm{LO}}\right) n_3(E + E_\mathrm{LO}) = 0, \quad (5.3)$$

for $E_4 < E < E_3 + E_\mathrm{LO}$ and $E_4 + E_\mathrm{LO} < E$

$$\frac{n_4(E)}{D_{\mathrm{e}3}\tau_\mathrm{ela}} + \frac{\mathrm{d}^2 n_3(E)}{\mathrm{d}E^2} - \frac{1}{D_{\mathrm{e}3}}\left(\frac{1}{\tau_\mathrm{ela}} + \frac{1}{\tau_3}\right) n_3(E) = 0, \quad (5.4)$$

and for $E_3 + E_\mathrm{LO} < E < E_4 + E_\mathrm{LO}$

$$\frac{n_4(E)}{D_{\mathrm{e}3}\tau_\mathrm{ela}} + \frac{\mathrm{d}^2 n_3(E)}{\mathrm{d}E^2} - \frac{1}{D_{\mathrm{e}3}}\left(\frac{1}{\tau_\mathrm{ela}} + \frac{1}{\tau_3} + \frac{1 + N_\mathrm{LO}}{\tau_\mathrm{LO}}\right) n_3(E) + \left(\frac{N_\mathrm{LO}}{D_{\mathrm{e}3}\tau_\mathrm{LO}}\right) n_3(E - E_\mathrm{LO}) = 0, \quad (5.5)$$

where g_0 is the generation rate, N_phonon is the LO phonon population, $D_{\mathrm{e}4}$ and $D_{\mathrm{e}3}$ are the energy-diffusion coefficients for subbands 4 and 3, τ_3 and τ_4 are the total relaxation times for subbands 4 and 3, τ_LO is scattering time due to LO phonon spontaneous emissions, and τ_ela is the elastic scattering time. Here, it should be noted that the energy-diffusion model is not applicable to well-thermalized electron systems but to highly nonequilibrium electron systems as in the present case. Fig. 5.9 shows the calculated energy-resolved electron populations in the subbands of the two upper laser states. As discussed above, the electrons in the two subbands interact due to the very fast transfer of injected electrons to subband 3 by extremely short elastic scattering time ≤ 100 fs. Electron–electron scatterings tend to smear out population distributions, resulting in cooler and hotter electrons, and consequently, the hotter electrons relax down around the bottom of the subband by LO phonon emission. Fig. 5.9 depicts the cooling of the electron gas of subband 3, which is caused by the larger energy diffusion range

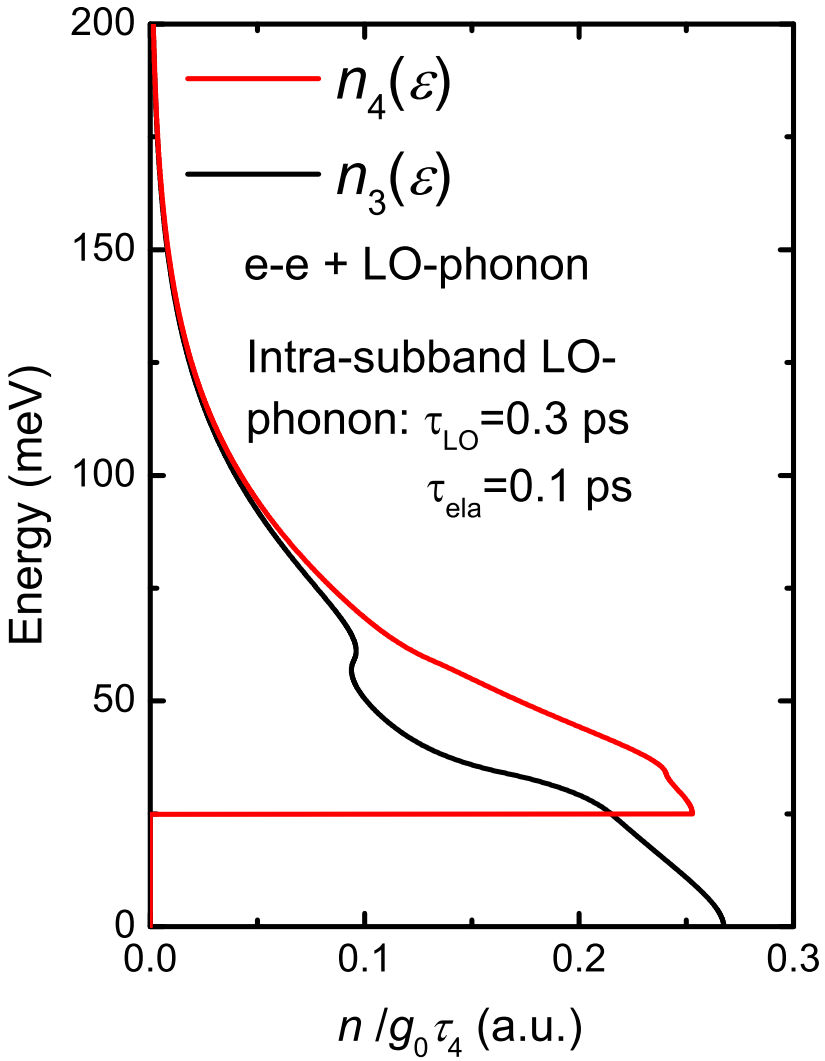

Figure 5.9: Calculated energy-resolved electron populations in the dual upper states. The calculation was carried out, based on the energy diffusion model, assuming reasonable values for parameters, $D_e = 1.16 \times 10^{14}$ (meV)^2/s, τ_{ela}=0.1 ps, τ_{LO}=0.3 ps, τ_3=1.1 ps.

$(D_e\tau_{tun})^{1/2}$ ∼16 meV and short relaxation time $\tau_{LO} \sim 0.2$ ps, calculated with the lifetime of subband 3, $\tau_3 = 1.1$ ps. As a result, the population balance between the subbands is calculated to be $N_3 \sim N_4$. This is a reason why spectrally homogeneous EL is achieved by the DAU-laser. In order to consider the electron populations of the two upper states above the threshold, we investigate the change of the electron population with changing ratio of upper-state lifetimes $\ln(\tau_3/\tau_4)$. The electron population of an upper laser state is clamped during lasing, while the electron population of the other upper state increases with increasing current. Fig. 5.10 shows the electron population of the upper laser state and the ratio of the populations with the ratio of the lifetimes $\ln(\tau_3/\tau_4)$. A small change of electron population ratio is obtained above the threshold: less than 10% increase. This indicates a spectrally almost homogeneous gain, i.e., no strong hole burning in the inhomogeneous system due to the ultrafast elastic scattering between the strongly coupled subbands. This allows us to obtain symmetric gain curves for the DAU laser.

5.5 Extremely temperature-insensitive QC laser

The high characteristic temperatures and super-linear current-light outputs of the DAU-QC lasers are substantially different from the characteristics of other broadband QC lasers [1, 14]. Such high characteristic temperatures provide great advantages for practical applications in addition to the potential of broadband tuning since practical lasers are expected to be used in a harsh environment where the temperature fluctuates. The distinctive characteristics of the DAU lasers are attributable to the optical absorption quenching which takes place in indirectly pumped QC lasers as described in Chapter 4. In the lasers, the non-resonant absorptions in the injector, $\alpha_{inj}^{(0)} = \alpha_{cinj} n_1$ where α_{cinj} is the absorption cross section in the injector, and n_1 is electron population in the ground state of injector, decrease steeply with increasing temperature, increasing the current. The steep decrease in the electron population could also be observed in the DAU-QC lasers since in this design, electrons are distributed in three states: 4, 3, and the ground state 1 in the injector. As a result, the electron population n_1 at high

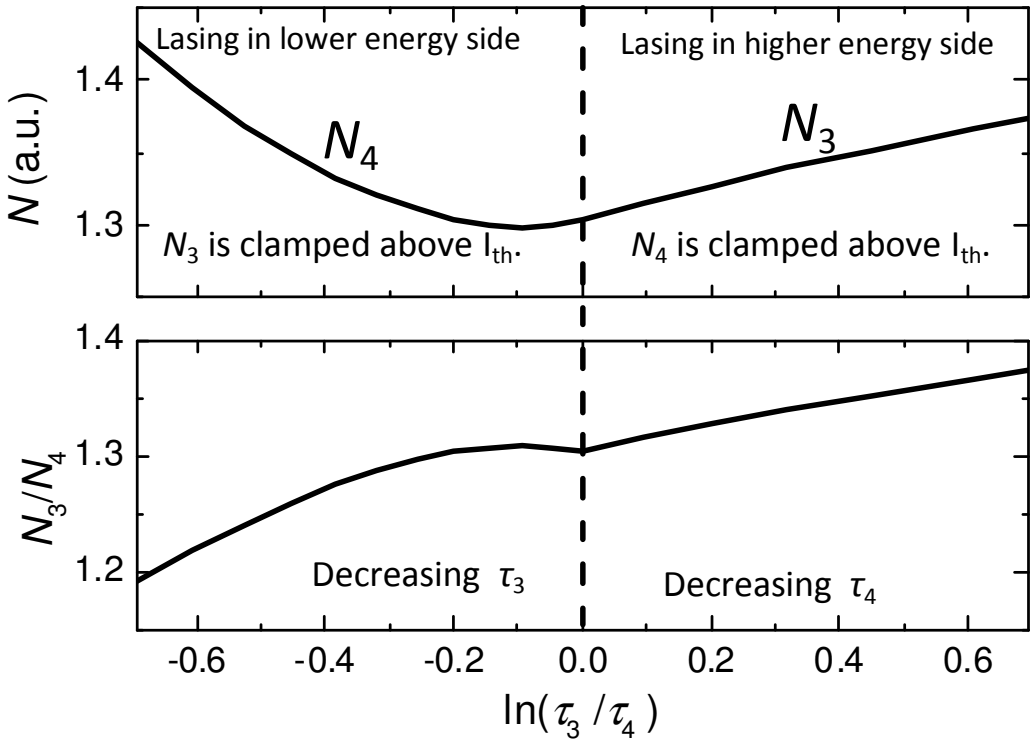

Figure 5.10: The electron population of the upper laser state and the ratio of the populations with the ratio of the lifetimes $\ln(\tau_3/\tau_4)$.

pump current is less than in the case of the conventional direct pump design. By taking advantage of such strong suppression of the electron populations in the injectors, QC lasers based on both the indirect pump scheme and the anticrossed DAU designs have demonstrated remarkably high characteristic temperatures, T_0=300–500 K. Moreover, for a λ ~8 μm DAU-QC laser, a constant slope efficiency has been obtained over a wide temperature range, 280-400 K, as discussed in Section 5.3. On the other hand, the deep well and shallow well designs incorporating various compositions in the QC structures have been reported to suppress the carrier leakage into higher parasitic states, which seriously degrades laser performances in particular for shorter wavelengths [15, 16, 17]. Obviously, the suppression of electron leakage from upper quantum states is also crucially important to improve the temperature-performance. In this section, we present striking characteristics of λ ~8.7 μm, strain-compensated QC lasers based on the anticrossed DAU design. The laser demonstrates strong super-linear current-light (I-L) output curves as well as extremely high characteristic temperatures, T_0=750 K, over 330-370 K, and a negative T_1-value in CW mode. The T_0-value is more than three times as high as that of reported CW-QC lasers. Furthermore, for a 1 mm-long device, a higher characteristic temperature, T_0=1085 K, is obtained in a pulsed operation above room temperature. In this case, the threshold current increases only 11% even with a temperature increase of 100 K.

5.5.1 Design of active region

The conduction-band diagram of injector-active-injector parts is shown in Fig. 5.11. We choose strain-compensated $In_{0.6}Ga_{0.4}As/In_{0.44}Al_{0.56}As$ layers for quantum wells to improve the confinement of the electrons of the upper laser states, despite designing a long wavelength (λ ~8.5 μm), since the characteristic temperatures T_0 and T_1 for the threshold current density and slope efficiency are easily masked by the presence of leakage current [15, 16, 17]. In fact, for the DAU laser, the stronger negative differential resistance (NDR), which implies a smaller leakage current, is clearly observed in the I-V curve at the maximum operating current at room temperature, compared to other state-of-the-art QC lasers in the mid infrared range [18, 19], despite a similarly designed energy spacing between

the upper state and higher state (E_{54} ∼60 meV). We have determined that the magnitude of the negative differential resistance (NDR) at maximum operating current in the I-V curve is sensitively changed by the energy position of the ground state in the thin quantum well of the DAU or IDP design. In present laser design, the energy separation E_{43} is designed to be comparable with that of the λ ∼8.5 μm DAU-laser, E_{43} ∼20 meV, while the energy differential $\Delta E_{\rm ul}$ between the upper level and the top of the exit barrier increases from ∼300 meV to ∼420 meV. As discussed by Botez et al. [15], the leakage current density is proportional to $\exp(-E_{54}/k_{\rm B}T_{\rm e4})$ where $T_{\rm e4}$ is the electric temperature in the upper state 4. Although the E_{54} value for the present laser is comparable to that of the previous lattice-matched DAU laser (E_{54} ∼60 meV), the electric temperature $T_{\rm e4}$ decreases with increasing conduction band offset due to increased coupling between the electronic ensemble and lattice [20, 21]. Thus, this may lead to the substantially suppressed current leakage. The relaxation times due to LO phonon emissions and elastic scatterings by interface roughness and alloy disorder are estimated: τ_{42}∼τ_{32}∼1.1 ps. The transition dipole moment for both upper laser states is also calculated: Z_{42}∼Z_{32} ∼1.7 nm. These values are also comparable to the previous laser. On the other hand, the energy separation between state 2 and the ground state 1 of the injector region is designed to be >120 meV, large enough to avoid the thermal backfilling. All of the layer structures were grown on an n type InP substrate using the MOVPE technique. The 40-period active region was used as the emitting region, and the waveguide structure is almost same as that in the previous section. After the growth, the wafer was processed into a buried hetero structure. Finally, the evaporation of the top Ti/Au contacts was followed by electroplating of a thick 10 μm Au layer on top of the ridge.

5.5.2 Device characterization

Figure 5.12(a) shows the CW current-light output and current-voltage characteristics for an 8 μm-wide, 3 mm-long, HR-coated, buried heterostructure laser mounted epi-side down on an AlN heat sink. For the current-light output characterization, the output power was measured with a calibrated thermopile detector. The CW threshold current density at 300 K was observed to be 2.8 kA/cm^2 and

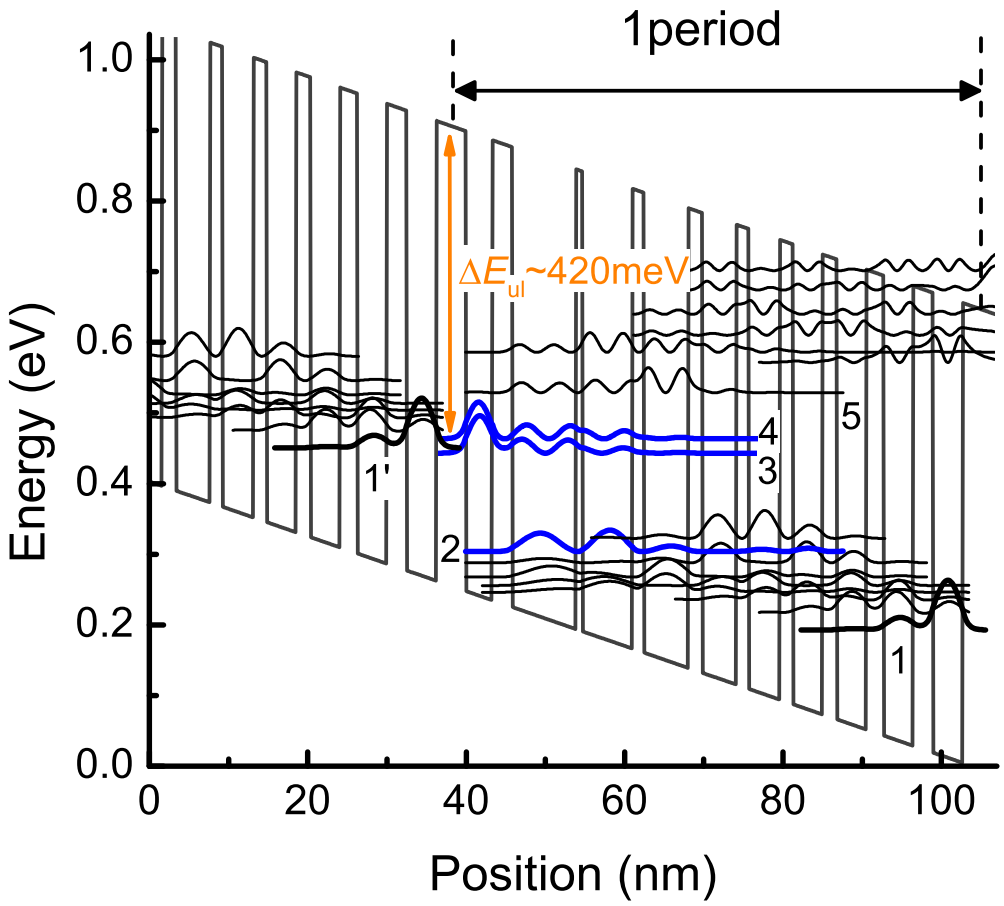

Figure 5.11: Schematic conduction band diagram and moduli squared of the relevant wavefunctions of the injector/active/injector parts in the strain-balanced DAU active region. An electric field of 41 kV/cm was applied to align the structure. The $In_{0.6}Ga_{0.4}As/In_{0.44}Al_{0.56}As$ layer sequence of one period of the active layers, in angstroms, starting from the injection barrier (toward the right side) is as follows: **35**/32/**23**/77/**7**/60/**13**/54/**16**/41/**14**/38/**15**/36/**16**/36/**20**/36/**23**/36/**26**/35 where InAlAs barrier layers are in bold, InGaAs QW layers in roman, and doped layers (Si, 5×10^{10} cm^{-2}) are underlined.

an optical output power of 170 mW with a slope efficiency of 0.8 W/A was obtained, again at 300 K. The maximum lasing temperature in the CW mode is 370 K. The subthreshold spectrum of the present laser, as shown in the inset of Fig. 5.12(a), exhibits very wide, over 250 cm^{-1}. Thus, this laser is suitable for broadband applications. The spectrum shows a single mode operation slightly above the threshold. The most notable characteristic of the laser performances is the super-linear slope efficiency as contrasted with that of all reported QC lasers which show a more or less gradual decrease with increasing current. These results imply a decrease of optical losses with increasing current, which could be qualitatively understood by the fact that the slope efficiency is represented as, in general, $\eta = \eta_i \left[\alpha_{\rm m}/(\alpha_{\rm m} + \alpha_{\rm i})\right]$, where η_i is internal efficiency, $\alpha_{\rm m}$ is the mirror losses in the front facet and $\alpha_{\rm i}$ is the total internal loss. The strong decrease of the internal loss leads to an increase in slope efficiency since the internal efficiency slightly decreases with increasing temperature due to the decrease of the injection efficiency and upper state lifetime.

The threshold current density and slope efficiency of the device as a function of temperature are shown in Fig. 5.12(b). The present laser demonstrates very striking features in terms of temperature performances; the enhanced slope efficiency with increasing temperature has an extremely high T_0-value of ∼750 K, which corresponds to the rate of temperature change, $\mathrm{d}(j_{\rm th}/j_{\rm th,300K})/\mathrm{d}T = 2 \times 10^{-3}$ 1/K. Increasing the slope efficiency, represented with negative characteristic temperatures T_1 (−330 K and −282 K for pulsed and cw operations) has never been reported for quantum cascade lasers in the literature. For pulsed operation, characteristic temperatures T_0 and T_1 are significantly improved compared to the values of the lattice-matched DAU laser case (T_0=306 K and a positive T_1 ∼10000 K). Since design parameters of both DAU lasers are basically comparable, the elevated temperature performance of the present DAU laser could be attributed to the smaller leakage current by increasing the energy differential $\Delta E_{\rm ul}$. The active region temperature rise in CW operation at 300 K is extrapolated to be ∼80 K from the threshold current density in pulsed operation. Besides, the extremely high T_0 of 750 K obtained with the CW DAU laser is outstanding, compared to T_0 ∼100 K of the room temperature CW QC laser. Further, the characteristic temperature increases from T_0 ∼428 K in the low temperature range, 280–330 K,

to T_0 ∼750 K in the high temperature range, 330-370 K as shown in Fig. 5.12(b). The CW T_0 in the lower temperature range corresponds approximately to the pulsed T_0 over the 290-400 K range. The remarkable elevation of the characteristic temperature has already been observed in IDP-QC lasers. The increased characteristic temperatures and super-linear slope efficiencies are consistent with the interpretation that the optical losses are quenched due to the decrease of the injector population n_1. Figure 5.13(a) depicts I-V-L characteristics for as cleaved device with a 1 mm-long cavity, for which the threshold current is relatively high (∼3 kA/cm^2) because of larger mirror losses. The threshold current at 300 K is found to be very close to the current at the NDR in the I-V curve and the slope efficiencies are strongly enhanced with increasing current. Despite an extremely small dynamic range close to room temperature, the maximum lasing temperature reaches above 370 K. The dependences of the threshold current density and the slope efficiency at the threshold on temperature are shown in Fig. 5.13(b). The T_0-values of the device are incredibly high: T_0=1085 K for above 340 K and T_0=525 K for 280-340 K. The T_0-value of 1085 K is the highest ever reported with QC lasers. Meanwhile the slope efficiency is also observed to dramatically increase with temperature (T_1= −146 K), compared to that of the 3 mm-long, HR coated laser. Obviously, the characteristic temperatures are enhanced when the threshold current density approaches the maximum current density. In fact, similar behavior when varying the cavity length is observed for IDP lasers (Fig. 4.7), though the T_1 for the IDP lasers decreases with temperature by the presence of leakage current, because of smaller ΔE_{ul} and E_{54}. In contrast to a typical QC laser where threshold current doubles with a temperature increase of 100 K, in the present laser, the threshold increases by only 11% even with a temperature increase of 100 K, $\mathrm{d}(j_{\mathrm{th}}/j_{\mathrm{th,300K}})/\mathrm{d}T$ =1.1×10^{-3} 1/K.

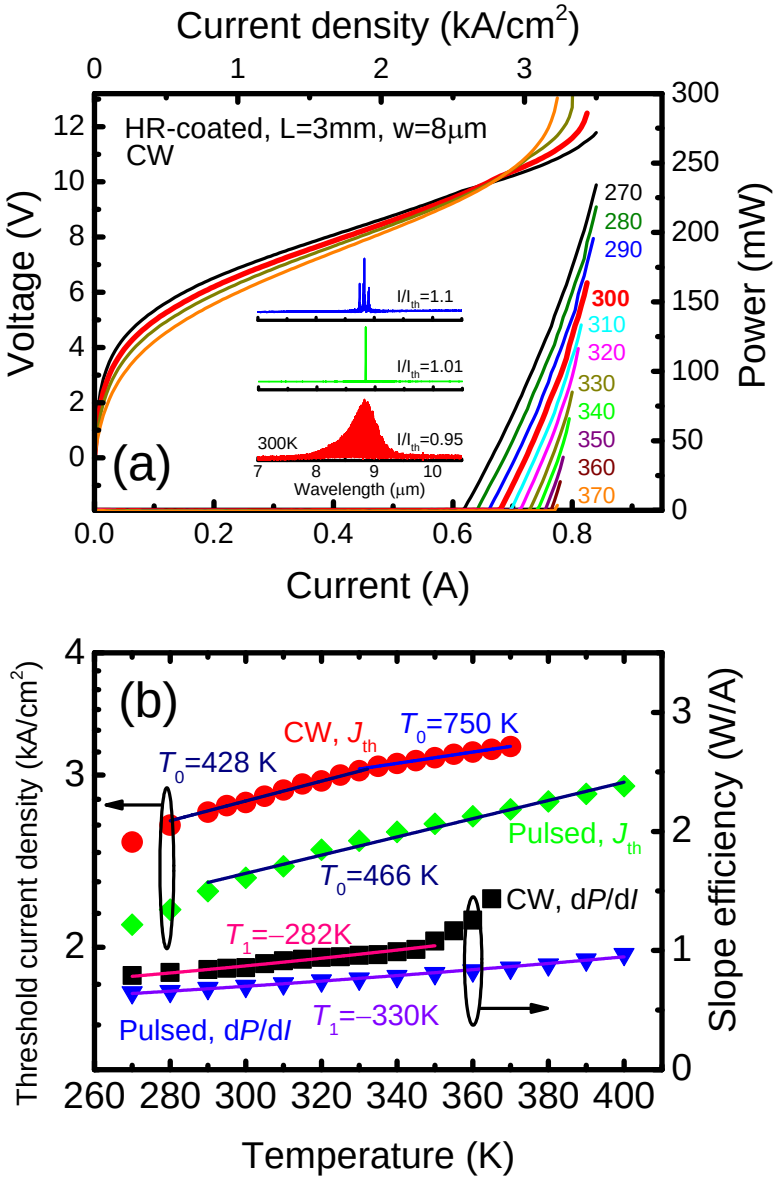

Figure 5.12: (a) CW current-light output characteristics of the 8 μm-wide, 3.0 mm-long, HR-coated, buried heterostructure laser with a thick gold film at different heat sink temperatures. The voltage-current characteristics are also shown. The inset shows the spectra in both subthreshold and above threshold operations of the strain balanced DAU laser at 300 K. (b) Temperature-dependent threshold current densities and slope efficiencies for pulsed and CW operations for the 8 μm-wide, 3 mm-long, epi-side down bonded laser. Solid curves are exponential fits with $J_{\rm th}$=J_0exp(T/T_0) and $\eta = \eta_0$exp($-T/T_1$) for the threshold current density and slope efficiency respectively.

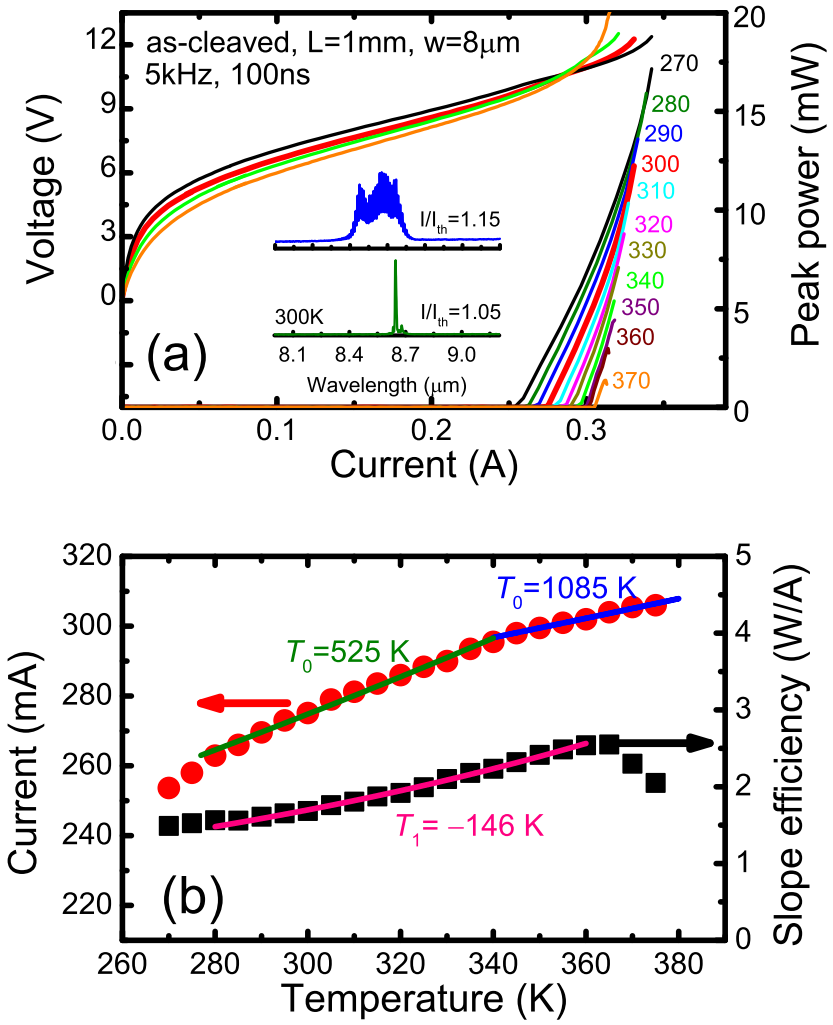

Figure 5.13: (a) Pulsed current-light output characteristics of the 8 μm-wide and 1.0 mm-long, as cleaved, buried heterostructure laser at different heat sink temperatures. The voltage-current characteristics are also shown. The inset shows the laser spectra at various currents at 300 K. (b)Threshold current density and slope efficiency at threshold as a function of heat sink temperature in pulsed operation.

5.5.3 Calculation and discussion

In order to consider the super-linear behavior in the DAU laser, we analyze the electron dynamics using the rate equation model. Assuming the injection efficiency is unity, the rate equation is,

$$n_4 = n_3, \tag{5.6}$$

$$\frac{\mathrm{d}n_3}{\mathrm{d}t} = j/e - \frac{n_3}{\tau_{\mathrm{up}}} - \frac{\beta}{\tau_{\mathrm{r}}}(n_3 - n_2)N_{\mathrm{photon}}, \tag{5.7}$$

$$\frac{\mathrm{d}n_2}{\mathrm{d}t} = -\frac{n_2}{\tau_2} + \frac{n_3}{\tau_{\mathrm{up}}} + \frac{\beta}{\tau_{\mathrm{r}}}(n_3 - n_2)N_{\mathrm{photon}}, \tag{5.8}$$

$$\frac{\mathrm{d}n_{\mathrm{mb}}}{\mathrm{d}t} = \frac{n_2}{\tau_2} - \frac{n_{\mathrm{mb}}}{\tau_{\mathrm{mb}}}, \tag{5.9}$$

where $n_1, n_2, n_3, n_4, n_{\mathrm{mb}}$ are the injector ground state, state 2, state 3, state 4, and the miniband electron density, respectively, N_{photon} is the photon density, β is the spontaneous emission factor, n_{inj} is the doping density, τ_{r} is the spontaneous emission lifetime, τ_{up} is the nonradiative lifetime of the upper laser state, τ_2 is the nonradiative lifetime of the lower laser state, τ_{mb} is the miniband transport time, and j is the tunneling current density. By putting $N_{\mathrm{photon}} \sim 0$ in Eqs. (5.7, 5.8) and by using the loss gain balance relation, $G_{\mathrm{c}}(n_3 - n_2) = \alpha_{\mathrm{m}} + \alpha_{\mathrm{w}} + A_{\mathrm{c}}n_1$, the threshold current density can be written

$$j_{\mathrm{th}} = \frac{e(\alpha_{\mathrm{m}} + \alpha_{\mathrm{w}} + A_{\mathrm{c}}n_{\mathrm{inj}})}{\tau_{\mathrm{up}}G_{\mathrm{c}}/n_{\mathrm{sp}} + A_{\mathrm{c}}[2\tau_{\mathrm{up}} + (1 + \tau_{\mathrm{mb}}/\tau_2)\tau_2]}, \tag{5.10}$$

where the population-inversion parameter n_{sp} and the gain coefficient are given by $n_{\mathrm{sp}} = 1/(1 - \tau_2/\tau_{\mathrm{up}})$ and $G_{\mathrm{c}} = (M\beta/\tau_{\mathrm{r}})[S/(c_0/n_{\mathrm{AR}})]$, and where A_{c} is the absorption coefficient, $M(=40)$ is the number of stages in the QC laser, S is the cross sectional area of the laser, n_{AR} is the refractive index when c_0 is the speed of light, α_{m} is the mirror loss, and α_{c} is the passive waveguide loss. The rate equations with the help of the Einstein relationship lead to the photon population

N_{photon} as a function of the current density j_0:

$$N_{\text{photon}} = \frac{(n/c_0)M\left(\frac{j_0 - j_{\text{th}}}{e}\right)\left[1 + \frac{A_{\text{c}}(1+\tau_{\text{mb}}/\tau_2) - G_{\text{c}}}{2A_c + G_{\text{c}}}\left(\frac{\tau_2}{\tau_{\text{up}}}\right)\right]}{\alpha_{\text{m}} + \alpha_0 + A_{\text{c}}\left[n_{1\text{th}} - \frac{3G_{\text{c}}\tau_2(1+\tau_{\text{mb}}/3\tau_2)}{2A_c + G_{\text{c}}} \times \frac{j_0 - j_{\text{th}}}{e}\right]}. \quad (5.11)$$

Due to particle conservation, $n_{\text{inj}} = n_1 + n_{\text{mb}} + n_2 + n_3 + n_4$, the electron populations for below the threshold can be expressed as

$$\begin{aligned} n_3 &= (j/e)\tau_{\text{up}}, \\ n_2 &= (j/e)\tau_2, \\ n_{\text{mb}} &= (j/e)\tau_{\text{mb}}, \\ n_1 &= n_{\text{inj}} - \left[2\tau_{\text{up}} + \tau_2\left(1 + \frac{\tau_{\text{mb}}}{\tau_2}\right)\right] j/e. \end{aligned} \quad (5.12)$$

For above threshold, the electron populations are

$$\begin{aligned} n_3 &= n_{3\text{th}} + \frac{(-\Gamma/2)(1+\tau_{\text{mb}}/\tau_2) + M\beta/2\tau_{\text{r}}}{\Gamma + M\beta/2\tau_{\text{r}}}\left(\frac{j_0 - j_{\text{th}}}{e}\right)\tau_2, \\ n_2 &= (j/e)\tau_2, \\ n_{\text{mb}} &= (j/e)\tau_{\text{mb}}, \\ n_1 &= n_{1\text{th}} - \frac{3}{2}\frac{(M\beta/\tau_{\text{r}})(1+\tau_{\text{mb}}/3\tau_2)}{\Gamma + M\beta/2\tau_{\text{r}}}\left(\frac{j_0 - j_{\text{th}}}{e}\right)\tau_2, \end{aligned} \quad (5.13)$$

where the loss term is given by, $\Gamma = (A_{\text{c}}/S)(c_0/n_{\text{AR}})$. The normalized electron populations computed with Eqs. (5.12) and (5.13) are shown in Fig. 5.14. In the present laser, the two upper level populations $n_4 + n_3$ can be higher than the ground state population n_1 near the maximum current. The ground state population n_1 decreases steeply with increasing current. In addition, surprisingly, the required population inversion $n_3 - n_2$ above threshold decreases with increasing current. This is due to the suppression of the injector population n_1 and in turn, there is a stronger quenching of the optical absorption in the injector.

From Eq. (5.11), the terms of the denominator except for the mirror loss represent the internal losses which depend on the current. Thus, the laser with a smaller mirror loss could have a stronger super-linear behavior if the strong absorption quenching in the injector takes place as expected. We measured two

devices with as cleaved (CL-CL laser) and high reflection coated for both facets (HR-HR laser). The assumed mirror losses are 4.2 cm^{-1} for the CL-CL laser and 0.1 cm^{-1} for the HR-HR laser. Fig. 5.15 depicts the I-L curves of both devices. The dashed curves represent the theoretical curves calculated using Eqs. (5.10) and (5.11). Excellent agreement between the experimental curve and the model curve exists for both lasers. Obviously, the I-L curve of the HR-HR laser exhibits a stronger super-linear behavior.

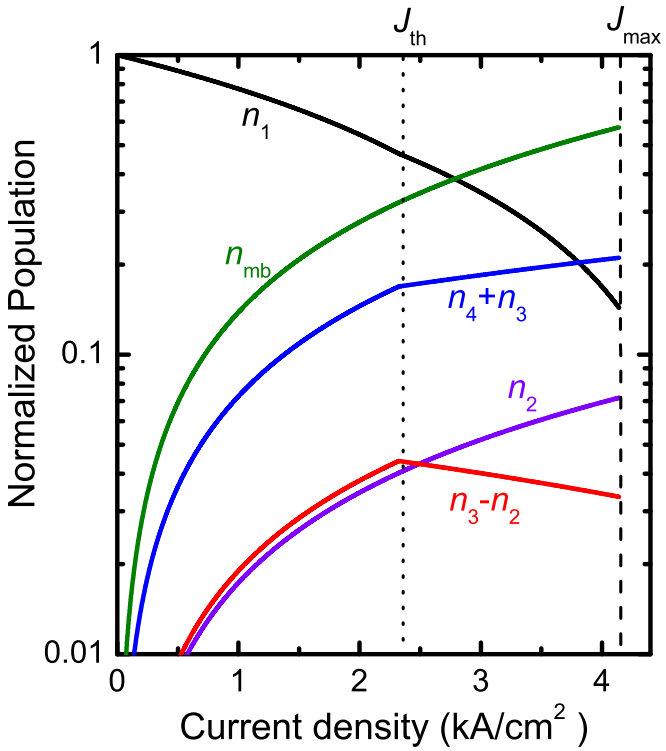

Figure 5.14: The normalized electron populations in the strain-balanced DAU-laser described in Fig. 5.11, computed with Eqs. (5.12) and (5.13), by using the corresponding parameters: n_{sp}=1.83, $\tau_3 = \tau_4$=1.1 ps, τ_2=0.3 ps, τ_r=22 ps, τ_{up}=0.6 ps, τ_{mb}=2 ps, $n_{inj} = 9 \times 10^{10}$ cm^{-2}, $A_c = 1.33 \times 10^{-10}$ cm, $G_c = 4.09 \times 10^{-9}$ cm and normalized maximum current density computed with Eq. (2.61) using τ_{tunn}/τ_3=0.18.

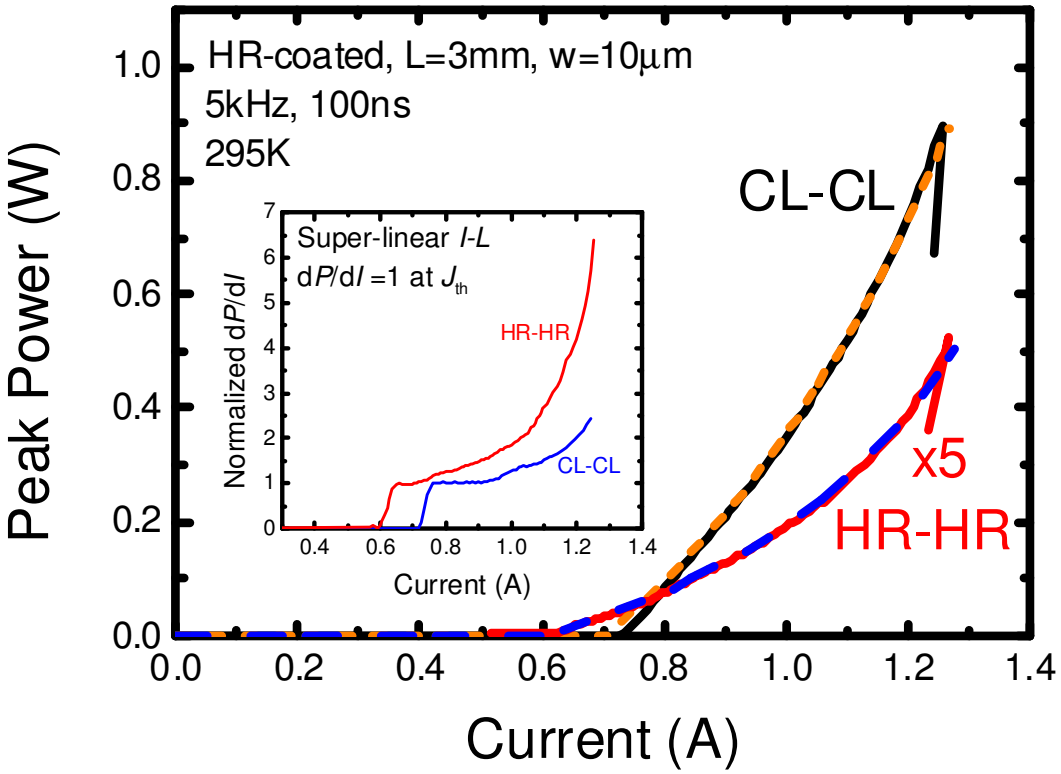

Figure 5.15: Theoretical (dashed) and experimental (solid line) I-L curves of the strain-balanced DAU lasers with as cleaved and HR-coated for both facets. The inset shows the normalized slope efficiencies of the lasers as functions of current.

5.6 Conclusion

In this chapter, QC lasers based on the anti-crossed dual-upper-state design have been studied. We have established that this design has many advantages for broad-gain operation as well as for temperature insensitive performance. The $\lambda\sim$8.4 μm lasers exhibit homogeneously wide (>330 cm^{-1}) EL spectra of which the shapes are insensitive to voltage changes. Besides, a buried hetero structured laser had a high continuous-wave output power of 152 mW together with a high constant slope efficiency of 518 mW/A at room temperature. Furthermore, the strain-compensated lasers emitting at $\lambda\sim$8.7 μm possessed conspicuous temperature performances. The laser characterized by super-linear current–light output curves exhibited an extremely high characteristic temperature for the threshold current density, above 330 K ($T_0\sim$750 K). On the other hand, the slope efficiency grows with increasing temperature (a negative value of T_1). Increasing the slope efficiencies has never before been reported for quantum cascade lasers in the literature. In addition, for the pulsed operation of a short 1 mm length laser, the T_0-value reaches a value of 1085 K above 340 K. This is the highest value ever reported for QC lasers. Room temperature T_0-values of high performance QC lasers are shown in Fig. 5.16. Obviously, T_0-values of DAU and IDP lasers are higher than those of conventional QC lasers. The striking performance of these lasers is caused by the effect of both the electron dynamics in the injector and the suppression of the leakage current due to the adoption of strain-compensated quantum wells. The anticrossed dual upper-state design offers great advantages for practical applications as well as broadband tuning of an external cavity QC laser.

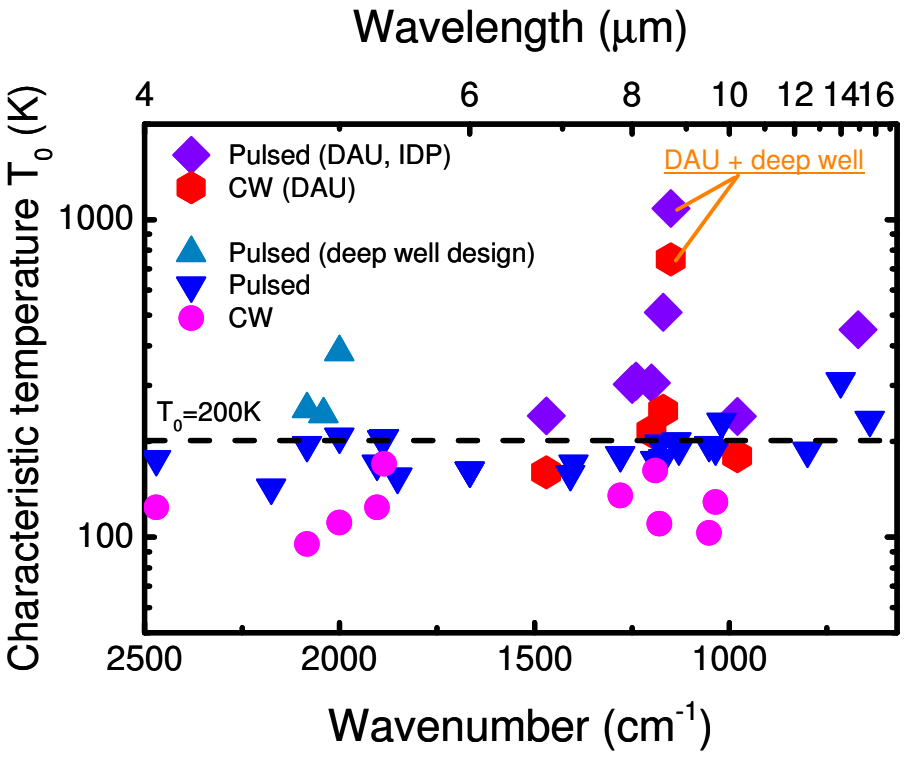

Figure 5.16: T_0-values of mid-infrared QC lasers as a function of wavenumber.

References

[1] Y. Yao, W. O. Charles, T. Tsai, J. Chen, G. Wysocki, and C. F. Gmachl, "Broadband quantum cascade laser gain medium based on a" continuum-to-bound "active region design," Appl. Phys. Lett. **96**, 211106 (2010).

[2] J. Faist, F. Capasso, C. Sirtori, D. Sivco, J. N. Baillargeon, A. Hutchinson, S. Chu, and A. Cho, "High power mid-infrared ($\lambda \sim 5$ μm) quantum cascade lasers operating above room temperature," Appl. Phys. Lett. **68**, 3680 (1996).

[3] T. Kubis, C. Yeh, P. Vogl, A. Benz, G. Fasching, and C. Deutsch, "Theory of nonequilibrium quantum transport and energy dissipation in terahertz quantum cascade lasers," Phys. Rev. B **79**, 195323 (2009).

[4] M. Yamanishi, K. Fujita, and T. Edamura, "Key concept of the mid-infrared dual-upper-states Quantum cascade laser," SPIE Photonics West **8277**, 28 (2012).

[5] M. Geiser, C. Pflugl, A. Belyanin, Q. J. Wang, N. Yu, T. Edamura, M. Yamanishi, H. Kan, M. Fischer, A. Wittmann, J. Faist, and F. Capasso, "Gain competition in dual wavelength quantum cascade lasers," Opt. Express **18**, 9900 (2010).

[6] A. Wittmann, Y. Bonetti, J. Faist, E. Gini, and M. Giovannini, "Intersubband linewidths in quantum cascade laser designs," Appl. Phys. Lett. **93**, 141103 (2008).

[7] The energy-diffusion model has been recently proposed by M. Yamanishi, unpublished note (2012).

[8] P. Harrison and R. W. Kelsall, "The relative importance of electron–electron and electron–phonon scattering in terahertz quantum cascade lasers," Solid-State Electron. **42**, 1449 (1998).

[9] A. Vasanelli, A. Leuliet, C. Sirtori, A. Wade, G. Fedorov, D. Smirnov, G. Bastard, B. Vinter, M. Giovannini, and J. Faist, "Role of elastic scattering mechanism in GaInAs/AlInAs quantum cascade lasers," Appl. Phys. Lett. **89**, 172120 (2006).

[10] M. Yamada and Y. Suematsu, "Analysis of gain suppression in undoped injection lasers," J. Appl. Phys. **52**, 2653 (1981).

[11] M. Yamanishi and Y. Lee, "Phase dampings of optical dipole moments and gain spectra in semiconductor lasers," IEEE J. Quantum Electron. **23**, 367 (1987).

[12] M. Yamanishi, T. Edamura, K. Fujita, N. Akikusa, and H. Kan, "Theory of the intrinsic linewidth of quantum-cascade lasers: Hidden reason for the narrow linewidth and line-broadening by thermal photons," IEEE J. Quantum Electron. **46**, 12 (2008).

[13] C. Y. Wang, L. Diehl, A. Gordon, C. Jirauschek, F. X. Kartner, A. Belyanin, D. Bour, S. Corzine, Hofler, M. Troccoli, J. Faist, and F. Capasso, "Coherent instabilities in a semiconductor laser with fast gain recovery," Phys. Rev. A **75**, 031802 (2007).

[14] A. Wittmann, A. Hugi, E. Gini, N. Hoyler, and J. Faist, "Heterogeneous High-Performance Quantum-Cascade Laser Sources for Broad-Band Tuning," IEEE J. Quantum Electron. **44**, 1083 (2008).

[15] J. C. Shin, M. D'Souza, Z. Liu, J. Kirch, L. J. Mawst, D. Botez, I. Vurgaftman, and J. R. Meyer, "Highly temperature insensitive, deep-well 4.8 μm emitting quantum cascade semiconductor lasers," Appl. Phys. Lett. **94**, 201103 (2009).

[16] D. Botez, S. Kumar, J. C. Shin, L. J. Mawst, I. Vurgaftman, and J. R. Meyer, "Temperature dependence of the key electro-optical characteristics for midinfrared emitting quantum cascade lasers," Appl. Phys. Lett. **97** 071101 (2010).

[17] Y. Bai, N. Bandyopadhyay, S. Tsao, E. Selcuk, S. Slivken, and M. Razeghi, "Highly temperature insensitive quantum cascade lasers," Appl. Phys. Lett. **97**, 251104 (2010).

[18] A. Bismuto, R. Terazzi, M. Beck, and J. Faist, "Electrically tunable, high performance quantum cascade laser," Appl. Phys. Lett. **96**, 141105 (2010).

[19] K. Fujita, S. Furuta, A. Sugiyama, T. Ochiai, T. Edamura, N. Akikusa, M. Yamanishi, and H. Kan,"High-Performance $\lambda\sim$8.6 μm Quantum Cascade Lasers with Single Phonon-Continuum Depopulation Structures," IEEE J. Quantum Electron. **46**, 683 (2010).

[20] V. Spagnolo, G. Scamarcio, W. Schrenk, and G. Strasser, "Influence of the band-offset on the electronic temperature of GaAs Al(Ga)As superlattice quantum cascade lasers," Semicond. Sci. Technol. **19**, S11 (2004).

[21] M. S. Vitiello, T. Gresch, A. Lops, V. Spagnolo, G. Scamarcio, N. Hoyler, M. Giovannini, and J. Faist, "Influence of InAs, AlAs δ layers on the optical, electronic, and thermal characteristics of strain-compensated GaInAs/AlInAs quantum-cascade lasers," Appl. Phys. Lett. **91**, 161111 (2007).

Chapter 6

Broadband quantum cascade lasers

6.1 Introduction

In Chapter 5, we demonstrated that the anti-crossed DAU designs lead broad symmetric EL spectra as well as excellent laser performances. Obviously the design would provide tremendous potential for the realization of broadband mid-infrared laser sources. In this chapter, we develop the potential of the anti-crossed DAU design and demonstrate an extremely broad EL spectrum ($\Delta\lambda/\lambda_0 \sim 0.4$) with its weak dependence on voltage and high laser performances. First we propose a dual-upper-state to multiple-lower-state (DAU/MS) transition design. Although the DAU active region described in Chapter 2 is based on dual-upper laser states to single-lower-state transition (DAU/SS), in principle, a dual-upper-state to multiple-lower-state (DAU/MS) transition design is also possible for the method to generate a broader gain spectrum [1] as demonstrated in bound-to-continuum design. Then, we present QC laser based on the DAU/MS transition to achieve broader gain spectra and demonstrate an extremely broad EL spectrum ($\Delta\lambda/\lambda_0 \sim 0.4$) with its weak dependence on voltage and high laser performances. Finally, high performance operation of the 6.8 μm QC laser based on the DAU/MS design will be presented.

6.2 Design and electroluminescence

External cavity systems [2] including QC lasers are the most promising configuration for broadband wavelength tuning. Recently, QC lasers with multiple stacks of active regions [3, 4] have been developed to expand the tuning wavelength range of external cavity QC lasers. However, in QC lasers of a number of stacks with different resonant wavelengths, a serious mode competition [5] inhibiting stable single mode operation may take place unless gain curves of different cascade stages overlap sufficiently. In this view, an inherently broad and homogeneous gain profile of the laser medium with translational symmetry is preferable for single mode operation in the external cavity application of QC lasers. At this moment, the most promising active-region-design for broad-gain is bound-to-continuum design which leads to high laser performance as well as broad EL spectrum [6]. However, in BTC transition, the EL spectrum exhibits asymmetric shape and the EL linewidth decreases steeply with increasing voltage. On the other hand, as an alternative approach, transitions from continuum states may also produce possibly broad-gain. However, the wide energy width of an upper miniband consisting of many upper states raise problems, such as difficulty of selective injection for each state, leakage current to higher spurious states and inhomogeneous broadening of spectra. In fact, $\lambda\sim8$ μm QC lasers with transitions from continuum states that are formed by complicate mixing of many states originated from active parts and injector [7], have exhibited a relatively high threshold current density with a low T_0-value and strong voltage-dependence of EL linewidth. Although much wider EL linewidth of $\lambda\sim4.8$ μm QC lasers has been reported recently [8], the EL linewidth from QC lasers without multiple stacks of active regions is limited to $\Delta\lambda/\lambda_0\sim0.2$. On the other hand, dual-upper-state to single-lower-state transition (DAU/SS), discussed in the previous chapter, consists of the same type of coupled (anti-crossed) two upper laser states in all stacks, in which shapes of wavefunctions and energy separations can be well-optimized for desired electron populations as well as nearly equal transition strength from both the upper-states. In addition, the two upper states are energetically separated from higher parasitic states for selective injection into the higher upper state. These carefully-designed structural features of the DAU/SS laser, unlike "Continuum-to-bound"

and "Continuum-to-Continuum" active region designs [7, 8], give rise to very distinctive device-performances: a weak voltage-dependence of EL linewidth as well as a broad symmetric EL curve, a very high T_0-value and super-linear behavior in I-L. Here, we describe a broad-gain QC laser design based on the dual-upper-state to multiple-lower-state transition (DAU/MS) design. The new design enables us to demonstrate an extremely broad EL spectrum ($\Delta\lambda/\lambda_0$ $\sim$0.4) with its weak dependence on voltage and temperature-insensitive laser performances (T_0 $\sim$510K).

6.2.1 Design of active region

The conduction-band diagram of injector-active-injector parts is shown in Fig. 6.1. The anticrossed two upper states in the same space are characterized by the wavefunctions labeled numbers 4 and 3, in which shapes of wavefunctions and energy separations can be well-optimized for desired electron populations as well as nearly equal transition strength from both the upper-states. In the DAU design, after turn-on, electrons are injected into the higher upper state, state 4, via resonant tunneling from ground state, state $1'$. In fact, we have, apparently, experienced that the energy alignment between state $1'$ and state 4 (not state 3) at the turn-on voltage results in successfully broad gain spectra. In this situation, electrons are quickly distributed in the two-upper-laser states by LO phonon scatterings and/or by elastic scatterings. The lower laser states consist of multiple states (miniband: 2mb), in which wavefunctions extend over the whole active-injector parts. Thus, in this design, the transitions take place from states 4 and 3 to the miniband 2mb and such many transition channels lead to a broad-gain spectrum. The energy separation between the upper laser state 4 and parasitic state 5 can be designed to be large, $\sim$60 meV, that preserves inherent characters of the DAU design such as high T_0-value and super linear I-L character, actually observed in the 8 μm DAU/SS-QC laser case. Figure 6.2 shows the calculated EL spectra and measured EL spectrum. Since there are ultrafast elastic scatterings in the strongly anticrossed two upper states, electrons distribute efficiently into two upper states. The EL curves are in good agreement with designed curves in which many transitions contribute to optical gain.

All the layer structures were grown on an n-type InP substrate by metal organic vapor phase epitaxy technique. The 40-period active regions with translational symmetry were used as the emitting region and sandwiched between two 0.25 μm thick n-$In_{0.53}Ga_{0.47}As$ layers (Si, 5×10^{16} cm^{-3}). The upper cladding layer consists of a 3.5 μm thick n-InP (Si, 1×10^{17} cm^{-3}) followed by a 0.3 μm thick n^+-InP (Si, $\sim10^{18}$ cm^{-3}) cap layer. After the growth, the wafer was processed into ridge structure. Finally, the evaporation of the top Ti/Au contacts was followed by electroplating of a thick 5 μm Au layer on top of the ridge.

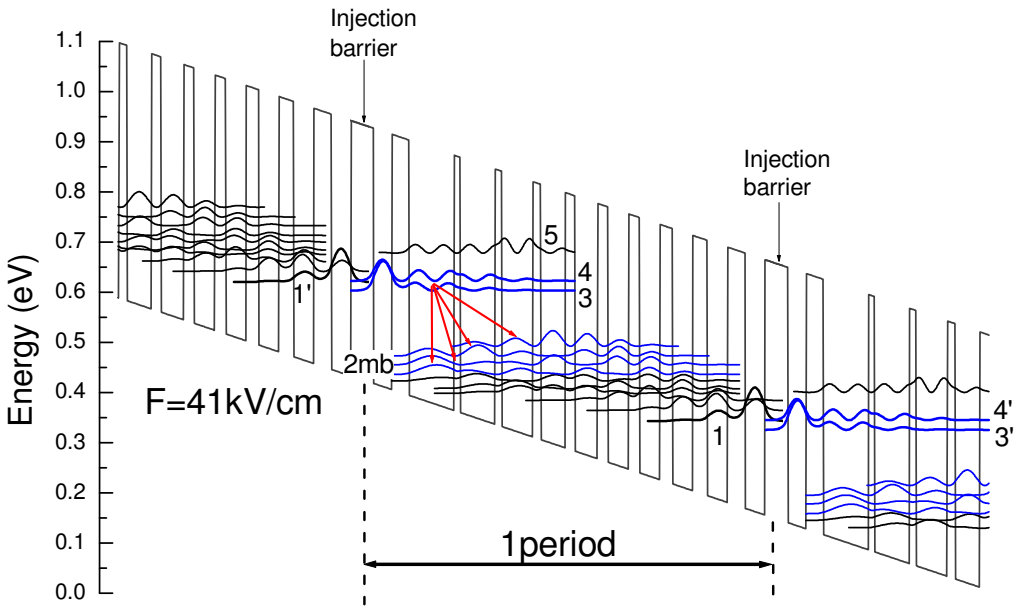

Figure 6.1: Schematic conduction band diagram and moduli squared of the relevant wavefunctions of injector/active/injector parts in a DAU/MS active region designed for operation at $\lambda\sim8.7$ μm. An electric field of 41 kV/cm was applied to align the structure. The InGaAs/InAlAs layer sequence of one period of the active layers, in angstroms, starting from the injection barrier (toward the right side) is as follows: **37**/31/**27**/75/**9**/58/**10**/52/**12**/41/**15**/38/**16**/35/**17**/34/**20**/34/**23**/34/**28**/33 where InAlAs barrier layers are in bold, InGaAs QW layers in roman, and doped layers (Si, 5×10^{10} cm^{-2}) are underlined.

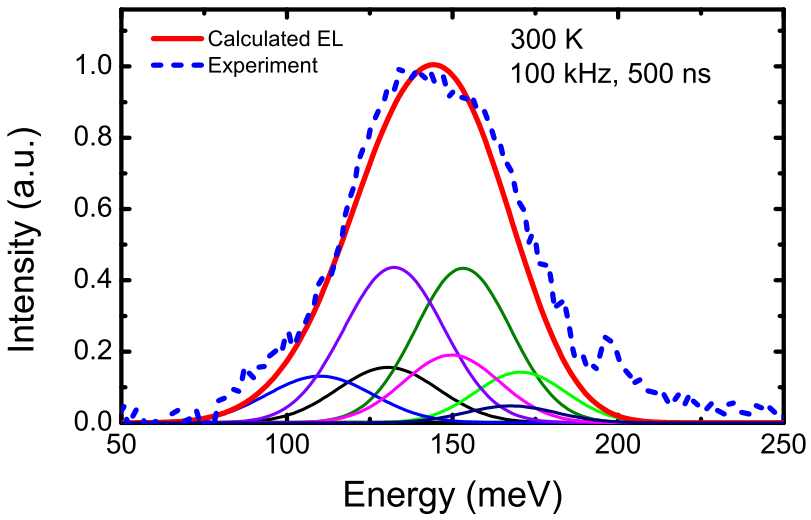

Figure 6.2: Calculated (solid line) and experimental (dashed line) EL (normalized) at an applied voltage of 7.6 V.

6.2.2 Electroluminescence

We measured EL spectra of a mesa device without stripe structure, of which results at various voltages at room temperature are shown in Fig. 6.3. The linewidth γ of the spectra taken with pulsed injection currents of 500 ns width at a repetition rate of 100 kHz was observed to be a highly wide, γ ~62 meV (~500 cm^{-1}), which is wider than the value of not only conventional QC lasers but also a 2-stack-BTC-QC laser operating at similar wavelength [3]. The ratio of EL linewidth and center wavelength is also very large, $\Delta\lambda/\lambda_0$~0.4. The wide EL curves, which are attributed to the transitions from the two-upper-state to multiple-lower-state, obviously show top wide- and flat-shapes over the whole voltage range. The EL linewidth of the present device together with of the bound-to-bound [9], DAU/SS [10], and BTC [11] devices, for a comparison, are shown in Fig. 6.4. The linewidth of the present device is revealed to be overwhelmingly wider than the value of conventional devices over the whole voltage range and its insensitivity to voltage changes since the anti-crossed wave functions of the both upper laser states are basically located in the same space.

In order to investigate temperature-dependence of the gain, in particular to

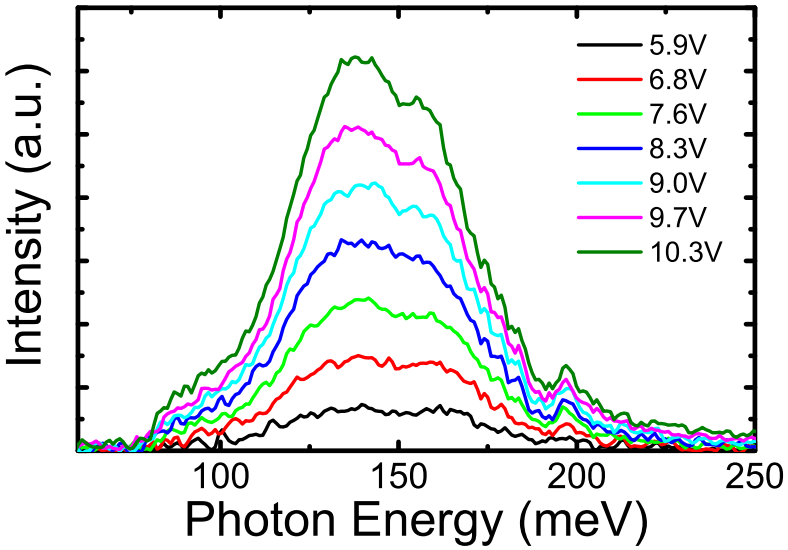

Figure 6.3: Intersubband EL spectra of the λ∼8.7 μm DAU/MS device with mesa structure for various voltages.

clarify whether gain of the present QC laser is spectrally homogeneous or inhomogeneous, we measured temperature-dependences of the EL spectra. The EL spectra at various temperatures at fixed current (500 mA) are shown in Fig. 6.5. Although at low temperature, 78–200 K, the EL curves split into two peaks because of narrow linewidth for each peaks, above room temperature the EL curves are kept to be top flat-shape and almost spectrally homogeneous. Temperature-dependences of ratios of reciprocal linewidth, $1/\gamma$, and peak intensities, which are normalized by the values at 78 K, are also shown in Fig. 6.6(a). In general, when the ratios are constant to temperature change, the EL curves are viewed to be spectrally homogeneous. In the case of the device with bound-to-bound vertical transition, the ratios range from 1.0 to 0.6 between 78 K and 300 K. Above 250 K the ratios for the bound-to-bound device are nearly constant to the temperature change within the temperature range; this suggests the EL spectra of the bound-to-bound device behave homogeneous above room temperature. Below room temperature the stronger temperature-dependences of the ratios for the bound-to-bound device is attributed to inhomogeneous components because of the fluctuation in subband energies for each cascade stage. Actually, the differ-

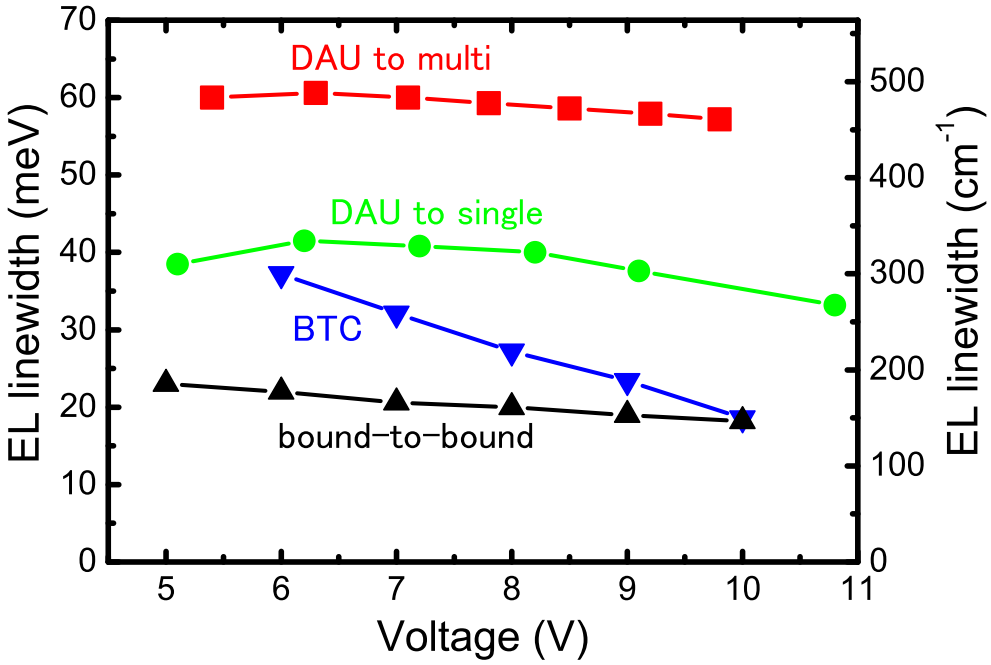

Figure 6.4: The FWHM of the spectra, for the $\lambda\sim8.7$ μm DAU/MS device as well as for the DAU/SS, the BTC, and the bound-to-bound devices, respectively, as a function of voltage.

ent temperature-dependence of EL linewidth for bound-to-bound QC lasers with the different number of cascade stages has been observed in Chapter 3. On the other hand, the ratio for the present device much steeply decreases from 1.0 to 0.4 between 78 K and 300 K, because of inhomogeneous spectral behavior at low temperature. For the higher temperature (>250 K), it shows weaker temperature-dependence and is regarded to be basically homogeneous broadening. Under such homogeneous situation, the temperature-dependence of the reciprocal linewidth represents that of gain coefficient as $g_{\mathrm{cpeak}} \sim 1/\gamma$. Figure 6.6(b) shows the reciprocal linewidth as a function of temperature. The weak temperature-dependence of the reciprocal linewidth of the DAU devices has been observed to be weak, T_{c} =1130 K for the DAU/SS device and T_{c} =2745 K for the DAU/MS device, as shown in Fig. 6.6(b), where the characteristic temperature T_{c} is defined by the relation: $1/T_{\mathrm{c}} = (1/\gamma)(\mathrm{d}\gamma\ /\mathrm{d}T)$. These high T_{c}-values of DAU devices originate from its wide EL linewidth since increase of linewidth with temperature change is basically in the same range for the every QC laser. The T_{c}-value of the DAU/MS QC laser plays a key role in the laser performance in terms of temperature stability.

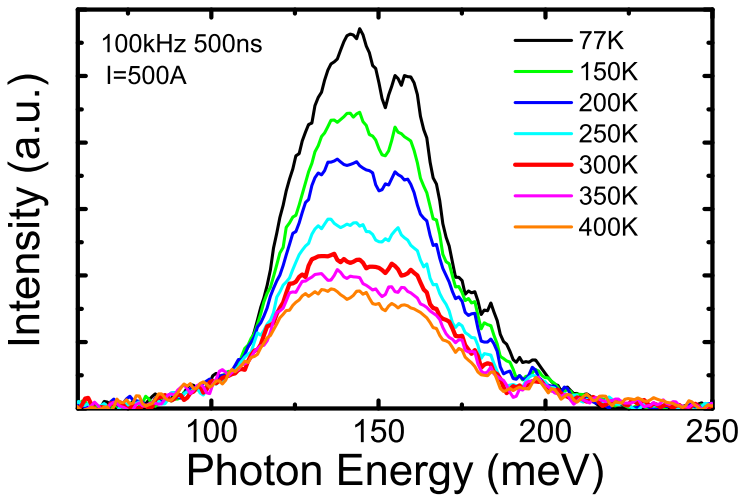

Figure 6.5: Intersubband EL spectra of the $\lambda \sim 8.7$ μm DAU/MS device for various temperatures.

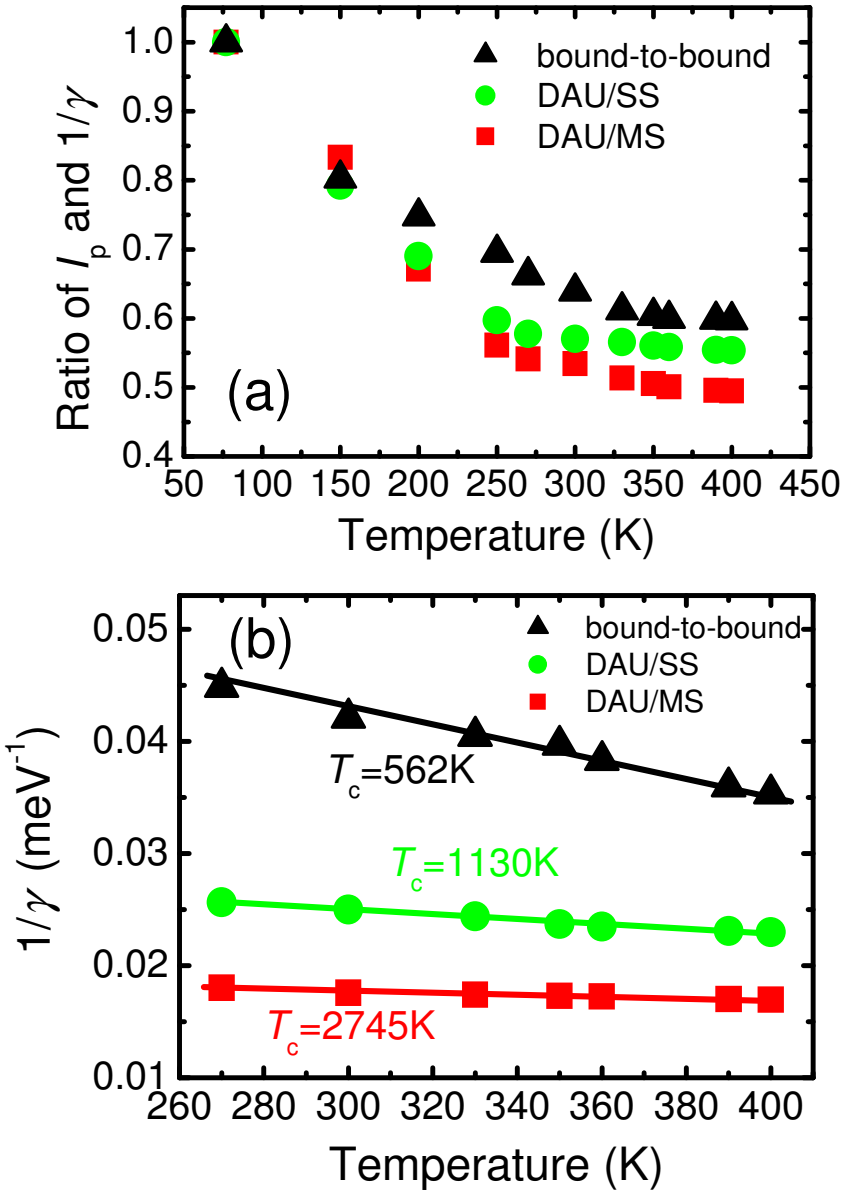

Figure 6.6: (a) The ratios of $1/\gamma$ and peak intensities of the EL spectra for the $\lambda\sim$8.7 μm DAU/MS device as well as for the DAU/SS, and the bound-to-bound devices, respectively, as a function of temperature. (b) $1/\gamma$ versus temperatures for the DAU/MS device as well as for the DAU/SS, and the bound-to-bound devices.

6.3 Laser performance

For current-light output characterization, the peak output power was measured with a calibrated thermopile detector. The pulsed I-L characteristics at different temperatures as well as the V-I characteristics for an 14 μm-wide, 4 mm-long, HR-coated device, are shown in Fig. 6.7(a). A threshold current density at 300 K was observed to be $\sim$2.6 kA/cm^2 and an optical output power of 930 mW with a slope efficiency of $\sim$1.0 W/A was obtained at 300 K in the pulsed operation: 100 kHz, 100 ns. At high temperatures (>380K), the I-L curves show super-linear behavior around maximum current, which may be ascribed to the dynamics of electron transport, similarly to DAU/SS case.

The threshold current density of the 8.7 μm DAU/MS device as a function of temperature is shown in Fig. 6.8. Below room temperature the characteristic temperature is identified to be $T_0\sim$200 K. Above room temperature the T_0-value is an astonishingly high value, $T_0\sim$510 K, which is roughly twice as high as the values of conventional QC lasers. As a consequence, although the threshold current density of the DAU/MS device at low temperature is higher than the value of conventional devices because of the broad EL linewidth, at high temperature, eventually the threshold current densities of the DAU devices are close to the values of state-of-the-art QC lasers. The high T_0-value of the DAU/MS-QC laser is mainly led by the weak temperature-dependence of the peak gain as shown in Fig. 6.6(b), though, it is also brought about by electron dynamics; the origin of the high T_0-value for the present device is very similar to quantum dot laser case[12], in which the gain cross section is also weakly temperature-dependent, as a result of the quantization of electronic density-of-states due to three dimensional confinement. As observed in the DAU/SS case, the slope efficiency at threshold is very insensitive to the temperature changes. In the spectral measurements (Fig. 6.7(b)), despite the wide EL linewidth the relatively narrow lasing spectrum has been observed, $\sim$60 cm^{-1}, at the current of $I_0/I_{\rm th}\sim$1.3 in contrast to 180 cm^{-1} of the 2-stack-BTC-QC laser [3].

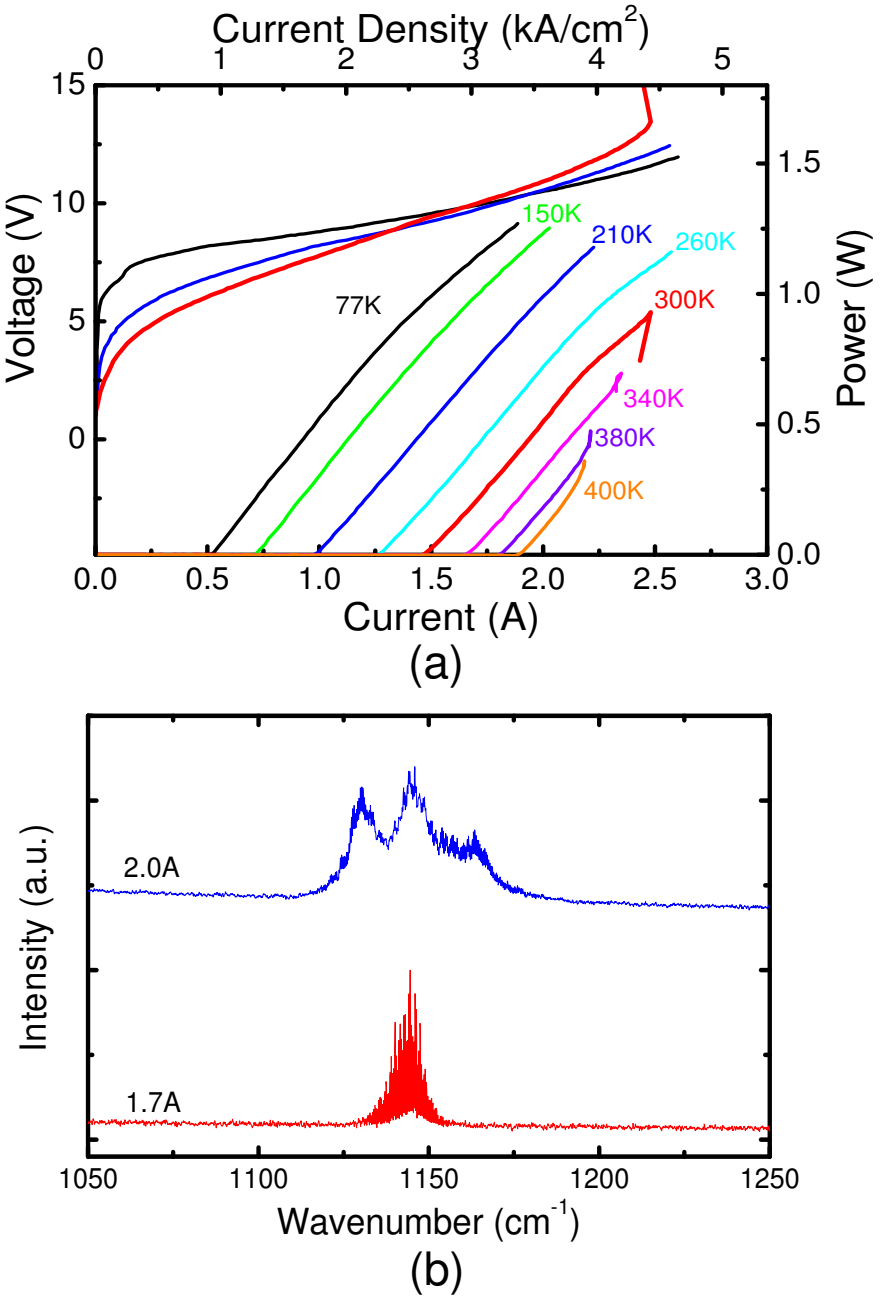

Figure 6.7: (a) Pulsed current-light output characteristics of the 14.0 μm-wide, 3.0 mm-long, HR-coated, λ~8.7 μm DAU/MS laser width ridge structure at different heat sink temperatures. The voltage-current characteristics at various temperatures are also shown. (b) The spectra of the laser at 300 K.

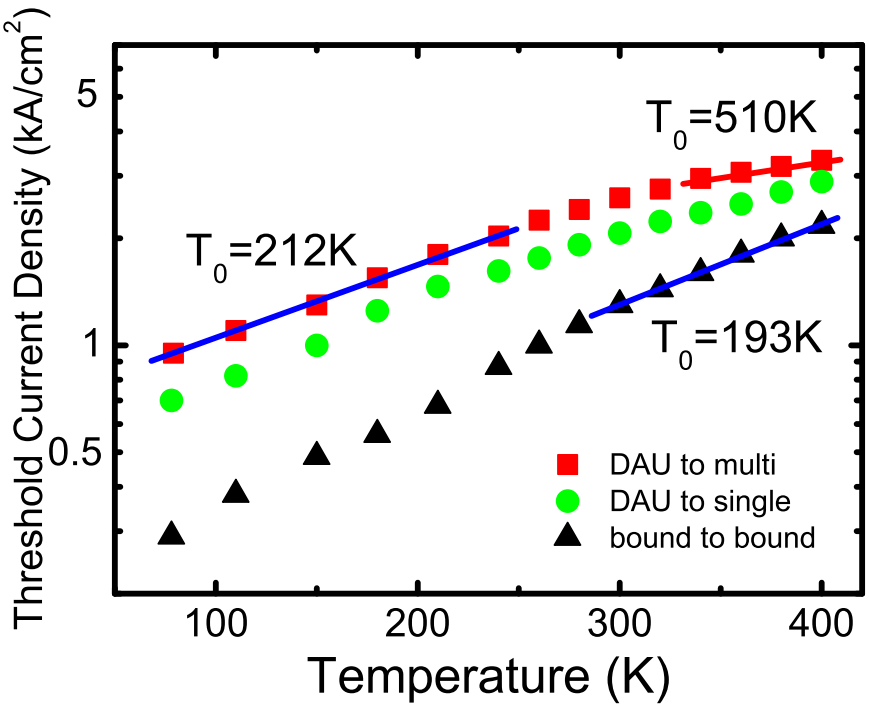

Figure 6.8: Threshold current densities as a function of heat sink temperature in pulsed operation. The solid curves represent fits by the empirical exponential functions, $J_{\mathrm{th}} = J_0 \exp(T/T_0)$.

For CW operation above room temperature, buried hetero (BH) structure lasers were processed with electroplated gold as the top contact metallization. The HR-coated, BH structured laser epi-side down mounted on an AlN sub-mount. As a result of the high T_0-value above room temperature, the present laser, despite the broad EL linewidth, has operated successfully in CW operation at room temperature. Figure 6.9 shows CW current-light curves of the device at different heat-sink temperatures. A threshold current density at 20 °C was observed to be 3.7 kA/cm^2 and a CW output power of 95 mW together with a high constant slope efficiency of ∼500 mW/A was obtained at 20 °C in CW operation. The device has operated in CW mode at higher temperatures up to 60 °C. The temperature-dependence of the CW threshold current density has been observed to be weak, T_0∼250 K, as shown in the inset of Fig. 6.9 inset, which is not only nearly twice as high as the value of the 2-stack-BTC-QC laser in CW operation [3], but also still higher than the values of conventional direct pumping QC lasers in pulsed operation, despite showing higher thermal resistance (15.2 K/W). The subthreshold spectra of the DAU/MS devices at different current are shown in Fig. 6.10. A spectral narrowing with increasing current and a wide spectral width of over 380 cm^{-1} which is a reference value for the tunable wavelength range of external cavity QC laser, have been observed. In addition, the spectral measurements reveal no sign of multiple wavelength emissions unlike QC lasers with multiple stacks of active regions [3, 4]. These results suggest that the DAU design is highly suitable for broadband tuning applications.

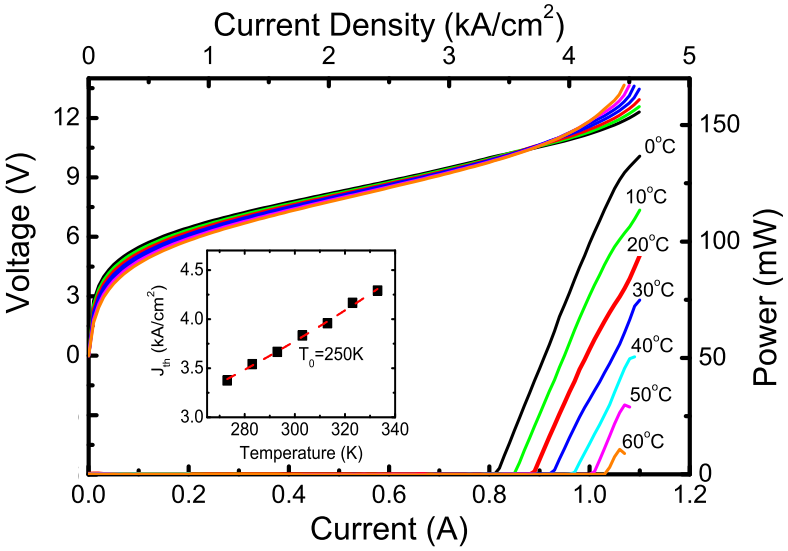

Figure 6.9: CW current-light output characteristics of the 8.0 μm-wide, 3.0 mm-long, HR-coated, $\lambda\sim$8.7 μm BH laser with a thick gold film at different heat sink temperatures. The voltage-current characteristics are also shown. The inset shows threshold current density as a function of heat sink temperature in CW operation.

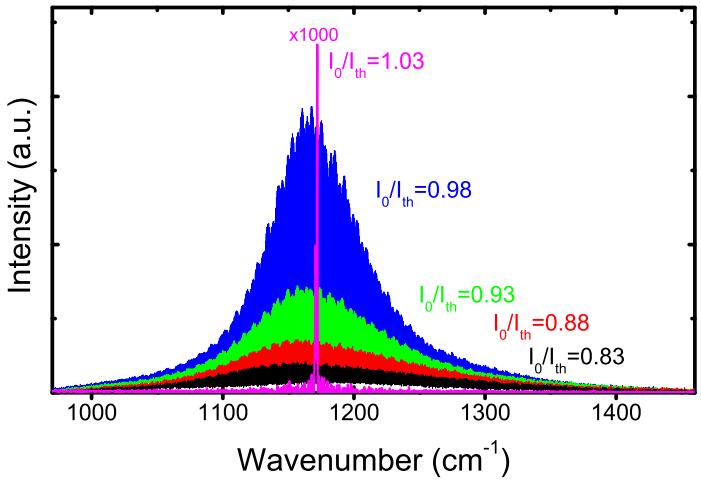

Figure 6.10: The spectra in both subthreshold and above-threshold operation of the $\lambda\sim$8.7 μm DAU/MS laser at 10 °C.

6.4 High-performance broadband QC laser

In the previous section, we reported broad-gain ($\Delta\lambda/\lambda_0 \sim 0.4$, ~ 500 cm^{-1} FWHM) and temperature insensitive ($T_0 \sim 510$ K) operations of QC lasers based on the active region with translational symmetry. However, the threshold current densities in pulsed and CW modes at room temperature still remain quite high values of 2.6 and 3.7 kA/cm^2. From a practical point of view, much lower threshold current density is preferable. In addition, the demonstration of DAU-QC lasers, so far described, are only around 8 μm. In order to assess the feasibility of the DAU-QC lasers, we need to fabricate another DAU-QC laser operating in shorter wavelength. In this section, we present high performance and broad-gain operations of QC lasers ($\lambda \sim 6.8$ μm) based on the DAU/MS design. The lasers demonstrate an extremely broad electroluminescence spectrum as well as high device performance in CW mode: a low threshold current density of ~ 1.5 kA/cm^2 and a high maximum output power of 528 mW both at 300 K. The threshold current density is significantly reduced to $\sim 40\%$ of the previous 8.7 μm DAU/MS laser; as a result, CW operation of the present lasers has been achieved up to 102 °C.

6.4.1 Design of active region

The conduction-band diagram of injector-active-injector parts consisting of strain-balanced $In_{0.6}Ga_{0.4}As/In_{0.44}Al_{0.56}As$ layers is shown in Fig. 6.11. The active region is based on the DAU/MS design in which the transitions take place from anti-crossed two upper states to multiple lower states and such many transition channels lead to a broad-gain spectrum. In DAU designs, equal oscillator strengths of the transitions from the two upper states to lower laser states are required to obtain the desirable broad EL spectrum. For this purpose, the two upper states are engineered to be strongly anti-crossed around operating bias. In order to verify the anti-crossed two upper state conditions, we have fabricated the devices based on the dual-upper-state to single-lower-state design and confirmed broad and symmetric EL spectra like the 8 μm DAU laser case. The energy separation (anticrossing gap) between two upper states is designed to be large enough $E_{43} \sim 25$ meV to obtain broader gain-width. The emission wavelength is chosen to be ~ 6.8 μm to avoid a large optical absorption. The lower laser states

consist of multiple states (miniband: 2mb) of which wavefunctions extend over the whole active-injector parts. The energy separation between the upper laser states and parasitic state 5 can be designed to be large, ∼60 meV. All the layer structures were grown on an n-type InP substrate by the MOVPE technique. The 40-period active region was used as the emitting region and the waveguide structure is almost same as the previous 8.7 μm laser. After the growth, the wafer was processed into buried hetero-structure. Finally, the evaporation of the top Ti/Au contacts was followed by electroplating of a thick 10 μm Au layer on top of the ridge.

6.4.2 Electroluminescence

EL spectra of a mesa device at various voltages at room temperature are shown in Fig. 6.12. The linewidth γ of the spectra taken with pulsed injection currents of 500 ns width at a repetition rate of 100 kHz was observed to be γ∼75 meV (∼600 cm^{-1}) at 10.6 V, corresponding to $\Delta\lambda/\lambda_0$ ∼0.4 that is comparable to the value of the 8 μm DAU-QC laser. The EL curves, which are attributed to the transitions from the two upper states to the multiple-lower-state, show extremely broad and spectrally homogeneous over whole voltage range thanks to the anticrossed wavefunctions of the both upper laser states in the same space. The linewidth of the present device is extremely wide over the whole voltage range and insensitive to voltage changes as shown inset of Fig. 6.12, since the anti-crossed wave functions of the both upper laser states are basically located in the same space.

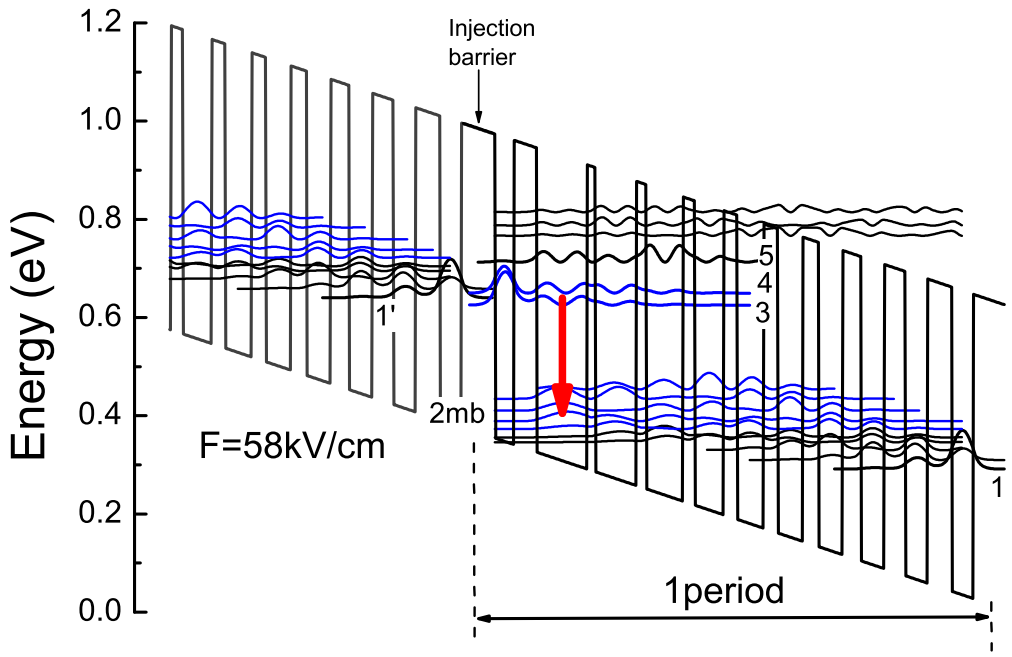

Figure 6.11: Schematic conduction band diagram and moduli squared of the relevant wavefunctions of injector/active/injector parts in the λ∼6.8 μm DAU/MS active region. An electric field of 58 kV/cm was applied to align the structure. The strain-balanced $In_{0.6}Ga_{0.4}As$/ $Al_{0.44}In_{0.56}As$ layer sequence of one period of the active layers, in angstroms, starting from the injection barrier (toward the right side) is as follows: **37**/24/**26**/60/**9**/49/**11**/44/**13**/35/**15**/32/**16**/30/**18**/29/**21**/28/**24**/27/**28**/26 where InAlAs barrier layers are in bold, InGaAs QW layers in roman, and doped layers (Si, 5×10^{10} cm^{-2}) are underlined.

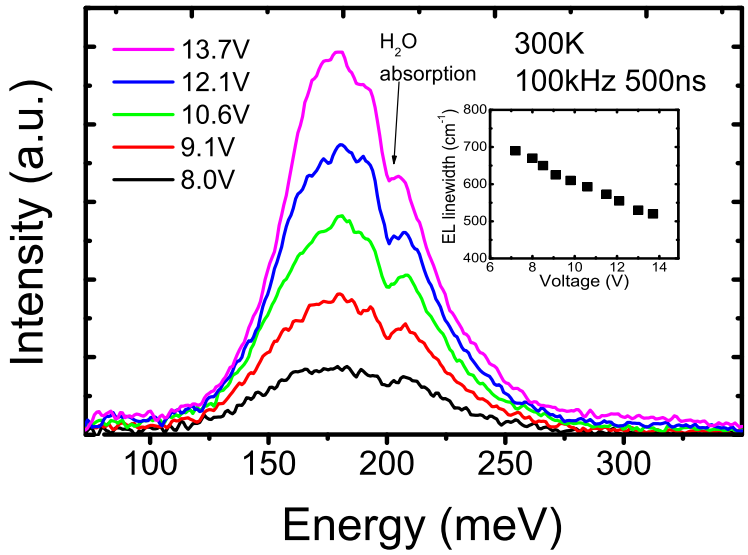

Figure 6.12: Intersubband EL spectra of the $\lambda\sim$6.8 μm DAU/MS device for various voltages at 300 K. The inset shows the FWHM of the spectra as a function of voltage.

6.4.3 Laser characterization

For laser measurements, the wafer was processed into the 12 μm-wide buried hetero-structure. The laser facets were HR coated and the lasers were bonded epi-side down on an AlN heat-sink. For current-light output characterization, the peak output power emitted from single facets of the lasers was measured with a calibrated thermopile detector. Figure 6.13 shows the pulsed I-L characteristics of a 3 mm long, buried hetero-structured laser with 40 stages at different temperatures as well as the V-I characteristic at 300 K. In spite of extremely broad EL spectra, high laser performances are demonstrated: a low threshold current of 1.2 kA/cm^2, a high output power of over 2 W and a high slope efficiency of 3.6 W/A at room temperature. The peak wall-plug efficiency in pulsed mode reaches $\sim$14% at a current of 0.97 A. At high temperature of 400 K, the output power still attains to 1.2 W with a threshold current density of 1.8 kA/cm^2 and a slope efficiency of 2.8 W/A. The threshold current density in pulsed mode is drastically decreased from 2.6 kA/cm^2 of the previous laser and is comparable to

the values in high-performance QC lasers with narrower gain. As a result of high device performance in pulsed mode, high temperature continuous wave operation has been demonstrated [13]. On the other hand, in contrast to the $\lambda\sim$8.7 μm DAU/MS QC laser showing super-linear I-L, the slope efficiencies per stage of the device varies from 3.6 to 2.8 W/A; the characteristic temperature for slope efficiencies, T_1=410 K. Although the T_1-value is very high compared to conventional QC lasers, this is different behaviour from the $\lambda\sim$8.7 μm DAU/MS QC laser. In addition, the T_0-value is relatively moderate compared to the $\lambda\sim$8.7 μm DAU/MS QC lasers. The lower values for T_0 and T_1 may be attributed to carrier leakage into higher states.

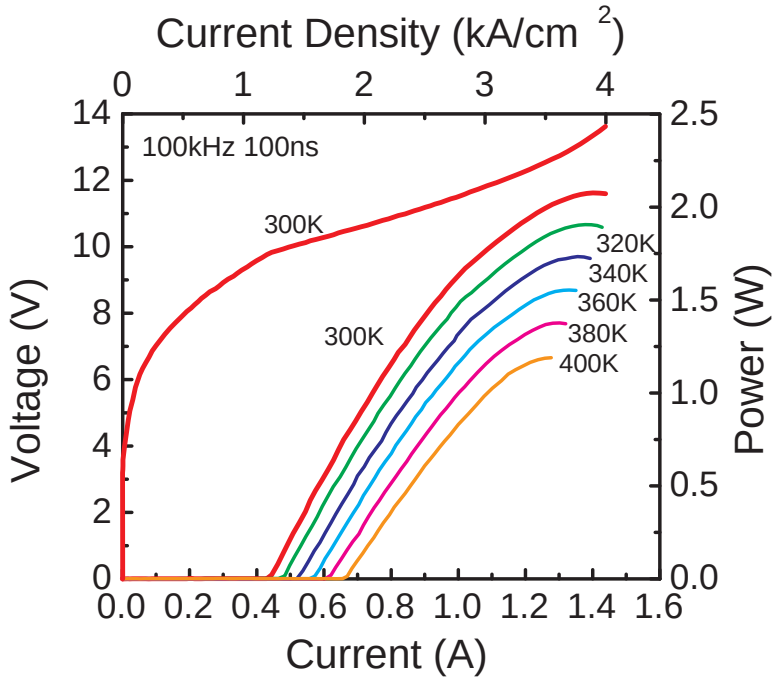

Figure 6.13: Pulsed current-light output characteristics of the 12 μm-wide, 3.0 mm-long, HR-coated, $\lambda\sim$6.8 μm DAU laser with a ridge structure at different heat sink temperatures. The voltage-current characteristic at 300 K is also shown.

Figure 6.14(a) shows CW current-light output and current-voltage characteristics. For current-light output characterization, the output power was measured with a calibrated thermopile detector. Room temperature CW operation of the present laser has been achieved without difficulty. A CW threshold current density at 300 K was observed to be very low, 1.6 kA/cm^2 and a high optical output power of 528 mW with a slope efficiency of 1.6 W/A was obtained at 300 K. The power consumption in CW at threshold is 17.4 kW/cm^2 which is reduced to 47% of that of the previous 8.7 μm DAU/MS laser. As a result, the laser has operated in CW mode at higher temperatures up to 102 °C. The threshold current densities for devices with 3 and 4 mm-long as a function of temperature are shown in Fig. 6.14(b). The characteristic temperatures T_0 for the present devices in pulsed and CW mode, deduced by the exponential function, $J_{\rm th} = J_0 \exp(T/T_0)$ are identified to be 241 K and 160 K. For epi-side up mounted, HR-coated laser with the 4 mm-long, 8 μm wide, lower threshold current densities are observed: 1.1 and 1.5 kA/cm^2 for pulsed and CW operations at 300 K.

The main reason for the decreased threshold current density is due to significantly reduced inter-subband absorption in the active region. The waveguide loss of the present devices which was extracted from the threshold current values at 300 K of the uncoated and HR-coated devices [14], are small value 6 cm^{-1} compared to the value 15 cm^{-1} in the previous 8.7 μm laser with similar doping level, fabricated by the same MOVPE machine. As the smaller waveguide loss of 7 cm^{-1} has been estimated in the bound-to-bound 8.6 μm lasers(Chapter 3) with the similar waveguide, injector structure and slightly higher doping level (Si, 8 $\times$ 10^{10} cm^{-2}), therefore, the loss in the previous DAU/MS laser can be regarded to be considerably high. For the dual-upper-state designs, there may exist larger absorption from the upper states to higher states, besides an inter-subband absorption in injector and free carrier absorption, since in the dual-upper-state designs an additional upper-state is inserted into an energy position of an original upper state. Unlike 8.7 μm DAU/MS QC laser case, for the present device the emission energy E_{43} is much larger value 183 meV compared to $E_{53}\sim$90 meV. Thus, the inter-subband absorption between state 5 and 3 can be regarded to be in an off-resonant condition.

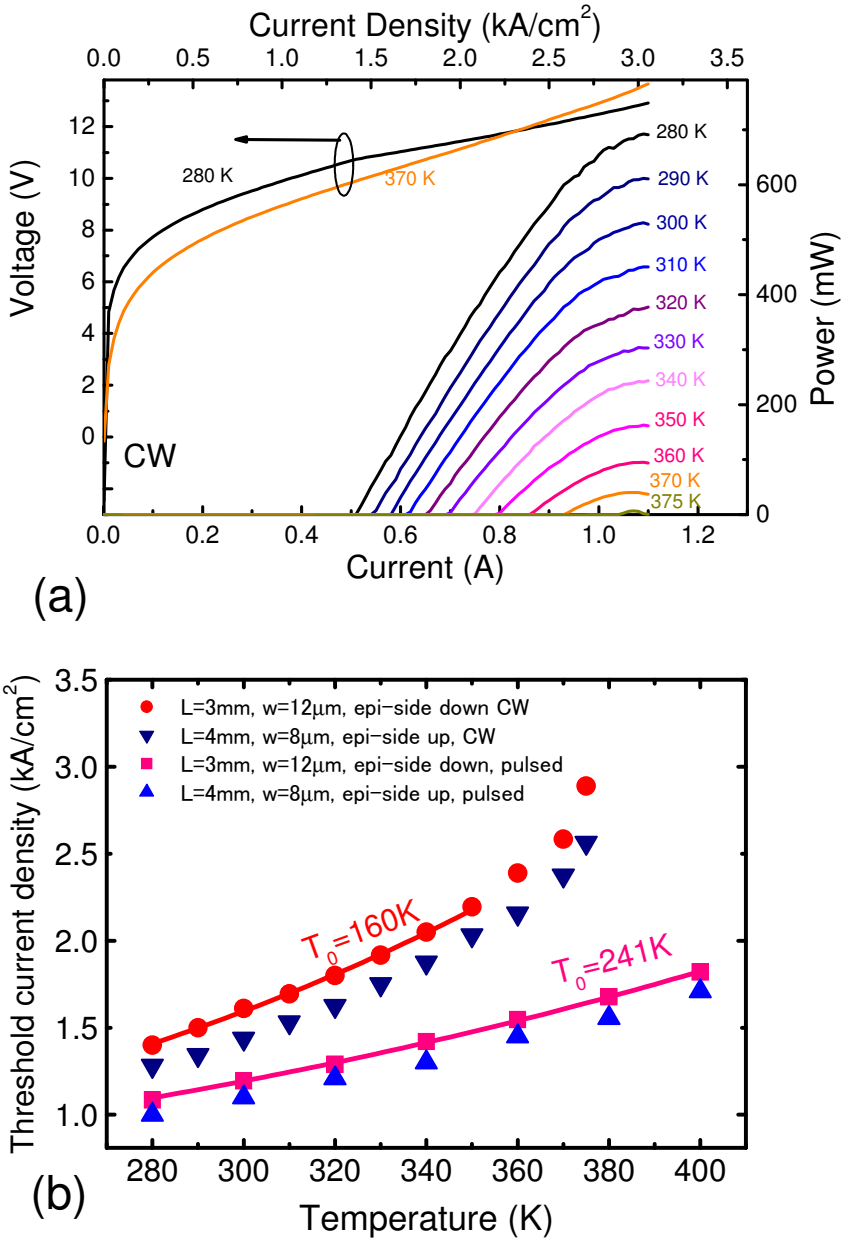

Figure 6.14: (a) CW current-light output characteristics of the 12 μm-wide, 3 mm-long, HR-coated, buried hetero-structured, $\lambda\sim$6.8 μm DAU/MS laser with a thick gold film at different heat sink temperatures. The voltage-current characteristics at 280 and 370 K are also shown. (b) Temperature-dependent threshold current densities for pulsed and CW modes for the 12 μm-wide, 3 mm-long, epi-side down bonded and 8 μm-wide, 4 mm-long, epi-side up bonded lasers.

The subthreshold amplified spontaneous emission and lasing spectra of the present laser at different currents (Fig. 6.15) exhibit its wide spectral width of over 570 cm^{-1} (from 1220 to 1780 cm^{-1}). The spectral measurements reveal a clear spectral narrowing with increasing current and no sign of multiple wavelength emissions unlike QC lasers with multiple stacks of active regions [4, 14]. The CW lasing spectra broaden as the current increased. The spectral width in pulsed operation around the maximum current reaches ~150 cm^{-1} which is broader than the values of identical-stack QC lasers with narrower EL width.

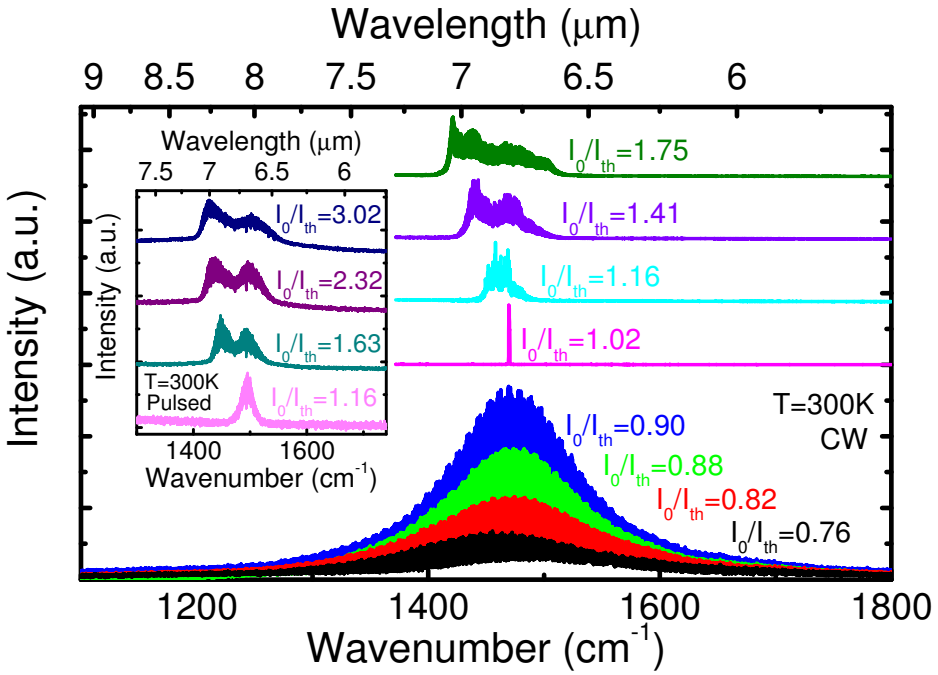

Figure 6.15: The sub-threshold amplified spontaneous emission and lasing spectra of the 3 mm-long, 12 μm-wide, HR-coated, buried hetero-structured, λ~6.8 μm DAU/MS laser in CW at 300 K at different currents. The inset shows lasing spectra in pulsed mode (100 kHz, 100 ns) at 300 K at different currents.

6.5 Conclusion

In this chapter, we further developed the design concept to achieve broadband QC laser and demonstrate a QC laser design based on the dual-upper-state to multiple-lower-state active region design. The 8.7 μm DAU devices exhibit a very wide EL spectrum ($\sim$500 cm^{-1}, $\Delta\lambda/\lambda_0\sim$0.4) as well as its voltage stability. The performance of the 8.7 μm laser with HR-coating has been demonstrated: a low threshold current density of 2.6 kA/cm^2 and a high maximum output power of 930 mW both at room temperature and a very high characteristic temperature of 510 K over the all temperature range of above room temperature. As a result of investigation on EL spectra, the observed high characteristic temperature has been interpreted in terms of a weak temperature-dependence of gain coefficient due to its spectrally homogeneous behavior and broad EL linewidth. Furthermore, for 6.8 μm DAU/MS design, high performance CW operation have been demonstrated: a low threshold current density of $\sim$1.5 kA/cm^2 and a high power of $>$500 mW with a high slope efficiency of $\sim$1.6 W/A in CW mode at 300 K. The HR-coated buried hetero-structured laser with an extremely wide EL, has operated in CW operation up to slightly above 100 °C. The DAU/MS design offer the great advantages for broadband tuning of an external cavity QC laser. In fact, using an external cavity set-up and the 6.8 μm DAU/MS device, a wide wavelength tuning has been demonstrated in CW operation at room temperature [15]. The tuning ranges of 248 cm^{-1} ($\Delta\lambda/\lambda_0 \sim 17\%$) in CW operation are achieved as shown in Fig. 6.16. The demonstrated tuning range in CW operation substantially exceeds the values obtained with the identical QC lasers based on conventional broadband active region designs (Fig. 6.17).

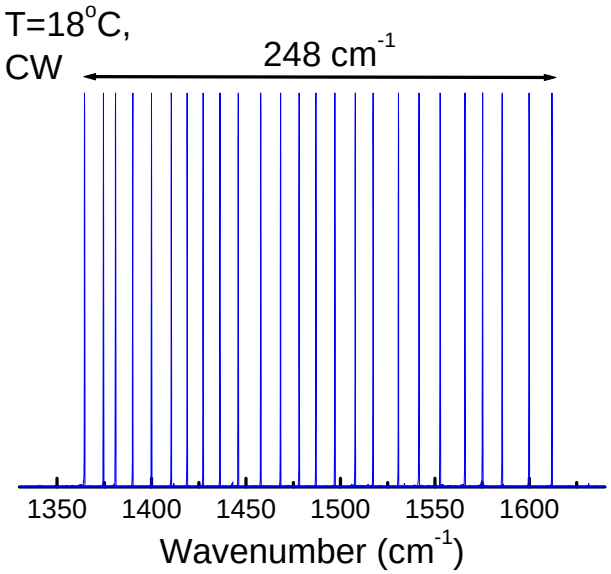

Figure 6.16: Tuning spectra of external cavity QC laser at various wavelengths. Spectra are measured at 18 °C in CW at fixed current of 700 mA.

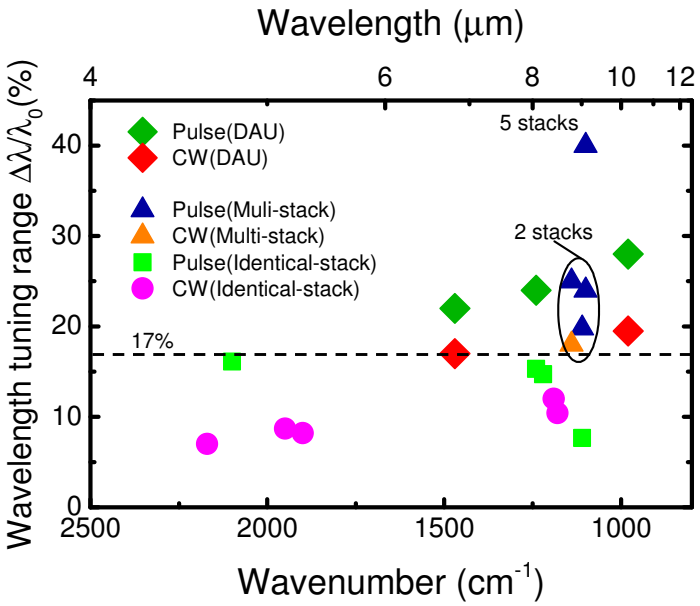

Figure 6.17: Current status of tuning ranges of external cavity QC lasers as a function of center wavenumber (wavelength).

References

[1] K. Fujita, S. Furuta, T. Dougakiuchi, A. Sugiyama, T. Edamura, and M. Yamanishi, "Broad-gain ($\Delta\lambda/\lambda_0$∼0.4), temperature-insensitive (T_0∼510K) quantum cascade lasers," Opt. Express **19**, 2694 (2011).

[2] G. P. Luo, C. Peng, H. Q. Le, S. S. Pei, W.-Y. Hwang, B. Ishaug, J. Um, J. N. Baillargeon, and C.-H. Lin, "Grating-tuned external-cavity quantum-cascade semiconductor lasers," Appl. Phys. Lett. **78**, 2834 (2001).

[3] A. Wittmann, A. Hugi, E. Gini, N. Hoyler, and J. Faist, "Heterogeneous High-Performance Quantum-Cascade Laser Sources for Broad-Band Tuning," IEEE J. Quantum Electron. **44**, 1083 (2008).

[4] A. Hugi, R. Terazzi, Y. Bonetti, A. Wittmann, M. Fischer, M. Beck, J. Faist, and E. Gini, "External cavity quantum cascade laser tunable from 7.6 to 11.4 μm," Appl. Phys. Lett. **95**, 061103 (2009).

[5] M. Geiser, C. Pflugl, A. Belyanin, Q. J. Wang, N. Yu, T. Edamura, M. Yamanishi, H. Kan, M. Fischer, A. Wittmann, J. Faist, and F. Capasso, "Gain competition in dual wavelength quantum cascade lasers," Opt. Express **18**, 9900 (2010).

[6] J. Faist, M. Beck, T. Aellen, and E. Gini, "Quantum Cascade Lasers based on a bound-to-continuum transition," Appl. Phys. Lett. **78**, 147 (2001).

[7] Y. Yao, W. O. Charles, T. Tsai, J. Chen, G. Wysocki, and C. F. Gmachl, "Broad-band quantum cascade laser gain medium based on a continuum-to-bound active region design," Appl. Phys. Lett. **96**, 211106 (2010).

[8] Y. Yao, X. Wang, J. Y. Fan, and C. F. Gmachl, "High performance continuum-to-continuum quantum cascade lasers with a broad gain bandwidth of over 400 cm^{-1}," Appl. Phys. Lett. **97**, 081115 (2010).

[9] K. Fujita, S. Furuta, A. Sugiyama, T. Ochiai, T. Edamura, N. Akikusa, M. Yamanishi, and H. Kan, "Room temperature, continuous-wave operation of quantum cascade lasers with single phonon resonance-continuum depopulation structures grown by metal organic vapor-phase epitaxy," Appl. Phys. Lett. **91**, 141121 (2007).

[10] K. Fujita, M. Yamanishi, T. Edamura, and S. Furuta, "High-performance, homogeneous broad-gain Quantum cascade lasers based on dual-upper-state design," Appl. Phys. Lett. **96**, 241107 (2010).

[11] A. Wittmann, Y. Bonetti, J. Faist, E. Gini, and M. Giovannini, "Intersubband linewidths in quantum cascade laser designs," Appl. Phys. Lett. **93**, 141103 (2008).

[12] Y. Arakawa and H. Sakaki, "Multidimensional quantum well laser and temperature dependence of its threshold current" Appl. Phys. Lett. **40**, 939 (1982).

[13] K. Fujita, S. Furuta, A. Sugiyama, T. Ochiai, A. Ito, T. Dougakiuchi, T. Edamura, and M. Yamanishi, "High-peformance quantum cascade lasers with wide electroluminescence ($\sim$600 cm^{-1}), operating in continuous-wave above 100 °C," Appl. Phys. Lett. **98**, 231102 (2011).

[14] A. Wittmann, T. Gresch, E. Gini, L. Hovzdara, N. Hoyler, M. Giovannini, and J. Faist, "High-performance bound-to-continuum quantum-cascade lasers for broad-gain applications," IEEE J. Quantum Electron. **44**, 36 (2008).

[15] T. Dougakiuchi, K. Fujita, N. Akikusa, A. Sugiyama, T. Edamura, and M. Yamanishi, "Broadband tuning of external cavity dual-upper-state quantum cascade lasers in continuous wave operation," Appl. Phys. Express **4**, 102101 (2011).

Chapter 7

Conclusions

In this thesis, creative new QC laser designs with designed upper-quantum-states, indirect pump (IDP) scheme and anti-crossed dual-upper-state (DAU) design, have been successfully demonstrated, and in addition extensive discussions of the physics of the IDP and DAU QC lasers have been presented. These structures offer the advantage, compared to conventional direct pump (DP)-QC lasers. We will summarize the contexts of this thesis below. After describing the background of this work in Chapter 1, we saw the basic principles of QC laser as well as the importance of electron dynamics in QC laser structures in Chapter 2.

The success of this work was based on wave function-engineering in quantum well structures. Thanks to the great flexibility of the wave function-engineering, electron transport in QC structure can be tailored to achieve strong population inversion. Quantum cascade laser relies on the method to improve the laser performances such as threshold current density and output power. Chapter 3 presents that our study of QC laser designs with conventional direct pump scheme shows that the threshold current density and the slope efficiency are sensitively affected by design parameters such as dipole moment, the number of cascade stages. Besides, for this study we propose a new depopulation structure, the single phonon resonance-continuum depopulation (SPC-depopulation) structure. We achieve CW operation of the QC lasers with the SPC-depopulation structure at room temperature by taking advantage of high device performance as well as expected allowance for thickness fluctuations of the energy separation between the

lower states. Moreover, we develop the SPC depopulation structure and achieve the highest wall-plug efficiency in the wavelength range of 7-9 μm.

Chapter 4 describes experimental results of QC lasers based on a novel pump scheme, named indirect pump scheme. The performance of the ridge-structured $\lambda \sim$8 μm QC laser based on the indirect pump scheme has been demonstrated: a threshold current density of 2.7 kA/cm^2 and a maximum output power of 362 mW both at room temperature, and a maximum lasing temperature of above 400 K. In particular, the lasers have exhibited high T_0-values of 310 K around room temperature. For temperature changes, the observed high stabilities of the threshold current and slope of the threshold current-versus-the inverse of cavity length have been interpreted in terms of suppressions of electron populations in the injectors caused by electron-transport dynamics, which were not visualized in the conventional direct pump scheme. Due to the strong suppression of electron populations in injectors, the long-wavelength $\lambda \sim$15 μm indirect pump QC laser with precisely designed active regions and low loss waveguide has exhibited very high performance: a low threshold-current-density of 3.5 kA/cm^2, a high maximum output power of 216 mW, and a high slope efficiency of 346 mW/A with recourse to the nonresonant absorption quenching in the injector, all at room temperature, and an extremely high characteristic temperature of T_0 $\sim$450 K over the high temperature range, 320-380 K. These are the best performance in long-wavelength >13 μm QC lasers at noncryogenic temperatures. The pump scheme would be a very powerful harness for high temperature operation of QC lasers operating in longer wavelength, in particular for terahertz region.

In Chapter 5, a broad-gain QC laser design with anti-crossed dual-upper-state design is proposed to clarify its own feasibility. Experimental results show homogeneous wide electroluminescence spectra of which shapes are insensitive to voltage changes. laser, emitting at $\lambda \sim$8.4 μm, demonstrates a high continuous-wave output power of 152 mW together with a high constant slope efficiency of 518 mW/A at room temperature. The spectrally homogeneous behavior of electroluminescence is interpreted in terms of the electron distribution model. Further, the strain-compensated lasers emitting $\lambda \sim$8.7 μm demonstrate conspicuous temperature performances. The laser characterized by super-linear current-light output

curves exhibit an extremely high characteristic temperature for the threshold current density above 330 K (T_0∼750 K). The slope efficiency grows with increasing temperature. Increasing the slope efficiencies has never been reported for quantum cascade lasers in the literature. In addition, for the pulsed operation of a short 1 mm length laser, the T_0-value reaches a value of 1085K above 340 K, which is highest value for ever reported QC lasers. These remarkable results are attributed to a strong suppression of electron populations in injectors, as well as to the suppression of the leakage current in the strain-compensated active region supplementarily.

In Chapter 6, we further improve the dual-upper-state design concept and fabricate QC lasers based on the anti-crossed dual-upper-state to continuum transition designs. As a result of felicitous designing of the active region, the devices exhibit an extremely wide EL spectrum (∼500cm^{-1}, $\lambda/\lambda_0 \sim 0.4$) as well as its voltage stability. Furthermore, the high performance of the λ ∼8 μm ridge laser with HR-coating has been demonstrated: a low threshold current density of 2.6 kA/cm^2 and a high maximum output power of 930 mW both at room temperature, and a maximum lasing temperature of above 400 K, and a very high characteristic temperature of 510 K over the all temperature range of above room temperature. The EL linewidth (λ/λ_0 ∼0.4) and the T_0-value (510 K) are far superior to the values of QCLs with conventional broad-gain designs. The observed high characteristic temperature has been interpreted in terms of a weak temperature-dependence of gain coefficient due to its spectrally homogeneous behavior and broad EL linewidth. Furthermore, as a result of the high T_0-value above room temperature, the HR-coated, BH structured laser, despite the broad EL linewidth, has operated successfully in CW operation up to slightly above 60 °C. Besides, the λ ∼6.8 μm devices exhibit extremely wide electroluminescence (>600 cm^{-1} FWHM) and subthreshold amplified spontaneous emission (∼570 cm^{-1}) spectra at room temperature. Despite showing such broad electroluminescence spectra, the buried hetero-structured lasers demonstrate a low threshold current density of ∼1.5 kA/cm^2 and a high power of >500 mW with a high slope efficiency of ∼1.6 W/A in CW mode at 300 K. The DAU design offers the great advantages for the broadband tuning of an external cavity QC laser. In fact, with

external cavity set-up, this device enables a wide tuning range even in the CW operation.

List of Publications

A. Journal Papers

1. Kazuue Fujita, Shinichi Furuta, Atsushi Sugiyama, Takahide Ochiai, Tadataka Edamura, Naota Akikusa, Masamichi Yamanishi, and Hirofumi Kan, "Room temperature, continuous-wave operation of quantum cascade lasers with single phonon resonance-continuum depopulation structures grown by metal organic vapor-phase epitaxy," Applied Physics Letters **91**, 141121-1 — 141121-3 (2007).

2. Masamichi Yamanishi, Kazuue Fujita, Tadataka Edamura, and Hirofumi Kan,"Indirect pump scheme for quantum cascade lasers: dynamics of electron-transport and very high T_0-values," Optics Express **16**, 20748 — 20758 (2008).

3. Kazuue Fujita, Shinich Furuta, Atsushi Sugiyama, Takahide Ochiai, Tadataka Edamura, Naota Akikusa, Masamichi Yamanishi and Hirofumi Kan, "High-performance $\lambda \sim$8.6 μm quantum cascade lasers with single phonon-continuum depopulation structures," IEEE Journal of Quantum Electronics **46**, 683 — 688 (2010).

4. Kazuue Fujita, Tadataka Edamura, Shinichi Furuta, and Masamichi Yamanishi, "High-performance, homogeneous broad-gain quantum cascade lasers based on dual-upper-state design," Applied Physics Letters **96**, 241107-1 — 241107-3 (2010).

5. Kazuue Fujita, Masamichi Yamanishi, Tadataka Edamura, Atsushi Sugiyama, and Shinichi Furuta, "Extremely high T_0-values ($\sim$450 K) of long-wavelength

($\sim$15 μm), low-threshold-current-density quantum-cascade lasers based on the indirect pump scheme," Applied Physics Letters **97**, 201109-1 — 201109-3 (2010).

6. Kazuue Fujita, Shinichi Furuta, Tatsuo Dougakiuchi, Atsushi Sugiyama, Tadataka Edamura, and Masamichi Yamanishi, "Extremely broad-gain ($\Delta\lambda/\lambda_0$ $\sim$0.4), temperature-insensitive (T_0 $\sim$510K) quantum cascade lasers," Optics Express **19**, 2694 — 2701 (2011).

7. Kazuue Fujita, Shinichi Furuta, Atsushi Sugiyama, Takahide Ochiai, Akio Ito, Tatsuo Dougakiuchi, Tadataka Edamura, and Masamichi Yamanishi, "High-temperature quantum cascade lasers with wide electroluminescence ($\sim$600 cm^{-1}), operationg in continuous wave above 100 °C," Applied Physics Letters **98**, 231102-1 — 231102-3 (2011).

8. Kazuue Fujita, Masamichi Yamanishi, Tatsuo Dougakiuchi, Shinich Furuta, Atsushi Sugiyama, and Tadataka Edamura, "Extremely temperature-insensitive continuous-wave quantum cascade lasers," Applied Physics Letters **101**, 181111-1 — 181111-3 (2012).

B. Proceedings of International Conferences

1. Kazuue Fujita, Tadataka Edamura, Naota Akikusa, Atsushi Sugiyama, Takahide Ochiai, Shinichi Furuta, Masamichi Yamanishi, and Hirofumi Kan, "Quantum cascade lasers based on single phonon resonance-continuum depopulation structures," SPIE Photonics West **7230**, 41 (2009)

2. Kazuue Fujita, Masamichi Yamanishi, Shinich Furuta, Tatsuo Dougakiuchi, Atsushi Sugiyama, and Tadataka Edamura, "Extremely temperature insensitive, continuous-wave broadband quantum cascade lasers," SPIE Photonics West **8640**, Novel In-Plane Semiconductor lasers XII, 86400R (2013)

C. Presentation at International Conferences

1. Kazuue Fujita, Shinichi Furuta, Atsushi Sugiyama, Takahide Ochiai, Tadataka Edamura, Naota Akikusa, Masamichi Yamanishi, and Hirofumi Kan, "Room Temperature Continuous-Wave Operation of Quantum Cascade Lasers with Single Phonon Resonance-Continuum Depopulation Structure," The 20th Annual Meeting of The IEEE Lasers and Electro-Optics Society (LEOS2007), ThJ2, September 2007, Orlando, FL.

2. Kazuue Fujita, Shinichi Furuta, Atsushi Sugiyama, Takahide Ochiai, Tadataka Edamura, Naota Akikusa, Masamichi Yamanishi, and Hirofumi Kan, and Hirofumi Kan, "Room Temperature CW Operation of 5.2 μm Quantum Cascade Lasers with Simple Ridge Structures Grown by MOVPE," CLEO, May 1-5, 2008, San Jose, CA.

3. Masamichi.Yamanishi, Kazuue Fujita, Tadataka Edamura, Atsushi Sugiyama, Takahide Ochiai, Shinichi Furuta, Naota Akikusa, Hirofumi Kan, "Quantum Cascade Lasers with Indirect Pump Scheme: High T_0-Values due to Dynamical Suppressions of Electron Populations in Injectors," The 3rd International Quantum Cascade Lasers School & Workshop (IQCLSW2008), 142, 2008, Monte Verita, Switzerland.

4. Tadataka Edamura, Naota Akikusa, Atsushi Sugiyama, Takahide Ochiai, Kazuue Fujita, Shinichi Furuta, Akio Ito, Masamichi Yamanishi, Hirofumi Kan, "Quantum Cascade Lasers Development at HAMAMATSU and Their Applications," The 3rd International Quantum Cascade Lasers School & Workshop (IQCLSW2008), 157, 2008, Monte Verita, Switzerland. [invited]

5. Kazuue Fujita, Tadataka Edamura, Naota Akikusa, Atsushi Sugiyama, Takahide Ochiai, Shinichi Furuta, Masamichi Yamanishi, and Hirofumi Kan, "Quantum cascade lasers based on single phonon resonance-continuum depopulation structures," SPIE Photonics West 7230-41, 2009, San Jose, CA.

6. Kazuue Fujita, Masamichi Yamanishi, Tadataka Edamura, Shinichi Furuta, Atsushi Sugiyama, Takahide Ochiai, Akio Ito, Naota Akikusa, and Hirofumi

Kan, "Long wavelength(>13.5 μm) quantum cascade lasers based on indirect pump scheme," SPIE Photonics West 7616-61, 2010, San Francisco, CA.

7. Kazuue Fujita, Masamichi Yamanishi, Tadataka Edamura, Shinichi.Furuta, "Homogeneous broad-gain quantum cascade lasers based on dual-upper design" The 4th International Quantum Cascade Lasers School & Workshop (IQCLSW2010), 2010, Florence, Italy.

8. Masamichi Yamanishi, Kazuue Fujita, Tadataka Edamura, "Indirect Pump Scheme for Quantum Cascade Lasers : Theory and Experiments," The 10th International Conference on Mid-IR Optoelectronics:Materials and Devices (MIOMD), 40, 2010, Shanghai, China.[Invited]

9. Tadataka Edamura, Kazuue Fujita, Shinichi Furuta, Tatsuo Dougakiuchi, Atsushi Sugiyama, Hirofumi Miyajima, Naota Akikusa, Masamichi Yamanishi, Hirofumi Kan, "High Power Broad-area Quantum Cascade Lasers based on SPC Design emitting at 8.5 μm," The 10th International Conference on Mid-IR Optoelectronics:Materials and Devices (MIOMD), 154, 2010, Shanghai, China.

10. Kazuue Fujita, Shinichi Furuta, Tatsuo Dougakiuchi, Atsushi Sugiyama, Tadataka Edamura and Masamichi Yamanishi," Extremely Broad-gain Quantum Cascade Lasers based on Dual-upper-state design," Conference on Lasers and Electro-Optics 2011, CMQ2, 2011, Baltimore, MD .

11. Masamichi Yamanishi, Tadataka Edamura, Kazuue Fujita, and Tatsuo Dougakiuchi,"Key design-concepts for mid-infrared and THz quantum cascade lasers : dual upper-states and indirect pumping," Photonics West 2012, 8277-28, 2012, San Francisco, CA. [Invited]

12. Tatsuo Dougakiuchi, Kazuue Fujita, Tadataka Edamura, Masamichi Yamanishi, Shinichi Furuta and Atsushi Sugiyama, "Broadband CW tuning of external cavity anticrossed dual upper-state quantum cascade lasers," Photonics West 2012, 8277-30, 2012, San Francisco, CA.

13. Kazuue Fujita, Masamichi Yamanishi, Shinichi Furuta, Atsushi Sugiyama, Tatsuo Dougakiuchi and Tadataka Edamura, "Super-linear performance of Dual-upper-state Quantum Cascade Lasers" Conference on Lasers and Electro-Optics 2012, JW2A.86, 2012, San Jose, CA.

14. Kazuue Fujita, Masamichi Yamanishi, Shinich Furuta, Tatsuo Dougakiuchi, Atsushi Sugiyama, and Tadataka Edamura, "Extremely temperature insensitive, continuous-wave broadband quantum cascade lasers," SPIE Photonics West 2013, 8640-26, 2013, San Francisco, CA.

15. Kazuue Fujita, Masamichi Yamanishi, Shinichi Furuta, Kazunori Tanaka, and Tadataka Edamura, "Relation between Excess Energy and Device Performance in THz Indirect Pumping Quantum-Cascade Lasers," International Workshop on Optical Terahertz Science and Technology (OTST 2013), Th3-27, 2013, Kyoto, Japan.

D. Related Publications

1. M. Yamanishi, T. Edamura, K. Fujita, N. Akikusa, and H. Kan, "Theory of the intrinsic linewidth of quantum-cascade lasers: Hidden reason for the narrow linewidth and line-broadening by thermal photons," IEEE J. Quantum Electron. **46**, 12 (2008).

2. Tatsuo Dougakiuchi, Kazuue Fujita, Naota Akikusa, Atsushi Sugiyama, Tadataka Edamura, and Masamichi Yamanishi, "Broadband Tuning of External Cavity Dual-Upper-State Quantum-Cascade Lasers in Continuous Wave Operation," Applied Physics Express **4**, 102101-1–102101-3, (2011).

3. Kazuue Fujita, Masamichi Yamanishi, Shinichi Furuta, Kazunori Tanaka, Tadataka Edamura, Tillmann Kubis, and Gerhard Klimeck, "Indirectly pumped 3.7 THz InGaAs/InAlAs quantum-cascade lasers grown by metal-organic vapor-phase epitaxy," Optics Express **20**, 20647–20658, (2012).

E. Patents

1. M. Yamanishi, T. Edamura, N. Akikusa, K. Fujita, QUANTUM CASCADE LASER, US7843981(2010).

2. T. Edamura, N. Akikusa, K. Fujita, A. Sugiyama, T. Ochiai, QUANTUM CASCADE LASER, US8068528 (2011).

3. A. Sugiyama, T. Ochiai, K. Fujita, N. Akikusa, T. Edamura, S. Furuta, QUANTUM CASCADE LASER ELEMENT, US8098701(2012).

4. T. Edamura, K. Fujita, A. Higuchi, N. Akikusa, M. Yamanishi, SEMICONDUCTOR LIGHT EMITTING DEVICE, US8330140 (2012).

5. M. Yamanishi, K. Fujita, T. Edamura, N. Akikusa, QUANTUM CASCADE LASER, US8374208 (2013).

Acknowledgements

First of all, I, the author, would like to express his deep gratitude to Prof. Masao Kitano, Kyoto University, for providing opportunity to accomplish this thesis and for his suggestion and guidance. I also would like to thank Prof. Yoichi Kawakami, and Prof. Osamu Sakai, Kyoto University, for their valuable advice and comments on the manuscript.

The present work has been performed mainly as a research and development program of Hamamatsu Photonics K.K. I am very grateful to former President Teruo Hiruma, President Akira Hiruma, and Director Dr. Tsutomu Hara of Hamamatsu Photonics K.K. for their encouragement and support for the present work.

I wish to express sincere gratitude to Emeritus Prof. Masamichi Yamanishi, Hiroshima University and currently Research Fellow of Central Research Laboratory, Hamamatsu Photonics K.K. for his continuous guidance, supervision, and encouragement for this study. He supported me during this study and was always available to discuss the physics of our devices and offer me advice and direction concerning the progression of my work.

I would like to express especially grateful appreciation to Dr. Hirofumi Kan, Director of Hamamatsu Photonics K.K. for his support and for providing the opportunity to initiate the research on quantum cascade laser at Hamamatsu Photonics K.K.

I also would like to express grateful to Mr. Minoru Niigaki for his encouragement as Manager of Central Research Laboratory, Hamamatsu Photonics K.K.

I wish to acknowledge Prof. Federico Capasso and Dr. Romain Blanchard, Harvard University for their fruitful discussions on quantum cascade laser designs.

The contents of the present thesis were performed in collaboration with QCL team of Hamamatsu Photonics K.K. I would also like to express my grateful thanks to my colleagues: Dr. Tadataka Edamura for his guidance for this study, for his management of QCL project, and for growth of device structures by MBE technique. Mr. Shinichi Furuta for growth of device structures by MOVPE technique. Their excellent growth technologies were crucial to this work. Mr. Naota Akikusa for his advice on laser measurements, and for his helpful discussion on applications (and commercialization) of QC lasers. Mr. Atsushi Sugiyama, Mr. Takahide Ochiai and Mr. Akio Ito for carrying out the device fabrications including wafer processing and laser mounting. Their support and techniques were absolutely essential to making this work. Mr. Tatsuo Dougakiuchi for his helpful assistance in measurements, and for his efforts in achieving nice broadband tuning results which make clear the powerful potential of the dual-upper-state design.

Thanks again to all of them for their cooperation and helpful discussions in creating and developing the present work.

I would also like to express my grateful to QCL team: Mr. Nobutaka Suzuki, Ms. Keiko Makita, Mr. Toshimasa Matsuno, Mr. Kousuke Shibata, Ms. Misa Ota, Mr. Yuji Kaneko, Mr. Tomotaka Suzuki, Mr. Kazuma Tanimura, Ms. Yoko Sugaya, and Mr. Masahiro Hitaka.

Furthermore, I would like to thank all the people working in the same office for sharing their technology and support, especially Mr. Toru

Hirohata, Dr. Harumasa Yoshida, Dr. Kazuyoshi Kuroyanagi, Mr. Kazunori Tanaka, and Dr. Yasufumi Takagi.

Finally, I would like to express my gratitude to my parents for their heartfelt encouragement. I would like to thank my wife, Iyoko, for her patience, great support, and understanding. This thesis would not have been possible without your help.

April 30, 2014

Kazuue Fujita